

KAUNAS UNIVERSITY OF TECHNOLOGY

MATAS STEPONAITIS

CHARGE TRANSPORTING MATERIALS
CONTAINING DIPHENYLETHENYL OR
DIAZACENE MOIETIES FOR APPLICATION
IN PEROVSKITE SOLAR CELLS

Doctoral Dissertation
Natural Sciences, Chemistry (N 003)

Kaunas, 2021

This doctoral dissertation was prepared at Kaunas University of Technology, Faculty of Chemical Technology, Department of Organic Chemistry during the period of 2017–2021.

Scientific Supervisor:

Assoc. Prof. Dr. Tadas MALINAUSKAS (Kaunas University of Technology, Natural Sciences, Chemistry, N 003).

Editor: Dr. Armandas Rumšas (Publishing House “Technologija”)

Dissertation Defence Board of Chemistry Science Field:

Prof. Dr. Saulius GRIGALEVIČIUS (Kaunas University of Technology, Natural Sciences, Chemistry, N 003) – **chairperson**;

Dr. Marius FRANCKEVIČIUS (State Research Institute Center for Physical Sciences and Technology, Natural Sciences, Physics, N 002);

Prof. Dr. Vytas MARTYNAITIS (Kaunas University of Technology, Natural Sciences, Chemistry, N 003);

Prof. Dr. Edvinas ORENTAS (Vilnius University, Natural Sciences, Chemistry, N 003);

Assoc. Prof. Dr. Jolanta ROUSSEAU (Artois University, France, Natural Sciences, Chemical Engineering, T 005).

The official defence of the dissertation will be held at 10 a.m. on 20 December, 2021 at the public meeting of Dissertation Defence Board of Chemistry Science Field in Dissertation defence Hall at Kaunas University of Technology.

Address: Donelaičio 73-403, LT-44249, Kaunas, Lithuania.

Phone: (+370) 37 300 042; fax: (+370) 37 324 144; email doktorantura@ktu.lt

This doctoral dissertation was sent out on 19 November, 2021.

The doctoral dissertation is available on the internet at <http://ktu.edu> and at the library of Kaunas University of Technology (Donelaičio 20, LT-44239, Kaunas, Lithuania).

© M. Steponaitis, 2021

KAUNO TECHNOLOGIJOS UNIVERSITETAS

MATAS STEPONAITIS

PEROVSKITINIAMS SAULĖS ELEMENTAMS
SKIRTOS KRŪVĮ PERNEŠANČIOS
MEDŽIAGOS SU DIFENILETENILO ARBA
DIAZAACENO FRAGMENTAIS

Daktaro disertacija
Gamtos mokslai, chemija (N 003)

Kaunas, 2021

Disertacija rengta 2017–2021 metais Kauno technologijos universiteto Cheminės technologijos fakulteto Organinės chemijos katedroje.

Mokslinis vadovas:

doc. dr. Tadas MALINAUSKAS (Kauno technologijos universitetas, gamtos mokslai, chemija, N 003).

Redagavo Violeta Meiliūnaitė (leidykla „Technologija“)

Chemijos mokslo krypties disertacijos gynimo taryba:

prof. dr. Saulius GRIGALEVIČIUS (Kauno technologijos universitetas, gamtos mokslai, chemija, N 003) – pirmininkas;

dr. Marius FRANCKEVIČIUS (Valstybinis mokslinių tyrimų institutas, Fizinių ir technologijos mokslų centras, gamtos mokslai, fizika, N 002);

prof. dr. Vytas MARTYNAITIS (Kauno technologijos universitetas, gamtos mokslai, chemija, N 003);

prof. dr. Edvinas ORENTAS (Vilniaus universitetas, gamtos mokslai, chemija, N 003);

doc. dr. Jolanta ROUSSEAU (Artua universitetas, Prancūzija, technologijos mokslai, chemijos inžinerija, T 005).

Disertacija bus ginama viešame Chemijos mokslo krypties disertacijos gynimo tarybos posėdyje 2021 m. gruodžio 20 d. 10 val. Kauno technologijos universiteto Disertacijų gynimo salėje.

Adresas: K. Donelaičio g. 73-403, 44249 Kaunas, Lietuva.

Tel. (370) 37 300 042; faks. (370) 37 324 144; el. paštas doktorantura@ktu.lt

Disertacija išsiųsta 2021 m. lapkričio 19 d.

Su disertacija galima susipažinti interneto svetainėje <http://ktu.edu> ir Kauno technologijos universiteto bibliotekoje (K. Donelaičio g. 20, 44239 Kaunas).

CONTENTS

| | |
|---|----|
| 1. INTRODUCTION | 11 |
| 2. LITERATURE REVIEW | 14 |
| 2.1. Perovskites and their properties..... | 14 |
| 2.2. Perovskite solar cells | 18 |
| 2.3. Doped hole transporting materials for perovskite solar cells | 22 |
| 2.4. Small molecular dopant-free hole transporting materials..... | 28 |
| 2.5. Polymeric, organometallic and inorganic materials as dopant-free HTMs | 34 |
| 2.6. Conclusions | 37 |
| 3. RESULTS AND DISCUSSION..... | 38 |
| 3.1. Triphenylamine derivatives as hole transporting materials | 38 |
| 3.1.1. Synthesis of quaternary ammonium compounds..... | 38 |
| 3.1.2. Thermal properties..... | 40 |
| 3.1.3. Photoelectrical properties | 43 |
| 3.1.4 Absorption and emission spectra..... | 45 |
| 3.1.5 Fluorescence quantum yield | 48 |
| 3.1.6 Photophysical properties in nanoparticles | 50 |
| 3.1.7 Conclusion of Chapter 3.1 | 51 |
| 3.2. Semiconductive polymers as hole transporting materials in perovskite solar cells..... | 52 |
| 3.2.1. Synthesis of triphenylamine based polymers | 53 |
| 3.2.2. Synthesis of polymers based on well performing hole transporting materials | 57 |
| 3.2.3. Synthesis of polymers containing dihydrodiazapentacene or dihydrodiazatetracene as the central core..... | 60 |
| 3.2.4. Thermal properties..... | 61 |
| 3.2.5. Optical properties | 63 |
| 3.2.6. Photoelectric properties | 67 |
| 3.2.7. Conclusion of Chapter 3.2..... | 69 |
| 3.3. Small-molecule diazacenes as hole transporting materials | 69 |

| | |
|---|-----|
| 3.3.1. Synthesis of dihydrodiazatetracene and dihydrodiazapentacene derivatives | 70 |
| 3.3.2. Thermal properties | 73 |
| 3.3.3. Optical properties | 78 |
| 3.3.4. Photoelectrical properties | 80 |
| 3.3.5. Conclusion of Chapter 3.3 | 85 |
| 3.4. Investigation of new chromophoric systems containing diphenylethenyl moieties | 85 |
| 3.4.1. Synthesis of novel compounds with multiple diphenylethenyl fragments in their structure | 85 |
| 3.4.2. Thermal properties | 89 |
| 3.4.3. Optical properties | 94 |
| 3.4.4. Photoelectrical properties | 98 |
| 3.4.5. Results of perovskite solar cells | 103 |
| 3.4.6. Conclusions of Chapter 3.4 | 106 |
| 3.5. Aniline based hole transporting materials | 107 |
| 3.5.1 Synthesis of 1,1-diphenylcyclohexane and biphenyl derivatives containing phenylethenyl moieties | 107 |
| 3.5.2. Thermal properties | 109 |
| 3.5.3. Optical properties | 114 |
| 3.5.4. Photophysical properties | 117 |
| 3.5.5. Results of perovskite solar cells | 122 |
| 3.5.6. Conclusion of Chapter 3.5 | 123 |
| 4. EXPERIMENTAL PART | 124 |
| 4.1. Instrumentation | 124 |
| 4.2. Materials | 128 |
| 5. MAIN RESULTS AND CONCLUSIONS | 163 |
| 6. SANTRAUKA | 165 |
| Įvadas | 165 |
| 1. Skyles pernešantys polimeriniai puslaidininkiniai perovskitiniam saulės elementams | 168 |
| 1.1. Trifenilamino polimerų ir monomerų su vinilo grupėmis sintezė | 169 |
| 1.2. Susintetintų junginių terminės savybės | 172 |

| | |
|---|-----|
| 1.3. Optinės susintetintų junginių savybės | 174 |
| 1.4. Fotolektrinės savybės..... | 175 |
| 1.5. Skyriaus išvados | 175 |
| 2. Mažamolekuliniai diazaacenu dariniai | 176 |
| 2.1. Dihydrodiazapentaceno ir dihydrodiazatetraceno darinių sintezė | 177 |
| 2.2. Terminės savybės | 179 |
| 2.3. Optinės savybės | 180 |
| 2.4. Fotolektrinės savybės..... | 183 |
| 2.5. Skyriaus išvados | 186 |
| 3. Naujų sistemų, turinčių difeniletetilfragmentų, tyrimas | 187 |
| 3.1. Junginių su keliais difeniletetilfragmentais sintezė | 187 |
| 3.2. Fotolektrinės savybės..... | 190 |
| 3.3. Perovskitinių saulės celių rezultatai | 192 |
| 3.4. Skyriaus išvados | 195 |
| 4. Anilino dariniai kaip skylės pernešančios medžiagos | 195 |
| 4.1. Anilino darinių, turinčių difeniletetilfragmentų, sintezė..... | 195 |
| 4.2. Terminės savybės | 197 |
| 4.3. Fotolektrinės savybės..... | 200 |
| 4.4. Perovskitinių saulės elementų rezultatai..... | 201 |
| 4.5. Skyriaus išvados | 201 |
| Pagrindiniai rezultatai ir išvados | 202 |
| 7. REFERENCES | 205 |
| 8. CURRICULUM VITAE..... | 231 |
| 9. LIST OF AUTHOR'S PUBLICATIONS AND CONFERENCES..... | 232 |
| 10. ACKNOWLEDGEMENTS..... | 233 |

LIST OF ABBREVIATIONS AND PHYSICAL UNITS

| | |
|-----------------------|---|
| μ | charge carrier mobility; |
| δ | chemical shifts parameter; |
| ν | wavelength in cm^{-1} ; |
| λ | wavelength; |
| σ | electrical conductivity; |
| μ_0 | zero field charge carrier mobility; |
| ^{13}C NMR | carbon (^{13}C) nuclear magnetic resonance; |
| ^1H NMR | proton nuclear magnetic resonance; |
| A | acceptor; |
| Ac_2O | acetic anhydride; |
| ACN | acetonitrile; |
| Ar | aromatic; |
| atm | atmosphere; |
| BCP | bathocuproine; |
| CCD | charge-coupled device; |
| CDCl_3 | deuterated chloroform; |
| CSA | (\pm)-camphor-10-sulfonic acid; |
| CT | charge transfer; |
| CV | cyclic voltammetry; |
| D | donor; |
| d | layer thickness; |
| DCM | dichloromethane; |
| DHDAA | dihydrodiazacene; |
| DHDAP | dihydrodiazapentacene; |
| DHDAT | dihydrodiazatetracene; |
| DJ | Dion-Jacobson; |
| DMA | dimethylacetamide; |
| DMF | <i>N,N</i> -dimethylformamide; |
| DMSO | dimethyl sulfoxide; |
| DSC | differential scanning calorimetry; |
| EA | electron affinity; |
| E_g | energy band gap; |
| E_g^{opt} | optical band gap; |
| ETL | electron transporting layer; |
| ETM | electron transporting material; |
| EtOH | ethanol; |
| FA | formamidinium; |
| Fc | ferrocene; |
| FF | fill factor; |
| FK209 | tris(2-(1 <i>H</i> -pyrazol-1-yl)-4- <i>tert</i> -butylpyridine)cobalt(III) tri[bis(trifluoromethane)sulfonamide]; |
| FL | fluorescence; |
| FTO | fluorine-doped tin oxide; |

| | |
|-------------------------|--|
| HOIP | hybrid organic-inorganic perovskite; |
| HOMO | highest occupied molecular orbital; |
| Ht | heterocycle; |
| HTL | hole transporting layer; |
| HTM | hole transporting material; |
| I_p | ionization potential; |
| IR | infrared; |
| ITO | indium tin oxide; |
| J | coupling constant in Hz; |
| J_{sc} | short circuit current; |
| LDA | lithium diisopropylamide; |
| LED | light-emitting diode; |
| LiTFSI | bis(trifluoromethane)sulfonimide lithium salt; |
| LUMO | lowest unoccupied molecular orbital; |
| MA | methylammonium; |
| MAI | methylammonium iodide; |
| MAPI | methylammonium lead iodide; |
| \overline{Mn} | number of the average molar mass; |
| $\overline{M_w}$ | molecular weight; |
| \overline{Mw} | mass average molar mass; |
| MWR | microwave reactor; |
| n-BuLi | butyl lithium; |
| NaHMDS | sodium bis(trimethylsilyl)amide; |
| NaOtBu | sodium <i>tert</i> -butoxide; |
| NPs | nanoparticles; |
| NBS | <i>N</i> -bromosuccinimide; |
| Ni(COD) | bis(1,5-cyclooctadiene)nickel(0); |
| NMR | nuclear magnetic resonance; |
| OBDA | 4,4'-oxybis[<i>N,N</i> -bis(2,2-diphenylethenyl)aniline] ; |
| ODCB | <i>o</i> -dichlorobenzene; |
| OFET | organic field-effect transistors; |
| OLED | organic light-emitting diode; |
| OLET | organic light-emitting transistors; |
| OPV | organic photovoltaics; |
| PCBM | phenyl-C61-butyric acid methyl ester; |
| PCE | solar-to-electric power conversion efficiencies; |
| PC-Z | bisphenol Z polycarbonate; |
| Pd(dppf)Cl ₂ | [1,1'-Bis(diphenylphosphino)ferrocene]dichloropalladium(II); |
| PESA | photoelectron spectroscopy in air; |
| Ph | phenyl; |
| PL | photoluminescence; |
| PPh ₃ | triphenylphosphine; |
| ppm | parts per million; |
| PS | polystyrene; |
| PSC | perovskite solar cells; |

| | |
|-------------------------|---|
| PTAA | poly[bis(4-phenyl)(2,4,6-trimethylphenyl)amine] ; |
| PTFE | polytetrafluoroethylene; |
| QY | quantum yield; |
| RP | Ruddlesden-Popper; |
| SAM | self-assembling monolayer; |
| SCE | standard-reference Calomel electrode; |
| SHE | standard hydrogen electrode; |
| spiro-OMeTAD | 2,2',7,7'-tetrakis-(<i>N,N</i> -di- <i>p</i> -methoxyphenylamine)-9,9'-spirobifluorene; |
| <i>T</i> | temperature; |
| <i>t</i> | time; |
| <i>t</i> BP | 4- <i>tert</i> -butyl pyridine; |
| <i>t</i> -Bu | <i>tert</i> -butyl; |
| TCO | transparent conductive oxide; |
| T_{cr} | crystallization temperature; |
| T_{dec} | decomposition temperature; |
| T_g | glass transition temperature; |
| TGA | thermogravimetric analysis; |
| THF | tetrahydrofuran; |
| TLC | thin layer chromatography; |
| T_m | melting point; |
| TMS | trimethylsilane; |
| T_{poly} | polymerization temperature; |
| t_{poly} | polymerization time; |
| TPA | triphenylamine; |
| TPD | <i>N,N</i> -bis(3-methylphenyl)- <i>N,N</i> -bis(phenyl) benzidine; |
| TTBP · HBF ₄ | tri- <i>tert</i> -butylphosphonium tetrafluoroborate; |
| UV-Vis | ultraviolet-visible; |
| V_{oc} | open circuit photovoltage; |
| W | watt; |
| XPhos-Pd-G2 | chloro(2-dicyclohexylphosphino-2',4',6'-triisopropyl-1,1'-biphenyl)[2-(2'-amino-1,1'-biphenyl)]palladium(II); |
| XTOF | xerographic time of flight technique; |
| ε | extinction coefficient. |

1. INTRODUCTION

Scientific and technological advancement enabled the use of a wide variety of organic optoelectronic materials in photovoltaics, such as organic light-emitting diodes (OLED), organic photovoltaic devices (OPV), organic field-effect transistors (OFET), organic photoreceptors and organic photorefractive devices [1]. The application of organic semiconductors as active emissive, charge transport or receptor layers is of great interest due to their advantages of low temperature processing, uniform thin film formation, and large-area flexible device fabrication. Moreover, optimization of organic structures in thin film fabrication led to the emergence of multifunctional devices, such as organic light-emitting transistors (OLET) employing charge transfer and emission capabilities in the same device [2]. Therefore, good charge transport, photostability and, in some cases, emission properties of organic compounds are crucial for further research and development of efficient optoelectronic devices.

One of the most promising technologies making use of charge carrying organic molecules is hybrid perovskite solar cells (PSCs). The fabrication process of these devices is relatively simple [3, 4], and it often employs organic hole transporting materials (HTM) [5], in some cases also organic electron transporting materials (ETM) [6]. Furthermore, the easily tuneable band gap of perovskite [7] allows usage of HTMs with various energy levels in order to reach the best possible performance. Having that in mind, it should come as no surprise that organic materials have been used time and time again to achieve great results in PSC whose power conversion efficiency (PCE) is currently reaching more than 25% [8]. Despite such success, PSCs are still suffering from some drawbacks which hold them back from being produced commercially. Such issues include unsolved fabrication issues, costly charge transporting materials, and the long term stability of the devices. There are mainly three intrinsic factors leading to instability of perovskite: hygroscopicity of perovskite itself, thermal instability, and ion migration [9]. The first two issues could be solved by modifying perovskite and the architecture of the device [10, 11, 12], while ion migration might be mitigated by either designing HTMs with appropriate properties [13, 14] or alternating the doping procedure that is usually used to improve the performance of the HTM [15, 16]. On the matter of cost of PSCs, a significant amount of it is attributed to the most commonly used organic HTMs 2,2',7,7'-tetrakis-(*N,N*-di-*p*-methoxyphenylamine)-9,9'-spirobifluorene (spiro-MeOTAD) and poly[bis(4-phenyl)(2,4,6-trimethylphenyl)amine] (PTAA) [17], thus a less costly alternative HTM with similar or better properties is desired.

Organic synthesis allows us to devise various ways to solve some of the aforementioned issues. One strategy is to synthesize polymeric additive free HTMs that could form great quality thin films to protect the perovskite layer from moisture [18]. On the other hand, π -stacking might be employed in order to improve the performance of the charge carrying layer [19]. Finally, inexpensive starting materials could be used in facile reactions without the use of expensive

transition metal catalysts in order to reduce the cost of HTM without incurring loss in device performance [20, 21].

The main aim of this work is synthesis and investigation of easily obtainable organic *p*-type semiconductors for application in perovskite solar cells.

The tasks proposed for the achievement of the above stated aim were as follows:

1. To investigate the applicability of triphenylamine quaternary ammonium compounds in optoelectronics.
2. To synthesize and investigate small molecule HTMs based on dihydrodiazatetracene and dihydrodiazapentacene derivatives.
3. To determine the best performing systems containing diphenylethenyl moieties and different cores.
4. To synthesize and investigate enamine based HTMs containing diphenylethenyl moieties using facile one-step synthesis.

Scientific novelty

During more than a decade of research, many HTMs of various structures were developed for PSCs; however, most of them are expensive or require multi-step synthesis, or both. The two most commonly used materials as *p*-type semiconductors, spiro-MeOTAD and PTAA, are no exception to the rule. Furthermore, spiro-MeOTAD raises long-term stability concerns due to the dopants which are necessary to achieve great optoelectronic performance. Despite the aforementioned issues, PSCs scientific community seems to have stagnated on spiro-MeOTAD and PTAA as HTMs of choice while in the same time demanding cheaper, more efficient and more stable alternatives for commercial applications. In this PhD thesis, various HTMs have been designed and synthesized in hope to eliminate at least some flaws of the predominantly used *p*-type charge carriers.

Despite difficulties in reproducibility, polymers are known to form uniform thin layers that are suitable for charge transport in PSCs. Having that in mind, several different polymerization methods have been attempted in order to obtain conjugated polymers.

Dihydrodiazacenes are a group of materials which were never tested in PSCs. They have amine groups in their backbones, which allows them to be easily modified; additionally, they possess relatively planar structures encouraging molecular packing, which is beneficial for efficient charge transport. The diazacenes described in this work are easy to synthesize, demonstrate good hole mobility (up to $2.5 \cdot 10^{-3} \text{ cm}^2 \text{ V}^{-1} \text{ s}^{-1}$ at zero field strength) as well as appropriate energy levels; also, they can be processed via the vacuum deposition technique. Thus they are considered to be attractive alternatives as HTMs for PSCs.

For many years, compounds containing diphenylethenyl moieties have been known for their relatively high hole mobility, relatively straightforward synthesis and a low cost, which makes them attractive for optoelectronic applications. A variety of different central cores have been investigated in this work in an attempt

to find new and promising candidates for the usage as diphenylethenyl-based HTMs for PSCs. Enamines containing the carbazole central fragment proved to be among the most promising candidates. Not only did they reach around 17% PCEs, but they achieved it without any dopants, which is beneficial for the longevity of the device. The same can be said for an aniline derivative that demonstrated more than 18% efficiency in a fully vacuum processed p-i-n PSC. Aniline based materials were synthesized in a facile one-step synthesis procedure without the use of expensive transition metal catalysts. Relatively high charge carrier mobility, with the highest value reaching $2.4 \cdot 10^{-3} \text{ cm}^2 \text{ V}^{-1} \text{ s}^{-1}$ at zero field strength, coupled with appropriate energy levels and, in most cases, high glass transition temperatures, makes them very attractive HTMs for application in PSCs.

The main statements of doctoral dissertation are as follows:

1. Cross-linkable HTMs were acquired which can be polymerized in the solid state allowing them to be cross-linked in a layer forming insoluble films.
2. New diazacene-based HTMs possess relatively high hole mobility reaching $2.5 \cdot 10^{-3} \text{ cm}^2 \text{ V}^{-1} \text{ s}^{-1}$ at zero field strength. Furthermore, some of them displayed rapid mass loss at elevated temperatures indicating potential for vacuum deposition.
3. Great photoelectrical and thermal properties of carbazole and aniline enamines containing diphenylethenyl derivatives resulted in efficient solar cells.
4. Enamines based on aniline derivatives were obtained in a facile one-step reaction without the use of expensive transition metal catalysts. Suitable energy levels, relatively high mobility of $2.4 \cdot 10^{-3} \text{ cm}^2 \text{ V}^{-1} \text{ s}^{-1}$ and high glass transition temperatures make them promising candidates for use in perovskite solar cells.

2. LITERATURE REVIEW

2.1. Perovskites and their properties

In the Ural Mountains, German mineralogist Gustav Rose discovered the mineral CaTiO_3 which he named perovskite in the honour of the Russian Count, Lev A. Perovski. Nowadays, the term perovskite refers to a wide class of materials that are structurally similar to CaTiO_3 . Generally, perovskite materials can be described by chemical formula ABX_3 , where A and B are cations of different sizes, and X is an anion that coordinates to B. The B type cations are usually smaller than the A type and are coordinated to the X anions to form a BX_6 octahedron. These octahedra form a 3D framework in which the framework cavities are filled with A type cations (Figure 2.1).

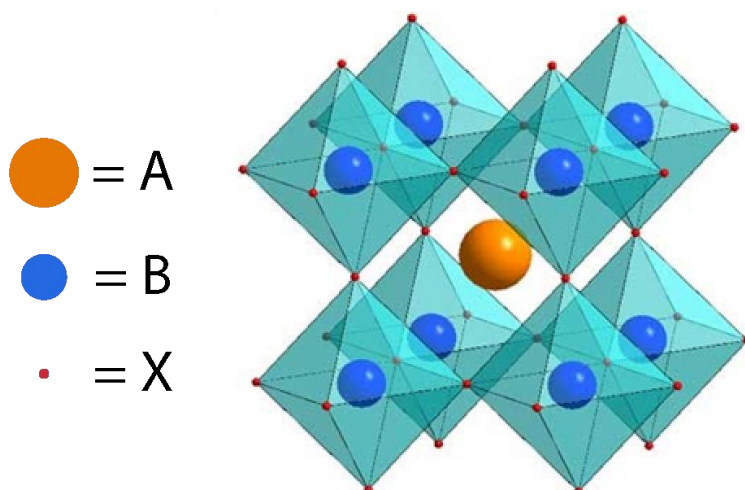


Figure 2.1. Crystal lattice structure of cubical perovskite ABX_3

A subclass of ABX_3 materials is hybrid organic-inorganic (HOIPs) perovskites where A type ions are replaced by organic amine cations. The introduction of organic components to the structure of HOIPs leads to additional functionalities and structural flexibility that would not be possible in fully inorganic perovskites. Most importantly, their physical properties can be tuned by facile chemical modifications [22] demonstrating the structural diversity of perovskites.

Different combinations of metal salts and organic components offer vast possibilities for creating HOIPs, hence, this class of materials now spans a considerable part of the periodic table. The size ratio of ions that are suitable for a perovskite structure is indicated by the Goldschmidt tolerance factor (t) [23]. However, this parameter is not absolute due to its limitations for the prediction of the stability of certain halide HOIPs [24]. This leads to the development of a modified tolerance factor that takes into account the covalency of the cation-

halogen (B-X) bonds. Additionally, the octahedral factor was suggested to determine the fit of a B type cation into the X_6 octahedron and could be used to determine the compatibility of A and B type cations for the perovskite [25].

In the 1990s, HOIPs were synthesized and researched as materials for solar cells, which paved the path for the study of perovskites as optoelectronic materials [26, 27]. The first major breakthrough came in 2009 when methylammonium (MA) lead bromide MAPbBr_3 was used as the sensitizer in mesoporous TiO_2 and demonstrated a PCE of $\sim 3.8\%$ [28]. Four years later, a planar architecture device with MAPbI_3 as the light-absorber and active layer reached an efficiency of $\sim 15\%$. The aforementioned research confirmed that the perovskite can act as both a charge-generating layer and an absorber, consequently simplifying the device design by allowing the exclusion of mesoporous TiO_2 [29]. Recently, a tandem configuration with a silicon cell pushed the PCE to over 29% when using a complex HOIP – $\text{Cs}_{0.05}(\text{FA}_{0.77}\text{MA}_{0.23})_{0.95}\text{Pb}(\text{I}_{0.77}\text{Br}_{0.23})_3$ [30].

The good performance of hybrid lead halide perovskites in solar cells could be attributed to the fact that they are direct-bandgap semiconductors with easily tunable bandgaps in the range of $\sim 1.2\text{--}2.8\text{ eV}$ [31, 32]. Due to their strong contribution of the p orbitals to the optical transition, the bandgap energy is mainly determined by the halides, but it can also be affected by the metal cation at site B. The most suitable halide for perovskite photovoltaic applications is iodide with which the bandgap is in the $\sim 1.2\text{--}1.6\text{ eV}$ range, which is close to the optimal value under standard solar spectrum as stated by the Shockley-Queisser model [33]. What makes HOIPs even more attractive is their set of properties, such as the sharp optical band edge, high absorption over the visible spectrum [34], low exciton binding energy [35, 36] and charge carrier diffusion lengths in the μm -range [37, 38]. Furthermore, many hybrid perovskites can be processed by various methods, e.g., vacuum deposition [39], spin coating [40], dip coating [41], spray pyrolysis [42], atomic layer deposition [43], inkjet printing [44], etc., thus making the device fabrication facile and commercially appealing.

Despite their huge potential for photovoltaics and other applications, only a few HOIPs are denoted by the necessary properties for use in solar cells [31]. The B type cation is limited to the divalent charge metals from group IVA, and the X site halide is mostly iodide or a mixture between it and bromine or chloride. The resulting BX_3 frameworks can only be filled with the smallest organic cations, such as formamidinium (FA) and MA as calculated by equations of Goldschmidt tolerance factors [23]. Larger A type cations result in layered structures that have limited charge transport properties [45]. On the other hand, bulky organic cations form 2D perovskites (Figure 2.2) which provide protection from water adsorption at the surface [46, 47]. The crystal lattice containing large hydrophobic cations can also suppress moisture intrusion [48, 49].

Generally, 2D perovskites are described with the formula $(\text{A}')_m(\text{A})_{n-1}\text{BnX}_{3n+1}$, where A' can be divalent ($m = 1$) or monovalent ($m = 2$) cations forming a monolayer or a bilayer connecting the inorganic $(\text{A})_{n-1}\text{BnX}_{3n+1}$ 2D sheets, where n indicates the layer thickness of metal halide sheets that are adjustable by changing the composition of the precursor [50, 51]. This class of materials can be further

divided into two main groups: Ruddlesden-Popper (RP) and Dion-Jacobson (DJ) phase perovskites [52–54].

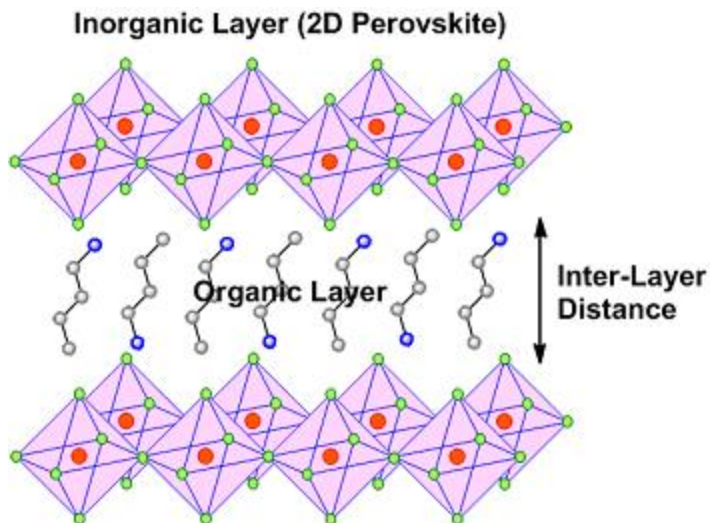


Figure 2.2. Example of a crystal lattice structure of 2D RP phase perovskite [55]

Out of the two, RP phase perovskites are more commonly studied, they are formed by a relatively weak van der Waals gap that occurs between two adjacent lead halide sheets and a bilayer of organic monovalent cations. The RP configuration can be generalized as $A'{}_2A_{n-1}B_nX_{3n+1}$ [54], where A' is an alkyl or aryl ammonium cation (Figure 2.3a), A is a cation, e.g., FA, MA or Cs^+ , B is divalent lead or tin, and X is a halogen. Alternatively, two amino groups containing compounds can form hydrogen bonds with two adjacent inorganic sheets [56] resulting in a more stable DJ phase that can be described with the formula $A'A_{n-1}B_nX_{3n+1}$. Examples of cations constituting DJ 2D perovskites are displayed in Figure 2.3b. The general requirements for a cation to be suitable for the formation of 2D perovskites are: the overall positive charge, stereochemical configuration (aromatic hydrocarbons < flexible aliphatic hydrocarbons), ability to form hydrogen bonds and space-filling (linear cross cations > branch irregular cations) [57].

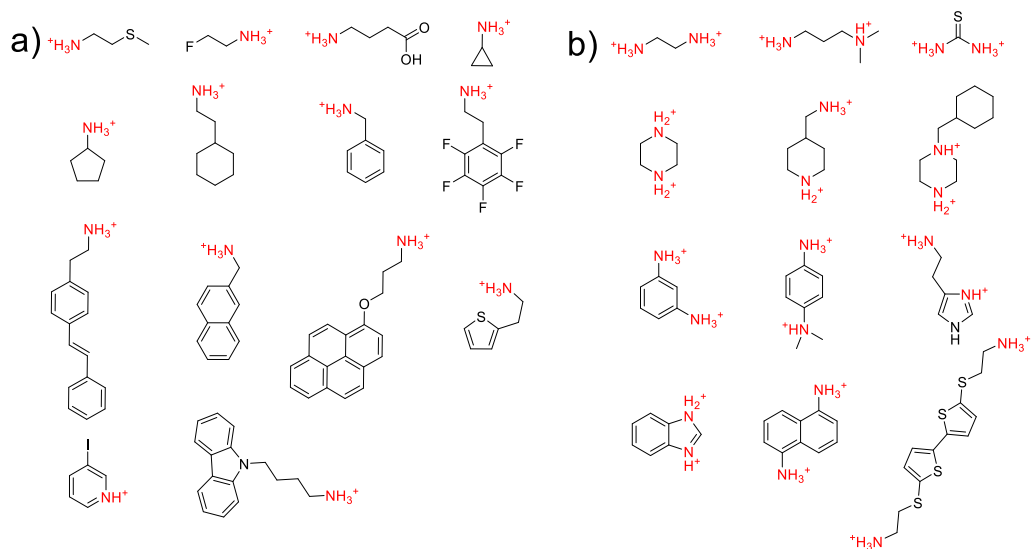


Figure 2.3. Examples of cations for the formation of 2D perovskites [58–80]:
 a) Ruddlesden-Popper b) Dion-Jacobson

Due to the previously mentioned limited charge transport properties of the 2D perovskites, they are used for surface enhancement of 3D perovskites (commonly referred to as 3D/2D perovskites) rather than light absorbers in a solar cell. This approach shows promise for increasing not only the stability but also the overall performance of PSCs through a wide range of compositions [81–83].

One of the issues that have been recently raised concerning the wide scale use of perovskites in the solar technology is the toxicity of lead and tin [84]. This arises from the instability of devices under ambient conditions, in particular, from their sensitivity to humidity which leads to the formation of heavy metal salts and a dramatic decline in PSC performance. A solution to this problem could be encapsulation, which is already an established process for commercial applications [85]. Another way to resolve the toxicity issue is to replace Pb and Sn with a different metal cation in the perovskite composition. Experiments with germanium led to the preparation of HOIPs: FAGeI_3 , MAGeI_3 and $[\text{ACA}][\text{GeI}_3]$ (ACA = acetamidinium) [86]. This resulted in higher bandgaps than for their Pb counterparts therefore making them less suitable for photovoltaic applications. Additionally, divalent germanium is more prone to oxidation than either Pb^{2+} or Sn^{2+} thus implying that this strategy is flawed. As an alternative, it was proposed to substitute the divalent metals with a combination of monovalent and trivalent metals. This led to the synthesis of bismuth perovskites – $\text{Cs}_2\text{AgBiCl}_6$, $\text{Cs}_2\text{AgBiBr}_6$ and $[(\text{MA})_2][\text{KBiCl}_6]$ [87–89]. These perovskites are eco-friendly, have good mechanical, moisture, and thermal stability, however, their bandgaps are too wide to produce efficient PSCs, which means that encapsulated lead or tin based perovskites are the more likely candidates for commercial applications.

Solar-cell HOIPs are denoted by great properties, such as long carrier lifetimes and low non-radiative recombination that can be exploited in lasing structures [90]. In 2016, W. Zhang *et al.* demonstrated the controlled growth of MAPbBr₃ microstructures from one-dimensional microwires to 2D microplates by the use of surfactant micelles as soft templates. This led to the change in emission properties, whereas the microwires emitted strong green light with intense spots at the end, while microplates gave bright emissions at the edges, but very weak emissions from the bodies (Figure 2.4) [91]. The aforementioned demonstration of structural and property change might be crucial in the development of perovskite based lasers.

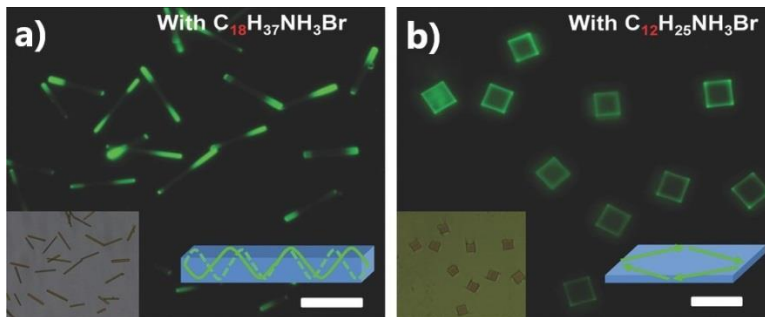


Figure 2.4. MAPbBr₃ microstructures a) one-dimensional nanowires b) 2D microplates [91]

Light-emitting diodes (LED) can also benefit from high photoluminescence (PL) quantum efficiencies and color tunability that perovskites offer. HOIP based LEDs demonstrated efficient room temperature emissions from green to near-infrared depending on the halide composition of the device [92]. However, the poor morphology of HOIP thin layers results in lower efficiencies than the conventional quantum dot or organic light-emitting diodes. This was improved by Y. Ling *et al.* who described highly efficient perovskite LEDs fabricated by employing the facile solution method [93]. The acquired LED had a uniform MAPbBr₃ layer and was moisture resistant, which enabled cheaper and scalable processing.

2.2. Perovskite solar cells

As mentioned in the previous chapter, PSC are among the most promising photovoltaic technologies, thus it is necessary to examine it in more detail. Generally, PSCs have a layered structure which includes a transparent conductive oxide (TCO), a perovskite sandwiched between electron and hole transporting layers (ETL and HTL, respectively), and a metal electrode, although additional layers might be included. By their architecture, PSCs can mainly be divided into two categories – mesoscopic and planar – which can each be further separated into regular (n-i-p) and inverted (p-i-n) configurations.

The mesoscopic, otherwise also known as mesoporous, architecture is based on the design originating from the solid state dye sensitized solar cell, and some time ago that was the most popular PSC configuration. The main component that

makes this design unique is the mesoporous TiO_2 layer which allows the perovskite to self-assemble within the interstice of the layer [94], while assisting the electron transfer between the perovskite and the fluorine-doped tin oxide (FTO) electrode [95]. An example of mesoporous PSC can be seen in Figure 2.5.

A variation of the mesoporous configuration is the meso-superstructured architecture. It was described in an article by M. Lee *et al.* [40] when they replaced the mesoporous TiO_2 scaffold with an inert mesoporous Al_2O_3 which is not directly involved in the charge transport. One of the advantages associated with the replacement of TiO_2 with Al_2O_3 is that this eliminated the chemical instability issue that derives from TiO_2 when it is subjected to UV light [96].

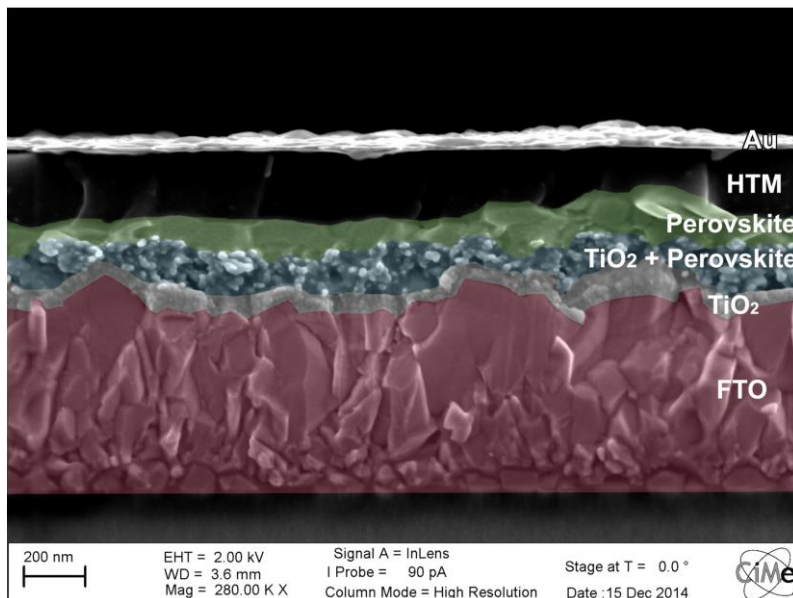


Figure 2.5. Cross section of mesoscopic perovskite solar cell under SEM [97]

Further research by M. Liu *et al.* [29] established that the complex nanostructuring of the perovskite is not necessary to reach high PCE. In their work, a planar heterojunction architecture solar cell with vapor-deposited perovskite reaching more than 15% efficiency was described. The structure of this device is similar to the conventional silicon based solar cells [98]. As mentioned above, planar architecture devices can be further classified into n-i-p and p-i-n configurations (though this can be applied to the mesoporous solar cells as well), identified depending on the type of the charge selective layer which is deposited onto the front transparent contact. In the n-i-p and p-i-n architectures, n- and p-type layers are used as the front contact, respectively. The regular planar device structure is glass/TCO/ETL/perovskite/HTL/metal, whereas the inverted configuration is glass/TCO/HTL/perovskite/ETL/metal (Figure 2.6) [99].

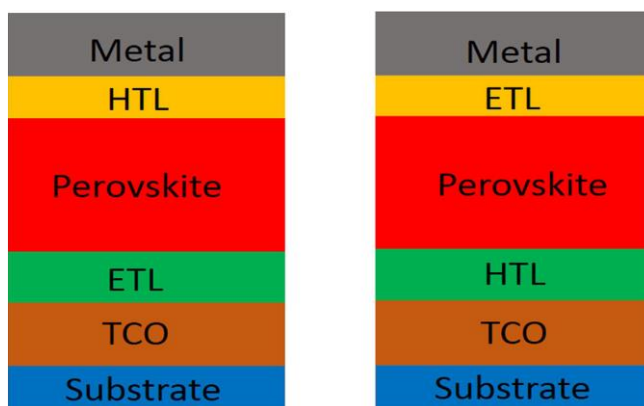


Figure 2.6. Planar n-i-p and p-i-n perovskite solar cell architectures [99]

For PSC to function efficiently, materials have to possess appropriate energy levels. In the example shown in Figure 2.7, $\text{CH}_3\text{NH}_3\text{PbI}_3$ is used as the perovskite absorber, TiO_2 as ETL, spiro as HTL, FTO as the anode, while several metals are displayed as possible candidates for usage as the cathode. This is done to show that there are cheaper alternatives with suitable energy levels to act as a metal electrode to the usually used expensive silver or gold [100].

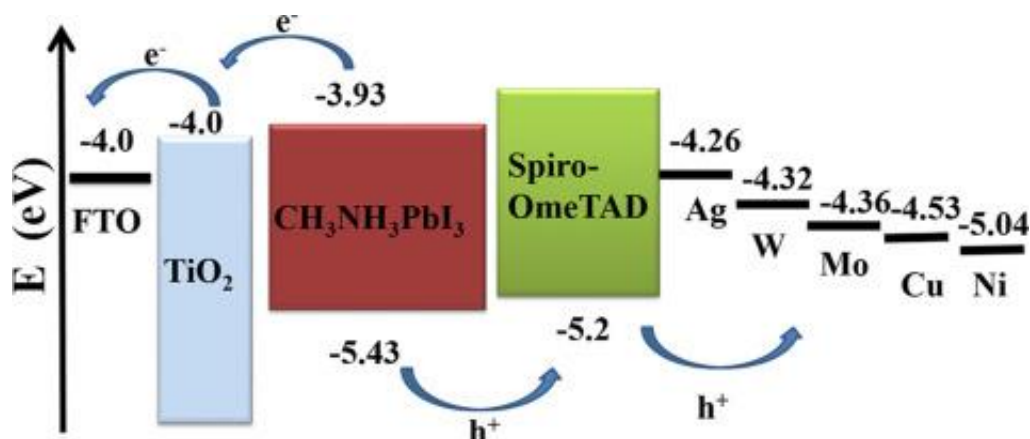


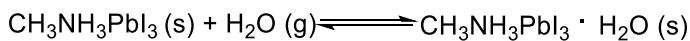
Figure 2.7. Hole and electron movement and energy levels of materials in perovskite solar cells with a variation of metal electrodes [100]

The easily tuneable band gap of the perovskite and different architectures of PSCs allow for the usage of many different materials as components for the device. Depending on the configuration of the solar cell, the most commonly used ETMs are TiO_2 , SnO_2 for planar and TiO_2 , Al_2O_3 scaffolding for a mesoporous n-i-p device, while phenyl-C61-butyric acid methyl ester (PCBM) and C60 are used for p-i-n planar and mesoscopic PSCs [99, 101]. The most popular HTMs for either architecture are spiro-MeOTAD and PTAA [17], while NiO has also been used as hole transport and as scaffolding in mesoporous p-i-n devices [102]. The most

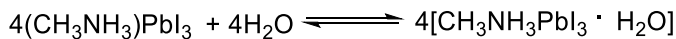
often used perovskites for all PSCs are methylammonium (MA) lead iodide (MAPI) [103, 104] and a variation of $Cs_x(MA_{0.17}FA_{0.83})_{(100-x)}Pb(I_{0.83}Br_{0.17})_3$ [30, 105]. FTO and either gold or silver electrodes are the habitual choice for the n-i-p structure [17, 100], while indium tin oxide (ITO) and Cu or Ag are the usual options for p-i-n [106, 107]. While the previously mentioned materials are the most popular, it is still worth to remember that they can all be substituted depending on the energy levels of the perovskite as well as on industrial and economic considerations.

The hype of PSCs comes from the rapid rise of PCE which went from 3.8% to more than 25% [8, 28] in less than a decade, while other technologies, such as silicon or cadmium telluride solar cells, needed more than forty years to achieve similar results [108]. Furthermore, as mentioned before, there are quite a few different compositions of perovskites that can be used, there are many ways to fabricate the device, and there are even more combinations of materials that can be used in PSCs. However, there are some key issues which hold PSCs back from commercialization. The three main factors that are detrimental for the stability of most perovskites used in PSCs are: moisture, temperature, and oxygen, while MAPI is also susceptible to photodegradation [109]. Most of the degradation mechanisms concerning PSCs were studied by using MAPI; therefore, the following examples will be described based on the processes occurring between it and the external factors.

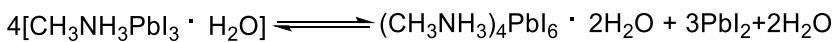
Generally, it has been shown that a monohydrate or monohydrate with dihydrate phases in perovskite single crystals are formed when they are exposed to water (Scheme 2.1). These reactions are reversible in both cases, thus, if the perovskite were put in an inert environment, it would revert back to the dehydrated state. However, this process has its limitations, as moisture induces structural deformations that remain despite the removal of water molecules [110, 111], thus weakening the bonds inside the perovskite crystal and leading to the decline in photovoltaic properties.



or



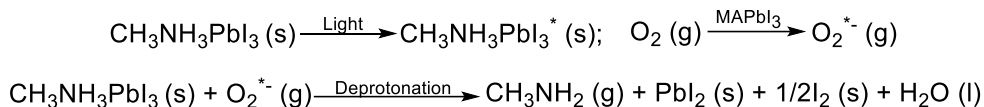
and



Scheme 2.1. Moisture induced perovskite degradation

Thermogravimetric analysis (TGA) was used to test the stability of MAPI. Degradation begins with the sublimation of organic halide components, which is followed by the decomposition of the metal halide at a higher temperature. Debate is still going on the exact temperature that is required to cause degradation and whether this produces methyl iodide and ammonia, hydroiodic acid and deprotonated methylammonium or both [112–117].

Halogen vacancies that occur due to thermal, photo or any other type of degradation are perfect places for oxygen to be adsorbed and diffused through. If the perovskite is in the excited state, oxygen can trap a photoexcited electron thus forming a highly reactive O_2^- superoxide. To become neutral, O_2^- reacts with the MA cation deprotonating it and producing methylamine gas, PbI_2 , H_2O and I_2 (Scheme 2.2) [118–120].



Scheme 2.2. Oxygen induced perovskite degradation

All of the above mentioned reactions are detrimental to the performance of PSCs despite of what structure perovskites are used. Even caesium-based perovskites containing small amounts of MA are susceptible to the same type of degradation. The biggest difference is the degradation mechanisms taking place during the phase transition, e.g., the thermal decay of $CS_{0.05}(MA_{0.17}FA_{0.83})_{0.95}Pb(I_{0.83}Br_{0.17})_3$ is a two-step process: the first stage is similar to that of MAPI, whereas the second one to FACs based perovskite [121]. Yet, further tests are required to exactly figure out other degradation pathways of caesium-based perovskites [109].

Despite all the stability issues, there are ways to avoid or at least mitigate them. The most obvious choice to resolve moisture and oxygen degradation is device encapsulation [85]. Combined with encapsulation, ionic liquids could be employed to passivate the surface of the perovskite thus increasing the overall long-term stability of PSC [122, 123]. Another way to increase the longevity of the device is to design HTMs that can perform dopant-free [124, 125].

2.3. Doped hole transporting materials for perovskite solar cells

The role of HTM in PSC is to efficiently extract holes at the perovskite/HTM interface and prevent the undesirable charge recombination processes that would lead to a drop in PCE. The basic requirements for HTMs are the ability to form good quality thin films, to minimize the aforementioned recombination as well as proper energy level alignment while enabling electron blocking and relatively high charge carrier mobility, and to ensure minimal losses during hole transport to the contact [124].

At times when the performance of HTM is not sufficient, additives are used to improve the photophysical properties of the material. The doping process in principle is used for the generation of additional charge carriers via electron acceptors which remove electrons from the highest occupied molecular orbital (HOMO) of the HTM thus inducing the formation of cation radicals [126, 127]. The prime requirement for efficient doping is the proper electron affinity (EA) of the dopant with respect to the energy levels of the HTM. The most commonly used

dopants for solution-based PSC fabrication are bis(trifluoromethane)sulfonimide lithium salt (LiTFSI), cobalt-based dopants, e.g., tris(2-(1*H*-pyrazol-1-yl)-4-*tert*-butylpyridine)cobalt(III) tri[bis(trifluoromethane)sulfonimide (FK209) and 4-*tert*-butyl pyridine (*t*BP) (Figure 2.7) [124, 125, 128]. The role of LiTFSI and FK209 is to oxidize the HTM [129], while *t*BP has demonstrated suppression of charge recombination [130]. Depending on the HTM, the aforementioned dopants can be used separate, in various combinations, or all together.

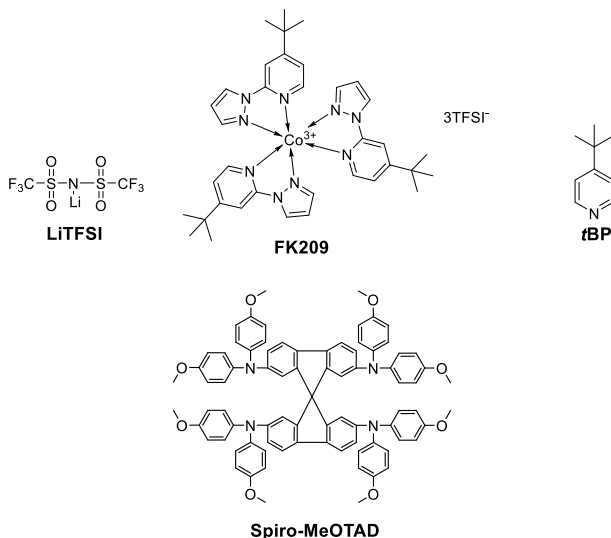
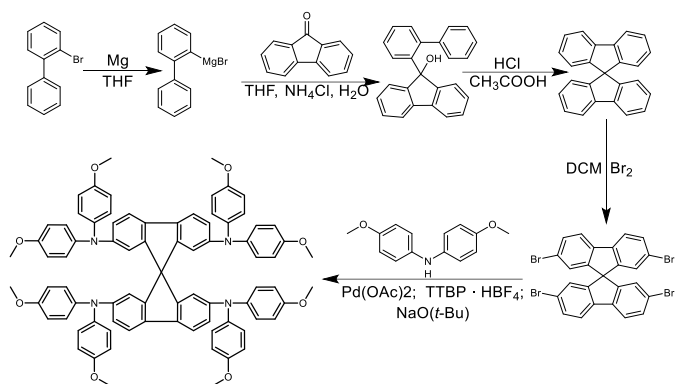


Figure 2.8. Structures of most commonly used dopants and HTM spiro-MeOTAD

As mentioned in the previous chapter, spiro-MeOTAD (Figure 2.8) is one of the most used HTMs in PSC. This is due to the fact that it is readily commercially available and was widely researched for more than a decade [131]. However, due to the high cost of the said material (up to 500\$ per gram) [125] deriving from the lengthy synthesis (Scheme 2.3), other alternatives must be explored. All of the following HTMs described in this chapter required additives to achieve peak performance, their solar cell PCE is compared with the efficiency of spiro-MeOTAD PSC (if possible) achieved in the same study to achieve better understanding of the relative performance of new charge transporting materials (Table 2.1).



Scheme 2.3. Synthesis of spiro-MeOTAD

Due to the great results of spiro-MeOTAD, many new materials were based on the same ‘award winning’ structural design in order to achieve high PCE, while still trying to reduce somewhat the cost of the material. Out of this group, one of the best options was organic semiconductor **X59** which was obtained in a two-step facile synthesis and achieved 19.8% PCE in mesoscopic n-i-p architecture PSC, which was only 1 percentage point lower than the reference device that reached 20.8% with spiro-MeOTAD as the HTM [132]. **X59** was modified by attaching pyridine units to the central core in order to cause an interaction between the nitrogen in the pyridine moieties and the lead in the perovskite; however, **XPP** demonstrated a slightly lower PCE value of 19.5% [133] (Figure 2.9). Similarly to **XPP**, the charge transporting material **FDT** was synthesized with the goal to increase the hole transfer at the perovskite/HTM interface, through thiophene-iodine interaction, thus yielding a champion mesoporous n-i-p device of 20.2% efficiency which outperformed spiro-MeOTAD by 0.5 percentage points in absolute terms [134].

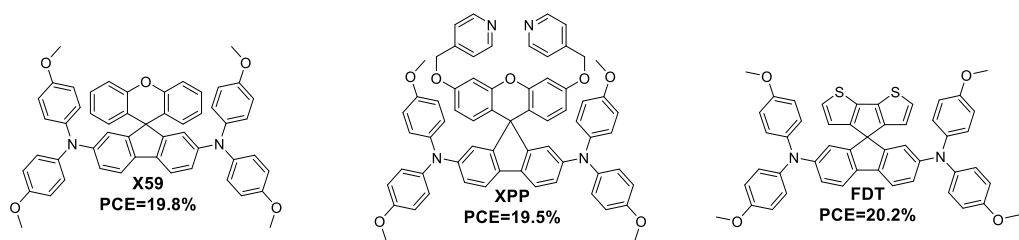


Figure 2.9. Spiro-MeOTAD inspired HTMs

Carbazole derivatives belong to another group of HTMs that have been extensively studied due to their low cost, easily tuneable energy levels and facile functionalization. Similarly to spiro-MeOTAD, many compounds of this class have employed dimethoxydiphenylamine fragments as donor units to tune the HOMO level of the HTM (Figure 2.10). In a study by V. Getautis *et al.*, HTMs containing two 4,4'-dimethoxydiphenylamine substituted carbazole derivatives linked by a

non-conjugated methylenebenzene moiety were described [135]. *Ortho*, *meta* and *para* isomers were synthesized and compared in order to determine the impact on the overall material properties by the position of the substituents. Not surprisingly, due to the size of the molecules, the positional variations did not induce any significant change in the properties of the materials. Nonetheless, organic semiconductors **V886**, **V885** and **V911** displayed excellent performance by virtue of reaching nearly 19% PCE in mesoscopic n-i-p PSCs, which was on par with the reference spiro-MeOTAD device.

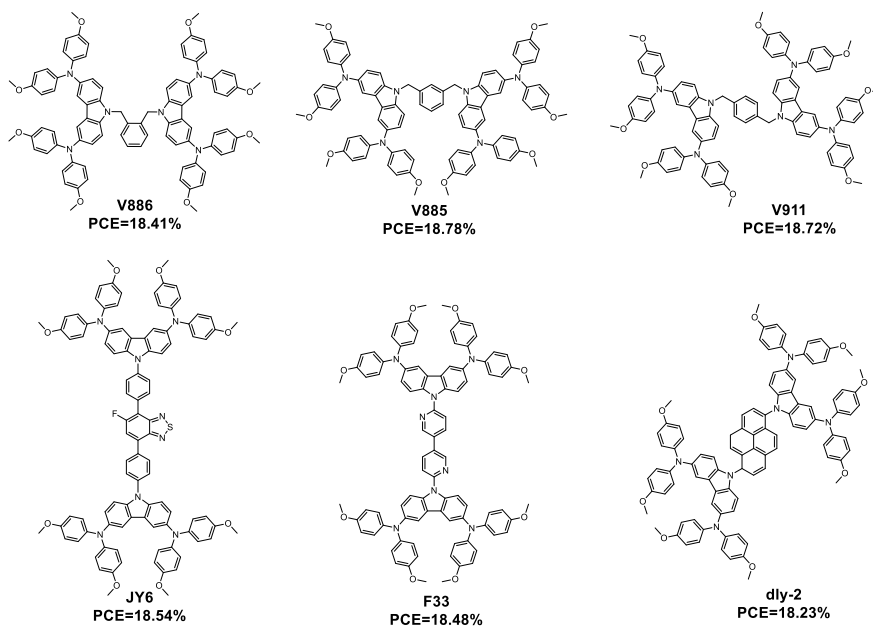
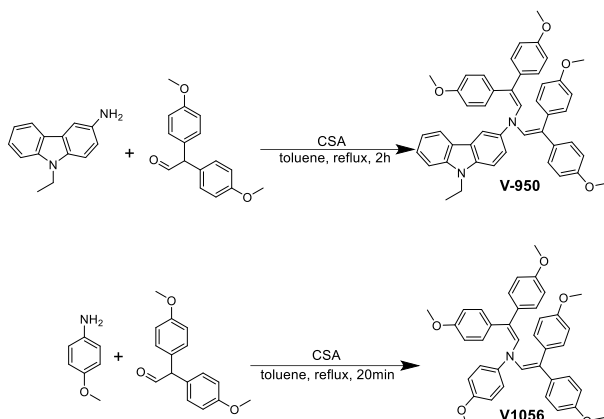


Figure 2.10. Carbazole based HTMs and their PCEs

Materials **JY6**, **F33** and **dly-2** follow a similar design as the V-series HTMs, with the main difference being the central core that was used instead of dimethylenebenzene (Figure 2.10). **JY6** employed a monofluorinated benzothiadiazole derivative as the central core in order to create a donor acceptor (D-A) system that would tune the energy levels and improve the hole mobility of the material [136]. PSC with **JY6** as HTL reached 18.54% PCE, while the reference spiro-MeOTAD device demonstrated 16.24% efficiency. In a similar manner to **JY6**, HTM **F33** was designed; it achieved PCE of 18.48% [137]. The planar core of pyrene derivative **dly-2** did not produce any improvement in the PCE of PSCs as the best device reached 1.3 percentage point lower absolute efficiency levels than spiro-MeOTAD [138]. It is worth noting that **JY6**, **F33** and **dly-2** were employed in a n-i-p configuration planar solar cell thus avoiding the usage of mesoporous TiO₂ that might be detrimental to the long-term stability of the device [96]. However, compared to the V-series HTMs, the synthesis cost of the aforementioned compounds is significantly higher (examples of V-series synthesis can be seen in Scheme 2.4).



Scheme 2.4. Synthesis of enamines V-950 and V1056

An emerging group of materials for the applications in PSCs are enamines containing diphenylethenyl moieties in their structure. The two major benefits of these HTMs are their facile synthesis without the use of expensive organometallic catalysts, which results in a very low cost and a high PCE that is similar to that of spiro-MeOTAD. One of the first enamines used as a *p*-type semiconductor in PSCs was **V-950** [139]. It was obtained via one step synthesis, and it was employed in both n-i-p mesoporous and planar device architectures, with the former producing 1 percentage point absolute higher efficiency ultimately reaching 17.8% PCE, which was close to the results obtained with spiro-MeOTAD (Table 2.1). In a later work by M. Daskeviciene *et al.*, modifications were made to **V-950** in order to evaluate the influence of alkyl chains to the properties of the material (Figure 2.11) [140]. The longer side chains of **V1000** and **V1013** led to the decrease in PCE, while the butyl substitution at the nitrogen atom combined with the *tert*-butyl group at the 6-position of the carbazole fragment slightly increased the efficiency. In the same study, HTM **V1021** with a double number of enamine chromophores, compared to **V-950**, was described. It reached 19.01% PCE, which was on par with the reference spiro-MeOTAD device.

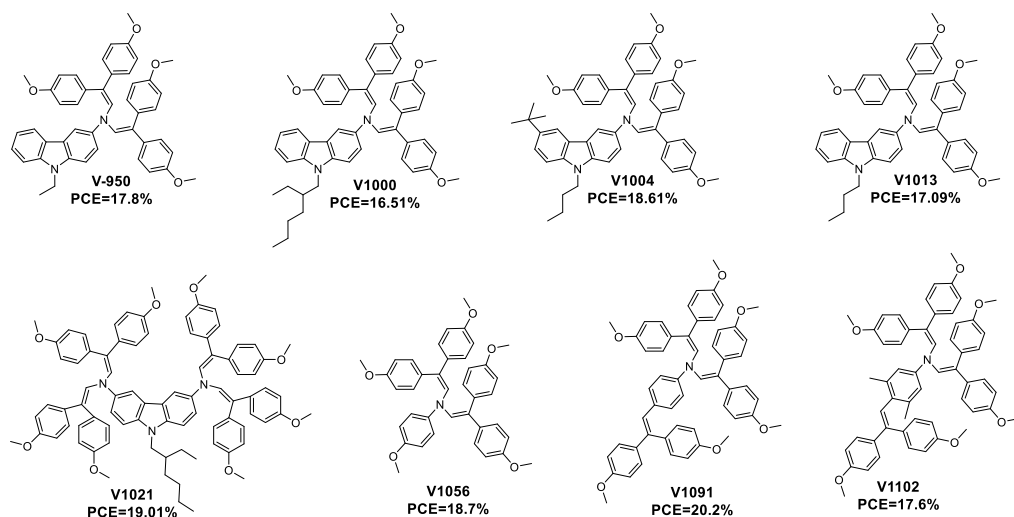


Figure 2.11. Enamine based HTMs

D. Vaitukaityte *et al.* coupled aniline derivatives with 2,2-bis(4-methoxyphenyl)acetaldehyde in order to obtain enamines **V1056**, **V1091** and **V1102** (Figure 2.11) [20]. They were tested in planar n-i-p configuration PSCs and demonstrated efficiencies between 17.6% and 20.2%. The champion solar cell exhibiting PCE of 20.2% was obtained with **V1091** as the HTM, rivalling the reference spiro-MeOTAD device.

Table 2.1. Doped HTMs results vs spiro-MeOTAD

| HTM | Device architecture | PCE, % | Ref. PCE, % | Lit. ref. No. |
|--------------|---------------------|--------|-------------|---------------|
| X59 | n-i-p mesoscopic | 19.8 | 20.8 | 132 |
| XPP | n-i-p planar | 19.5 | - | 133 |
| FDT | n-i-p mesoscopic | 20.2 | 19.7 | 134 |
| V886 | n-i-p mesoscopic | 18.41 | 18.79 | 135 |
| V885 | n-i-p mesoscopic | 18.78 | 18.79 | 135 |
| V911 | n-i-p mesoscopic | 18.72 | 18.79 | 135 |
| JY6 | n-i-p planar | 18.54 | 16.24 | 136 |
| F33 | n-i-p planar | 18.48 | 20.64 | 137 |
| dly-2 | n-i-p planar | 18.23 | 19.59 | 138 |
| V-950 | n-i-p mesoscopic | 17.8 | 18.6 | 139 |
| V1000 | n-i-p mesoscopic | 16.51 | 19.1 | 140 |
| V1004 | n-i-p mesoscopic | 18.61 | 19.1 | 140 |
| V1013 | n-i-p mesoscopic | 17.09 | 19.1 | 140 |
| V1021 | n-i-p mesoscopic | 19.01 | 19.1 | 140 |
| V1056 | n-i-p planar | 18.7 | 20.2 | 20 |
| V1091 | n-i-p planar | 20.2 | 20.2 | 20 |
| V1102 | n-i-p planar | 17.6 | 20.2 | 20 |

In conclusion, there is a wide variety of new low-cost and efficient alternatives to replace spiro-MeOTAD as the HTL in PSCs, however, the most popular dopants that are used to improve the photoelectrical properties of HTMs are still suffering from their drawbacks. LiTFSI and FK209 are hygroscopic and can help moisture reach and degrade the perovskite layer, while *t*BP is volatile and can dissolve perovskite [141]. That said, there are still ways to increase the stability of PSCs with encapsulation, perovskite surface passivation and alternative doping procedures [128]; nevertheless, in order to avoid additive related stability problems, dopant free HTMs are desired.

2.4. Small molecular dopant-free hole transporting materials

There are mainly four groups of additive-free HTMs: small molecules, polymers, organometallic and inorganic. Out of them, small molecular *p*-type semiconductors are the most extensively studied class. One of the earliest reported dopant-free HTMs was TIPS-pentacene (Figure 2.12) [142]. Due to the cofacial-stacking, TIPS-pentacene demonstrated excellent charge carrier mobility of over $1 \text{ cm}^2 \text{ V}^{-1} \text{ s}^{-1}$; however, the best device achieved a PCE as low as 11.82%.

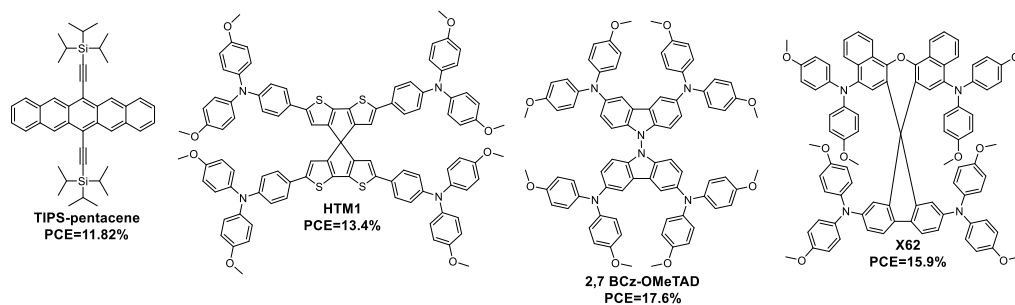
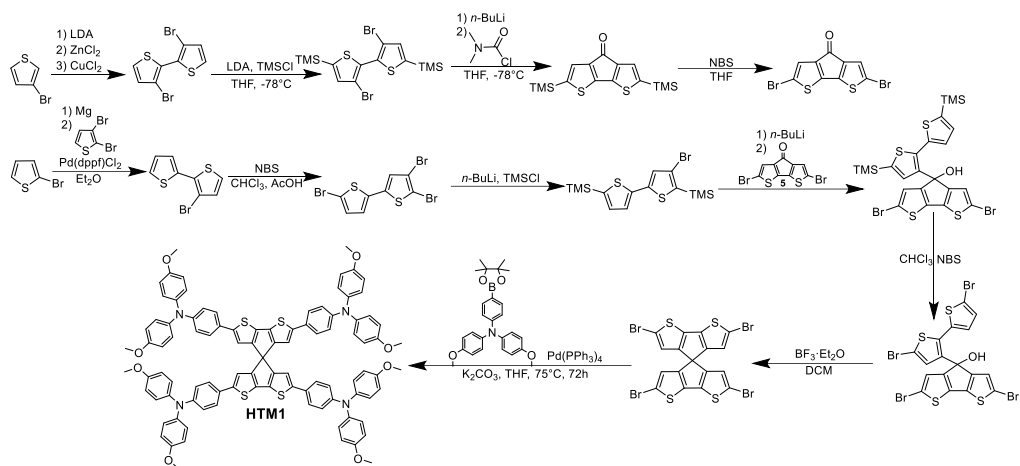


Figure 2.12. Structures and PCEs of TIPS–pentacene and spiro inspired dopant-free HTMs

Similarly to doped HTMs, spiro-MeOTAD inspired the design of new dopant free organic semiconductors **HTM1**, **2,7 BCz-OMeTAD** and **X62** (Figure 2.12) [143–145]. By substituting benzene rings in spirobifluorene with thiophene units, **HTM1** was designed, while the introduction of two carbazole groups connected by a N–N bond instead of the spirobifluorene central core led to the synthesis of **2,7 BCz-OMeTAD**. PSCs employing the aforementioned HTMs reached 13.4% and 17.6% efficiencies, respectively. Spiro[dibenzo[*c,h*]xanthene-7,90-fluorene] was chosen by L. Wang *et al.* as the central core to synthesize **X62**, which achieved a PCE of 15.9%.



Scheme 2.5. Synthesis of **HTM1**

The synthesis of **HTM1** (Scheme 2.5) is used as an example to demonstrate how some *p*-type semiconductors are inappropriate for wide scale applications due to the high cost of the final product. In this instance, **HTM1** requires eleven steps to be obtained, in some of them using expensive transition metal catalysts and purification techniques.

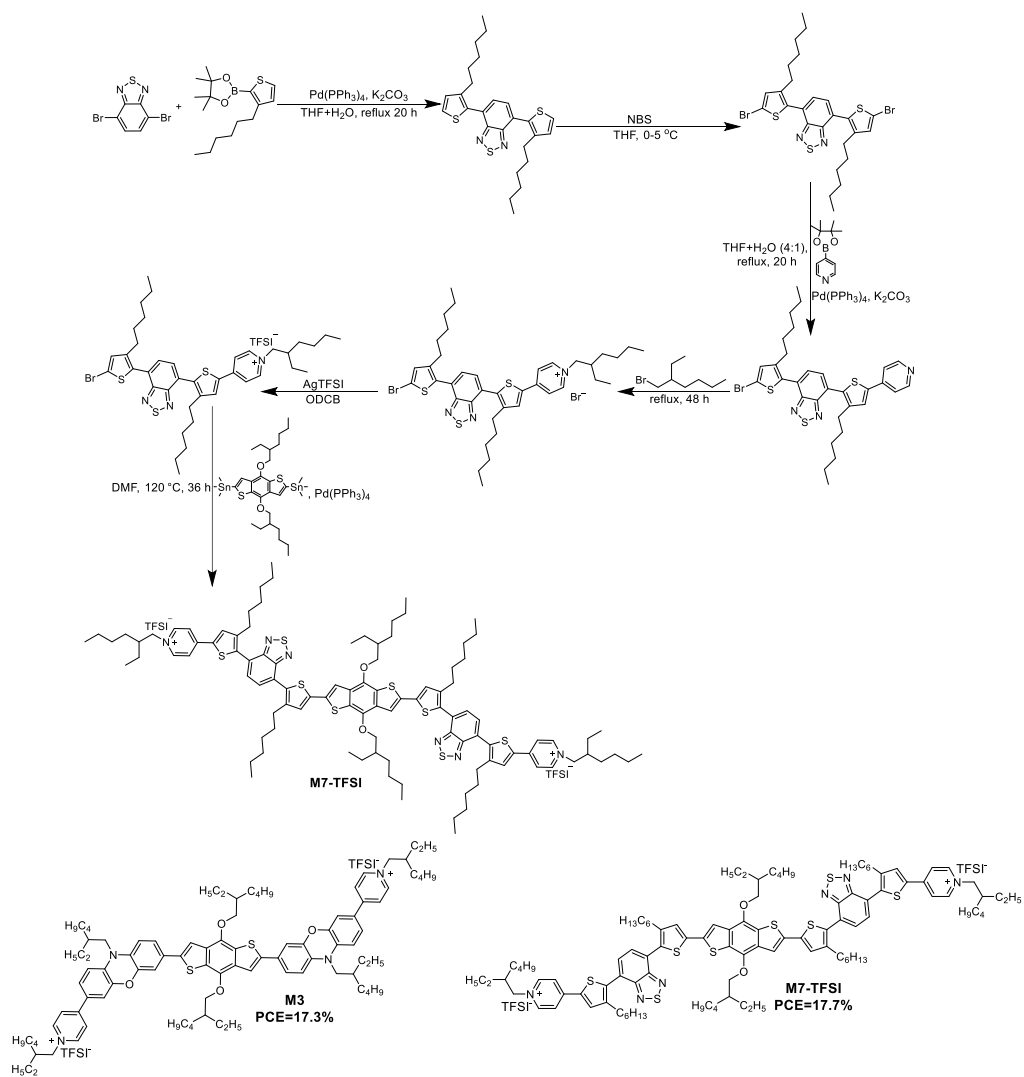


Figure 2.13. Examples of A-D-A type HTMs and synthesis of **M7-TFSI**

A sort of a subgroup of small molecular HTMs is the acceptor-donor-acceptor, or – in short – A-D-A compounds. Often serving as the backbone for these molecules, oligothiophene or other electron-donating moieties are chosen to bridge the donor unit with the acceptor units. This strategy was used in OPVs with positive results [146, 147]. The modifications of the aforementioned units can lead to better film morphology, more suitable energy levels and improved charge transport. However, the synthesis of the A-D-A type HTMs is either long or expensive, or both; as an illustration six-step synthesis procedure using expensive transitional metal catalysts and organic tin compounds for **M7-TFSI** can be seen in Figure 2.13 [148, 149].

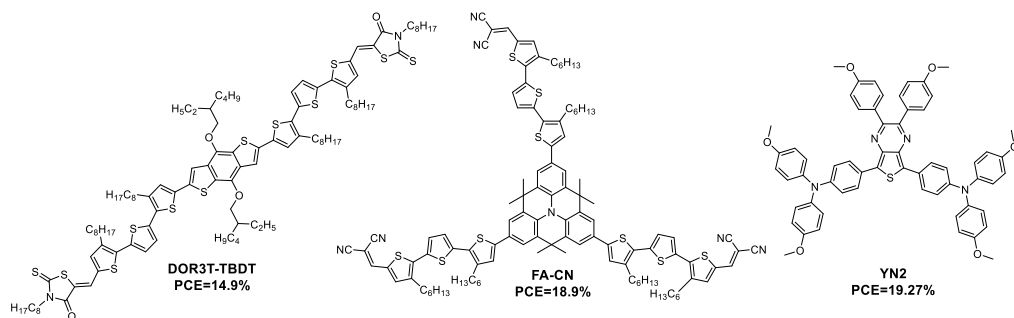


Figure 2.14. D-A class HTMs

An alternative strategy is to construct D-A alternating molecules. D-A class HTMs are less complicated than A-D-A and have also been widely investigated and often adopted in the fields of OPV and OLED. Energy level tuning of D-A semiconductors is quite facile since the donor part of the molecule mostly affects the HOMO level, while the acceptor unit mainly determines the lowest unoccupied molecular orbital (LUMO) [125]. It is believed that the main reason why D-A type HTMs do not require dopants is mainly due to the strong intramolecular charge transfer and the high dipole moment [150]. A variety of different structures were developed while using the D-A molecular design such as **DOR3T-TBDT**, **FA-CN** and **YN2** as shown in Figure 2.14. The former was described in the study by Y. Liu. *et al.* where it slightly outperformed doped spiro-MeTAD displaying 14.3% PCE [151]. Bigger is not always better, however, as the charge transporting material **FA-CN** [152, 153] demonstrated a PCE of 18.9%, while the much smaller **YN2** achieved 19.27% efficiency.

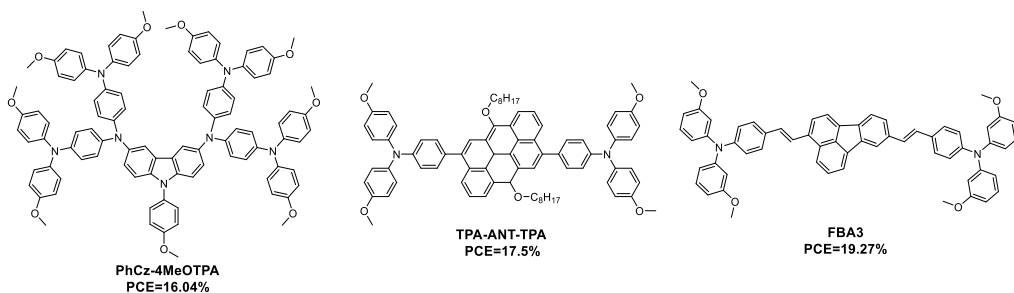


Figure 2.15. Examples of D-D' class HTMs

Another subgroup of small molecular HTMs is D-D' materials. These HTMs offer better molecular packing and improved charge transport due to the two donor units, which led to a rise of many new molecules, such as **PhCz-4MeOTPA**, **TPA-ANT-TPA** and **FBA3** (Figure 2.15) [154–156]. Out of the aforementioned HTMs, highest PCE of 19.3% belongs to the fluorenone central core containing **FBA3**, while the triphenylamine (TPA) derivative **PhCz-4MeOTPA** demonstrated the lowest efficiency of 16.04%.

In this chapter, each previously mentioned HTM was employed in n-i-p configuration PSCs, while the following small molecular materials were used in p-i-n architecture devices. The reason why these two groups of HTMs are separated is the lower mobility requirements for p-i-n devices due to the thinner HTM layers typically needed for the fabrication of PSCs in comparison to n-i-p devices [125]. Furthermore, HTL should be poorly soluble in DMF and DMSO which are used to prepare the perovskite precursor solution. The aforementioned requirement can only be avoided if the perovskite is deposited via the vacuum deposition method [39]. This limits the choice of HTMs; therefore, slightly different strategies are used in order to design new small molecular *p*-type semiconductors.

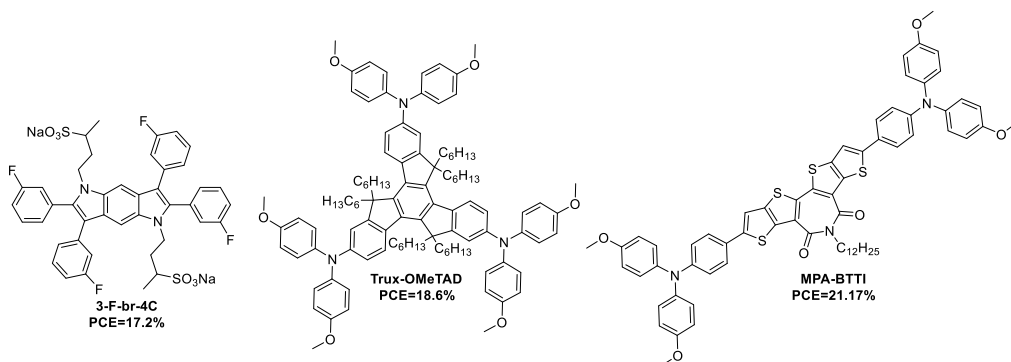


Figure 2.16. Examples of HTMs used in p-i-n configuration PSCs

Due to their selective solubility and appropriate energy levels, organic-inorganic salts might be considered for applications in PSCs. An example of such HTM is sodium salt **3-F-br-4C** which displayed 17.2% efficiency (Figure 2.16) [157]. Similar to HTMs reported for n-i-p devices, the incorporation of a planar core is a proven method to design efficient charge transporting molecules for p-i-n devices. In a study by C. Huand *et al.*, rigid truxene central fragment containing **Trux-OMeTAD** demonstrating 18.6% PCE was described (Figure 2.15) [158]. Y. Wang *et al.* took advantage of both the central core planarity and the D-A strategy combining them in order to synthesize the *p*-type semiconductor **MPA-BTTI** which achieved an astonishing PCE of 21.17% (Figure 2.16) [159].

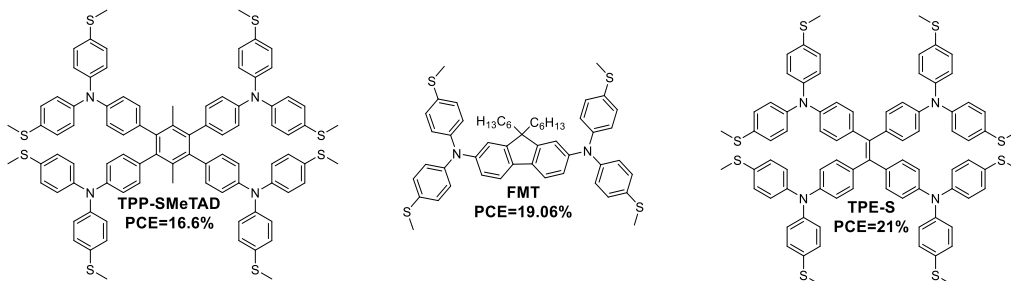


Figure 2.17. Examples of sulphur containing HTMs

Another way to create efficient HTMs for p-i-n PSCs is to make use of interactions between HTM-perovskite or TCO-HTM. The fact that sulphur atoms can effectively passivate perovskite defects by forming coordination bonds with lead was taken into account when designing the structures of **TPP-SMeTAD**, **FMT** and **TPE-S** (Figure 2.17). In an article by H. Chen *et al.*, methylthio groups containing **TPP-SMeTAD** were synthesized and compared to its methoxy analogue **TPP-OMeTAD**. It was found that **TPP-SMeTAD** demonstrated Pb-S interaction with perovskite, which led to surface passivation and enhanced charge extraction resulting in a PCE of 16.6%, which was 2 percentage points more (in absolute terms) than **TPP-OMeTAD** described in the same article [160]. In a similar fashion, fluorene derivative **FMT** and tetraphenylethylene-based HTM **TPE-S** were designed [161, 162]. They achieved 19.06% and 21% efficiencies in p-i-n PSCs, respectively.

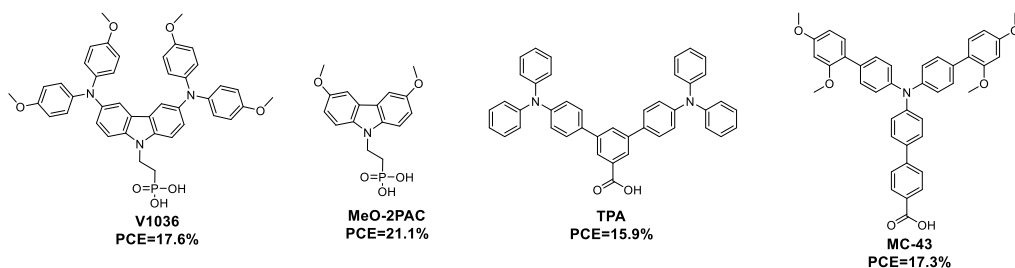


Figure 2.18. Monolayer forming HTMs for inverted PSCs

Recently, self-assembling monolayers (SAMs) were demonstrated as a highly promising new generation of materials for PSCs (Figure 2.18). The monolayer is formed due to the interaction between the functional group of HTM and TCO. The main benefit of these materials is their low consumption during device fabrication making them very attractive for commercial applications. In a work by A. Magomedov *et al.*, carbazole based HTM **V1036** containing the phosphonic acid group was mixed with butylphosphonic acid to form mixed SAM during the interaction with ITO [163]. The device employing the aforementioned SAM reached efficiency of 17.6%. Furthermore, the simplification of the structure of **V1036** led to the development of **MeO-2PAC** which achieved 21.1% PCE [13]. As an alternative to phosphonic acid, the carboxyl group was suggested by E. Yalcin *et al.* for the formation of SAM. In their study, triphenylamine derivatives **TPA** and **MC-43** were used as HTLs resulting in PCE of 15.9% and 17.3%, respectively [164].

Table 2.2. Dopant-free small molecule HTM results

| HTM | Device architecture | PCE, % | Lit. ref. No. |
|-----------------------|---------------------|--------|---------------|
| TIPS-pentacene | n-i-p | 11.82 | 142 |
| HTM1 | n-i-p | 13.4 | 143 |
| 2,7 BCz-OMeTAD | n-i-p | 17.6 | 144 |
| X62 | n-i-p | 15.9 | 145 |
| M3 | n-i-p | 17.3 | 148 |
| M7-TFSI | n-i-p | 17.7 | 149 |
| DOR3T-TBDT | n-i-p | 14.9 | 151 |
| FA-CN | n-i-p | 18.9 | 152 |
| YN2 | n-i-p | 19.27 | 153 |
| PCz-4MeOTPA | n-i-p | 16.04 | 154 |
| TPA-ANT-TPA | n-i-p | 17.5 | 155 |
| FBA3 | n-i-p | 19.27 | 156 |
| 3-F-br-4C | p-i-n | 17.2 | 157 |
| Trux-OMeTAD | p-i-n | 18.6 | 158 |
| MPA-BTTI | p-i-n | 21.17 | 159 |
| TPP-SMeTAD | p-i-n | 16.6 | 160 |
| FMT | p-i-n | 19.06 | 161 |
| TPE-S | p-i-n | 21 | 162 |
| V1036 | p-i-n | 17.6 | 163 |
| MeO-2PAC | p-i-n | 21.1 | 13 |
| TPA | p-i-n | 15.9 | 164 |
| MC-43 | p-i-n | 17.3 | 164 |

To sum up this chapter, there are many different ways to design small molecular dopant-free HTMs that would reach a high PCE value in either n-i-p or p-i-n device configurations (Table 2.2). However, not all HTMs are created equal, some of them require a relatively expensive starting material, e.g., **FA-CN**, **MPA-BTTI**, whereas others involve lengthy synthesis procedures, which adds to the cost of the HTM (for example, **HTM1**, **M7-TFSI**). Out of all *p*-type semiconductors mentioned in this chapter, the most promising for commercial applications appear to be monolayer forming HTMs due to their high efficiencies, low costs of synthesis and low material consumption during device fabrication.

2.5. Polymeric, organometallic and inorganic materials as dopant-free HTMs

Due to long conjugated chains, charge transport in polymers can occur through both intermolecular hopping and intramolecular transfer, which often results in relatively high hole mobility without the need of additives. However, polymeric HTMs suffer from batch-to-batch reproducibility issues and the necessity for tedious purification. Generally, *p*-type semiconducting polymers can be used in both regular n-i-p and inverted p-i-n architectures and can be further categorized into homopolymers and copolymers.

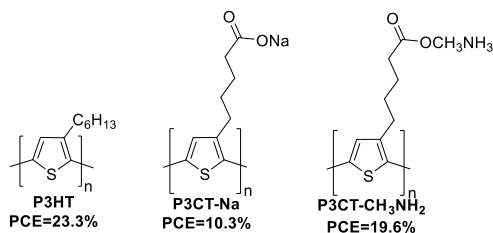


Figure 2.19. Thiophene based polymers as HTMs

One of the most basic polymeric HTMs used in PSCs is **P3HT** (Figure 2.19), however the strong electronic coupling, poor physical contact, and undesirable nonradiative recombination loss at the perovskite/**P3HT** interface limit the performance of the PSC, which results in a PCE value of 6.3% [165]. In order to solve these issues and improve the efficiency of the device, E. Jung *et al.* proposed the insertion of an ultrathin layer of wide-bandgap halide to induce self-assembly of **P3HT**. Regular configuration PSCs built this way reached a PCE of 23.3% [81]. In a study by X. Li *et al.*, modified versions of **P3HT** were used to achieve respectable results in a p-i-n architecture device (Figure 2.19). HTM **P3CT-Na** demonstrated 10.3% efficiency, while **P3CT-CH₃NH₂** reached 19.6% PCE [166].

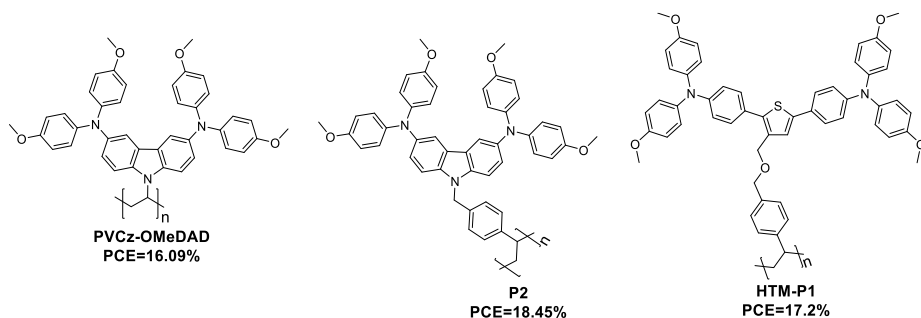


Figure 2.20. Nonconjugated polymeric HTMs

Even though high conjugation tends to lead to the appropriate hole mobility, which in turn allows them to be used in the pristine state and reach high efficiencies, nonconjugated polymers **PVCz-OMeDAD**, **P2** and **HTM-P1** also demonstrated high PCE values in regular architecture devices (Figure 2.20) [167–169]. Carbazole based HTM **PVCz-OMeDAD** exhibited 16.09% efficiency, while an additional benzyl group containing a *p*-type semiconductor **P2** achieved a PCE of 18.45%. Exchanging carbazole central core in **P2** to thiophene in **HTM-P1** resulted in a slight drop of efficiency to 17.2%.

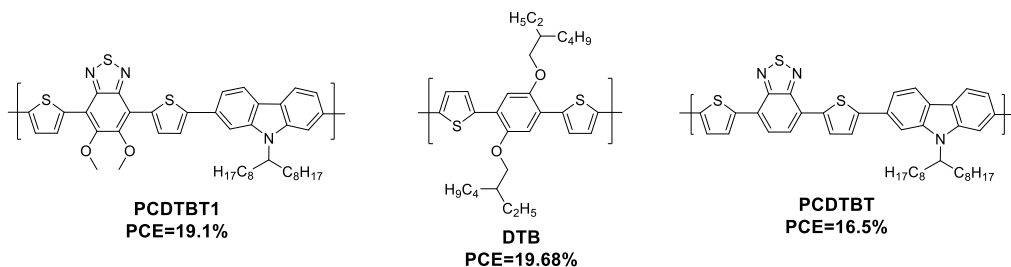


Figure 2.21. Copolymers as HTMs for PSCs

Examples of copolymers for PSCs can be seen in Figure 2.21. Polymeric HTMs **PCDTBT1** and **DTB** were employed in regular configuration devices and demonstrated 19.1% and 19.68% efficiencies respectively, while **PCDTBT** recorded 16.5% PCE in a p-i-n architecture PSC [170, 171].

Organometallic HTMs most commonly adopt porphyrin or phthalocyanine cores complexed with divalent metal cations, such as Cu^{2+} , Ni^{2+} , Co^{2+} , and Zn^{2+} . These compounds usually sport high hole mobility and can be used dopant-free; however, their application is limited to regular architecture PSCs due to the strong absorption in the visible region which overlaps with the absorption of the perovskite [172]. **ZnP**, **CuPC-TIPS** and **NiPc-(OBu)₈** are examples of this group of HTMs (Figure 2.22). Porphyrin derivative **ZnP** demonstrated an efficiency of 17.78% [173], while phthalocyanine based copper and nickel complexes reached 14% and 17.8% PCE values, respectively [174, 175].

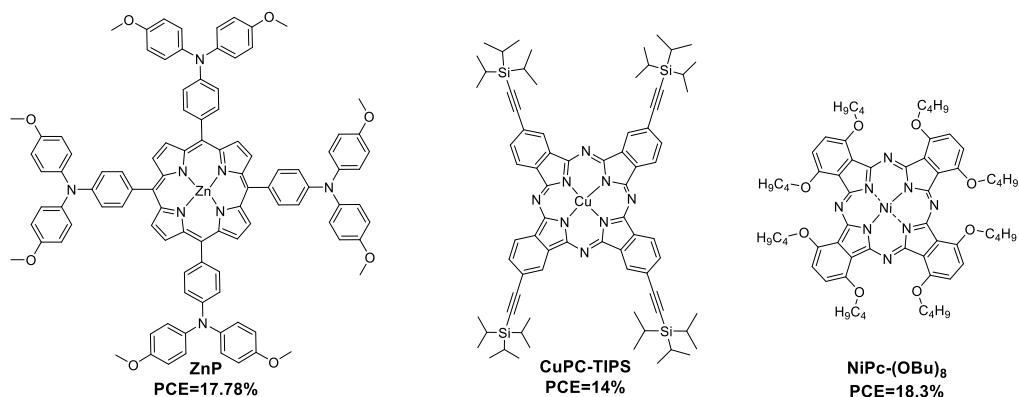


Figure 2.22. Examples of organometallic HTMs

Inorganic materials can be great dopant-free HTMs due to their low cost as well as a relatively high charge carrier mobility and stability, however, inorganic materials often are poorly soluble, and only a limited number of them are suitable for solution processing. The most efficient inorganic HTM for PSCs is CuSCN. The p-type conductivity of CuSCN arises from the copper vacancies in the crystal lattice allowing n-i-p devices to reach over 20% PCE [176]. Despite its high efficiency, CuSCN is properly soluble only in solvents that are detrimental to

perovskite, and the material is known to degrade at the gold electrode, which suggests that different deposition techniques and electrodes are required to improve the longevity of the device. As an alternative to CuSCN, quantum dots of monovalent copper oxide modified with a silane coupling agent can be employed as a HTM. Due to surface modifications, Cu₂O can be directly spin-coated on top of perovskite from the appropriate solvent without damaging the perovskite active layer. Regular configuration PSCs made with the aforementioned quantum dots reached 18.9% efficiency [177]. A good example of an inorganic HTM for p-i-n architecture PSCs is nanocrystalline CuCrO₂ which can function as the HTM delivering a PCE value of 19% as well as a UV-blocking layer improving the photostability of the device [178].

Table 2.3. Dopant-free polymeric, organometallic and inorganic HTM results

| HTM | Device architecture | PCE, % | Lit. ref. No. |
|--|---------------------|--------|---------------|
| P3HT | n-i-p | 23.3 | 81, 165 |
| P3CT-Na | p-i-n | 10.3 | 166 |
| P3CT-CH₃NH₂ | p-i-n | 19.6 | 166 |
| PVCz-OMeDAD | n-i-p | 16.09 | 167 |
| P2 | n-i-p | 18.45 | 168 |
| HTM-P1 | n-i-p | 17.2 | 169 |
| PCDTBT1 | n-i-p | 19.1 | 170 |
| DTB | n-i-p | 19.68 | 171 |
| PCDTBT | p-i-n | 16.5 | 170 |
| ZnP | n-i-p | 17.78 | 173 |
| CuPC-TIPS | n-i-p | 14 | 174 |
| NiPc-(OBu)₈ | n-i-p | 18.3 | 175 |
| CuSCN | n-i-p | 20.4 | 176 |
| Cu ₂ O | n-i-p | 18.9 | 177 |
| CuCrO ₂ | p-i-n | 19 | 178 |

To sum up, polymers, organometallic and inorganic materials used as HTMs can reach high efficiencies in regular and inverted PSCs (Table 2.3), however, they all have their drawbacks. Polymeric *p*-type semiconductors suffer from batch-to-batch reproducibility, whereas organometallic complexes can only be adopted in n-i-p configuration devices, while inorganic materials need elaborate deposition techniques or surface modifications to form good quality thin films.

2.6. Conclusions

The wide diversity of perovskites makes them attractive for multiple optoelectronic applications; however, the optimal band gap for solar cells is around 1.2–1.6 eV. Nonetheless, that leaves enough room for modifications of the perovskite composition. Furthermore, the tuneable bandgap of HOIPs and different device configurations allows the application of various HTMs in order to find the best match for efficient PSCs. Besides the energy levels, *p*-type semiconductors

have many requirements. Unfortunately, most of the published HTMs for PSCs struggle either with cost, long term stability, or both. As seen in Chapter 2.3, there are a lot of HTMs that are inexpensive and demonstrate high PCEs, however, they still need additives that are detrimental to the longevity of PSCs, thus alternative doping or additional protection for the perovskite layer is required when using doped HTMs. As an attempt to avoid additives, dopant-free semiconductors can be employed. For the time being, the most promising group of HTMs for commercial applications seems to be monolayer forming materials, however, they can only be applied in the p-i-n architecture PSCs limiting the choice of materials for device fabrication. Despite many HTMs published over the years, the scientific community appears to have stagnated on the usage of expensive and unreliable *p*-type semiconductor spiro-MeOTAD leaving room for attempts to design HTMs that would replace spiro as the new benchmark material for PSCs.

3. RESULTS AND DISCUSSION

3.1. Triphenylamine derivatives as hole transporting materials

TPA derivatives are versatile charge transport materials possessing high emission efficiencies [179] and interesting interactions in the solid phase. Good charge transfer characteristics of TPA compounds led to their use in the fabrication of OFETs [180, 181]. The efficient hole transport properties of such TPAs as 3-methyldiphenylamine and carbazole substituted TPAs [182], tetramer of TPA [183] and oligomeric TPA [184] derivatives were successfully employed in OLED devices. Moreover, due to good charge transport properties, TPA derivatives are used in combination with fluorene and polyfluorene fluorophores [185, 186] or metalorganic iridium complexes [187] to enhance charge injection to the emissive site.

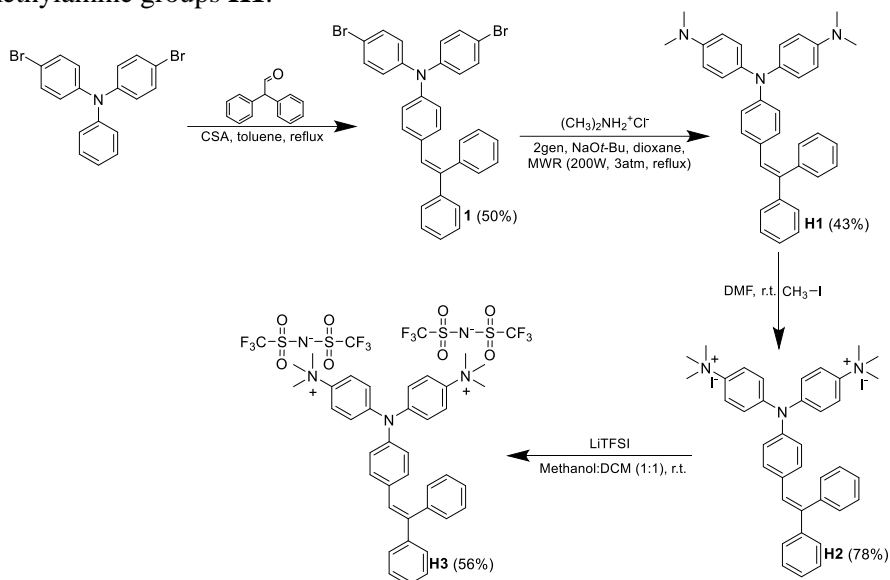
Another important area of the utilization of triphenylamine based compounds is OPV, where charge transport is a key factor for good solar cell performance [188]. TPAs are often used in PSCs as well as dye-sensitized solar cells [189]. For example, in PSCs, TPA moieties can be found in many well performing HTMs such as *N,N'*-bis(3-methylphenyl)-*N,N'*-diphenylbenzidine (TPD) [190], the previously mentioned PhCz-4MeOTPA, TPA-ANT-TPA, FBA3, etc. [153–155].

As stated in the literature review, the introduction of additives to HTMs partially oxidizes them, thus improving their electronic properties. Developing compounds that already have a positive and/or negative charge in their structure could result in improved conductivity and allow skipping the doping stage.

3.1.1. Synthesis of triphenylamine quaternary ammonium compounds

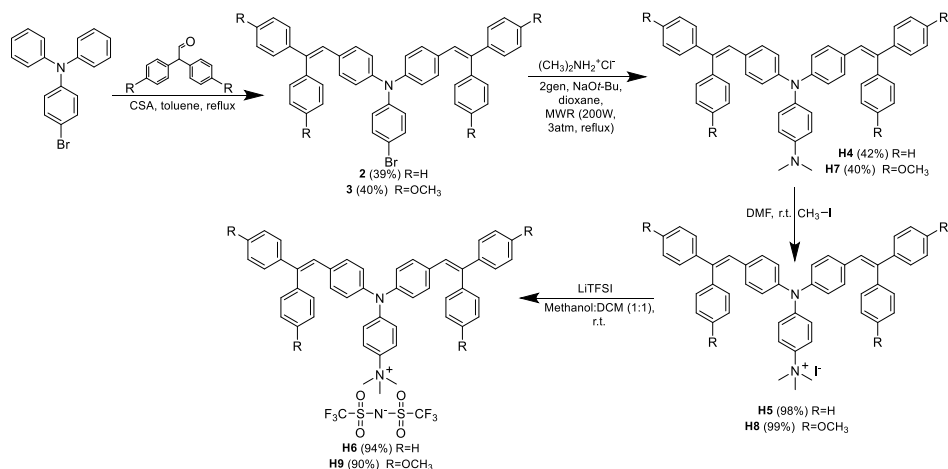
TPA derivatives **H1-H3** were synthesized as shown in Scheme 3.1. The initial step was the condensation of diphenylacetaldehyde with 4,4'-dibromotriphenylamine via camphor-10-sulfonic acid (CSA) catalyzed condensation reaction yielding dibrominated TPA derivative **1** as the desired product. The acquired compound was used in the Buchwald-Hartwig coupling reaction under argon atmosphere in anhydrous dioxane while using a microwave

reactor (MWR) to synthesize the substituted TPA compound with two dimethylamine groups **H1**.



Scheme 3.1. Synthesis of TPA derivatives **H1-H3**

The quaternarization of tertiary amine groups by using methyl iodide was conducted in anhydrous DMF at room temperature giving quaternary iodine salt **H2** as the desired product. Iodine ions were exchanged to bistrifluoromethanesulfonylimide anion (TFSI) via an exchange reaction between TPA derivative **H2** and lithium bistrifluoromethanesulfonylimide (LiTFSI) in a mixture of methanol and DCM.



Scheme 3.2. Synthesis of tertiary amines **H4, H7** and their ionic derivatives **H5, H6, H8, H9**

Monoamine derivatives **H4** and **H7** were synthesized by using a similar approach (Scheme 3.2). Phenylethenyl substituted TPA derivative **2** and its methoxy containing analogue **3** were synthesized, by CSA catalyzed condensation reaction between 4-bromotriphenylamine and either diphenylacetaldehyde or 2,2-bis(4-methoxyphenyl)acetaldehyde. The acquired products were used in Pd catalyzed coupling reaction with dimethyl amine hydrochloride under argon in anhydrous dioxane under pressure and elevated temperature in MWR, yielding monoamine products **H4** and **H7** (Scheme 3.2).

Quaternary ammonium compounds were obtained by the identical synthesis path as described above: the respective amines **H4** and **H7** were reacted with iodomethane in DMF thus giving iodine salts **H5** and **H8** accordingly. LiTFSI was used to exchange the iodine ion to TFSI in a mixture of methanol and DCM, and consequently yielding quaternary ammonium compounds **H6** and **H9**, respectively (Scheme 3.2).

3.1.2. Thermal properties

The thermal properties of the synthesized materials were investigated by the TGA and differential scanning calorimetry (DSC) methods (Table 3.1). TGA analysis showed that quaternary iodine salts are denoted by relatively low thermal stability as they degrade in temperatures lower than 200 °C. The 35% loss in mass in compound **H2**, and more than 15% loss in materials **H5**, **H8** could be attributed to the elimination of methyl iodide from the molecule at higher temperatures (Figure 3.1). Other compounds are significantly more thermally stable and start to decompose in temperatures above 300 °C.

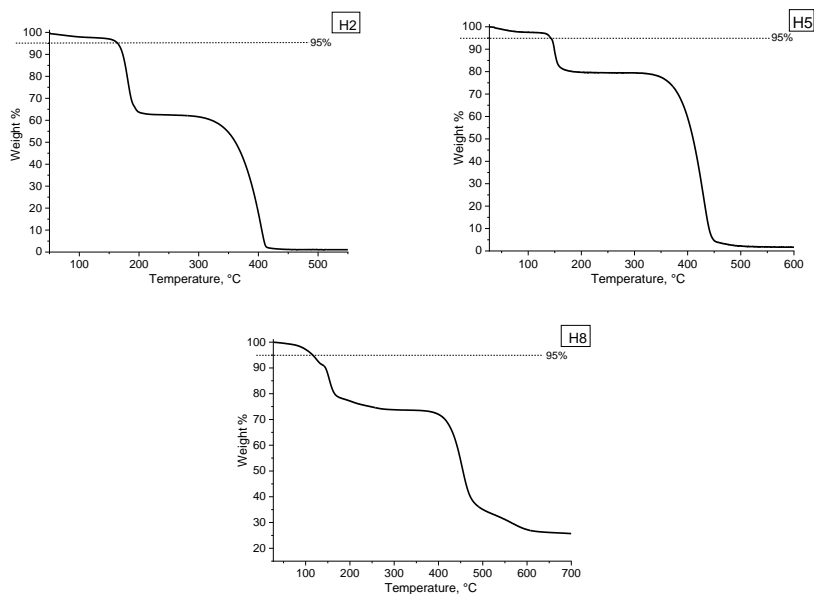


Figure 3.1. TGA of iodinated TPA derivatives **H2**, **H5**, **H8**

Analysis of DSC results showed that, out of all tested tertiary amine compounds, only **H1** has the crystalline state and demonstrates two melting points, which indicates that the material is polymorphous (Figure 3.2).

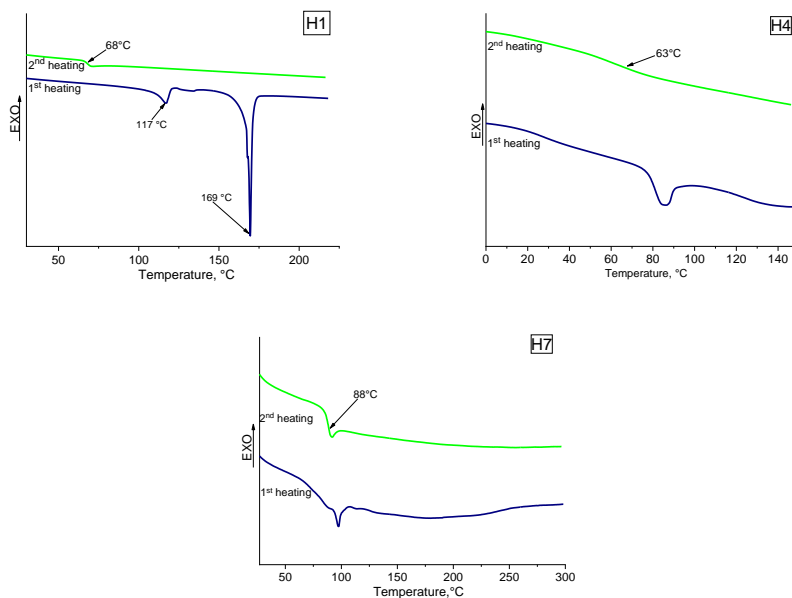
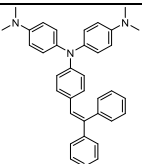
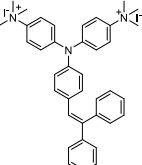
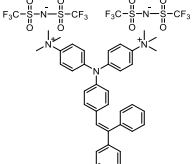
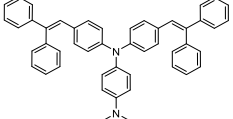
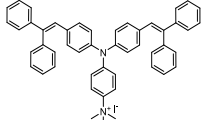
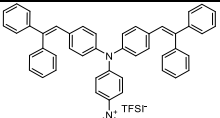
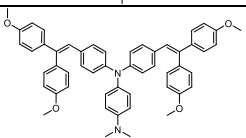
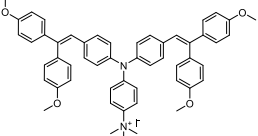
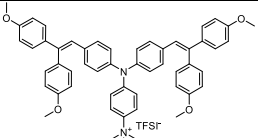


Figure 3.2. DSC curves for tertiary amines **H1**, **H4** and **H7**

The introduction of iodine anions leads to the formation of a crystalline structure for **H5**, **H8** or to an increase in the melting temperature for **H2**; however, all iodine salts undergo decomposition during melting of the crystals. With the exchange of iodine anions to TFSI⁻, the investigated materials become amorphous. Meanwhile, the addition of the methoxy groups tends to increase the T_g of neutral molecules; however, the aforementioned groups have the opposite effect on T_m of quaternary iodine compounds, thus lowering T_m by almost 20 °C and causing the formation of the amorphous state (Table 3.1).

Table 3.1. Thermal characteristics of TPA derivatives **H1-H9**.

| Nr. | Structure | T_g^a , °C | T_m^b , °C | T_{dec}^c , °C |
|-----------|---|--------------|--------------|------------------|
| H1 |  | 68 | 169 | 333 |
| H2 |  | - | 182 | 170 |
| H3 |  | 58 | - | 328 |
| H4 |  | 63 | - | 396 |
| H5 |  | - | 146 | 145 |
| H6 |  | 85 | - | 345 |
| H7 |  | 88 | - | 407 |
| H8 |  | 62 | 129 | 126 |
| H9 |  | 83 | - | 326 |

a) Determined by DSC: scan rate = 10 °C min⁻¹, N₂ atmosphere; second run; b) Determined by DSC: scan rate = 10 °C min⁻¹, N₂ atmosphere; first run; c) Onset of decomposition determined by TGA: heating rate = 10 °C min⁻¹, N₂ atmosphere

3.1.3. Photoelectrical properties

To evaluate energy levels of tested materials in the solid state, the ionization potential (I_p) was measured by the photoelectron spectroscopy in air (PESA) method, where the measurement error was evaluated as 0.03 eV. An example of an I_p graph can be seen in Figure 3.3¹.

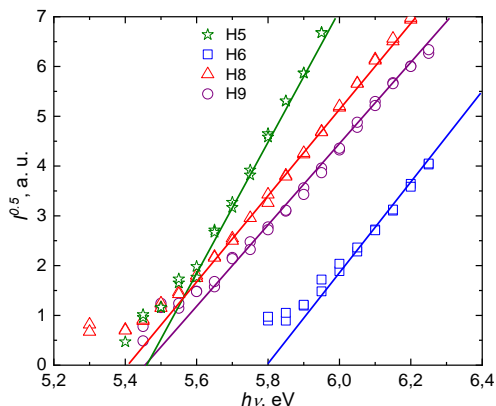


Figure 3.3. Photoemission in air spectra of quaternary ammonium compounds **H5**, **H6**, **H8**, **H9**

The I_p measurements shown in Table 3.2 display the growth of energy required to transfer an electron from the highest occupied molecular orbital to the lowest unoccupied molecular orbital upon the introduction of quaternary ammonium groups to the molecule. Compounds with one tertiary amine or quaternary ammonium group **H4–H9** have shown higher I_p values than the respective derivatives with two groups (**H1–H3**). Additionally, in almost all the cases, quaternary TPA compounds with TFSI⁻ anions exhibit the highest ionization energies.

While comparing structurally similar compounds, **H4–H6** with **H7–H9**, it can be observed that the addition of the methoxy groups to the molecule tends to lower the ionization energy due to the electron donating properties of these groups, which correlates well with the previously published results [191].

¹ Measurements of ionization potential were performed at the Institute of Chemical Physics, Vilnius University, by E. Kamarauskas

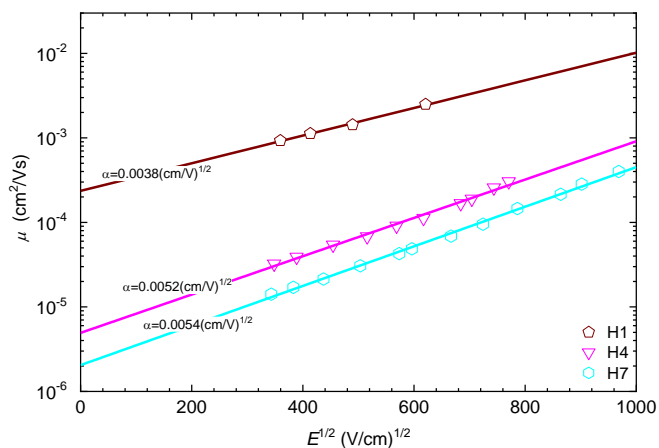


Figure 3.4. Charge carrier mobility of tertiary amines **H1**, **H4**, **H9**

Another important property offering better insight into the possible applicability of the materials in optoelectronics is charge carrier mobility². The charge drift mobility was measured from films by the xerographic time-of-flight (XTOF) method (Table 3.2). Tertiary amine **H1** demonstrated the highest drift mobility reaching $2.4 \cdot 10^{-4} \text{ cm}^2 \text{ V}^{-1} \text{ s}^{-1}$ at the zero field strength, while the lowest value belongs to TPA derivative **H7** (Figure 3.4). On the other hand, the measurement of quaternary ammonium compounds could not be conducted due to insufficient film forming properties and because of the ionic nature of these materials.

Table 3.2. Physical properties and PCE of TPA derivatives **H1-H9**

| Compound | I_p , eV ^a | μ_0 , $\text{cm}^2 \text{V}^{-1} \text{s}^{-1}$ ^b | μ , $\text{cm}^2 \text{V}^{-1} \text{s}^{-1}$ ^c | PCE, % | σ , S/cm^d |
|-----------|-------------------------|--|--|--------|----------------------------|
| H1 | 4.90 | $2.4 \cdot 10^{-4}$ | $4.7 \cdot 10^{-3}$ | 0.0 | $3 \cdot 10^{-13}$ |
| H2 | 5.40 | - | - | 0.0 | $4 \cdot 10^{-13}$ |
| H3 | 5.30 | - | - | 0.0 | $6 \cdot 10^{-12}$ |
| H4 | 5.30 | $5 \cdot 10^{-6}$ | $3.2 \cdot 10^{-4}$ | 3.5 | $5 \cdot 10^{-12}$ |
| H5 | 5.46 | - | - | 0.3 | $1.7 \cdot 10^{-11}$ |
| H6 | 5.79 | - | - | 0.0 | $6 \cdot 10^{-11}$ |
| H7 | 5.10 | $2 \cdot 10^{-6}$ | $1.5 \cdot 10^{-4}$ | 3.5 | $1 \cdot 10^{-11}$ |
| H8 | 5.41 | - | - | 0.2 | $0.7 \cdot 10^{-11}$ |
| H9 | 5.45 | - | - | 0.0 | $1 \cdot 10^{-11}$ |

a) Ionization potential was measured by the photoemission in air method from films; b) Mobility value at zero field strength; c) Mobility value at the electric field strength of $6.4 \cdot 10^5 \text{ V cm}^{-1}$; d) Electric conductivity

The difference in the carrier mobility of TPA derivative **H1** compared to **H4** and **H7** could be attributed to the neater packing of molecules in the film [191].

² Charge mobility measurements were performed at the Institute of Chemical Physics, Vilnius University, by Dr. V. Jankauskas.

Increased steric hindrance, caused by additional methoxy groups, leads to worse packing of molecules in the methoxy substituted phenylethenyl TPA derivative **H7**, thus leading to the lowest drift mobility among the investigated compounds (Table 3.2).

All HTMs were tested in regular configuration PSCs with the structure FTO/compact TiO₂/MAPI/HTM/Ag. The best performing devices were fabricated by using doped HTMs **H4** and **H7**, however, they both reached only 3.5% PCE. Since the main idea behind ionic materials was not to use any dopants, all quaternary ammonium compounds were tested pristine, unfortunately, the results were unsatisfactory. Iodine salts **H5** and **H8** showed efficiencies lower than 0.5%, while the remaining materials did not produce any electrical current when tested in PSCs. Conductivity (σ)³ measurements results can offer better understanding as to why the researched materials demonstrated quite poor results. According to V. Le Corre *et al.*, for a typical well performing PSC, the conductivity should be around 3·10⁻⁶ S/cm [192], however, none of the measured materials came close to the required value, thus explaining why additive-free TPA compounds did not work well in the researched PSC devices.

3.1.4 Absorption and emission spectra⁴

As mentioned in Chapter 3.1, TPA compounds are versatile charge transport materials possessing high emission efficiency, thus it was decided to further investigate the change in properties after the formation of quaternary ammonium salts.

The optical absorption and emission characteristics of TPA compounds **H1-H9** are presented in Figure 3.5. With the increasing number of phenylethenyl substituents in the TPA core, a slight redshift in the absorption is observed: **H1** absorbs light at 383 nm, while two phenylethenyl fragments containing **H4**, **H7** have absorption maxima at 403 nm and 394 nm, respectively. The observed bathochromic shift is attributed to the extended π -conjugation system. Meanwhile, the introduction of iodine or TFSI ions disturbs the charge transfer (CT) transition in the absorption band, compared with neutral analogues. After the incorporation of iodine and TFSI ions, the absorption peaks at 365 nm and 362 nm, respectively, were observed, while additional methoxy substituents do not influence the absorption bands.

³ Measurements of conductivity were performed at the Institute of Chemical Physics, Vilnius University, by Prof. G. Juška

⁴ Done in collaboration with Prof. Saulius Juršėnas research group at the Institute of Photonics and Nanotechnology, Vilnius University

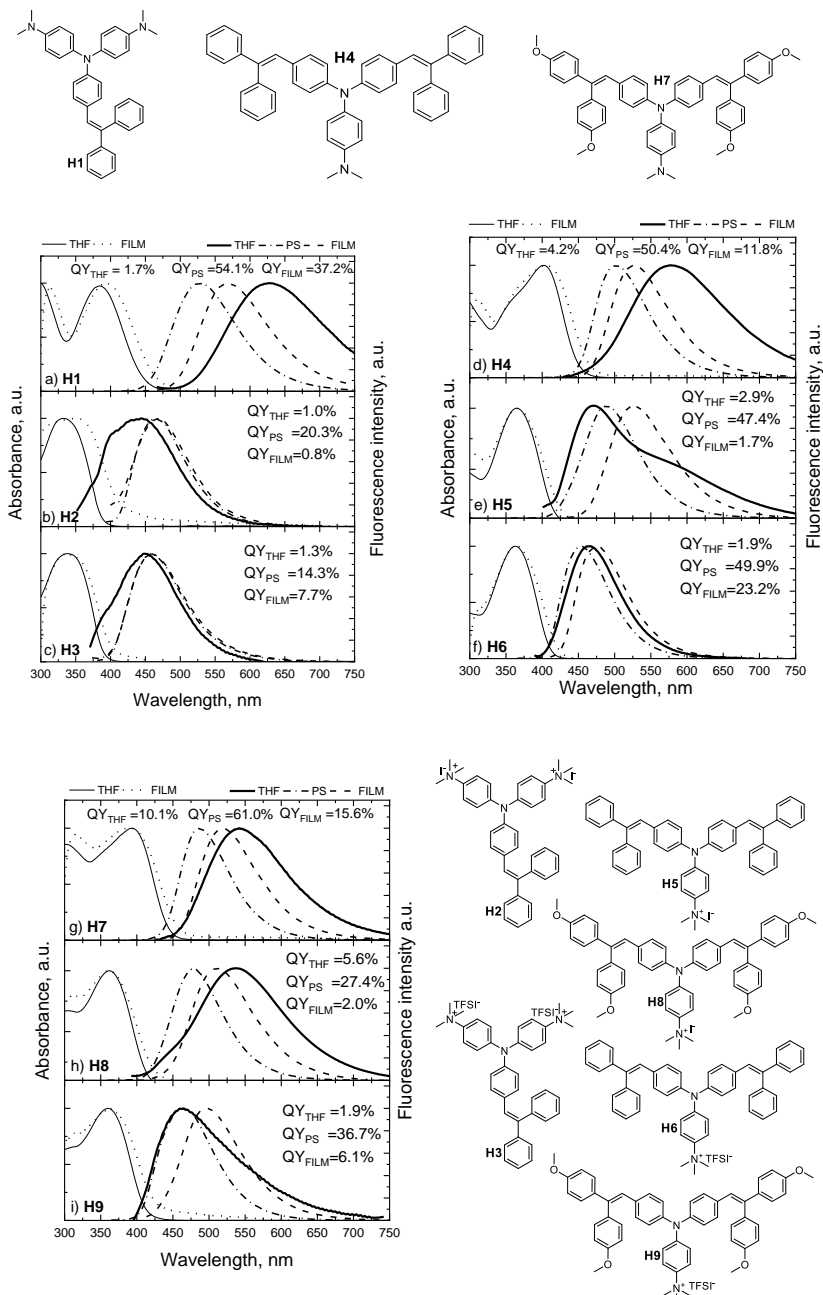


Figure 3.5. Absorption and emission (FL) spectra of TPA derivatives **H1-H9**. Black line – absorption in THF (10^{-6} M) solution, black dot line absorption in spin coated neat film (~ 100 nm in thickness, THF solution), black bold line – fluorescence (FL) in THF solution, dash dot line – fluorescence in PS film (0.1 wt%) dash line – fluorescence in neat film

A TPA derivative with two methylamine fragments **H1** demonstrated structureless emission in amber spectral region at 626 nm (in THF), leading to a large (243 nm) Stokes shift. The introduction of a second phenylethenyl substituent into the TPA core mitigates the relaxation of the excited state as the Stokes shift decreases to 174 nm for **H4** (fluorescence peak at 577 nm). Moreover, the methoxy substituents in **H7** further decrease the charge transfer while reducing the Stokes shift to 149 nm (fluorescence peak at 543 nm), which indicates changes in the donoric properties of the methoxy groups and π -conjugation across the TPA-dimethylamine backbone due to the different twist angles in the excited state conformation.

The incorporation of iodine and TFSI⁻ ions into the TPA-dimethylamine core greatly reduces the CT character. The deactivation of two strong donoric dimethylamine substituents causes a bathochromic shift (~110 nm) with the emission maxima peaking at around 440 nm, independent on the ion used (Table 3.3).

Weak influence of the iodine ion is observed as **H5** exhibits twofold emission characteristics with the red edge emission shoulder at around 580 nm (**Figure 3.5e**), which implies a residual CT transition from the dimethylamine fragment. Interestingly, the introduction of iodine and TFSI⁻ ions into TPA-dimethylamine compounds with phenylethenyl methoxy substituents (**H8**, **H9**) influenced the CT transition differently. Iodine does not perturb the CT transition via the TPA core as similar emission maximums for **H7** and **H8** at around 540 nm are observed. Meanwhile, the presence of a TFSI⁻ ion reduces the Stokes shift from 150 nm for **H7** to roughly 100 nm for **H9** with the emission peaking at 461 nm (Table 3.3).

Table 3.3. Absorption and emission maxima of investigated TPA derivatives in various environments

| Compound | H1 | H2 | H3 | H4 | H5 | H6 | H7 | H8 | H9 |
|---|-----------|-----------|-----------|-----------|-----------|-----------|-----------|-----------|-----------|
| λ_{abs} (nm) (Solution) | 383 | 332 | 339 | 403 | 365 | 362 | 394 | 361 | 359 |
| λ_{FL} (nm) (Solution) | 626 | 442 | 442 | 577 | 470 | 460 | 543 | 537 | 461 |
| λ_{FL} (nm) (PS matrix) | 527 | 465 | 447 | 500 | 486 | 452 | 486 | 477 | 460 |
| λ_{abs} (nm) (Film) | 393 | 346 | 339 | 405 | 365 | 362 | 394 | 361 | 359 |
| λ_{FL} (nm) (Film) | 568 | 465 | 447 | 527 | 525 | 475 | 511 | 498 | 496 |

TPA derivatives were dispersed in a rigid, non-polar polystyrene (PS) matrix with low 1 wt% concentration of the investigated compound. This was done to avoid any interactions between chromophores and to suppress molecular torsions. The absorption spectra for all of the tested compounds are almost identical to the dilute solution environment. Furthermore, all tested TPA compounds exhibited structureless emission because of the wide variety of ‘frozen’ molecular conformations in a rigid polymer matrix. The suppression of molecular torsions in

a rigid non-polar medium blueshifts the emission spectra about 100 nm for **H1** (maximum at 527 nm in PS) in comparison with the dilute solution (maximum at 626 nm). This is due to the polar molecule-solvent interaction and the relatively small size of the molecules, which leads to more molecular torsions in the solution. Meanwhile, **H4** and **H7**, with their larger and less polar diphenylethenyl groups, demonstrated a somewhat smaller blueshift of emission – 77 nm (at 500 nm) and 57 nm (at 486 nm), respectively (Table 3.3). The fluorescence spectra of the quaternary ammonium compounds **H5** and **H6** in a rigid polymer matrix essentially do not differ from the emission spectra in the THF solution. Additional methoxy substituents in phenylethenyl groups (**H7–H9**) influence the emission spectra differently, and the fluorescence shift varies depending on the structure. With the iodine ion, a 60 nm blueshift is observed (**H8**), while the compound with the TFSI⁻ substituent (**H9**) fluorescents in the same spectral region as the dilute solution.

Additionally, the influence of intermolecular interactions on the spectral emission characteristics in solid-state films was investigated. All compounds demonstrated structureless fluorescence bands. In the neutral molecules (**H1**, **H4**, **H7**), the peak of the emission spectra in the solid state falls in the region between that of the solution and the PS film: 568 nm, 527 nm and 511 nm for **H1**, **H4** and **H7**, respectively (Table 3.3). Compared to dilute solutions, the suppression of molecular torsions in films and the elimination of interaction with solvent molecules causes blueshift in emission. On the other hand, compared to the PS environment, the redshift of the fluorescence emission maxima in the films of **H1**, **H4**, **H7** is due to the more polar nature of the surrounding molecules. In the solid state, the peak position and shape of the spectra of ionic TPA compounds with two dimethylamine moieties **H2** and **H3** does not depend on the structure, resembling emission in dilute solution and polymer matrix. However, for quaternary ammonium compounds with two phenylethenyl substituents **H5** and **H6**, the iodine ion enhances the interaction between molecules and redshifts the emission (compared to the solution and polymer matrix) in the solid state (525 nm), while the TFSI⁻ ion effectively suppresses the aforementioned red shift in the fluorescence, and emission occurs at 475 nm, similarly to the results seen in the dilute solution and the polymer matrix. Virtually no spectral changes are observed in the solid state with the inclusion of an iodine (**H8**) or a TFSI⁻ (**H9**) ion in the compounds containing methoxy substituted phenylethenyl moieties.

3.1.5 Fluorescence quantum yield

The fluorescence quantum efficiency of TPA compounds in various mediums was investigated, and the obtained results can be seen in Table 3.4. All of the TPA derivatives exhibited low quantum efficiency (QY) in THF. The lowest QY of the investigated neutral compounds is observed for **H1** (1.7%). The result could be explained by the labile molecular structure, an additional donoric dimethylamine moiety compared to **H4** and **H7**, and the prominent CT transition. The emission efficiency increases to 4.2% with the introduction of the second phenylethenyl substituent in **H4**. Additional methoxy substituents double the fluorescence QY to 10.1%, which is in line with the consistently decreasing Stokes shift of the

investigated compounds. Fluorescence QY in dilute solutions diminishes with a similar trend after the quaternization of amine in the TPA-dimethylamine core, independently of the used ion. When the appropriate neutral, iodine and TFSI⁻ compounds are compared, the observed steady decrease in the quantum efficiency is associated with new non-radiative decay pathways at the ion-dimethylamine site, while the significance of the effect is attributed to the differences in the electronegativity of the iodine and TFSI⁻ ions and a different level of the deactivation of the CT transition.

A non-polar, rigid polymer environment effectively suppresses the CT transition and non-radiative pathways through molecular torsions and enhances the emission from the unrelaxed Franck-Condon state, thus enhancing the fluorescence quantum efficiency for all the three neutral molecules (**H1**, **H4**, **H7**) by up to 32 times from 1.7% to 54.1% specifically in the case of **H1**. The quaternization of the tertiary amine induces non-radiative decay sites with the corresponding decrease in the quantum yield from 54.1% to 20.3% and 14.3% for **H2** and **H3**, respectively. Meanwhile, the incorporation of the second diphenylethenyl substituent in **H4** diminishes the effect of amine quaternization on QY. In **H5** and **H6**, the QY values become ion-independent with QY at around 50%. This does not apply, however, to the compounds with additional methoxy substituents. The incorporation of iodine and TFSI⁻ ions (**H8** and **H9**) reduces the fluorescence quantum efficiency. The non-trivial behavior of fluorescence QY of structurally similar compounds **H5**, **H6** and **H8**, **H9** could be explained by the introduction of new, non-radiative relaxation pathways via intersystem crossing to the triplet states due to the introduction of iodine and TFSI⁻ ions and the residual CT emission.

Table 3.4. Fluorescence QY and fluorescence emission peak data of TPA–dimethylamine compounds in various mediums: THF (10⁻⁶ M), PS (1% w.t.), Film

| Compound | THF | | PS 1% w.t. | | Film | |
|-----------|-------|---------------------|------------|---------------------|-------|---------------------|
| | QY, % | λ_{FL} , nm | QY, % | λ_{FL} , nm | QY, % | λ_{FL} , nm |
| H1 | 1.7 | 626 | 54.1 | 527 | 37.2 | 568 |
| H2 | 1.0 | 442 | 20.3 | 465 | 0.8 | 465 |
| H3 | 1.3 | 442 | 14.3 | 447 | 7.7 | 447 |
| H4 | 4.2 | 577 | 50.4 | 500 | 11.8 | 527 |
| H5 | 2.9 | 470 | 47.4 | 486 | 1.7 | 525 |
| H6 | 1.9 | 460 | 49.9 | 452 | 23.2 | 475 |
| H7 | 10.1 | 543 | 61.0 | 486 | 15.6 | 511 |
| H8 | 5.6 | 537 | 27.4 | 477 | 2.0 | 498 |
| H9 | 1.9 | 461 | 36.7 | 460 | 6.1 | 496 |

The films of all three neutral compounds **H1**, **H4**, **H7** exhibited aggregation induced emission enhancement phenomena. The most prominent change was observed for **H1**. QY increased by more than 22 times, from 1.7% in the THF solution to 37.2% in the film. With the introduction of an additional bulkier diphenylethenyl substituent, the aggregation induced emission enhancement effect diminishes. For **H4**, the QY increases from 4.2% in the solution to 11.8% in the

film, whereas, for **H7**, the QY changes from 10.1% to 15.5%, respectively. Most likely, the enhanced exciton migration and the recombination at defect sites in the solid state are the reasons for such a prominent drop in the aggregation induced emission enhancement. Similarly, as with phenylethenyl moieties, the introduction of ionic substituents also diminishes aggregation induced fluorescence QY enhancement. For compounds containing a iodine ion (specifically, **H2**, **H5** and **H8**), the quantum efficiency does not exceed 2%. Iodine ions induce defect rich non-radiative recombination centers in the solid state, thus quenching exciton migration. A somewhat higher fluorescence quantum yield is observed for TFSI-substituted compounds, where QY is 7.7% and 6.1% for **H3** and **H9**, respectively. Meanwhile, a small QY enhancement over the neutral counterpart (**H4**, 11.8%) is observed for **H6** (23.2%).

3.1.6 Photophysical properties in aggregated particles

Particles were prepared by the precipitation method [193], with the aggregated phase being dispersed in a solution. Aggregated particles are formed due to the insolubility of a compound in a solvent. In our particular case, particles are formed from the THF solution via the aggregation of the investigated material being dispersed in water. Usually, the photophysics of aggregated particles is similar to the characteristics of neat films, yet with some differences related to the aggregate size. Neutral TPA analogues **H1**, **H4** and **H7** formed nanoaggregates with the average size of 140–190 nm. The introduction of iodine and TFSI ions resulted in significant changes in the size of aggregated particles, from 60 nm with iodine to 560 nm with TFSI counterions, and the difference could be associated with the changes in the solubility of the investigated molecules in water.

The absorption spectra of TPA derivative particles highly resemble the ones obtained in the THF solution and in the solid-state environment (Figure 3.6). The lowest absorption band peaks at 393–408 nm, with a blueshift towards the 330–360 nm spectral region after the quaternization of the amine moiety.

The fluorescence of neutral compounds **H1**, **H4** and **H7** in the aggregated state is similar to neat films, mostly due to suppressed molecular torsions. A slight red-shift in the PL spectra (around 10 nm) in relation to the emission from neat films is caused by residual fluorescence from a very small fraction of the dissolved material. The quaternization of the amine moiety further blueshifts the emission. Different trends for iodine and TFSI salts are observed due to different aggregation induced molecular packing and interaction with water. This falls in line with the observations made from the fluorescence spectra in thin films.

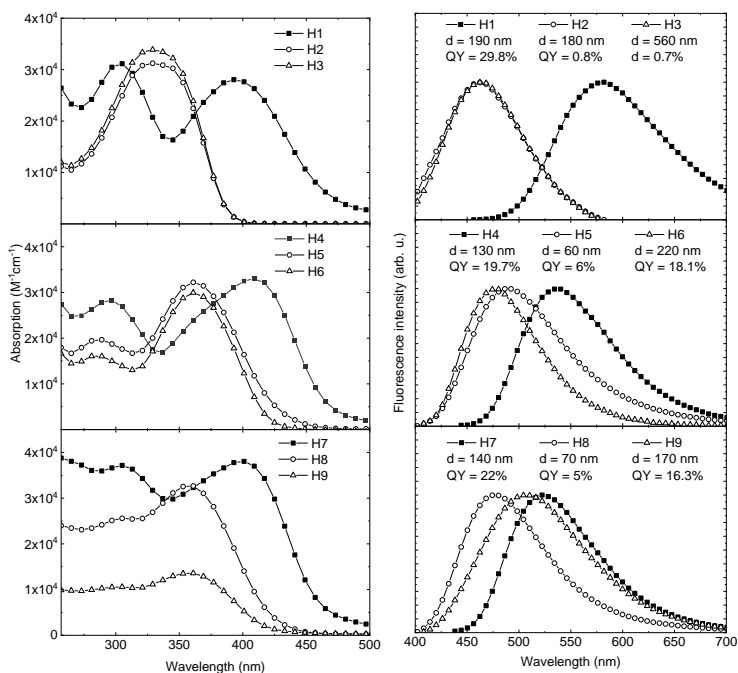


Figure 3.6. Photophysical properties of **H1-H9** aggregated particles in THF/H₂O environment. Left side – absorption spectra. Right side – emission spectra, insets in the graphs – fluorescence QY and average particle size, respectively

With the suppression of molecular torsions, particles of TPA derivatives **H1-H9** (similarly to the solid state) exhibit aggregation induced emission enhancement phenomena. Moreover, if compared with the solid state, somewhat higher fluorescence quantum efficiency is observed due to restricted exciton diffusion outside aggregated particles via the liquid phase. Particles of neutral compounds demonstrate a higher QY in comparison to the fluorescence efficiency in neat films, 29.8%, 19.7% and 22.0% for **H1**, **H4** and **H7**, accordingly. Somewhat different results were observed for TPA ionic compounds. **H9**, containing TFSI⁻ counterion and donoric methoxy groups, exhibits a higher fluorescence QY compared with the one measured in the film. On the other hand, the absence of donoric methoxy groups in **H3** and **H6** results in a lower fluorescence QY compared with the one registered in the film, while iodine counter ion bearing derivatives (**H2**, **H5**, **H8**) demonstrated little to no change in QY. Most likely, the results of the investigated ionic materials could be attributed to the different solubility in water, and therefore to a higher fraction of non-emissive dissolved material.

3.1.7 Conclusion of Chapter 3.1

Due to unsuccessful attempts to employ TPA derivatives **H1-H9** as HTMs in PSCs, their absorption and emission properties were thoroughly investigated in hopes to find an alternative use in optoelectronics. All of the tested compounds

exhibited aggregation induced emission enhancement in the solid state due to suppressed molecular torsions, while reaching a QY of 37.2% in the thin film for tertiary amine **H1** and 61% in the PS matrix for **H7**. Despite improvements in the solid state, quaternary ammonium compounds are not suitable candidates for optoelectronic applications due to their low QY, high I_p and uncertain drift carrier mobility, while neutral molecules **H1**, **H4** and **H7** might be used as multifunctional charge transport and emissive layers in the future optoelectronic device research.

3.2. Semiconductive polymers as hole transporting materials in perovskite solar cells

One of the biggest challenges in the development of high-performance devices is the process of designing efficient charge-transporting materials [194, 195]. Organic chemistry offers ways to solve this problem by allowing us to synthesize a countless variety of different compounds as well as to use simple processing techniques for device fabrication by solution or vacuum deposition methods, preferably while using simple, cheap and easily purifiable materials [3, 196]. Small-molecule HTMs exhibit many advantages over polymeric materials, such as the constant molecular weight, structural versatility, and relatively easy purification by crystallization, chromatography or vacuum sublimation [197, 198]. Unfortunately, a large amount of these charge transporting compounds have relatively low glass transition temperatures (T_g) [131, 196, 199], which can lead to glass-to-liquid or glass-to-crystals transitions potentially diminishing the performance and longevity of the device [200, 201]. Furthermore, often, small-molecule HTMs do not form uniform layers, which results in charge recombination [202–204] and in the overall decline in the solar cell efficiency [203].

Polymeric HTMs must meet most of the same requirements as small-molecule charge carriers: compatibility with the perovskite layer, tunable energy levels, suitable carrier mobility and a low cost [205]. There are two kinds of polymers used as HTMs: D–A type copolymers and homopolymers with the majority of them being conjugated while there are only very few nonconjugated examples [167].

A fair amount of D–A conjugated copolymers display excellent film forming properties, tunable energy levels, a low band gap and high mobility without the need for dopants [205]. Despite the presently listed advantages, these HTMs are not practical as they usually require long and difficult synthetic pathways leading to a high cost thus making them unsuitable for large-scale applications [206–208].

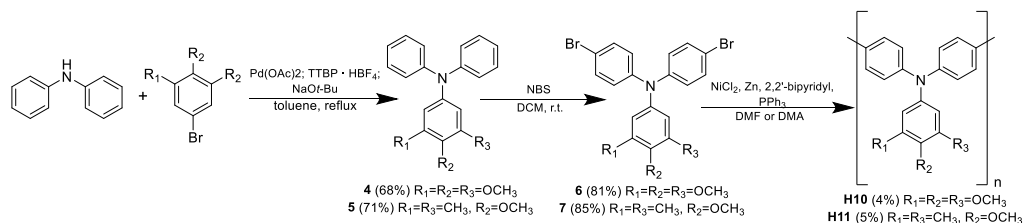
One of the largest groups of conducting polymers is based on the TPA backbone with the most widely used one being PTAA. The performance obtained with this HTM is highly comparable to the standard reference charge carrier spiro-OMeTAD [209]. Despite PTAA showing respectable stability at higher temperatures and not requiring dopants, its wide scale applicability suffers from the extremely high cost [81]. On the other hand, in a work by T. Matsui *et al.* [18], three new low cost triarylamine-based polymers were tested as HTMs without the use of additives. The champion solar cell was stable for more than 140 h without significant changes in the efficiency, while the PCE of the devices with the

respective doped polymer significantly decreased in the first few hours. However, the highest PCE value of 12.3% must still be improved in order for these materials to be seriously considered for commercial usage.

A different strategy is to conduct thermal or photocrosslinking of the monomer containing multiple reactive groups (for example, vinyl or methacryl). The acquired polymer is nonconjugated; however, it does not require any performance boosting additives, while also forming a reliable barrier against moisture [210]. This chapter is dedicated to the synthesis and investigation of TPA based polymers and cross-linkable monomers.

3.2.1. Synthesis of triphenylamine based polymers

Synthesis of 3,4,5-trimethoxy-*N,N*-diphenylaniline (**4**) was conducted by the Buchwald-Hartwig coupling reaction from diphenylamine and 1,2,3-trimethoxybenzene under argon in anhydrous toluene in the presence of sodium *tert*-butoxide. The same conditions were also applied in the reaction of diphenylamine with 4-bromo-2,6-dimethylanisole yielding 4-methoxy-3,5-dimethyl-*N,N*-diphenylaniline (**5**) (Scheme 3.3).



Scheme 3.3. Synthesis of polymers **H10** and **H11**

The acquired compounds were brominated with *N*-bromosuccinimide (NBS) in DCM yielding *N,N*-bis(4-bromophenyl)-3,4,5-trimethoxyaniline (**6**) and *N,N*-bis(4-bromophenyl)-4-methoxy-3,5-dimethylaniline (**7**), respectively. Both TPA derivatives were used in Yamamoto homopolymerization in the presence of triphenylphosphine (TPP), Zn, 2,2'-bipyridine, and NiCl₂ under argon to give polymers **H10** and **H11** in low yields (Scheme 3.3). Attempts were made to optimize the aforementioned polymerization reaction based on the findings of I. Colon *et al.*, V. Percec *et al.* and G. T. Kwiatkowski *et al.* [211–213] with little success (Table 3.1). Before going deeper into the analysis of results in Table 3.5, it is worth mentioning that these reactions are very delicate and are especially sensitive to oxygen and moisture [211–213]; even the smallest amounts of them may potentially influence the outcome of the reaction significantly. To reduce the aforementioned risks, flasks were preheated for ten minutes at 180 °C and purged with argon gas for more than an hour.

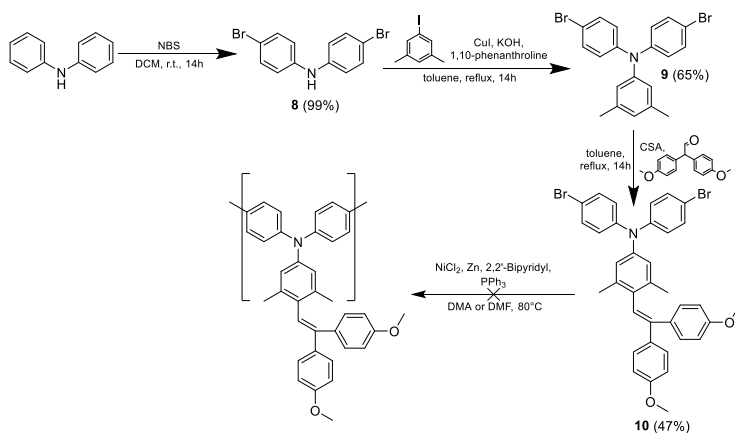
Since the monomers must be properly dissolved and reactions can only be conducted in dipolar aprotic solvents, DMA and DMF were tested as candidates in the first two attempts. The desired product was only obtained in DMF, which led to its usage in the following experiments. After attempts 3 and 4, it was determined

that the period of 14 hours should be the optimal duration of the reaction, while test 5 proved that there is no benefit in going above 80 °C temperature. As stated by I. Colon *et al.* [211], in order to produce high polymer yields, the NiCl₂ level should be less than 2 mol% based on the amount of the monomer, and the TPP concentration should be about 0.25 M or higher, while 2,2'-bipyridine should not exceed 1.25 times the amount of nickel on a mole basis. Having that in mind, attempts 6–12 were conducted to find the best balance between the aforementioned compounds in relation to the monomer; unfortunately, only 5% yield was reached during these experiments.

Table 3.5. Yamamoto polymerization experiments of **H11**

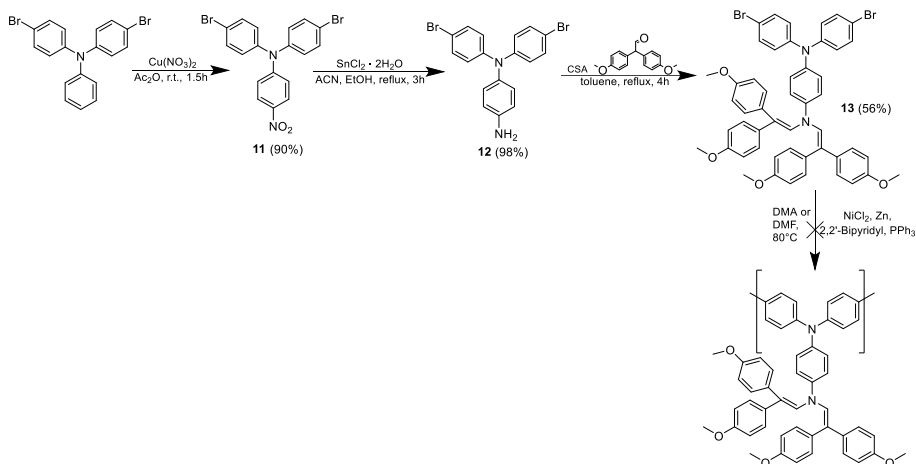
| Attempt No. | Monomer, mmol | NiCl ₂ , mmol | Zn, mmol | 2,2'-bipyridine, mmol | TPP, mmol | Solvent, ml | T, °C | t, h | Yield, % |
|-------------|---------------|--------------------------|----------|-----------------------|-----------|-------------|-------|------|----------|
| 1 | 0.65 | 0.047 | 2.05 | 0.07 | 0.47 | DMA, 2 | 80 | 6 | 0 |
| 2 | 0.65 | 0.047 | 2.05 | 0.07 | 0.47 | DMF, 2 | 80 | 6 | 2 |
| 3 | 0.65 | 0.047 | 2.05 | 0.07 | 0.47 | DMF, 2 | 80 | 14 | 3 |
| 4 | 0.65 | 0.047 | 2.05 | 0.07 | 0.47 | DMF, 2 | 80 | 48 | 3 |
| 5 | 0.65 | 0.047 | 2.05 | 0.07 | 0.47 | DMF, 2 | 140 | 14 | 3 |
| 6 | 0.65 | 0.01 | 4.0 | 0.01 | 0.9 | DMF, 2 | 80 | 14 | 2 |
| 7 | 0.65 | 0.01 | 4.0 | 0.01 | 0.9 | DMF, 1 | 80 | 14 | 2 |
| 8 | 0.65 | 0.01 | 4.0 | 0.01 | 0.9 | DMF, 4 | 80 | 14 | 2 |
| 9 | 0.65 | 0.01 | 4.0 | 0.01 | 1.37 | DMF, 2 | 80 | 14 | 2 |
| 10 | 0.65 | 0.09 | 4.0 | 0.15 | 0.9 | DMF, 2 | 80 | 14 | 5 |
| 11 | 0.65 | 0.18 | 4.0 | 0.15 | 0.9 | DMF, 2 | 80 | 14 | 3 |
| 12 | 0.65 | 0.09 | 4.0 | 0.09 | 0.9 | DMF, 2 | 80 | 14 | 5 |

Due to the unsuccessful attempts to optimize the conditions of Yamamoto polymerization with the chosen monomers, a choice was made to carry out the synthesis with molecules similar to the ones described in an article by T. Matsui *et al.* [21]. The first step was the synthesis of bis(4-bromophenyl)amine (**8**) via bromination of diphenylamine with NBS in DCM. The acquired compound was then reacted with 3,5-dimethyliodobenzene in an Ullmann-type reaction in the presence of CuI, KOH and 1,10-phenanthroline in toluene, thus giving TPA derivative **9**. Condensation of **9** with 2,2-bis(4-methoxyphenyl)acetaldehyde in the presence of camphor-10-sulfonic acid (β) (CSA) yielded compound **10** as a product (Scheme 3.4). Unfortunately, the homopolymerization of **10** under the conditions described by T. Matsui *et al.* was unsuccessful.



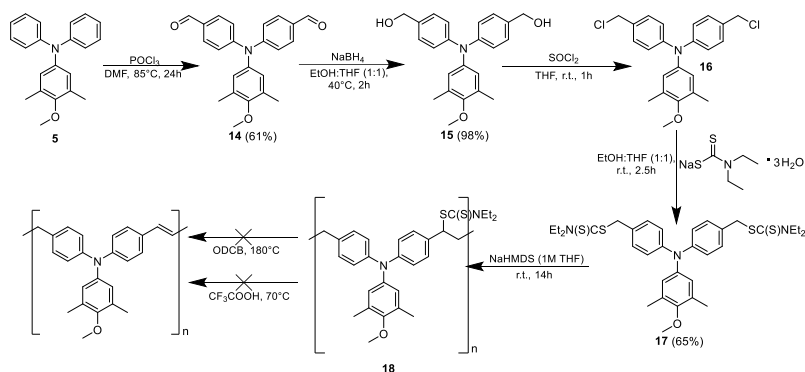
Scheme 3.4. Attempts of polymerization of **10**

After the unsuccessful polymerization attempts of monomer **10**, a decision was made to slightly change the structure of the monomer in hope that a larger conjugated system will lead to the better outcome of the reaction (Scheme 3.5). To achieve this goal, a nitro group was introduced to 4,4'-dibromotriphenylamine in the presence of copper (II) nitrate in acetic anhydride, thus giving triphenylamine **11**. The nitro group of **11** was then reduced with stannous chloride dihydrate yielding 4-amino-4',4''-dibromotriphenylamine (**12**). The condensation of **12** with 2,2-bis(4-methoxyphenyl)acetaldehyde in the presence of CSA in toluene gave enamine **13** as the desired product. Unfortunately, the polymerization results were identical to the ones described in Scheme 3.2 – i.e., no polymer was obtained. The lack of success with the NiCl₂ system Yamamoto polymerization could probably be attributed to moisture and oxygen getting in the reaction mixture despite the adopted precautions. The use of bis(1,5-cyclooctadiene)nickel(0) (Ni(COD)₂) was considered, as it is widely used for Yamamoto coupling. However, the idea was scrapped due to the difficulties of working with Ni(COD)₂, as it is limited by its complicated reaction setup requiring the Schlenk technique or the use of a glove box to avoid immediate decomposition upon exposure to air [214]; therefore, such an approach would be incompatible with our goal of simple-to-make, efficient hole transporting materials.



Scheme 3.5. Attempts to synthesize a polymer from monomer **13**

The failure to obtain polymeric HTM in good yields via the Yamamoto route led us to attempt polymerization via the dithiocarbamate (DTC) route (Scheme 3.6). DMF and phosphorus oxychloride were used to obtain the Vilsmeier reagent, which, in turn, reacted with TPA derivative **5** yielding dialdehyde **14**. The reduction of aldehyde groups of **14** was achieved with sodium borohydride in a mixture of THF and ethanol (1:1) giving TPA derivative **15** as the desired product. *N,N*-bis[4-(chloromethyl)phenyl]-4-methoxy-3,5-dimethylaniline (**16**) was synthesized via the substitution reaction with thionyl chloride in THF. The reaction of **16** with sodium diethyldithiocarbamate trihydrate in equal parts of THF and ethanol yielded premonomer **17**.



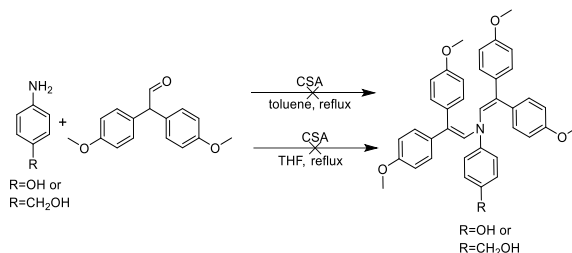
Scheme 3.6. Synthesis of TPA based polymer via DTC route

Based on an article by H. Dilien *et al.* [215], polymerization from dithiocarbamate derivatives is a two-step process. In the first stage, a prepolymer is formed by the reaction between **17** and a solution of sodium bis(trimethylsilyl)amide in THF under argon, while the second step consists either of heating prepolymer **18** in *o*-dichlorobenzene, or it involves reacting it with

trifluoroacetic acid. Despite the obvious visual change in the first step, no goal polymer was obtained during the second step of the process. The thermal degradation or low reactivity of **18** could be the reason(s).

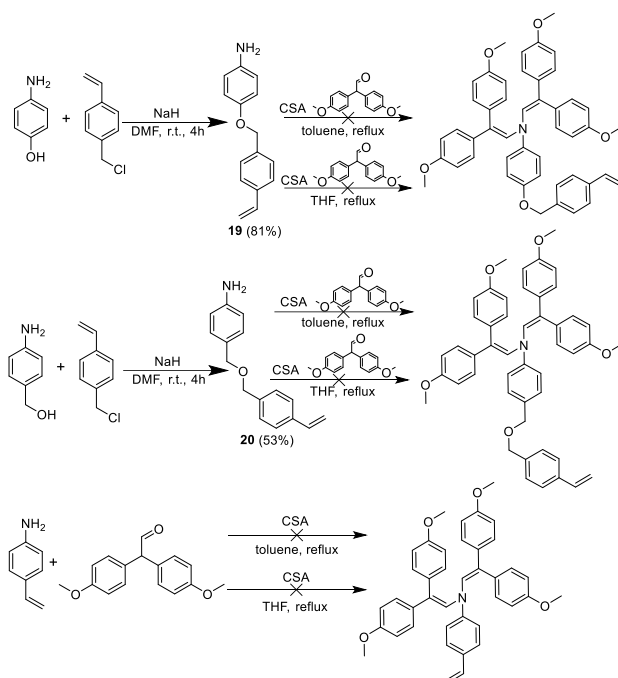
3.2.2. Synthesis of polymers based on well performing hole transporting materials

An approach was adopted to acquire materials that could polymerize in a solution or a layer by thermal annealing or photopolymerization. For this task, well performing and easily obtainable HTMs were selected, and attempts were made to produce their polymerizable versions (Schemes 3.7, 3.8). The reasoning behind it was to synthesize polymeric versions of efficiently performing hole conductors and compare the change in the properties after the formation of macromolecules. Firstly, it was attempted to synthesize a modified **V1092** derivative [20] by obtaining an intermediate compound with a hydroxyl group (Scheme 3.7). Unfortunately, CSA catalyzed condensation reaction between 4-aminophenol and 2,2-bis(4-methoxyphenyl)acetaldehyde in toluene or THF was unsuccessful due to the formation of side products only. In the second attempt, the OH group was moved further from the benzene ring in hopes to mitigate the electron withdrawing properties of the hydroxyl group. Despite these changes the goal product was not obtained due to the formation of multiple side products.



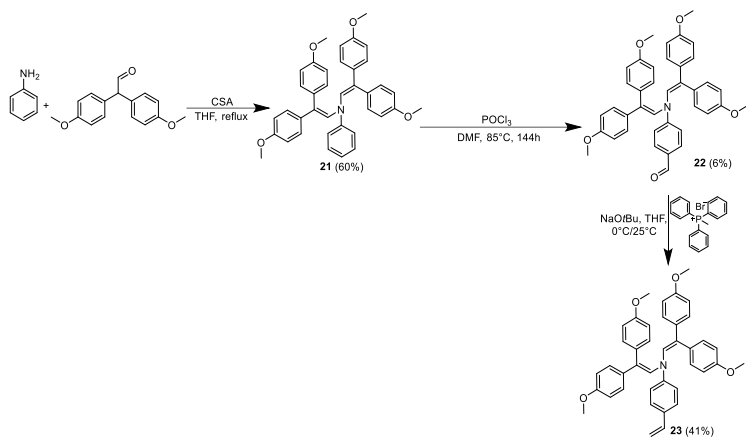
Scheme 3.7. Unsuccessful synthesis of aniline derivatives

An alternative path was chosen in an effort to synthesize the desired polymeric derivative of **V1056** (Scheme 3.8). 4-Aminophenol and 4-aminobenzyl alcohol reacted with 4-vinylbenzyl chloride in DMF using sodium hydride as a base, yielding intermediates 4-[(4-ethenylphenyl)methoxy]aniline (**19**) and 4-[(4-ethenylphenyl)methoxy]methyl}aniline (**20**), respectively. The acquired compounds were unsuccessfully used in condensation reactions with 2,2-bis(4-methoxyphenyl)acetaldehyde in toluene while using CSA as a catalyst (Scheme 3.8). The change of the solvent from toluene to THF did not yield any positive effect on the outcome of the reaction. 4-Vinylaniline was also tested in the reaction with 2,2-bis(4-methoxyphenyl)acetaldehyde under the same conditions as mentioned in the previous examples, yet the desired product was not obtained (Scheme 3.8). Polymerization of vinyl group containing compounds at elevated temperatures [216] could be one of the main reasons why the desired product was not obtained in this reaction.



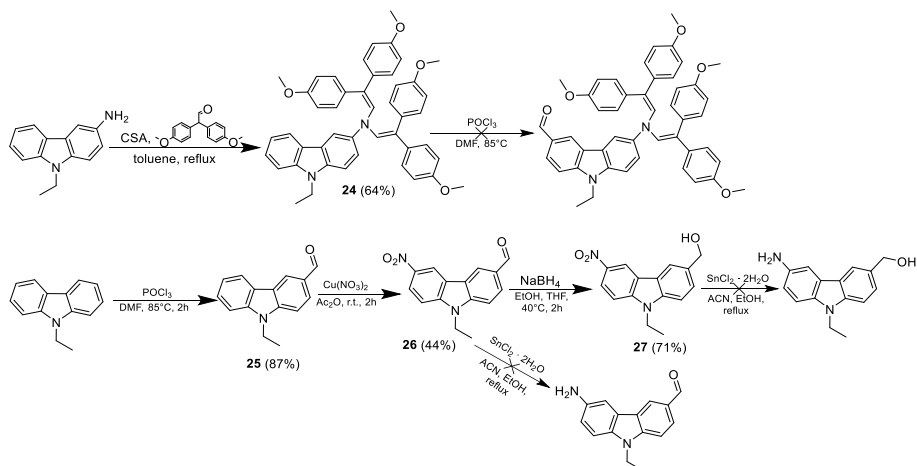
Scheme 3.8. Unsuccessful attempts to synthesize aniline derivatives containing vinyl groups

Another synthetic pathway was explored by virtue of utilizing unsubstituted aniline rather than vinyl containing derivative and functionalizing the obtained HTM afterwards (Scheme 3.9). Reaction with 2,2-bis(4-methoxyphenyl)acetaldehyde in THF while using CSA as a catalyst, which resulted in *N,N*-bis[2,2-bis(4-methoxyphenyl)vinyl]aniline (**21**). It was used in the synthesis of aldehyde **22** by the Vilsmeier–Haack reaction. Finally, sodium *tert*-butoxide together with methyltriphenylphosphonium bromide in THF were used to acquire vinyl group containing aniline derivative **23** (Scheme 3.9). Despite the success in obtaining **23**, further experiments were not conducted with this compound due to the very low yield of aldehyde **22**.



Scheme 3.9. Synthesis of aniline derivative **23**

Very problematic synthesis of aniline derivative **22** led to the decision to change the central core of the molecule from aniline to carbazole with the same goal in mind as before – to obtain a polymer by modifying a well performing HTM. Carbazole **24** was chosen as a testing platform [140]. Compound **24** was synthesized by CSA catalyzed reaction between 3-amino-9-ethylcarbazole and 2,2-bis(4-methoxyphenyl)acetaldehyde in toluene. The acquired enamine **24** was then used in the Vilsmeier–Haack reaction in an attempt to introduce an aldehyde group to the carbazole derivative (Scheme 3.10). Unfortunately, the aforementioned compound was not obtained probably due to the simultaneous introduction of multiple aldehyde groups to the molecule.



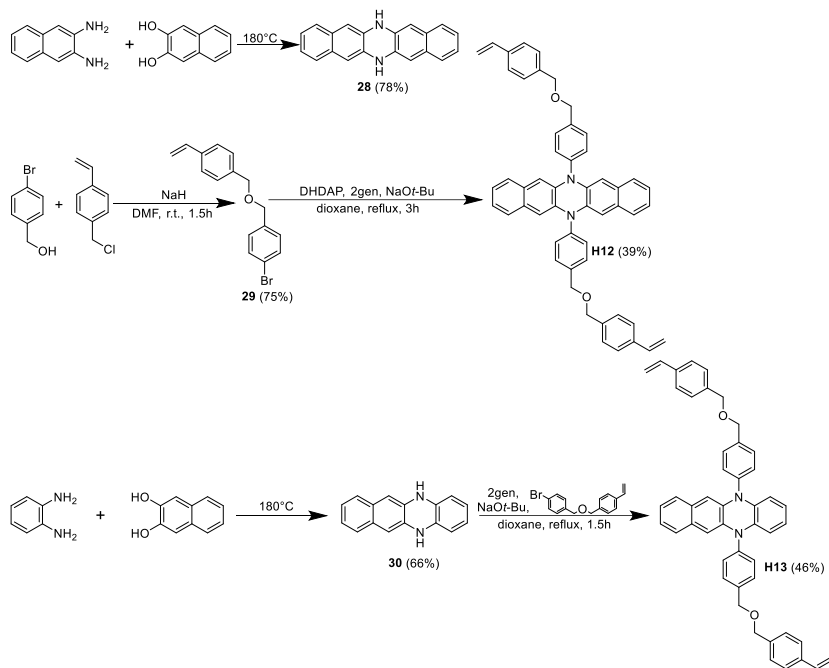
Scheme 3.10. Attempts to acquire a modified carbazole derivative

As an alternative, it was decided to start the synthesis from the formylation of 9-ethylcarbazole with the Vilsmeier reagent thus giving 9-ethyl-9*H*-carbazole-3-carbaldehyde (**25**). Afterwards, **25** reacted with copper (II) nitrate in acetic

anhydride to give 9-ethyl-6-nitro-9*H*-carbazole-3-carbaldehyde (**26**). The aldehyde group of **26** was then reduced with sodium borohydride in a mixture of ethanol and THF thus yielding carbazole derivative **27**. The next step was the reduction of the nitro group of **27** with stannous chloride dehydrate; unfortunately, the reaction was unsuccessful probably due to the rapid formation of side products (Scheme 3.10). Similarly, an attempt to reduce the nitro group of **26** with stannous chloride dihydrate did not result in the carbazole compound containing amino group (Scheme 3.10).

3.2.3. Synthesis of polymers containing dihydrodiazapentacene or dihydrodiazatetracene as the central core

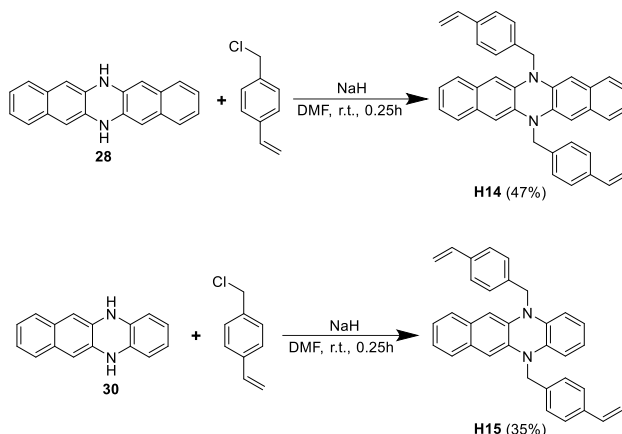
As previous attempts of synthesis were of little success, it was decided to design molecules which would have the ability to cross-link in a layer. For that, monomers with two vinyl groups were synthesized (Scheme 3.11).



Scheme 3.11. Synthesis of compounds **H12** and **H13** containing vinyl groups

At first, dihydrodiazapentacene (DHDAP) (**28**) was synthesized in a condensation reaction between 2,3-diaminonaphthalene and 2,3-dihydroxynaphthalene without the use of any solvent. Afterwards, intermediate 1-bromo-4-[[4-(ethenylphenyl)methoxy]methyl]benzene (**29**) was obtained by Williamson ether synthesis from 4-bromobenzyl alcohol and 4-vinylbenzyl chloride by using sodium hydride as the base in DMF. The obtained compound was used together with **28** in the Buchwald-Hartwig coupling reaction conducted under argon in anhydrous dioxane giving **H12** as the desired product. The same reaction

conditions were applied when **H13** was synthesized from ether **29** and dihydrodiazatetracene (DHDAT) (**30**) (Scheme 3.11). In turn, DHDAT was acquired by condensing 1,2-phenyldiamine with 2,3-dihydroxynaphthalene without the use of any solvent.



To find the most suitable candidate for the application in PSCs, two more compounds with a pair of vinyl groups were synthesized. The reaction between **28** and 4-vinylbenzyl chloride in the presence of sodium hydride in DMF yielded monomer **H14**, while the coupling of **30** with 4-vinylbenzyl chloride under the same conditions gave **H15** as the desired product (Scheme 3.12).

3.2.4. Thermal properties

To evaluate the thermal stability of the materials and their ability to undergo crosslinking, the thermal properties were studied by means of DSC and thermogravimetric analysis TGA. Examples of TGA curves can be seen in Figure 3.7, while the thermal properties of all compounds can be found in Table 3.6. All of the tested materials demonstrated excellent thermal stability after crosslinking above 350 °C.

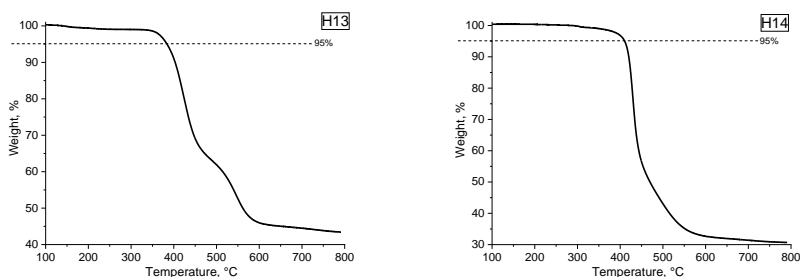


Figure 3.7. Thermal stability of H13 and H14

For compound **H12**, during the first DSC heating cycle (Figure 3.8a), the melting process was detected at 223 °C, followed by an exothermic process at 243 °C, which suggests that thermal polymerization occurs at this temperature. During the second heating cycle, no phase transitions were observed, which confirmed the formation of the cross-linked polymer. Similar changes at lower temperatures can be observed for DHDAT derivative **H13** – crystal melting occurs at 161 °C, while polymerization takes place at 204 °C (Figure 3.8b).

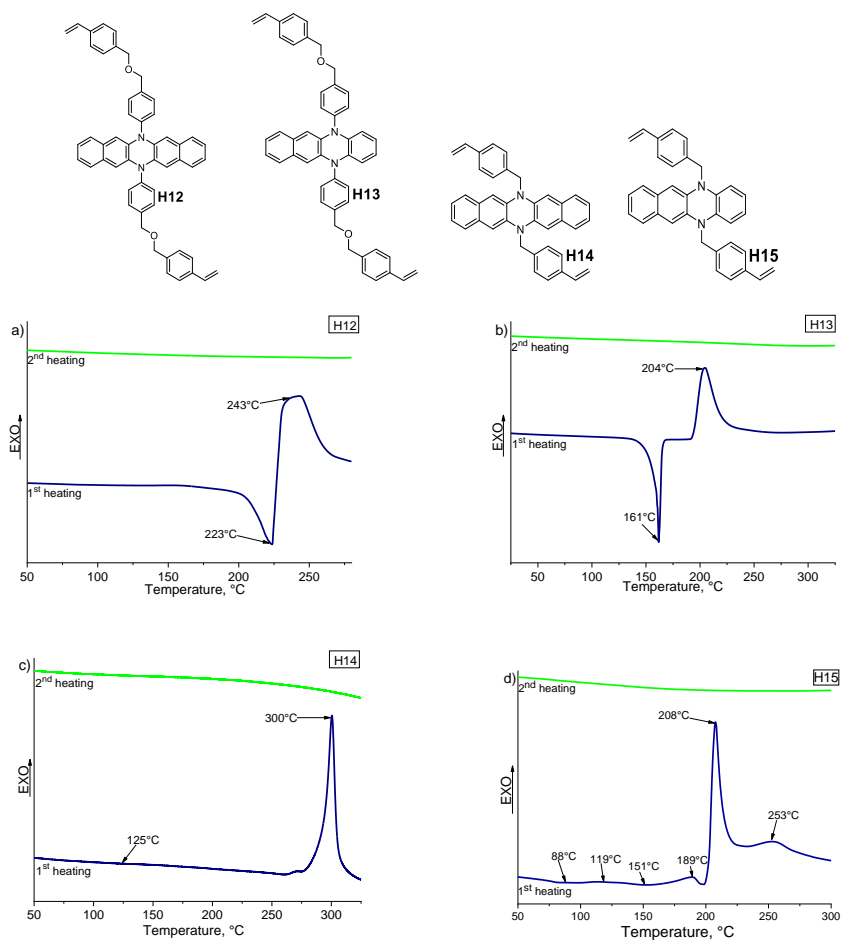


Figure 3.8. DSC curves of compounds: a) **H12** b) **H13** c) **H14** d) **H15**

A different polymerization behavior is seen for **H14** and **H15**. Diazapentacene **H14** demonstrates polymerization temperature at 300 °C, while T_g is observable at 125 °C; although, it is barely visible due to the intensity of the exothermic peak attributed to cross-linking (Figure 3.8c). Quite complex phase transitions can be seen for DHDAT derivative **H15**; it is really difficult to determine which of them can be attributed to T_g . In this particular situation, at

208 °C, intensive crystallization peaks appear, followed by polymerization at 253 °C. During the second heating cycle, no phase transitions were observed. This confirms the formation of the cross-linked polymer.

It is also worth noting that diazapentacenes **H12**, **H14** have higher melting and polymerization temperatures than DHDAT derivatives **H13** and **H15**, respectively, probably due to the larger and more rigid DHDAP core. Furthermore, shorter aliphatic chains in **H14** lead to an increase in the melting and thermal polymerization temperatures.

Table 3.6. Thermal properties of compounds **H12-H15**

| Compound | T_g^a , °C | T_m^b , °C | T_{cr}^c , °C | T_{poly}^c , °C | T_{dec}^d , °C |
|------------|--------------|--------------|-----------------|-------------------|------------------|
| H12 | - | 223 | - | 243 | 360* |
| H13 | - | 161 | - | 204 | 384* |
| H14 | 125 | - | - | 300 | 410* |
| H15 | 88 | | 208 | 253 | 371* |

a) Determined by DSC: scan rate = 10 °C min⁻¹, N₂ atmosphere; second run; b) Determined by DSC: scan rate = 10 °C min⁻¹, N₂ atmosphere; first run; c) Determined by DSC: scan rate = 10 °C min⁻¹, N₂ atmosphere; d) Onset of decomposition determined by TGA: heating rate = 10 °C min⁻¹, N₂ atmosphere; * thermal stability after polymerization

3.2.5. Optical properties

Ultraviolet-visible (UV-Vis) absorption spectra were measured in THF solutions and on glass substrate. In the solution, diazacenes exhibit n- π^* electron transitions in the range of 400–420 nm, while the absorption maxima of the said compounds are between 287 nm and 299 nm (Figure 3.9a). It is also worth noting that the extra phenyl ring in diazapentacenes **H12** and **H14** leads to a 10 nm bathochromic shift compared to their respective DHDAT derivatives **H13**, **H15**.

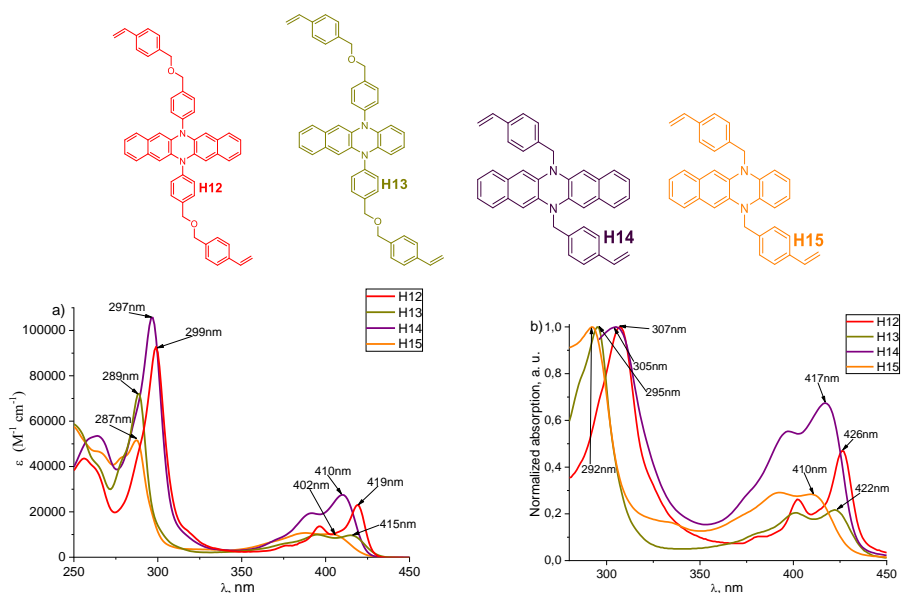


Figure 3.9. a) UV-Vis absorption spectra of **H12-H15** in THF and b) thin-films on glass

In the solid state, the diazacene absorption maxima redshifts by around 8 nm for DHDAP derivatives **H12**, **H14** and roughly by 6 nm for diazatetracenes **H13**, **H15** in comparison to the respective electron transitions in THF (Figure 3.9b). This suggests that materials can exhibit packing in the solid state, which coincides with the observations made in the literature [191, 217].

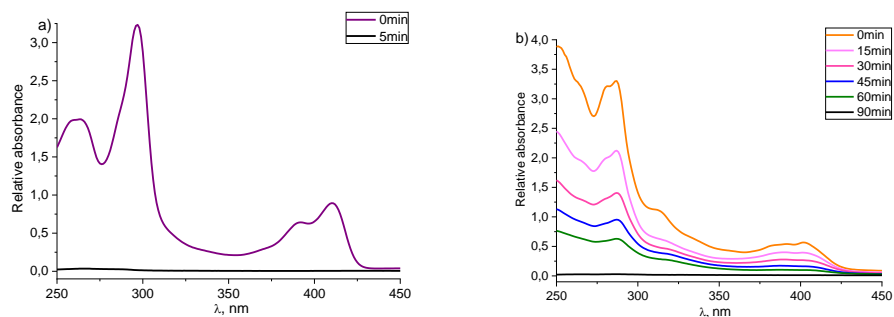


Figure 3.10. UV-Vis absorption spectra in the solution at different times after heating and washing thin films with THF of a) **H14** and b) **H15**

The thin films of compounds **H12-H15** were heated at their polymerization temperatures and washed with 3 ml of THF at various intervals. Afterwards, the absorption spectra of solutions, collected after washing, were measured to determine the time it takes for the material to cross-link (t_{poly}) (Table 3.7, Figure 3.10).

Table 3.7. Light absorption properties and polymerization time of compounds **H12-H15**

| Compound | $\lambda_{\text{max}}^{\text{abs}}$, nm ^a | $\lambda_{\text{max}}^{\text{abs}}$, nm ^b | t_{poly} , min ^c |
|------------|---|---|--------------------------------------|
| H12 | 307 | 303 | 210 |
| H13 | 295 | 292 | 120 |
| H14 | 305 | 272 | 5 |
| H15 | 292 | - | 90 |

a) UV-Vis spectra maxima of thin films on glass. b) UV-Vis spectra maxima of thin films on glass after thermal cross-linking. c) Duration time of polymerization

The duration of cross-linking varies quite significantly from 5 min for **H14** to 210 min for **H12** (Table 3.7). DHDAT derivative **H13** takes half an hour longer to fully react compared with **H15**, while DHDAP derivative **H14** reacts practically instantly, while it takes more than three hours for **H12** to polymerize. It could be argued that the distance of vinyl groups from the central core affects the crosslinking time, thus diazacenes containing longer aliphatic chains **H12** and **H13** have longer polymerization times than the respective analogues.

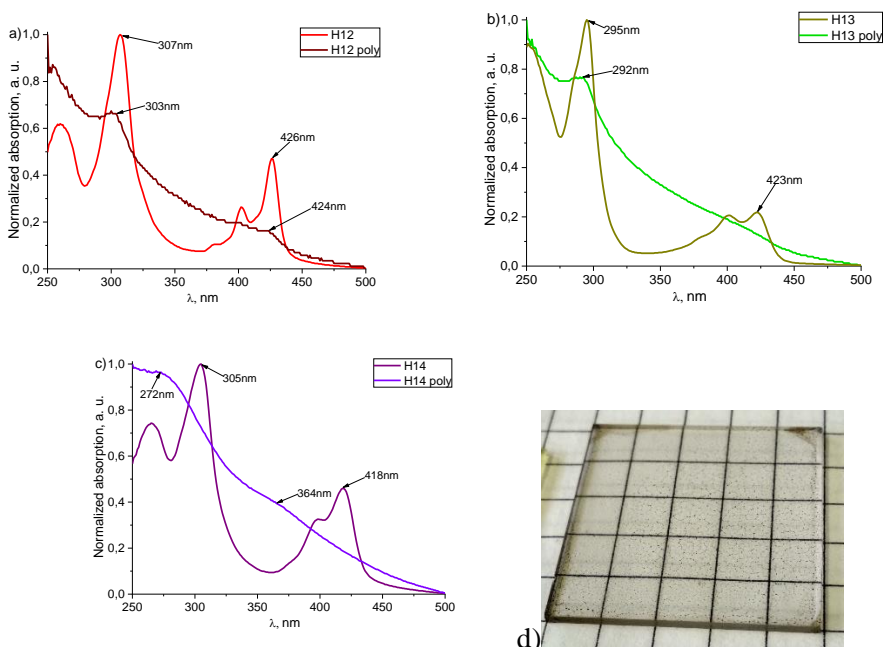


Figure 3.11. UV-Vis absorption spectra on glass before and after polymerization of: a) **H12**, b) **H13** and c) **H14** d) picture of a **H15** layer after polymerization

To observe the absorption changes after thermal annealing, the UV-vis spectra of **H12-H14** films on the glass substrate were recorded (Figure 3.11), while the spectrum of DHDAT derivative **H15** could not be recorded due to the

formation of droplets instead of a thin film after heating (Figure 3.11d). The π - π^* transition of pentacene analogue **H12** poly is blueshifted by 4 nm and n - π^* transition by 2 nm after thermal annealing (Figure 3.11a). A similar hypsochromic shift at a shorter wavelength is seen for DHDAT derivative **H13 poly**; however, no distinguishable peak is observed at a longer wavelength (Figure 3.11b). Interestingly, after heating, diazapentacene **H14** demonstrates a relatively large blueshift of around 30 nm at 272 nm, while an even bigger hypsochromic shift (52 nm) occurs at longer wavelengths, specifically, from 418 nm to 364 nm (Figure 3.11c). This might be due to the high cross-linking temperature of **H14** as similar observations were reported in the literature [218].

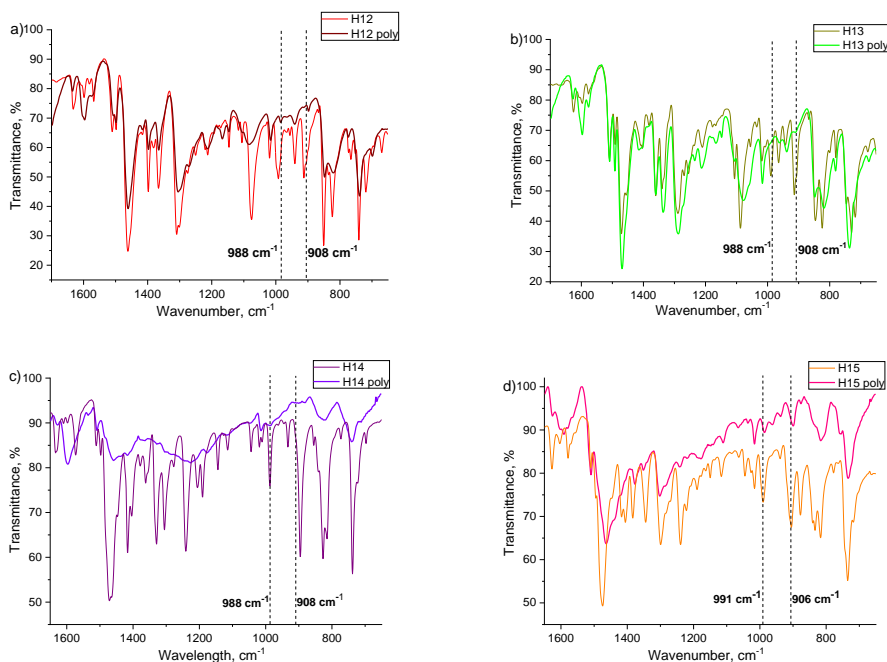


Figure 3.12. FT-IR spectra of **H12-H15** on glass before and after polymerization

As an additional proof of the conversion of vinyl groups, the FT-IR spectra of diazacenes **H12-H15** were recorded and can be seen in Figure 3.12. After heating each compound for the appropriate amount of time (Table 3.7), the characteristic peaks of vinyl groups at 988–991 cm^{-1} and 904–908 cm^{-1} completely disappeared only for tetracene analogue **H13** and DHDAP derivative **H14** (Figure 3.12b and Figure 3.12c), which indicates their complete cross-linking [210]. On the other hand, small intensity peaks at the aforementioned wavelengths are seen for diazapentacene **H12** (Figure 3.12a), suggesting the incomplete (yet relatively high) level of cross-linking, while the more intense peaks at the same positions after

thermal annealing for DHDAT derivative **H15** (Figure 3.12d) are indicative of the formation of macromolecules of a shorter length.

3.2.6. Photoelectric properties

In order for materials to be used in optoelectronic applications, they have to endure countless cycles of oxidation and reduction, thus cyclic voltammetry (CV) is an important measurement to determine the electrochemical stability of potential HTMs. In our case, all of the tested materials demonstrated reversible oxidation, and examples of voltammograms are presented in Figure 3.13. Furthermore, the CV technique can be applied in order to find out the HOMO and LUMO energy levels in a solution. These values do not represent any absolute solid-state or gas-phase ionization energies but can be used to compare different compounds that are relative to one another. Diazacenes **H12-H14** feature similar E_{HOMO} and E_{LUMO} , while **H15** has somewhat higher energy levels in the solution (Table 3.8).

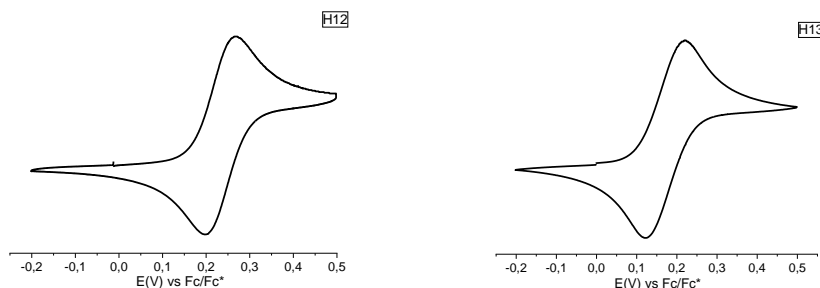


Figure 3.13. Voltammograms of compounds **H12** and **H13**

In order to evaluate the energy levels of tested materials in the solid state, I_p was measured (Figure 3.14a), and it was determined that DHDAT derivatives **H13**, **H15** have identical I_p despite the structural differences between them, while the additional phenyl ring in compounds **H12** and **H14** increases the I_p value by approx. 0.1 eV. All the ionization potential values displayed in Table 3.8 are suitable for the applications in perovskite solar cells as the valence band of the lead perovskite absorber is situated between 5.0 and 5.6 eV [125].

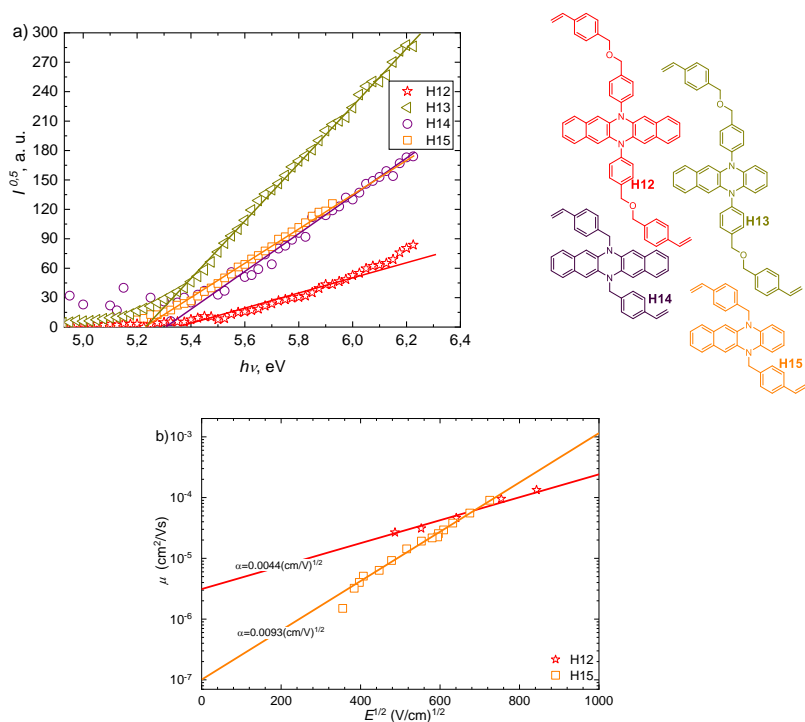


Figure 3.14. a) I_p measurements of compounds **H12-H15** b) charge carrier mobility of **H12** and **H15**

The charge transport properties of the tested HTMs were measured from films by the xerographic time-of-flight (XTOF) method. Compound **H13** could not be measured due to the poor film formation, while the high crystallinity of **H14** limited its solubility, which also led to bad quality layers that were not suitable for assessment with this technique. The solubility of DHDAP derivative **H12** was increased by the additional aliphatic chains, which resulted in the recorded mobility of $3 \cdot 10^{-6} \text{ cm}^2 \text{ V}^{-1} \text{ s}^{-1}$ at zero field strength and $2.4 \cdot 10^{-4} \text{ cm}^2 \text{ V}^{-1} \text{ s}^{-1}$ at stronger electric fields (Figure 3.14b, Table 3.8). There were no issues with material **H15**, although the recorded charge mobility was slightly lower.

Table 3.8. Energy level and hole mobility data for **H12-H15** ^a

| Compound | E_{HOMO} , eV ^b | $E_{\text{g}}^{\text{opt1}}$, eV ^c | E_{LUMO} , eV ^d | I_{p} , eV ^e | $E_{\text{g}}^{\text{opt2}}$, eV ^f | EA , eV ^g | μ_{h} , cm ² V ⁻¹ s ⁻¹ h | μ_{li} , cm ² V ⁻¹ s ⁻¹ li |
|------------|--|---|--|-------------------------------------|---|---------------------------|--|--|
| H12 | -5.17 | 2.88 | -2.29 | 5.36 | 2.79 | 2.57 | $3 \cdot 10^{-6}$ | $2.4 \cdot 10^{-4}$ |
| H13 | -5.11 | 2.86 | -2.25 | 5.23 | 2.78 | 2.45 | - | - |
| H14 | -5.16 | 2.91 | -2.25 | 5.31 | 2.84 | 2.47 | - | - |
| H15 | -5.33 | 2.89 | -2.44 | 5.23 | 2.84 | 2.39 | $1 \cdot 10^{-7}$ | $1.8 \cdot 10^{-4}$ |

a) The CV measurements were carried out at a glassy carbon electrode in dichloromethane solutions containing 0.1 M tetrabutylammonium hexafluorophosphate as the electrolyte and Ag/AgNO₃ as the reference electrode. Each measurement was calibrated with ferrocene (Fc). The potentials were measured vs. Fc+/Fc. b) Conversion factors: ferrocene in DCM vs SCE 0.46 [219], SCE vs SHE: 0.244 [220], SHE vs. vacuum: 4.43 [221]. c) The optical band gaps $E_{\text{g}}^{\text{opt1}}$ were estimated from the edges of electronic absorption spectra in solution. d) E_{LUMO} was calculated from the equation $E_{\text{LUMO}} = E_{\text{HOMO}} - E_{\text{g}}^{\text{opt1}}$. e) The solid-state ionization potential (I_{p}) was measured by the photoemission in the air method from films. f) The optical band gaps $E_{\text{g}}^{\text{opt2}}$ were estimated from the edges of electronic absorption spectra in the solid state. g) EA was calculated from the equation $EA = I_{\text{p}} - E_{\text{g}}^{\text{opt2}}$. h) Mobility value at zero field strength. i) Mobility value at 6.4×10^5 V cm⁻¹ field strength

3.2.7. Conclusion of Chapter 3.2

After many unsuccessful attempts to acquire conjugated polymers in acceptable quantities, it was decided to synthesize monomers **H12-H15** which could form non-conjugated macromolecules on the substrate surface after heating. All obtained compounds demonstrated the ability to crosslink, thermal and electrochemical stability, appropriate energy levels and the capability to pack in the solid state. Due to the relatively high polymerization temperatures, materials **H12-H14** could only be employed in the inverted p-i-n PSC architecture, while the formation of droplets instead of a layer after heating **H15** makes them unsuitable for application in optoelectronic devices.

3.3. Small-molecule diazacenes as hole transporting materials

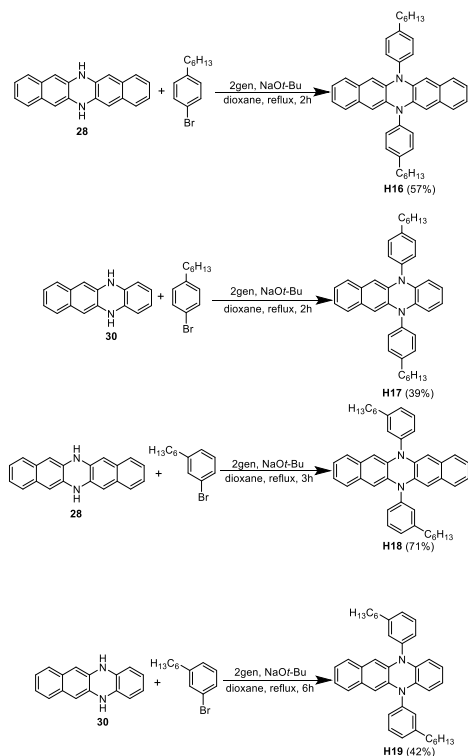
As mentioned in the previous chapter, small-molecule organic HTMs have many advantages over polymers. By carefully designing the structures of new charge carriers, it is possible to achieve enhanced properties due to the increased molecular interaction in the solid state [191, 222, 223]. The most commonly used strategy for high hole mobility HTMs is to increase the planarity of the molecules by the introduction of fused rings, such as truxene [224], pyrene [225], fused tetrathienoanthracene [226] and other polycyclic aromatic hydrocarbons [227] so that to increase the π - π stacking of HTM molecules. However, the planar structures of fused rings make it difficult to form good thin films owing to their solubility and crystallinity problems [5].

Dihydroazaacenes (DHDA) constitute an interesting group of materials that have not yet been tested in PSCs. They are structurally very similar to highly planar acenes [228, 229], however, secondary amines in the backbone of DHDA allow them to be more easily modified, therefore opening many possibilities for

future synthesis. A common strategy to control molecular packing derives from the use of functional side groups. For example, alkylation is often found to lead to slip-stacking [230, 231]. Moreover, studies have reported packing abilities of DHDA [217, 229], in some cases even surpassing similar acene HTMs [232]. This chapter is dedicated to easily synthesizable dihydroazaacene derivatives with different substituents for better solubility and charge transport properties.

3.3.1. Synthesis of dihydrodiazatetracene and dihydrodiazapentacene derivatives

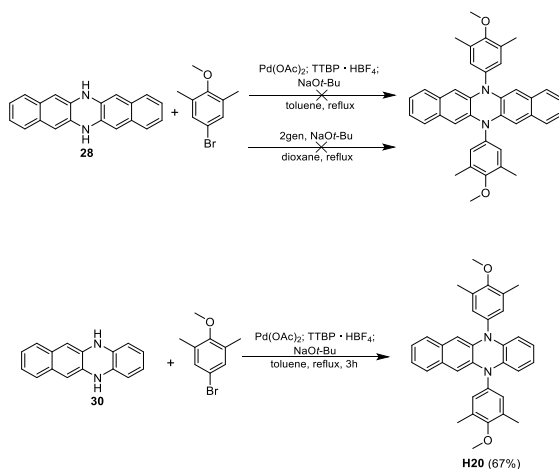
DHDAP and DHDAT derivatives 6,13-bis(4-hexylphenyl)-6,13-dihydrodibenzo[*b,i*]phenazine (**H16**), 5,12-bis(4-hexylphenyl)-5,12-dihydrobenzo[*b*]phenazine (**H17**), 6,13-bis(3-hexylphenyl)-6,13-dihydrodibenzo[*b,i*]phenazine (**H18**) and 5,12-bis(3-hexylphenyl)-5,12-dihydrobenzo[*b*]phenazine (**H19**) were synthesized from the corresponding brominated hexylbenzenes (1-bromo-4-hexylbenzene, 1-bromo-3-hexylbenzene) and **28**, **30** respectively via the Buchwald-Hartwig coupling reaction under argon in anhydrous dioxane in the presence of sodium *tert*-butoxide (Scheme 3.13).



Scheme 3.13. Synthesis of diazacenes **H16-H19**

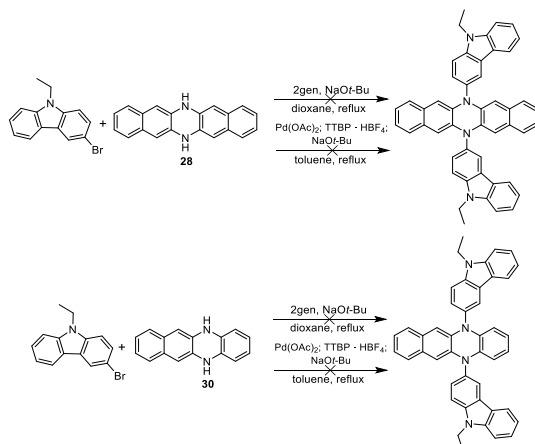
Palladium catalyzed cross-coupling reaction of diazatetracene **30** with 4-bromo-2,6-dimethylanisole under argon in anhydrous dioxane yielded DHDAT derivative **H20** (Scheme 3.14). Applying the same conditions to the coupling

between **28** and 4-bromo-2,6-dimethylanisole yielded no product. A decision was made to change the palladium catalyst and solvent from toluene to dioxane however, this had no effect on the outcome of the reaction (Scheme 3.14).



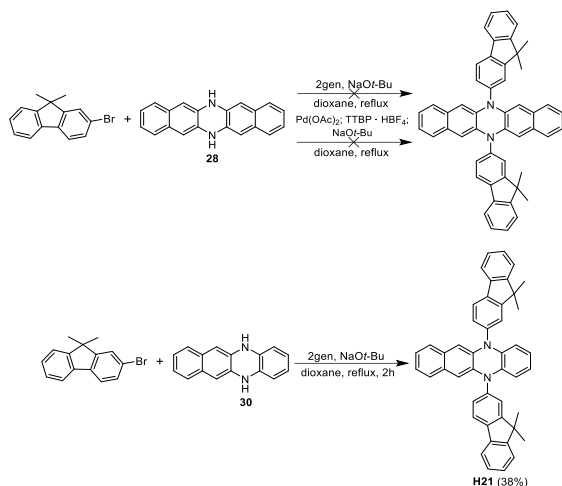
Scheme 3.14. Synthesis of diazatetracene **H20**

The Buchwald-Hartwig cross-coupling between DHDAP **28** and 3-bromo-9-ethylcarbazole under argon in anhydrous dioxane or toluene yielded no desired product (Scheme 3.15). The reaction of diazatetracene **30** with 3-bromo-9-ethylcarbazole under the same conditions did not result in the desired derivative, either (Scheme 3.15). The latter outcome might be due to the rapid degradation of **30** at elevated temperatures, while no reaction occurred between DHDAP **28** and the aforementioned carbazole derivative.



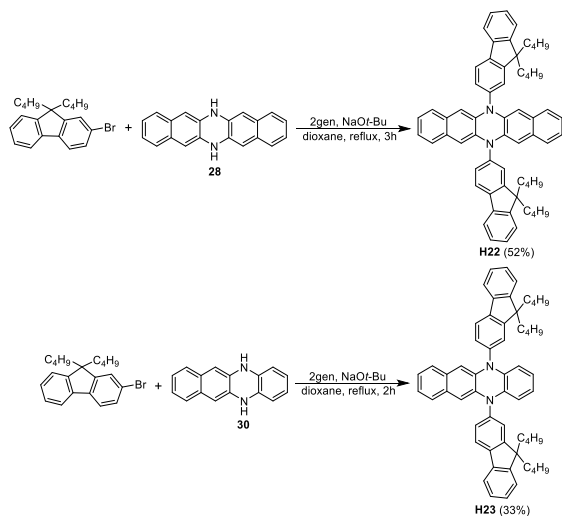
Scheme 3.15. Unsuccessful cross-coupling reaction between DHDAP or DHDAT and carbazole moiety

The previously described unsuccessful synthesis of DHDAP and DHDAT derivatives with carbazole fragments led us to the substitution of carbazole with the less donoric fluorene. Palladium catalyzed cross-coupling reaction of diazapentacene **28** with 2-bromo-9,9-dimethylfluorene in anhydrous dioxane or toluene (Scheme 3.16) resulted in a precipitate that formed after the reaction and proved to be too poorly soluble to separate and characterize a single product from it.



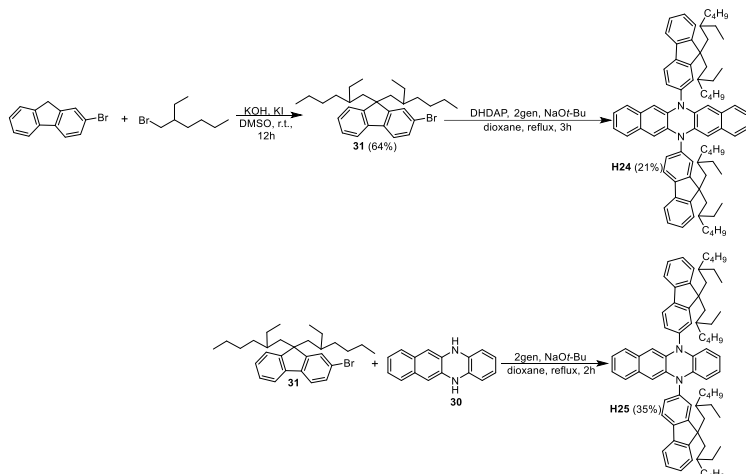
Scheme 3.16. Synthesis of fluorene-containing diazacene **H21**

Diazatetracene **30**, however, reacted with 2-bromo-9,9-dimethylfluorene in the Buchwald-Hartwig cross-coupling reaction yielding a more soluble compound **H21** as the desired product (Scheme 3.16).



Scheme 3.17. Synthesis of fluorene-containing diazacenes **H22** and **H23**

To improve the solubility of fluorene containing DHDAP and DHDAT derivatives, longer alkyl chains were used, and, consequently, 6,13-bis(9,9-dibutyl-9*H*-fluoren-2-yl)-6,13-dihydrodibenzo[*b,i*]phenazine (**H22**) and 5,12-bis(9,9-dibutyl-9*H*-fluoren-2-yl)-5,12-dihydrobenzo[*b*]phenazine (**H23**) were isolated (Scheme 3.17).



Scheme 3.18. Synthesis of fluorene-containing diazocenes **H24** and **H25**

To further increase the solubility of DHDAP and DHDAT derivatives, 2-bromo-9,9-di(2-ethylhexyl)-9*H*-fluorene (**31**) was prepared by alkylation of 2-bromo-9,9-dibutylfluorene with 2-ethylhexyl bromide in the presence of potassium hydroxide. The obtained compound was then used in a reaction with diazocenes **28** and **30** yielding diazapentacene **H24** and a tetracene analogue **H25**, respectively (Scheme 3.18).

3.3.2. Thermal properties

One of the basic requirements for optoelectronic device fabrication is the thermal stability and the ability to form good quality amorphous, or, in rare cases, crystalline films [233]. For this purpose, organic semiconductors must exhibit sufficiently high T_g or T_m values.

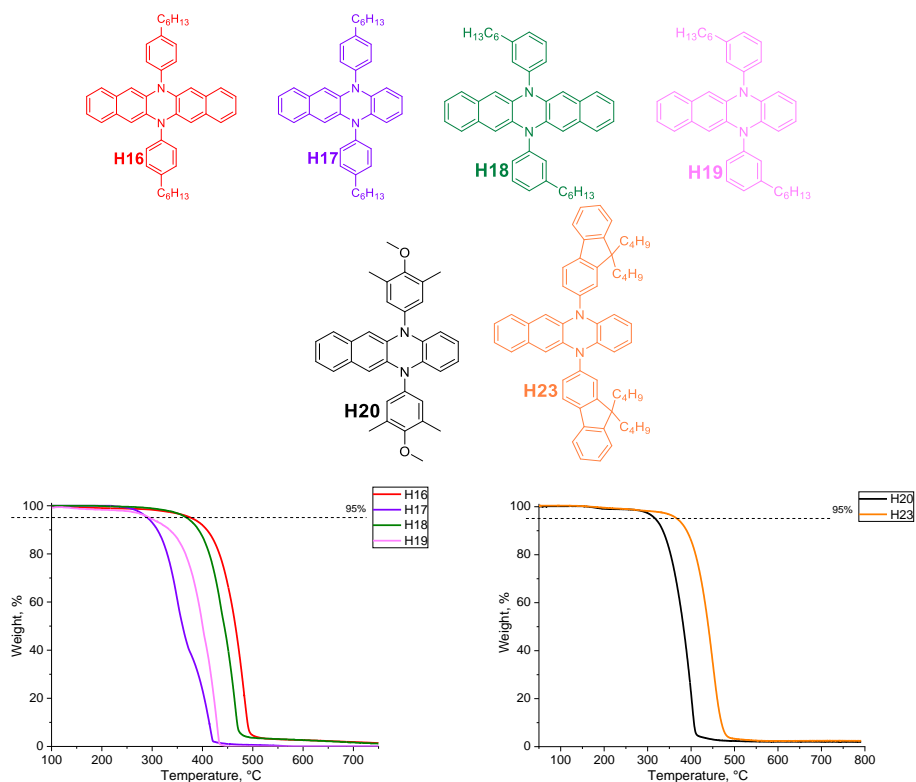


Figure 3.15. TGA curves of selected diazacenes **H16-H20** and **H23**

The thermal stability of diazacenes **H16-H25** was measured by using TGA, and the results can be seen in Table 3.9 and Figure 3.15. All tested HTMs showed 5% weight loss at temperatures higher than 290 °C, thereby proving that they are sufficiently thermally stable for the application in PSCs. Furthermore, the rapid weight loss (Figure 3.15) indicates that materials **H16-H20** and **H23** undergo rapid evaporation and have a potential to be used in vacuum deposited devices.

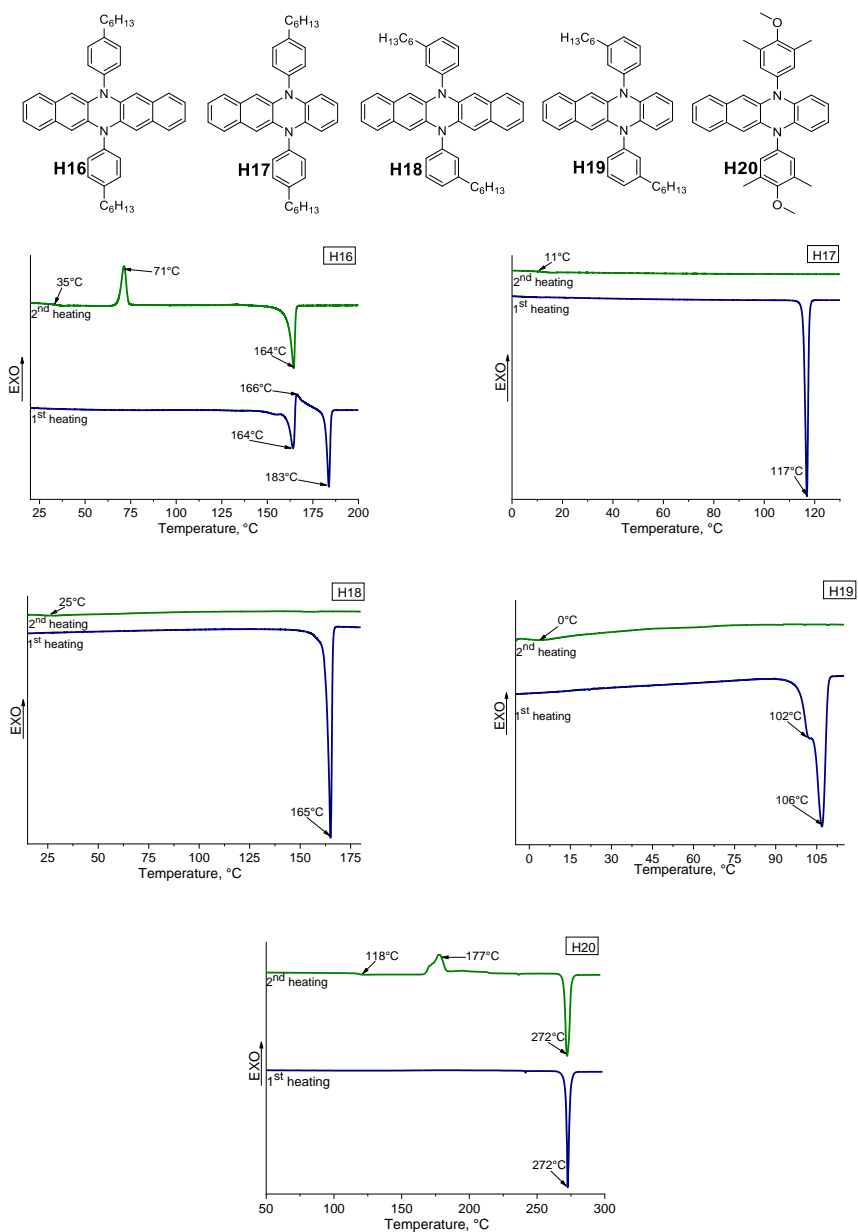


Figure 3.16. DSC curves of compounds **H16-H20**

The changes in the morphology of compounds **H16-H19** can be observed in Figure 3.16. DHDAP derivative **H16** displays polymorphism and has two T_m at 164 °C and 183 °C; however, the latter melting peak is not seen during the 2nd heating, which suggests that, during crystallization, the crystal structure with T_m of 164 °C is predominantly formed. Furthermore, during the 2nd heating, T_g can be seen at 35 °C, thereby showing that the material can be amorphous

as well as crystalline. Changing the position of the alkyl chain from *para* to *meta* has little effect on the T_m of **H18**, however, T_g is lower by 10 °C due to the increased structural disorder introduced into the system via *meta* substituents. Furthermore, after the second heating, **H18** remains amorphous, while its structural isomer **H16** recrystallizes at 71 °C thus demonstrating that substituents at the *para* position lead to a more orderly structure.

DHDAT derivatives **H17**, **H19** demonstrate overall lower T_m and T_g temperatures than **H16** and **H18**, and this could be attributed to a less symmetrical structure and a smaller size of the above mentioned compounds. Interestingly polymorphism can be seen at 102 °C and 106 °C for **H19**, while **H17** has a clearly defined single melting peak at 117 °C. Furthermore, a drop of 11 °C in T_g as well as T_m for **H19** compared to **H17** could be due to slightly more steric hindrances caused by the shift of the hexyl substituent to the *meta* position. A separate case is **H20**, where the phenyl rings attached to the DHDAT core have shorter methoxy and methyl substituents, which significantly affects T_g and T_m , with the former being 100 °C higher, while the latter increased by 150 °C compared to the previously described DHDAT derivatives (Table 3.9, Figure 3.16).

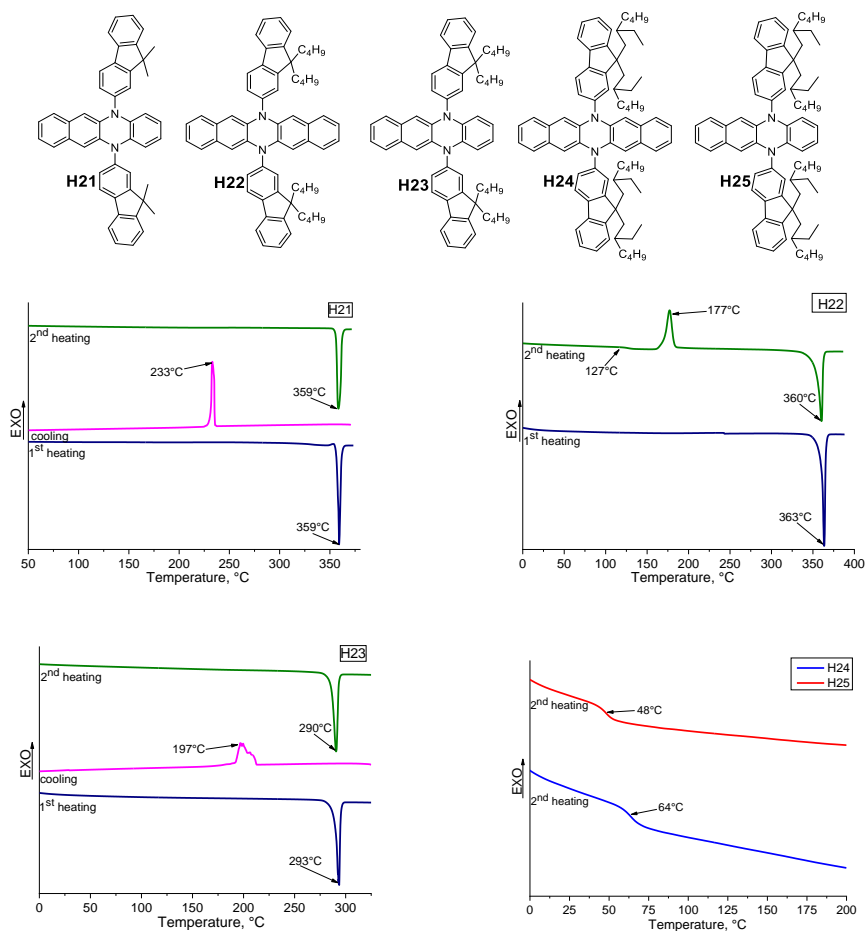


Figure 3.17. DSC curves of compounds **H21-H25**

The DSC results of diazacenes **H21-H25** containing fluorene fragments can be seen in Figure 3.17 and Table 3.9. Diazatetracene **H21** is purely crystalline with a very high T_m of around 360 °C. The change from methyl to butyl substituted fluorene moieties in DHDAT derivative **H23** leads to the lowering of T_m by more than 60 °C. When comparing a pentacene analogue **H22** to diazatetracene **H23**, it becomes clear that the additional structural bulk in the form of the extra phenyl ring in the central core of **H22** increases T_m and allows for the formation of the amorphous state, although both materials still retain a strong tendency to crystallize. A further increase in the length of the alkyl chains attached to the fluorene fragments lead to the fully amorphous derivatives **H24** and **H25**, similarly as in the case of previous examples, the additional phenyl ring leads to a higher glass transition temperature.

Table 3.9. Thermal properties of compounds **H16-H25**

| Compound | T_g^a , °C | T_m^b , °C | T_{cr}^c , °C | T_{dec}^d , °C |
|------------|--------------|--------------|-----------------|------------------|
| H16 | 35 | 164, 183 | 71, 166 | 377 |
| H17 | 11 | 117 | - | 291 |
| H18 | 25 | 165 | - | 367 |
| H19 | 0 | 106 | - | 295 |
| H20 | 118 | 272 | 177 | 318 |
| H21 | - | 359 | 233 | 367 |
| H22 | 127 | 363 | 177 | 400 |
| H23 | - | 293 | 197 | 368 |
| H24 | 64 | - | - | 369 |
| H25 | 48 | - | - | 366 |

a) Determined by DSC: scan rate = 10 °C min⁻¹, N₂ atmosphere; second run; b) Determined by DSC: scan rate = 10 °C min⁻¹, N₂ atmosphere; first run; c) Determined by DSC: scan rate = 10 °C min⁻¹, N₂ atmosphere; d) Onset of decomposition determined by TGA: heating rate = 10 °C min⁻¹, N₂ atmosphere

To sum up, the increase in the length of alkyl chains leads to the increased tendency to form the amorphous state, lowering of T_m , and, in some cases, even the absence of a crystalline structure, which coincides with observations found in literature [234]. Furthermore, derivatives with a larger and more symmetrical DHDAP core demonstrate increased T_m and T_g compared to the compounds containing the DHDAT central fragment.

3.3.3. Optical properties

To evaluate the change in the size of the conjugation system and the ability to pack in the solid state, UV-Vis absorption spectra were measured in toluene or THF solutions and on the glass substrate (Figure 3.18). All the compounds exhibit n- π^* electron transitions at around 420 nm, while the π - π^* absorption maxima are at 291 nm for DHDAT derivatives **H17**, **H19** and at 301 nm for diazapentacenes **H16**, **H18** (Figure 3.18a). The 10 nm bathochromic shift of DHDAP derivatives compared to diazatetracenes **H17**, **H19** can be attributed to the larger conjugated system resulting from an additional phenyl ring in pentacene analogues **H16** and **H18**. The change of the position of the hexyl chain from *para* to *meta* in **H18** and **H19** has little effect on the size of the conjugated system compared with **H16** and **H17**.

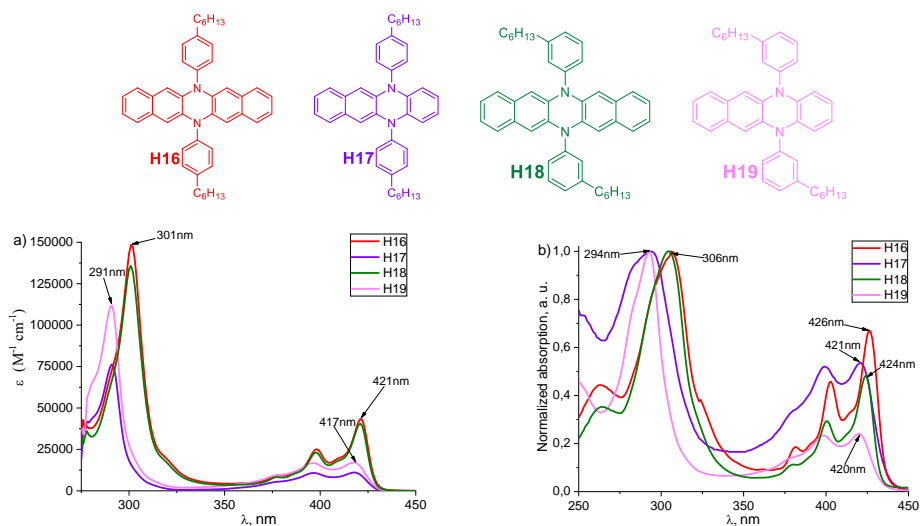


Figure 3.18 a) UV-vis absorption spectra of **H16**, **H17**, **H18**, **H19** in toluene and b) thin films on glass

In the solid state, all maxima redshift by roughly 5 nm and 3 nm for DHDAP and DHDAT derivatives, respectively (Figure 3.18b).

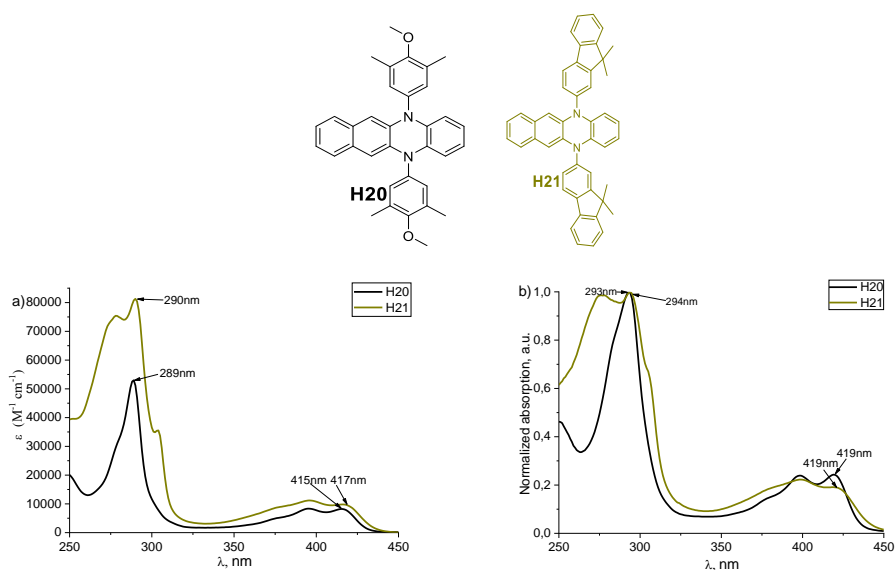


Figure 3.19. a) UV-Vis absorption spectra of **H20**, **H21** in THF and b) thin films on glass

The $n-\pi^*$ electron transition of DHDAT derivatives **H20** and **H21** can be seen at around 415 nm in THF, while the $\pi-\pi^*$ absorption peaks roughly at 290 nm. However, the shape and intensity of the spectra vary due to different substituents.

Diazacene **H21**, containing fluorene moieties, has wider absorption with a new shoulder from fluorene moieties at around 280 nm; a hyperchromic shift is also observed when comparing it with **H20** (Figure 3.19a). The bathochromic shift of 4 nm at roughly 290 nm is seen for each DHDAT derivative in the solid state compared to the absorption in a solution, while the position of the $n-\pi^*$ electron transition absorption peak is shifted by 4 nm for **H20** and 2 nm for **H21** (Figure 3.19b).

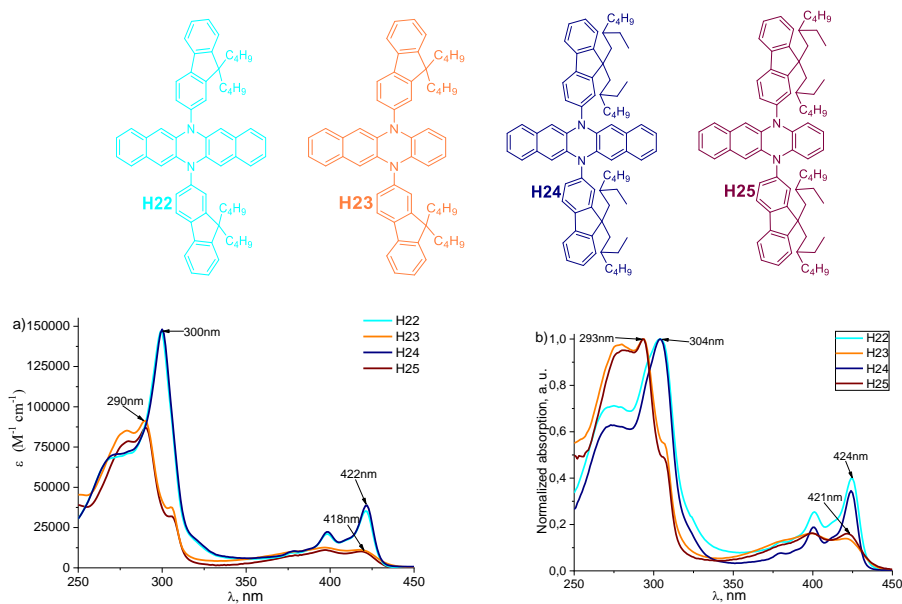


Figure 3.20 a) UV-Vis absorption spectra of **H22**, **H23**, **H24**, **H25** in THF and b) thin films on glass

The absorption spectra of compounds **H22-H25** in THF and on the glass substrate can be seen in Figure 3.14. The $\pi-\pi^*$ electron transition maxima for DHDAP derivatives in a solution are at 300 nm, while **H23** and **H24** possessing a smaller conjugated system peak at 290 nm, the $n-\pi^*$ transition maxima for all diazacenes are around 420 nm (Figure 3.20a). Despite the change of the length of alkyl chains in fluorene substituents, the spectra are nearly identical between the pairs of molecules with the same central core. Only minor bathochromic shifts are observed between the same core compounds when comparing spectra in the solid state and in THF.

3.3.4. Photoelectrical properties

To evaluate the electrochemical stability of compounds **H16-H25**, CV measurements were conducted, and voltammograms of some of the tested materials are presented in Figure 3.21. All HTMs demonstrated reversible oxidation thereby proving that they are electrochemically stable. Furthermore, the data acquired from

CV measurements can be used to calculate HOMO and LUMO energies in the solution; the results are shown in Table 3.10. Diazacenes feature E_{HOMO} between -5.04 eV and -5.20 eV, while E_{LUMO} is in the range of -2.18 eV and -2.35 eV. The main tendency observed among these compounds is that DHDAP derivatives tend to have slightly higher HOMO and LUMO energies than the respective diazatetracenes.

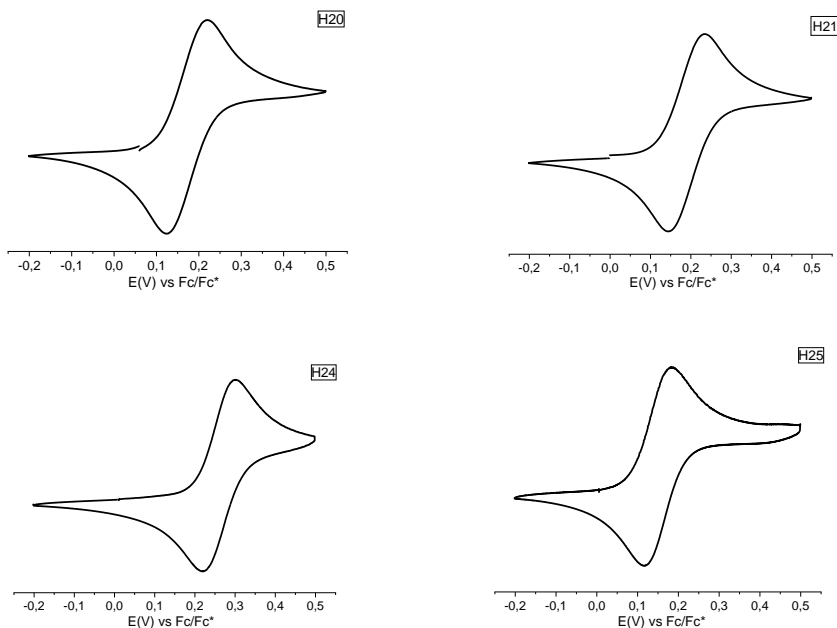


Figure 3.21. CV voltammograms of **H20**, **H21**, **H24** and **H25**

To evaluate energy levels of the tested materials, I_p was measured with the PESA method (Figure 3.22). HTM **H16**, despite having an extra phenyl ring, demonstrated similar I_p values to those of tetracene analogue **H17**. Change of the position of the hexyl groups from *para* to *meta* leads to a slight decrease in I_p of diazatetracene-based HTM **H19**, if compared with **H17**. *Meta* substituted DHDAP derivative **H18**, however, demonstrates a significantly higher ionization energy level than the *para*-substituted analogue **H16**. This could be explained by the different rigidity of the central core: DHDAP is symmetrical and less flexible than DHDAT [217]; therefore, long aliphatic chains in the *meta* position might cause steric hindrances leading to changes in molecule packing and an increase in I_p for **H18**, while the position of the hexyl groups has very little effect for the I_p of DHDAT derivatives (Table 3.10).

The introduction of the methoxy groups and multiple short alkyl chains instead of hexyl fragments in **H20** leads to the I_p value drop below 5.00 eV. This result is still acceptable for applications in PSCs, however, a further decrease in ionization energy could lead to an increased interfacial recombination [235].

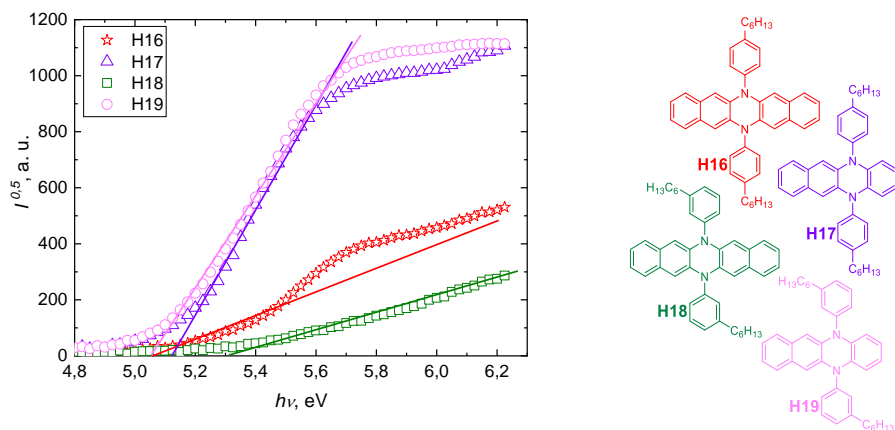


Figure 3.22. I_p measurements of compounds **H16-H19**

The change in the length of alkyl chains has very little effect on the ionization energies of the tested compounds. DHDAT derivatives containing fluorene moieties **H21**, **H23** and **H25**, despite having methyl, butyl and ethylhexyl side chains, respectively, have similar I_p values (Table 3.10). The same tendencies are observed for diazapentacenes **H22** and **H24**. The most notable difference can be seen when comparing DHDAP derivatives containing fluorene substituents with alkyl chains of different lengths **H22**, **H24** with DHDAT analogues **H23** and **H25**, respectively, with the latter pair having around 0.1 eV lower I_p than the former. Changes in the size of the central core and more steric hindrances occurring in DHDAP derivatives could be the main reasons.

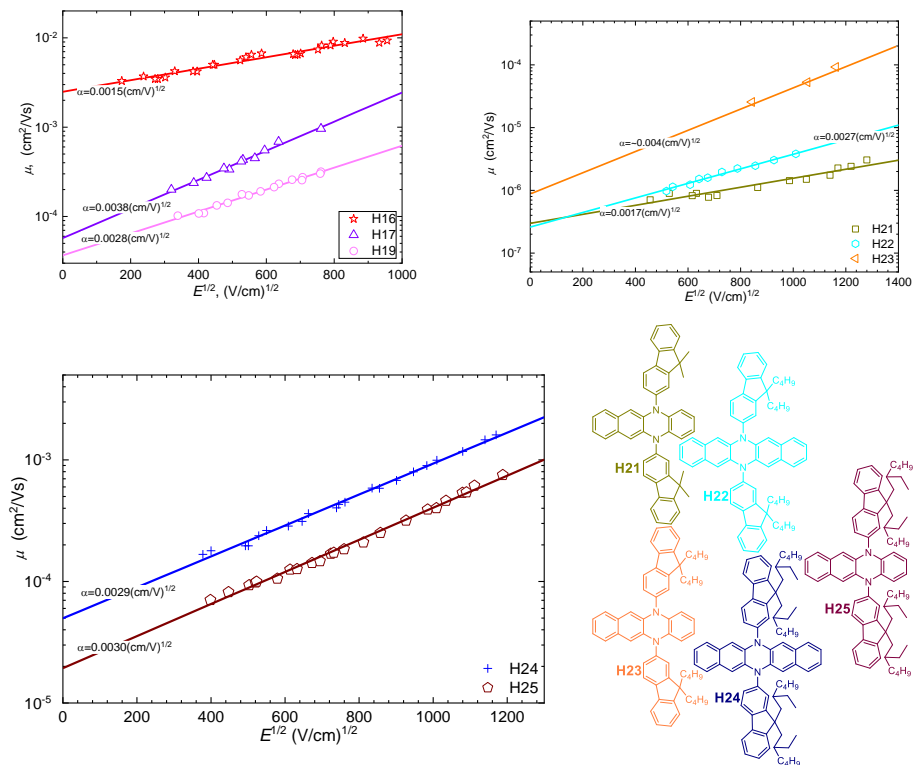


Figure 3.23. Charge carrier mobility of **H16**, **H17**, **H19** and **H21-H25**

The charge transport properties of the tested HTMs were measured from films by employing the xerographic time-of-flight (XTOF) method. Charge carrier mobility graphs of the tested materials can be observed in Figure 3.23. The values of the charge mobility defining parameters: zero field mobility (μ_0) and the mobility at the electric field of $6.4 \times 10^5 \text{ V cm}^{-1}$ for compounds **H16-H25** can be seen in Table 3.10. Two of the tested materials **H18** and **H20** could not be measured, the former due to the high crystallinity, while the latter formed poor quality thin films. DHDAP derivative **H16** demonstrated high charge carrier mobility reaching $2.5 \cdot 10^{-3} \text{ cm}^2 \text{ V}^{-1} \text{ s}^{-1}$ at zero field strength and $1.1 \cdot 10^{-2} \text{ cm}^2 \text{ V}^{-1} \text{ s}^{-1}$ at a stronger field.

Table 3.10. Energy level and hole mobility data for **H16-H25**^a

| Compound | E_{HOMO} , eV ^b | $E_{\text{g}}^{\text{opt1}}$, eV ^c | E_{LUMO} , eV ^d | I_{p} , eV ^e | $E_{\text{g}}^{\text{opt2}}$, eV ^f | EA , eV ^g | μ_0 , $\text{cm}^2 \text{V}^{-1} \text{s}^{-1}$ h | μ_{h} , $\text{cm}^2 \text{V}^{-1} \text{s}^{-1}$ i |
|------------|--|---|--|-------------------------------------|---|---------------------------|--|---|
| H16 | -5.13 | 2.87 | -2.26 | 5.07 | 2.83 | 2.24 | $2.5 \cdot 10^{-3}$ | $1.1 \cdot 10^{-2}$ |
| H17 | -5.06 | 2.86 | -2.20 | 5.12 | 2.82 | 2.30 | $5.8 \cdot 10^{-5}$ | $1.15 \cdot 10^{-3}$ |
| H18 | -5.16 | 2.87 | -2.29 | 5.31 | 2.84 | 2.47 | - | - |
| H19 | -5.04 | 2.86 | -2.18 | 5.06 | 2.84 | 2.22 | $3.7 \cdot 10^{-5}$ | $3.5 \cdot 10^{-4}$ |
| H20 | -5.11 | 2.86 | -2.25 | 4.98 | 2.83 | 2.15 | - | - |
| H21 | -5.13 | 2.80 | -2.33 | 5.18 | 2.78 | 2.40 | $3 \cdot 10^{-7*}$ | $1.6 \cdot 10^{-6*}$ |
| H22 | -5.15 | 2.83 | -2.32 | 5.28 | 2.83 | 2.45 | $2.7 \cdot 10^{-7*}$ | $3.8 \cdot 10^{-6*}$ |
| H23 | -5.10 | 2.79 | -2.31 | 5.19 | 2.79 | 2.40 | $9 \cdot 10^{-7}$ | $5 \cdot 10^{-5}$ |
| H24 | -5.20 | 2.85 | -2.35 | 5.31 | 2.84 | 2.47 | $5 \cdot 10^{-5}$ | $9.3 \cdot 10^{-4}$ |
| H25 | -5.09 | 2.82 | -2.27 | 5.23 | 2.78 | 2.45 | $2 \cdot 10^{-5}$ | $4 \cdot 10^{-4}$ |

a) The CV measurements were carried out at a glassy carbon electrode in dichloromethane solutions containing 0.1 M tetrabutylammonium hexafluorophosphate as electrolyte and Ag/AgNO₃ as the reference electrode. Each measurement was calibrated with ferrocene (Fc). Potentials measured vs. Fc+/Fc. b) Conversion factors: ferrocene in DCM vs. SCE 0.46 [219], SCE vs SHE: 0.244 [220], SHE vs. vacuum: 4.43 [221]. c) The optical band gaps $E_{\text{g}}^{\text{opt1}}$ estimated from the edges of electronic absorption spectra in solution. d) E_{LUMO} calculated from the equation $E_{\text{LUMO}} = E_{\text{HOMO}} - E_{\text{g}}^{\text{opt1}}$. e) Solid-state ionization potential (I_{p}) was measured by the photoemission in the air method from films. f) The optical band gaps $E_{\text{g}}^{\text{opt2}}$ estimated from the edges of electronic absorption spectra in the solid state. g) EA calculated from the equation $EA = I_{\text{p}} - E_{\text{g}}^{\text{opt2}}$ h) Mobility value at zero field strength. i) Mobility value at $6.4 \times 10^5 \text{ V cm}^{-1}$ field strength. * drift carrier mobility measured with PC-Z

Structural isomers **H17** and **H19** have similar hole mobility at the zero field strength, however, at the electric field of $6.4 \times 10^5 \text{ V cm}^{-1}$, the charge transport of **H17** is more than 3 times faster than **H19**. This might be due to the less tight packing of the molecules caused by hexyl substituents at the *meta* position for **H19**, and, as a consequence, larger distances between the charge hopping sites. The poor layer formation can sometimes be improved by mixing the investigated compound with bisphenol Z polycarbonate (PC-Z) (weight ratio 1:1); such was the case for materials **H21** and **H22** which could not have been measured otherwise. Diazacene **H21** reached a charge carrier mobility of $3 \cdot 10^{-7} \text{ cm}^2 \text{V}^{-1} \text{s}^{-1}$, while DHDAP derivative **H22** demonstrated similar results of $2.7 \cdot 10^{-7} \text{ cm}^2 \text{V}^{-1} \text{s}^{-1}$ at zero field strength; however, at an electric field of $6.4 \times 10^5 \text{ V cm}^{-1}$, pentacene analogue **H22** demonstrated a charge transport which was more than two times greater than that of diazatetracene **H21**. It is worth noting that the results acquired this way are generally one order of magnitude lower than those of the pristine material without PC-Z.

Despite containing shorter aliphatic chains and thus less steric hindrance, DHDAT derivative **H23** demonstrated roughly one order of magnitude lower charge transport than **H25**. This might be explained by the crystallinity of **H23** since crystallization in thin films could cause a decrease in hole mobility, while longer 2-ethylhexyl aliphatic chains in **H24** and **H25** result in the formation of

better quality thin films due to the amorphous nature of said compounds (Figure 3.17).

3.3.5. Conclusion of Chapter 3.3

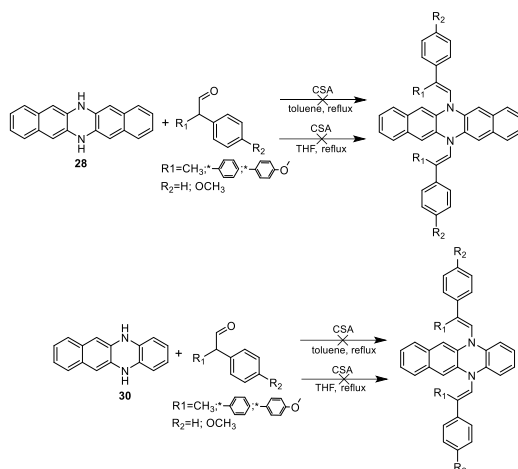
In this chapter, DHDAP and DHDAT derivatives were synthesized, and their thermal as well as photophysical properties were investigated. All the materials proved to exhibit good thermal and electrochemical stability. Furthermore, high crystallinity is a common property among the tested HTMs with the exception of **H24** and **H25**, containing 2-ethylhexyl aliphatic chains, which are fully amorphous. All the materials demonstrated energy levels that are appropriate for the applications in PSCs, while HTMs **H16**, **H17**, **H19**, **H24** and **H25** also displayed relatively high charge transport. Most of the times when selecting suitable HTM candidates for PSCs, one good property is not enough as we must look at the whole picture. Having that in mind, the most promising materials described in this chapter are **H16**, **H17** and **H19**. These HTMs are denoted by great characteristics, such as packing in the solid state, the appropriate energy level and high drift carrier mobility, but they would have to be used in a device in the crystalline state due to their low T_g and a high tendency to crystallize. Compounds **H24** and **H25** could not be used in PSCs due to their very low T_g , while the application of other investigated materials in PSCs is questionable due to their poor charge transport properties.

3.4. Investigation of new chromophoric systems containing diphenylethenyl moieties

Over the last decade, by virtue of using costly HTMs spiro-MeOTAD and PTAA, perovskite solar cells reached a power conversion efficiency of over 25% [8]. To make a positive impact towards commercialization of PSCs, it is important to reduce the cost of HTM without a significant loss in efficiency. One way to achieve it is to use simple reactions so that to expand the π -conjugated system of the inexpensive and commercially available semiconducting core. Such compounds have been previously reported to possess high hole drift mobilities [191, 236, 237]. For example, the introduction of phenylethenyl moieties could deliver compounds with such desirable properties [237] as an increased glass transition temperature and thermal stability. This chapter is dedicated to the investigation of systems that could benefit the most from the incorporation of multiple diphenylethenyl moieties.

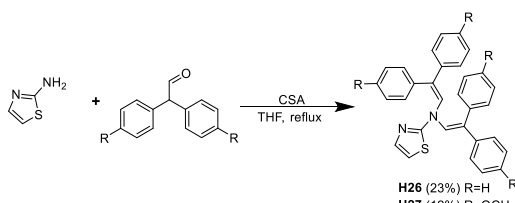
3.4.1. Synthesis of novel compounds with multiple diphenylethenyl fragments in their structure

Multiple attempts with various phenylethenyl derivatives to synthesize enamines from diazacenes **28** and **30** (Scheme 3.19) have been conducted. Unfortunately, none of the reactions yielded the desired product despite different aldehydes being used and reaction conditions applied. This could be due to side reactions occurring between the phenylethenyl derivative and the phenyl ring of either **28** or **30** [236].



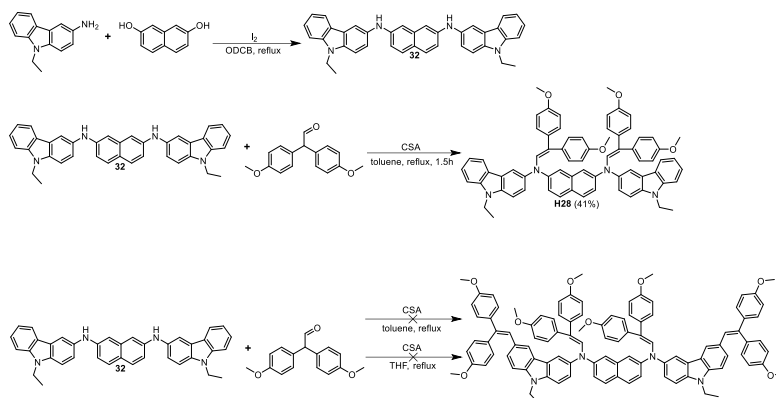
Scheme 3.19. Attempts to synthesize enamines from diazacenes **28**, **30**

After the previous unsuccessful synthesis, it was decided to use thiazole moiety as the central core due to its planarity in hope to induce interaction in the solid state similarly to diazacenes mentioned in Chapter 3.3. *N,N*-bis(2,2-diphenylethenyl)-1,3-thiazol-2-amine (**H26**) was synthesized via CSA catalyzed condensation reaction between 2-aminothiazole and diphenylacetaldehyde in THF. Identical conditions were applied when 2,2-bis(4-methoxyphenyl)acetaldehyde was condensed with the aforementioned amine thus yielding enamine **H27** (Scheme 3.20).



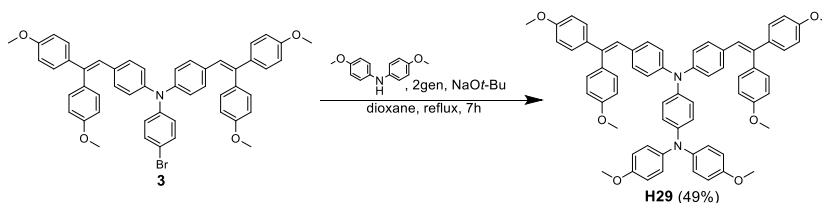
Scheme 3.20. Synthesis of thiazole derivatives **H26** and **H27**

For decades, carbazole has been used as one of the basic building blocks for optoelectronic materials due to its low cost, good chemical stability, simple functionalization, and good photovoltaic properties [140, 236]. Having that in mind, carbazole moieties containing compound **H28** were synthesized. The reaction of 3-amino-9*H*-ethylcarbazole with 2,7-dihydroxynaphthalene gave the central core **32** which, in turn, was condensed with 2,2-bis(4-methoxyphenyl)acetaldehyde thus yielding the aforementioned carbazole derivative **H28**. The attempt to acquire a naphthalene derivative containing four methoxy phenylethenyl moieties was unsuccessful, as a mixture of products, due to the aldehyde reacting to various carbazole positions, was obtained (Scheme 3.21) [236].



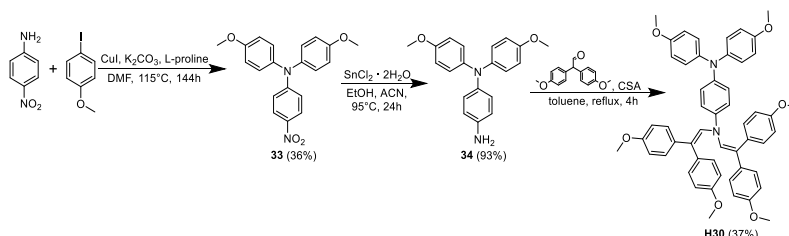
Scheme 3.21. Synthesis of enamine **H28**

Triphenylamine is also considered as one of the basic building blocks in optoelectronics; therefore, TPA derivatives should be included when searching for the optimal chromophoric system. Diphenylethenyl derivatives containing compound **3** were used in the Buchwald-Hartwig amination with 4,4'-dimethoxydiphenylamine to yield TPA analogue **H29** (Scheme 3.22).



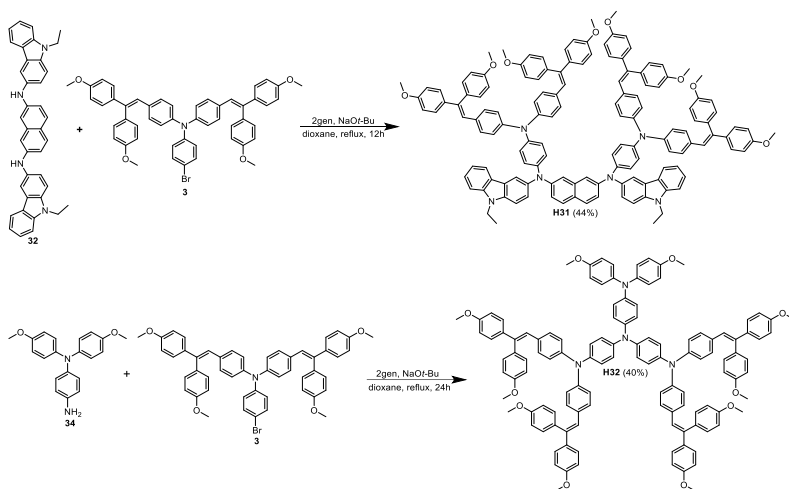
Scheme 3.22. Synthesis of TPA derivative **H29**

p-Nitroaniline and *p*-iodoanisole were coupled by using the Ullmann-type reaction under argon in anhydrous DMF to give 4-nitro-4',4''-dimethoxytriphenylamine (**34**). Afterwards, the reduction of the nitro group was carried out by using stannous chloride dihydrate in a mixture of ethanol and acetonitrile thereby yielding amine **35**. Condensation of **35** with 2,2-bis(4-methoxyphenyl)acetaldehyde in the presence of CSA resulted in enamine **H30** (Scheme 3.23).



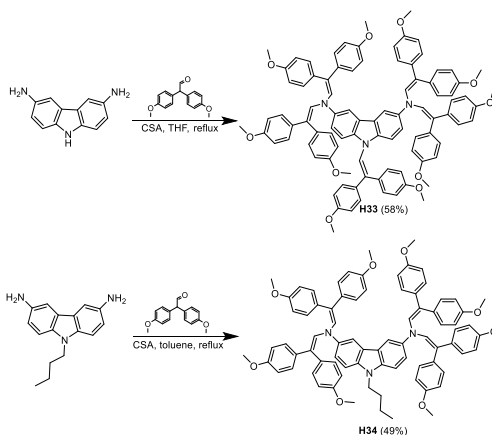
Scheme 3.23. Synthesis of triphenylamine-based enamine **H30**

TPA derivatives **H31** and **H32** were synthesized via the reaction of brominated triphenylamine **3** with the corresponding amine **32** or **35** in a palladium-catalyzed reaction under argon in anhydrous dioxane (Scheme 3.24).



Scheme 3.24. Synthesis of TPA derivatives **H31** and **H32**

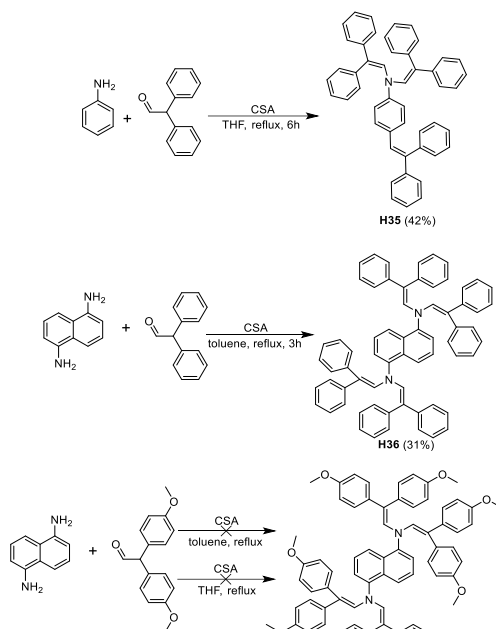
To obtain better understanding of different systems containing carbazole moieties, it was decided to synthesize enamines **H33** and **H34** by an acid-catalyzed condensation reaction between the respective carbazole derivatives and 2,2-bis(4-methoxyphenyl)acetaldehyde (Scheme 3.25).



Scheme 3.25. Synthesis of carbazole derivatives **H33** and **H34**

Recently, it has been demonstrated that inexpensive compounds, such as aniline, can make great starting materials for HTMs [20], and this led to the exploration of simple aromatic amines as suitable building blocks for optoelectronic applications. The reaction between aniline and diphenylacetaldehyde in the presence of CSA in THF gave *N,N*,4-tris(2,2-

diphenylethenyl)aniline (**H35**). Under similar conditions, just except that toluene was used as a solvent, naphthalene-based enamine **H36** was synthesized from 1,5-naphthalenediamine (Scheme 3.26).



Scheme 3.26. Synthesis of **H35** and **H36**

The condensation between 1,5-naphthalenediamine and 2,2-bis(4-methoxyphenyl)acetaldehyde yielded no desired product (Scheme 3.26) as side reactions occurred between the phenylethenyl derivative and naphthalene [236].

3.4.2. Thermal properties

The thermal stability of thiazoles **H26** and **H27** was measured by using TGA. Both materials lose 5% of their mass at relatively low temperatures – 190 °C and 228 °C, respectively (Table 3.11).

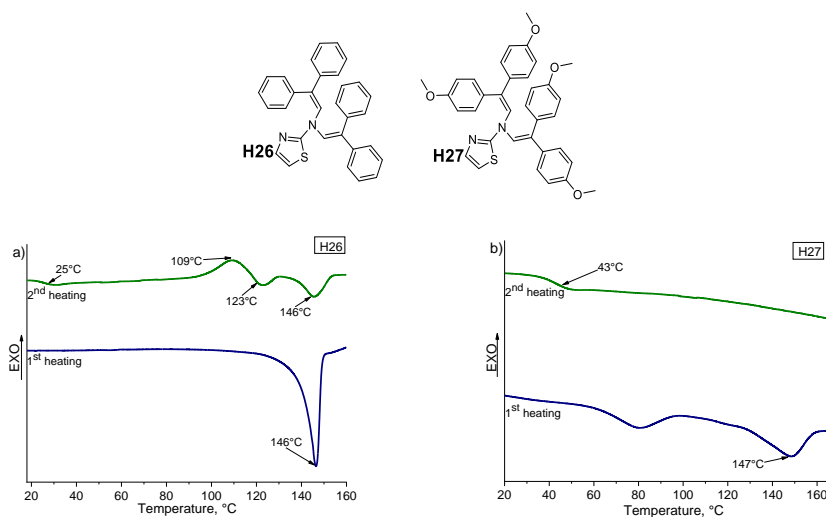


Figure 3.24. DSC curves of compounds **H26** (a) and **H27** (b)

During the 1st heating, thiazole derivative **H26** shows a behavior typical for fully crystalline materials, and only the melting of crystals is observed at 146 °C; however, the 2nd heating reveals that the compound can also be amorphous ($T_g = 25$ °C). Nevertheless, at 109 °C, **H26** recrystallizes and displays polymorphism as seen from T_m peaks at 123 °C and 146 °C (Figure 3.24a). The addition of methoxy groups lowers its T_m by more than 50 °C and increases the T_g value by nearly 20 °C for **H27**. It is also worth noting that no melting peak is observable during the 2nd heating of **H27** (Figure 3.24b), which could mean a less orderly structure compared to **H26** due to the presence of methoxy groups in enamine **H27**.

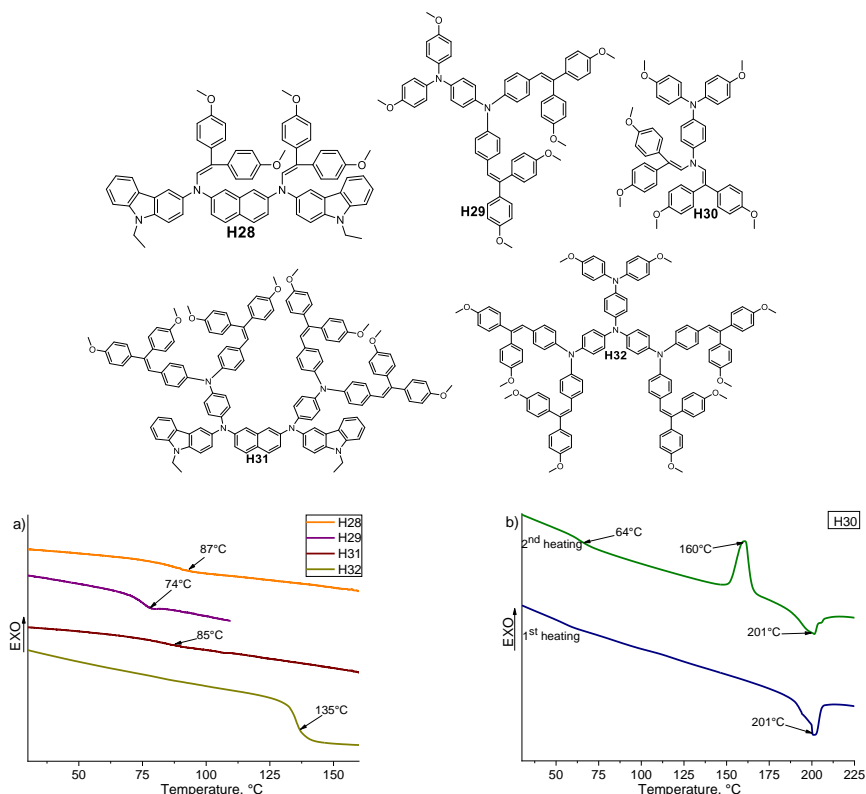


Figure 3.25. a) DSC second heating curves of **H28**, **H29**, **H31** and **H32** b) DSC curves of compound **H30**

The thermal stability of **H28-H32** was measured by using TGA and can be seen in Table 3.11. The temperature at which 5% of mass is lost varies from compound to compound from as low as 226 °C for **H31** to as high as 441 °C for **H32** due to the different central cores of the materials.

The analysis of DSC data shows that TPA derivatives **H29** and **H32** are fully amorphous materials (Figure 3.25a), while TPA-based enamine **H30** exhibits a strong tendency to crystallize with T_m at 201 °C (Figure 3.25b). Although it can exist in the amorphous state, it undergoes crystallization at 160 °C. This could be explained by the size of the molecule, with **H30** being the smallest of the three and being able to form more orderly structures.

Enamine **H28**, containing the naphthalene-carbazole central core, is an amorphous material with a T_g value of 87 °C. Interestingly, the addition of more structural bulk to the aforementioned core in **H31** does not increase the T_g , which thus remains around 87 °C.

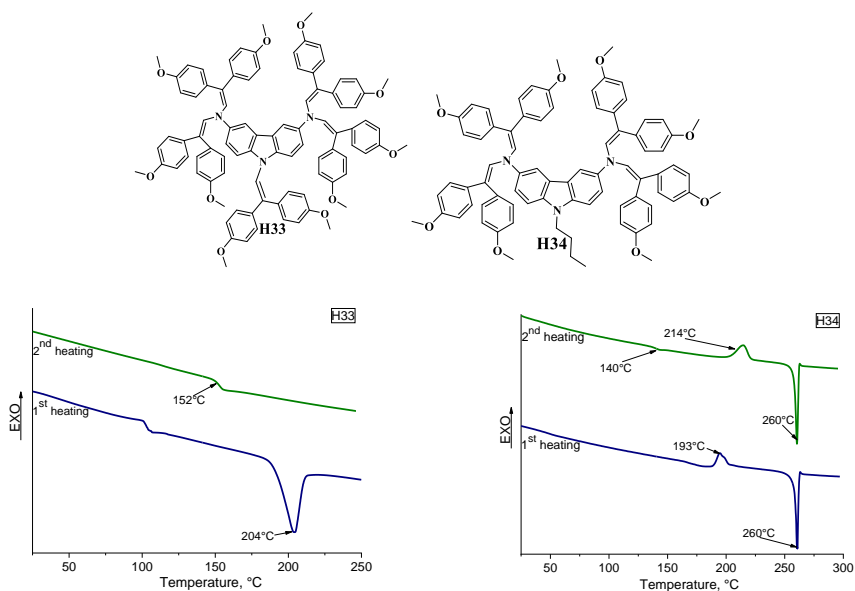


Figure 3.26. DSC curves of compounds **H33**, **H34**

The phase transition curves of carbazole derivatives **H33** and **H34** can be seen in Figure 3.26. The results showed that both **H33** and **H34** have relatively high T_g values, 152 °C and 140 °C, respectively. The difference in T_g becomes clearer when we look at the structure of the HTMs. Both organic semiconductors are carbazole derivatives, however, **H33** has an additional bis(4-methoxyphenyl)ethenyl fragment at the 9-position of the carbazole moiety, while **H34** has an aliphatic butyl chain instead, which reduces the bulkiness of the molecule thus lowering the T_g value. In addition, both new compounds demonstrate excellent thermal stability as they lose 5% of their mass at 395 °C (Table 3.11).

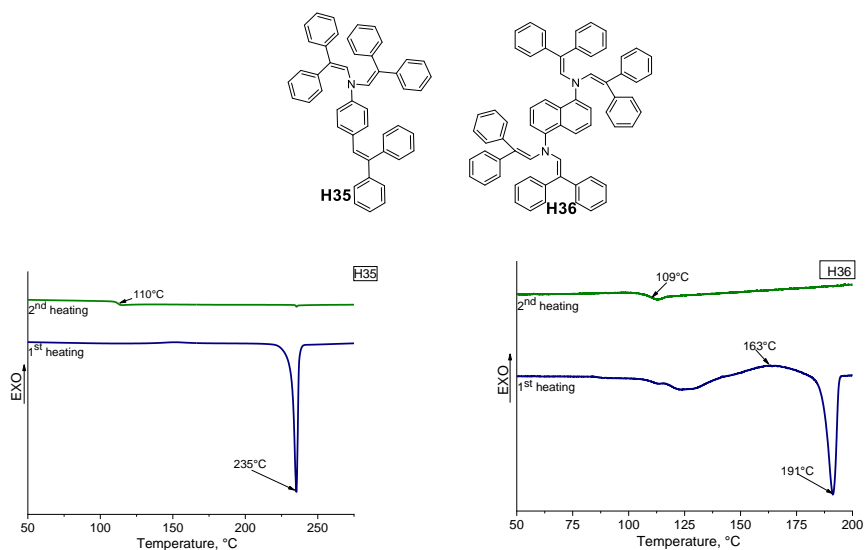


Figure 3.27. DSC curves of enamines **H35** and **H36**

The DSC curves of enamines **H35** and **H36** can be seen in Figure 3.27. Both compounds exhibit relatively high T_m and T_g . Furthermore, during the 2nd heating, **H35** and **H36** do not show melting of crystals, which means that they remain fully amorphous.

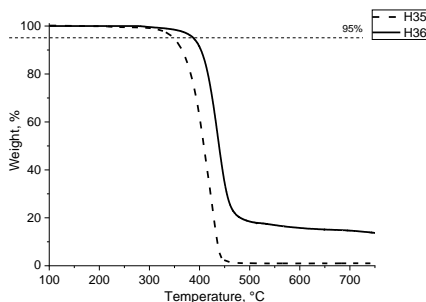


Figure 3.28. TGA curves of **H35** and **H36**

Both materials lose 5% of their mass at temperatures higher than 340 °C thereby demonstrating their great thermal stability (Table 3.11). Both materials display rapid weight loss thus indicating rapid evaporation and show potential for vacuum deposition (Figure 3.28).

Table 3.11. Thermal properties of compounds **H26-H36**

| Compound | T_g^a , °C | T_m^b , °C | T_{cr}^c , °C | T_{dec}^d , °C |
|------------|--------------|--------------|-----------------|------------------|
| H26 | 25 | 146 | 109 | 190 |
| H27 | 43 | 70 147 | - | 228 |
| H28 | 87 | - | - | 232 |
| H29 | 74 | - | - | 414 |
| H30 | 64 | 201 | 160 | 259 |
| H31 | 85 | - | - | 226 |
| H32 | 135 | - | - | 441 |
| H33 | 152 | 204 | - | 395 |
| H34 | 140 | 260 | 193 | 395 |
| H35 | 110 | 235 | - | 348 |
| H36 | 109 | 191 | 163 | 388 |

a) Determined by DSC: scan rate = 10 °C min⁻¹, N₂ atmosphere; second run; b) Determined by DSC: scan rate = 10 °C min⁻¹, N₂ atmosphere; first run; c) Determined by DSC: scan rate = 10 °C min⁻¹, N₂ atmosphere; d) Onset of decomposition determined by TGA: heating rate = 10 °C min⁻¹, N₂ atmosphere

3.4.3. Optical properties

The UV-Vis spectra of thiazoles **H26** and **H27** can be seen in Figure 3.29. The absorption maximum of thiazole derivative **H26** peaks at 329 nm in THF, while a redshift of 8 nm occurs when the measurements are done by using a thin film. The addition of methoxy groups to the molecule causes a bathochromic shift of the spectra of **H27** by more than 50 nm in a solution and on the glass substrate compared to **H26**, however, virtually no change in the position of the maximum is observed when comparing **H27** absorption in THF and in the solid state, which indicates little tendency to form orderly aggregates.

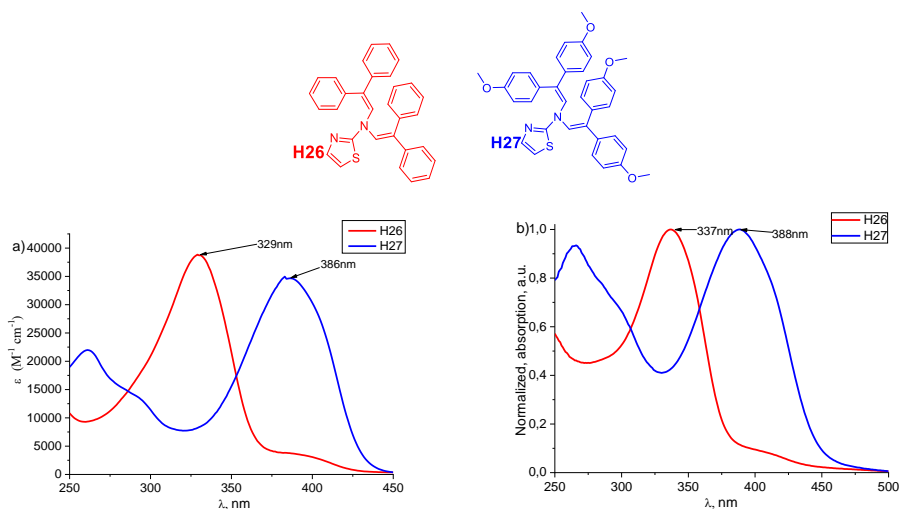


Figure 3.29 a) UV-Vis absorption spectra of **H26**, **H27** in THF and b) thin films on glass

Light absorption properties of compounds **H28**, **H29** and **H30**, containing multiple bis(4-methoxyphenyl)ethenyl fragments, were measured and can be observed in Figure 3.30. The carbazole and naphthalene central core containing enamine **H28** differs significantly from the other two substances, and that is reflected in the absorption spectra. **H28** has a less detailed absorption spectrum peaking at 298 nm in THF, with little change occurring in the solid state.

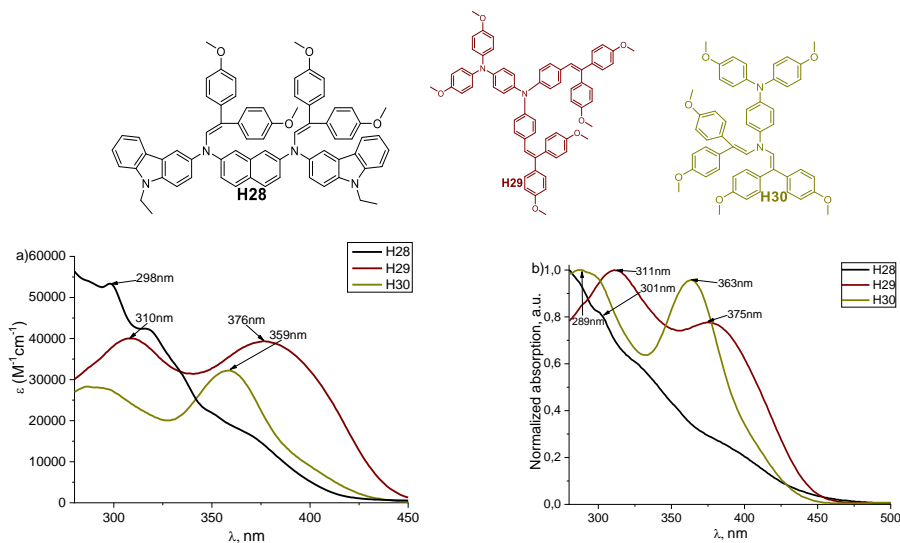


Figure 3.30 a) UV-Vis absorption spectra of **H28**, **H29**, **H30** in THF and b) thin films on glass

TPA derivative **H29** features two similar intensity absorption maxima in a solution at 310 nm and 376 nm. The place of the maxima practically does not change in the solid state for **H29**, however, the electron transition at 311 nm intensifies and becomes the more dominant peak. In comparison to **H29**, **H30** is blueshifted by more than 10 nm due to its smaller conjugated system; however, **H30** follows the same tendency on the glass substrate as **H29**, and the electron transition at a shorter wavelength is intensified (Figure 3.30b). This could be attributed to the different interaction between molecules in the solid state compared to the one in THF.

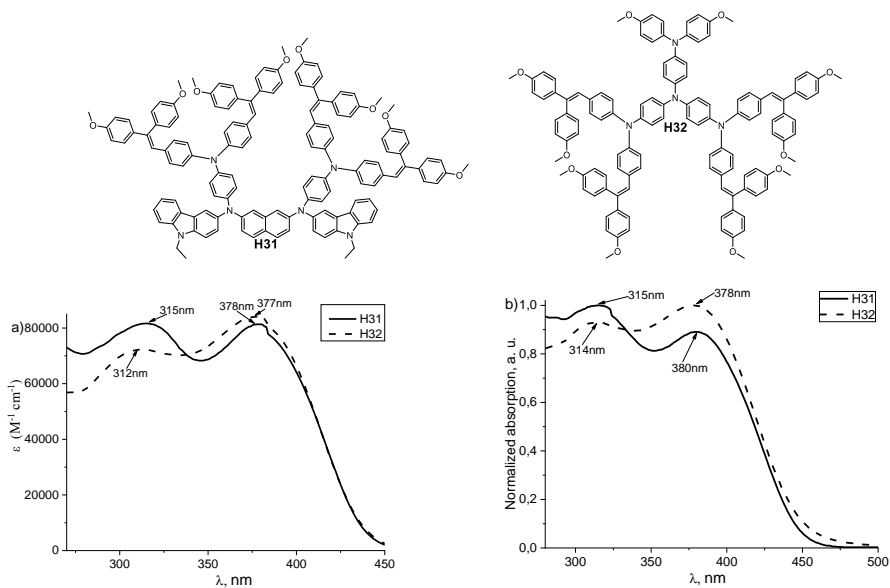


Figure 3.31 a) UV-Vis absorption spectra of **H31** **H32** in THF and b) thin films on glass

Compounds **H31** and **H32** are denoted by similarly shaped UV-Vis absorption spectra (Figure 3.31). They both exhibit two visible electron transition peaks at around 315 nm and 380 nm. No significant change is observed in the solid state. The differences between **H31** and **H32** could be attributed to the different central cores of molecules determining slightly varying absorption intensities.

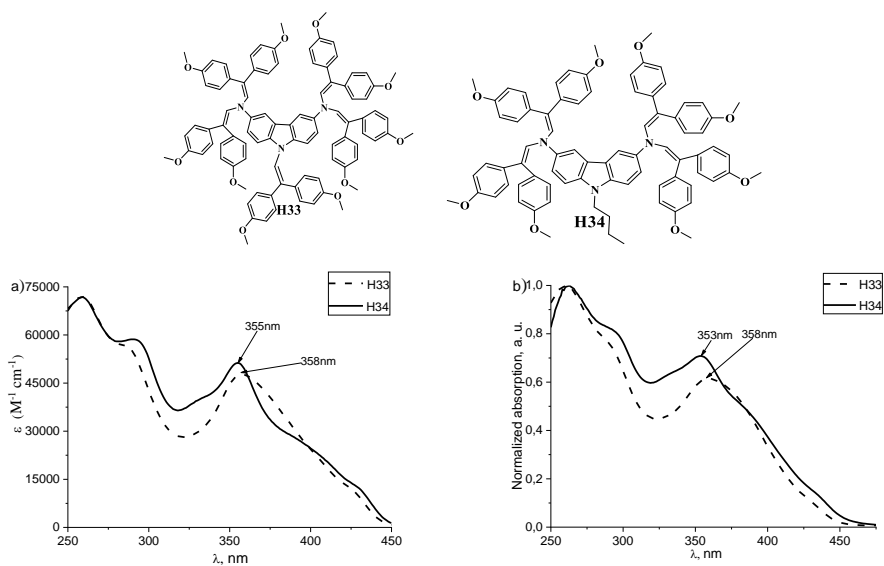


Figure 3.32 a) UV-Vis absorption spectra of carbazole-based enamines **H33**, **H34** in THF and b) thin films on glass

The UV-Vis absorption spectra of carbazole derivatives **H33** and **H34** were recorded in THF solutions and on glass substrates. Apparently, the additional bis(4-methoxyphenyl)ethenyl moiety in enamine **H33** does not increase the size of the π -conjugated system very significantly, and only a small bathochromic shift (~ 3 – 5 nm) is observed compared with **H34**, thus the absorption spectra are very similar for both compounds (Figure 3.32).

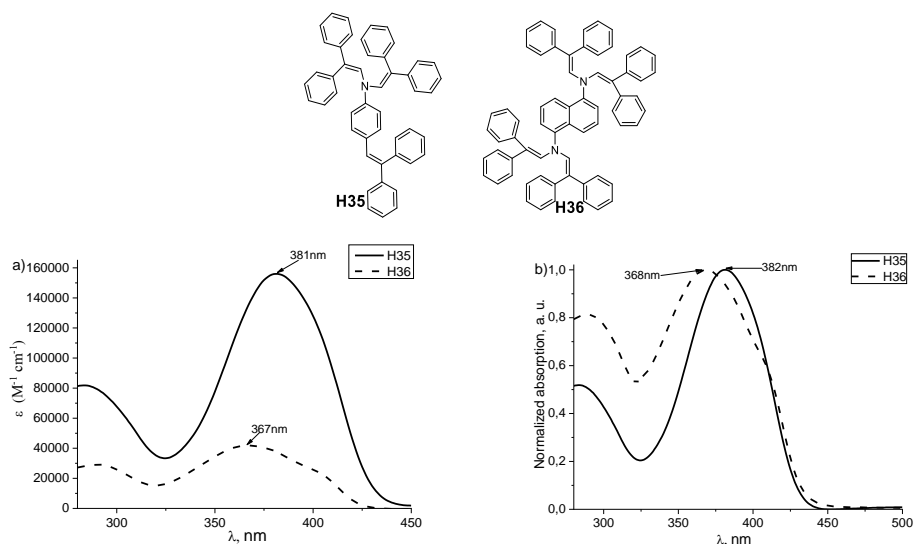


Figure 3.33 a) UV-Vis absorption spectra of **H35**, **H36** in THF and b) thin films on glass

The light absorption of aniline and naphthalene-based enamines **H35** and **H36** can be seen in Figure 3.33. The absorption maximum of **H35** in THF and on the glass substrate peaks at around 381 nm, while, in comparison, **H36** is blueshifted by 14 nm. Furthermore, **H35** absorbs light more intensively than **H36** in THF. This could be explained by the disrupted conjugation of **H36** due to the spatial arrangement of diphenylethenyl moieties leading to the less intensive absorption and a hypsochromic shift.

3.4.4. Photoelectrical properties

The oxidation potentials of compounds **H26-H36** were measured by employing the cyclic voltammetry technique (Table 3.12). Examples of voltammograms are presented in Figure 3.28.

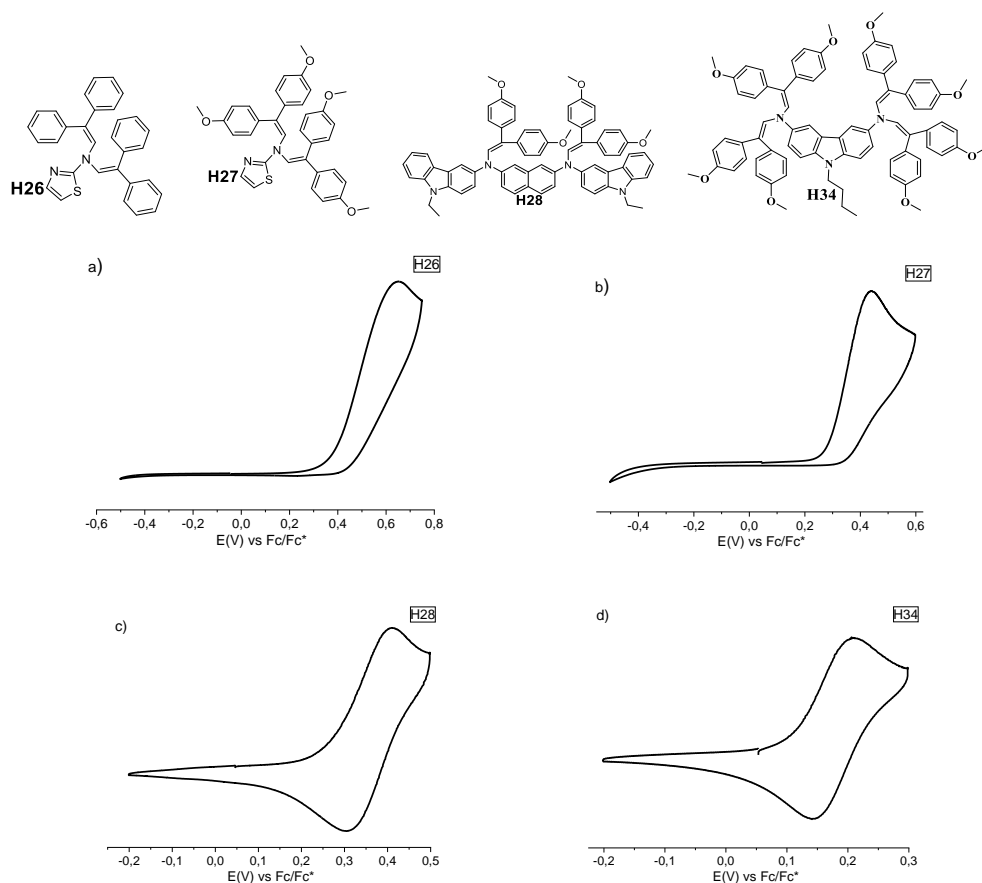


Figure 3.34. CV voltammograms of a) **H26** b) **H27** c) **H28** d) **H34**

With the exception of **H26** and **H27** (Figure 3.34 a and b), all the materials displayed reversible oxidation, thus demonstrating that they are electrochemically stable.

The highest HOMO and LUMO energies calculated from the CV data (Table 3.12) belong to aniline derivative **H35** and naphthalene derivative **H36**, while the TPA moiety containing **H32** and carbazole enamine **H33** have the lowest E_{HOMO} and E_{LUMO} . Even though the structure of the aforementioned material differs significantly, the lowering of energies could partially be attributed to the methoxy groups in the structure of **H32**, **H33** that are known to increase the donoric properties of molecules [191].

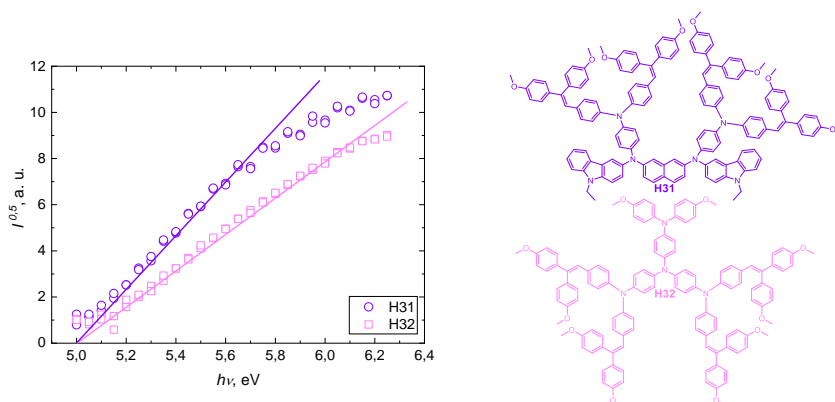


Figure 3.35. I_p measurements of compounds **H31** and **H32**

The solid-state ionization potentials of the investigated materials **H26-H36** were measured by photoemission spectroscopy in air, and the results are shown in Table 3.12. An example of I_p graph can be seen in Figure 3.35. Due to the somewhat different structures of the compounds described in this chapter, a general tendency between them is difficult to observe; however, there are still a few separate cases that could be noted. The additional methoxy groups in thiazole **H27** lowers the I_p value by more than 0.1 eV compared with **H26**, which correlates with the data found in the literature [191]. A different case could be made for carbazole derivatives with five (**H33**) and four (**H34**) phenylethenyl fragments. Both materials have a similar I_p of ~ 5.00 eV; interestingly, the additional electron donating bis(4-methoxyphenyl)ethenyl moiety in **H33** has a negligible effect on the energy levels compared with **H34**, and I_p even slightly increases. The increased steric hindrance resulting from the fifth bis(4-methoxyphenyl)ethenyl fragment connected to the carbazole core could be the main factor behind it.

Table 3.12. Energy level and hole mobility data for **H26-H36** ^a

| Compound | E_{HOMO} , eV ^b | $E_{\text{g}}^{\text{opt1}}$, eV ^c | E_{LUMO} , eV ^d | I_{p} , eV ^e | $E_{\text{g}}^{\text{opt2}}$, eV ^f | EA , eV ^g | μ_0 , $\text{cm}^2 \text{V}^{-1} \text{s}^{-1}$ ^h | μ_h , $\text{cm}^2 \text{V}^{-1} \text{s}^{-1}$ ⁱ |
|------------|--|---|--|-------------------------------------|---|---------------------------|---|---|
| H26 | -5.21 | 2.85 | -2.36 | 5.52 | 2.71 | 2.81 | $1 \cdot 10^{-11}$ | $8 \cdot 10^{-9}$ |
| H27 | -5.14 | 2.82 | -2.32 | 5.40 | 2.68 | 2.72 | $4 \cdot 10^{-10}$ | $1.2 \cdot 10^{-7}$ |
| H28 | -5.20 | 2.98 | -2.22 | 5.00 | 2.79 | 2.21 | - | - |
| H29 | -5.17 | 2.73 | -2.44 | 5.21 | 2.75 | 2.46 | $5 \cdot 10^{-7}$ | $4.5 \cdot 10^{-5}$ |
| H30 | -5.14 | 3.03 | -2.11 | 5.06 | 2.95 | 2.11 | $6 \cdot 10^{-7}$ | $1.1 \cdot 10^{-4}$ |
| H31 | -5.01 | 2.75 | -2.26 | 5.00 | 2.71 | 2.29 | $3 \cdot 10^{-8*}$ | $4.4 \cdot 10^{-7*}$ |
| H32 | -4.96 | 2.74 | -2.22 | 5.00 | 2.67 | 2.33 | $3 \cdot 10^{-8*}$ | $1.2 \cdot 10^{-6*}$ |
| H33 | -5.03 | 2.81 | -2.22 | 5.01 | 2.75 | 2.26 | $3.7 \cdot 10^{-5}$ | $7.8 \cdot 10^{-4}$ |
| H34 | -5.04 | 2.75 | -2.29 | 4.96 | 2.73 | 2.23 | $1.2 \cdot 10^{-4}$ | $1.1 \cdot 10^{-3}$ |
| H35 | -5.29 | 2.82 | -2.47 | 5.31 | 2.83 | 2.48 | $6 \cdot 10^{-4}$ | $2.5 \cdot 10^{-2}$ |
| H36 | -5.33 | 2.75 | -2.58 | 5.31 | 2.68 | 2.63 | - | - |

a) The CV measurements were carried out at a glassy carbon electrode in dichloromethane solutions containing 0.1 M tetrabutylammonium hexafluorophosphate as the electrolyte and Ag/AgNO₃ as the reference electrode. Each measurement was calibrated with ferrocene (Fc). Potentials measured vs. Fc+/Fc. b) Conversion factors: ferrocene in DCM vs SCE 0.46 [219], SCE vs SHE: 0.244 [220], SHE vs. vacuum: 4.43 [221]. c) The optical band gaps $E_{\text{g}}^{\text{opt1}}$ estimated from the edges of electronic absorption spectra in solution. d) E_{LUMO} calculated from the equation $E_{\text{LUMO}} = E_{\text{HOMO}} - E_{\text{g}}^{\text{opt1}}$. e) Solid-state ionization potential (I_{p}) was measured by the photoemission in the air method from films. f) The optical band gaps $E_{\text{g}}^{\text{opt2}}$ estimated from the edges of electronic absorption spectra in the solid state. g) EA calculated from the equation $EA = I_{\text{p}} - E_{\text{g}}^{\text{opt2}}$ h) Mobility value at zero field strength. i) Mobility value at $6.4 \times 10^5 \text{ V cm}^{-1}$ field strength. * drift carrier mobility measured with PC-Z

Some additional observations of the energy levels in a solution and in the solid state of the tested materials could be made after further analyzing Table 3.12. The CV results of compounds **H29-H36** in the solution correlate well with the ionization potential measurement data that was obtained from films, thus indicating limited intermolecular interaction in the solid state. On the other hand, the energy levels of materials **H26-H28** significantly vary depending on the state they are in. In the case of thiazoles **H26** and **H27**, this could be due to the irreversible oxidation during CV measurements which slightly changes the way the energy level calculations are made, making them somewhat less precise; furthermore, the molecules of **H26-H28** most likely arrange themselves in the solid state in such a way that it affects the distribution of the molecular orbitals around the molecules.

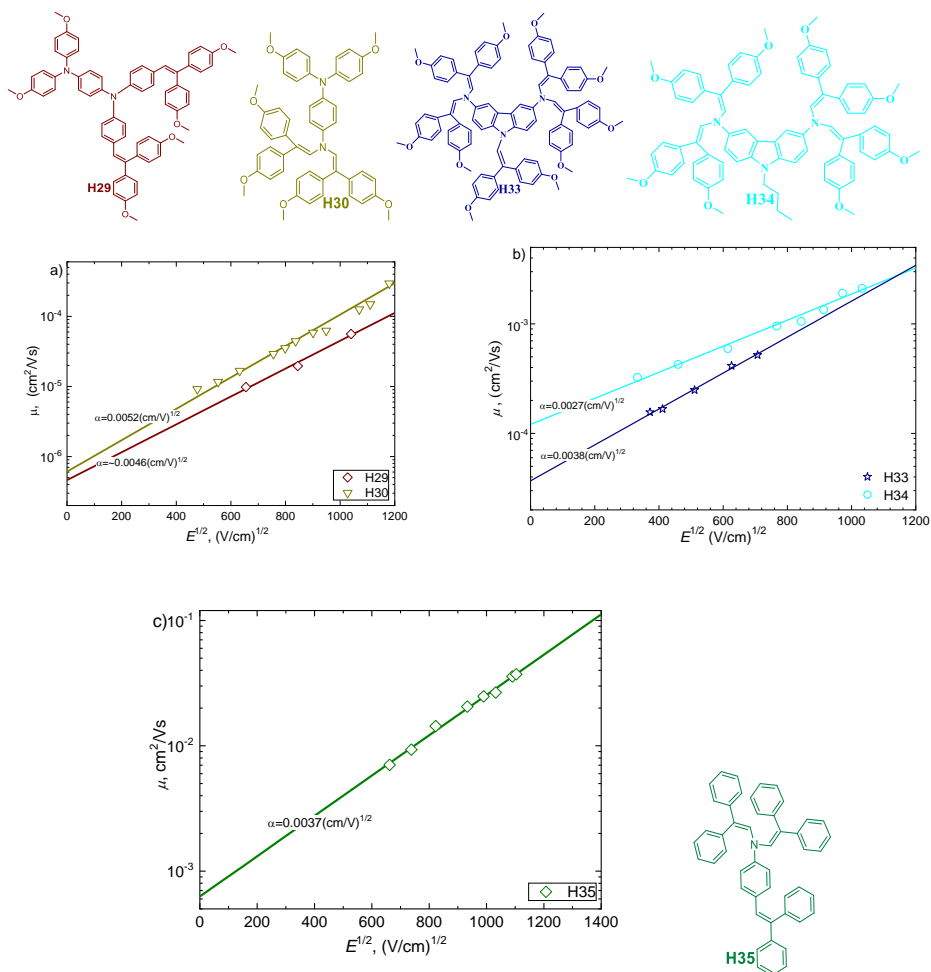


Figure 3.36. Charge carrier mobility of the HTMs a) **H29, H30** b) **H33, H34** c) **H35**

The charge transport properties of HTMs were measured from films by the xerographic time-of-flight (XTOF) method. Examples of charge carrier mobility graphs of the tested materials can be observed in Figure 3.36. The values of the charge mobility defining parameters: zero field mobility (μ_0) and the mobility at the electric field of $6.4 \times 10^5 \text{ V cm}^{-1}$ for compounds **H26**, **H27** and **H29-H35** are given in Table 3.12. The mobility results of the naphthalene moiety containing material **H28** were inconclusive due to the very weak charge transport properties, while naphthalene enamine **H36** could not be measured because of its poor film quality.

Since the molecular structures of the tested HTMs are quite different, there are some mobility values that stand out among the rest. For example, thiazole compounds **H26** and **H27** exhibit a very low charge carrier mobility, while TPA derivatives **H31**, **H32** display two orders of magnitude better results compared to the aforementioned materials **H26**, **H27** even when mixed with PC-Z (weight ratio

1:1), which generally diminishes the charge transport properties by at least one order of magnitude. The poor mobility of **H26** and **H27** could be explained by the thiazole fragment having electron accepting properties due to its electron-withdrawing nitrogen of imine (C = N) [238]. On the other hand, carbazole enamine **H34** and aniline derivative **H35** display excellent mobility despite their structural differences.

Considering the photoelectric properties alone, HTMs **H33-H35** are the most likely candidates for applications in PSCs due to the high charge carrier mobility and the appropriate energy levels (Table 3.12). As a secondary option, materials **H31** and **H32** could be tested in PSCs as, despite their low mobility, they have appropriate energy levels that are compatible with perovskites of various types [239].

3.4.5. Results of perovskite solar cells

TPA derivative **H32** was preliminarily tested in a n-i-p architecture perovskite solar cell⁵. The structure of the device goes as follows: a glass slide with fluorinated tin oxide (FTO) was spin coated with SnO₂ nanoparticles (NPs), phenyl-C61-butyric acid methyl ester (PCBM), perovskite with a composition of FA_{0.83}CS_{0.17}Pb(I_{0.9}Br_{0.1})₃, a HTM layer, and a gold electrode was evaporated on top. All the measurements were done under AM 1.5G illumination, HTM was doped with LiTFSI and 4-*tert*-butylpyridine (tBP).

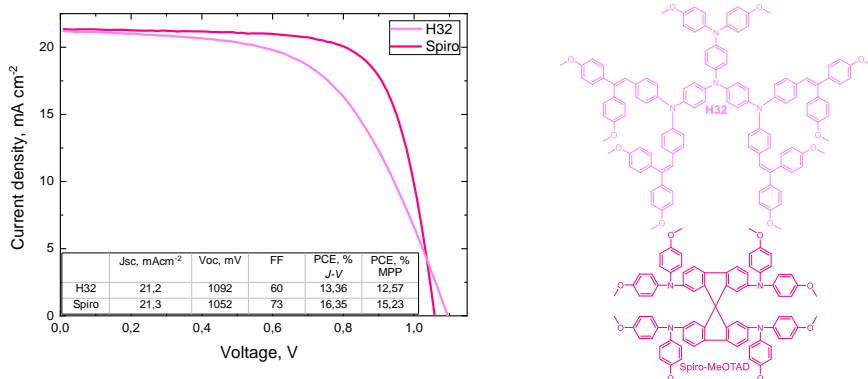


Figure 3.37. Best performing perovskite solar cells current density-voltage characteristics with **H32** and spiro-OMeTAD as hole transporting materials

The best performing solar cell made with **H32** as HTM demonstrated a short circuit current (J_{sc}) of 21.2 mA cm⁻², an open circuit voltage (V_{oc}) of 1092 mV, a fill factor (FF) of 60% and an efficiency of more than 13%. Compared to the standard HTM, spiro-MeOTAD, **H32** demonstrates similar J_{sc} and V_{oc} values;

⁵ N-i-p architecture solar cells were fabricated and tested in the Department of Physics, Clarendon Laboratory, University of Oxford, by Prof. H. J. Snaith research group

however, due to the lower FF , **H32** was 3 percentage points less efficient (in absolute terms) than spiro-MeOTAD (Figure 3.37), which indicates lower conductivity and a suboptimal HTM doping procedure. Despite demonstrating lower performance than the standard material, TPA derivative **H32** shows promise of reaching a higher PCE if FF could be improved via optimization of the doping procedure [128, 129, 240]. Additionally, we should consider changing the perovskite absorber or ETM to tune the band gap in favor of the tested material [239, 241], or modify the architecture of the device [17, 242].

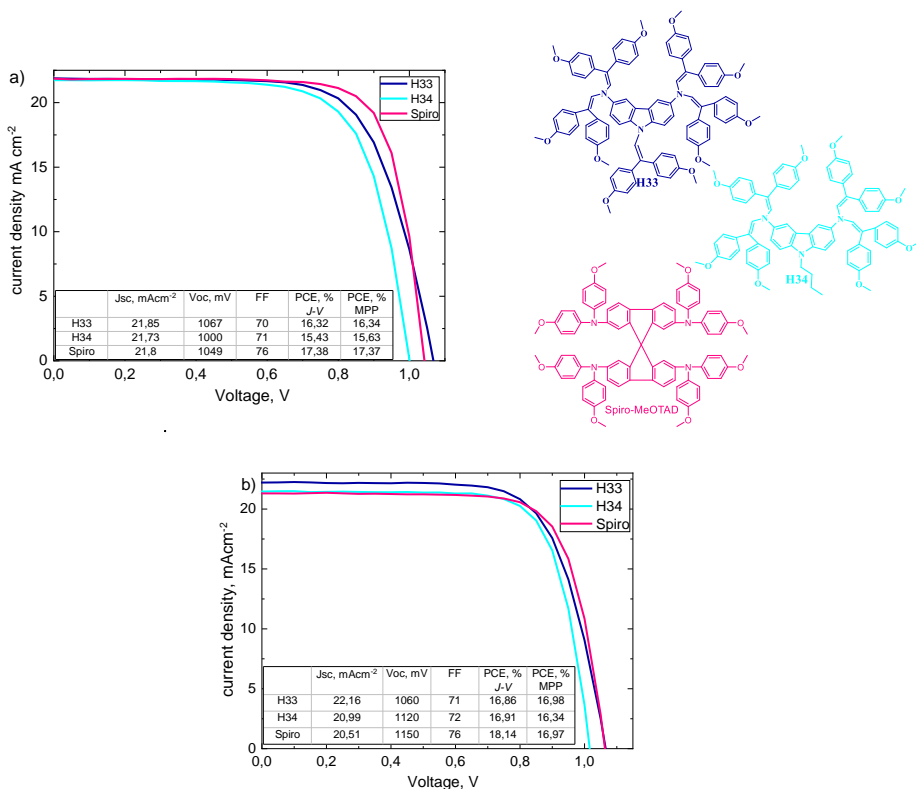


Figure 3.38. Best performing perovskite solar cells current density-voltage characteristics with a) doped HTMs **H33**, **H34** and spiro-OMeTAD b) undoped **H33**, **H34** and doped spiro-OMeTAD

The preliminary results of carbazole derivatives **H33** and **H34** in comparison to spiro-MeOTAD are presented in Figure 3.38a. The device architecture is as follows: FTO/SnO₂ (NPs)/FA_{0.83}Cs_{0.17}Pb(I_{0.9}Br_{0.1})₃/HTM/Au. In this case, the HTM layers of **H33**, **H34** and spiro-OMeTAD were doped with 50 mol% of LiTFSI (respectively to each compound) and 33 μl *t*BP. All measurements were made under AM 1.5 G illumination. Materials **H33** and **H34** demonstrated similar J_{sc} and FF ; however, **H33** reached a higher V_{oc} value which led to PCE being almost

one percentage point higher than that of **H34**. Compared to spiro-MeOTAD, both carbazole derivatives are slightly less efficient, mostly due to the lower *FF*.

However, after further testing, it was discovered that enamines **H33** and **H34** performed even better without the additives, while spiro-MeOTAD still needed to be chemically oxidized to show good results (Figure 3.38b). The devices were optimized by decreasing the thickness of the layers of **H33** and **H34** to 45~55 nm (spiro-MeOTAD required a thickness of 200 nm). Carbazole derivative **H33** demonstrated more than 0.5% higher PCE, and **H34** exhibited roughly a 1.5% increase without the chemical doping, while the slight increase in PCE of spiro-MeOTAD might be the result of the more appropriate level of chemical oxidation [129]. The improved performance of carbazole enamines without additives might be attributed to the sufficient hole mobility of pristine HTMs [125]. It is worth noting that the absence of dopants is advantageous for the longevity of the device [109, 243], which makes materials **H33** and **H34** candidates to replace spiro-MeOTAD as HTM in PSCs.

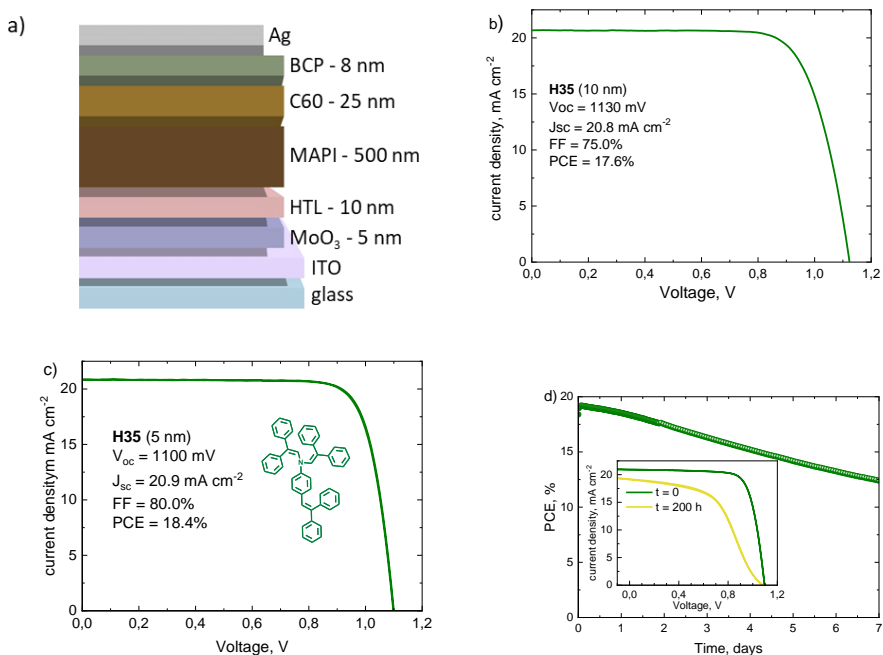


Figure 3.39. a) Solar cell layout with materials and corresponding film thickness. b) J-V curve of solar cell using a 10 nm thick **H35** as the hole transporting layer. c) J-V curve of solar cell using a 5 nm thick **H35** film as the HTM. d) Evolution of the efficiency measured under continuous illumination with maximum power point tracking over a week. The inset shows the J-V curves of the device before and after 200 hours of continuous illumination

Perovskite solar cells with the p-i-n configuration (Figure 3.39a) were prepared by vacuum deposition⁶, and the device architecture was as follows: a glass slide with ITO patterned electrodes, coated with MoO₃ (5 nm), the hole transport layer (HTL, 10 nm), a 500 nm thick MAPI absorber, electron transporting material C₆₀ (25 nm), bathocuproine (BCP, 8 nm), and a silver electrode (100 nm). MoO₃ was used to increase the work function at the front electrode and to enhance the charge extraction from HTL to ITO [244].

PSCs fabricated this way with HTM **H35** demonstrated PCE of 17.6% (Figure 3.39b). In view of the promising performance of **H35** in vacuum deposited PSCs, additional cells with thinner HTL (5 nm instead of 10 nm) were fabricated, as this might alleviate transport losses within the organic semiconductor and increase the built-in potential [245]. Solar cells with 5 nm thick **H35** show a very good rectification, with *FF* as being high as 80%, while maintaining essentially unvaried the other photovoltaic parameters (Figure 3.39c). The improvement in *FF* compared to the cell with a 10 nm thick layer of **H35** (Figure 3.39b) led to a PCE value as high as 18.4%, which is close to the highest ever reported for vacuum-processed p-i-n devices (about 19%) [245, 246]. The long term light soaking stability of solar cells was further tested under continuous simulated solar illumination. The devices were encapsulated with a UV-curable resin and a glass slide and kept at 25 °C under a nitrogen flow (at max relative humidity 10%) with the objective to minimize the effect of the environment. The maximum power point was continuously tracked, and the evolution of the PCE over time is depicted in Figure 3.33d. The solar cell showed an initial rise in efficiency (to about 19%) followed by a slow but continuous decay for the 7 days of characterization. After one week of continuous operation, the device with an **H35** contact delivered a PCE of 12.5%, which was found to be mainly determined by the decrease in *FF* (see the inset in Figure 3.39d), and, to less extent, by a lower current density. While the latter factor points towards degradation of the MAPI perovskite film, other degradation pathways related with interfacial effects at the front contact cannot be excluded.

3.4.6. Conclusions of Chapter 3.4

To sum up, a variety of hole transporting materials with phenylethynyl moieties were synthesized, and compounds with the best package of properties were tested in perovskite solar cells. TPA derivative **H32**, despite its low mobility, demonstrated respectable current density-voltage characteristics, and, with the further optimization of the doping procedure, they might rival spiro-MeOTAD. The same could be said about carbazole enamines **H33** and **H34**. Not only did they reach almost 17% efficiencies, but they also did not need any dopants, which is important to the longevity of the device. The final HTM tested in PSC was aniline

⁶ P-i-n architecture solar cells were fabricated and tested at Instituto de Ciencia Molecular, Universidad de Valencia, in Prof. H. J. Bolink research group.

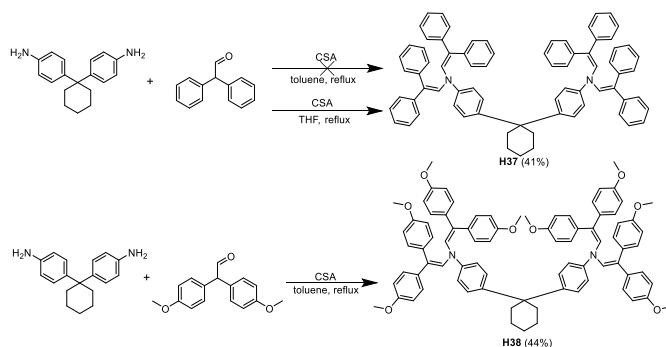
derivative **H35**, which demonstrated more than 18% PCE in a fully vacuum deposited solar cell thus rivalling the highest reported device for vacuum-processed p-i-n devices [245, 246]. Having this in mind, it was decided to further research aniline-based semiconductors in the next chapter.

3.5. Aniline based hole transporting materials

Aniline, as one of the most basic and widely used precursors in the chemical industry, was applied in the synthesis of numerous chemicals. It is extremely cheap and produced on a vast scale [247]. It should come to no surprise that aniline is also employed in the synthesis of semiconducting materials for the use in optoelectronics [20, 248]. When continuing the work described in the previous chapter, it was decided to synthesize charge transporting enamines employing aniline based precursors via a cost-effective single step, a transition-metal-catalysts-free route that had been established previously [20, 140].

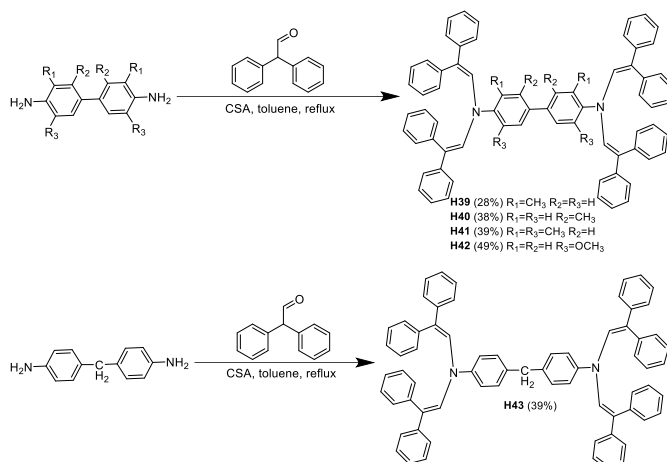
3.5.1 Synthesis of 1,1-diphenylcyclohexane and biphenyl derivatives containing phenylethenyl moieties

The condensation reaction between 1,1-bis(4-aminophenyl)cyclohexane and diphenylacetaldehyde using CSA as the catalyst was conducted in toluene with no product being formed; however, changing the solvent to THF yielded enamine **H37**. This could be explained by the different reaction rates in the investigated solvents and by the more favorable conditions for side reactions to take place in a toluene-based system. Methoxy enamine **H38** was synthesized in a similar manner by condensing 1,1-bis(4-aminophenyl)cyclohexane with 2,2-bis(4-methoxyphenyl)acetaldehyde in the presence of an acid catalyst in toluene (Scheme 3.27).



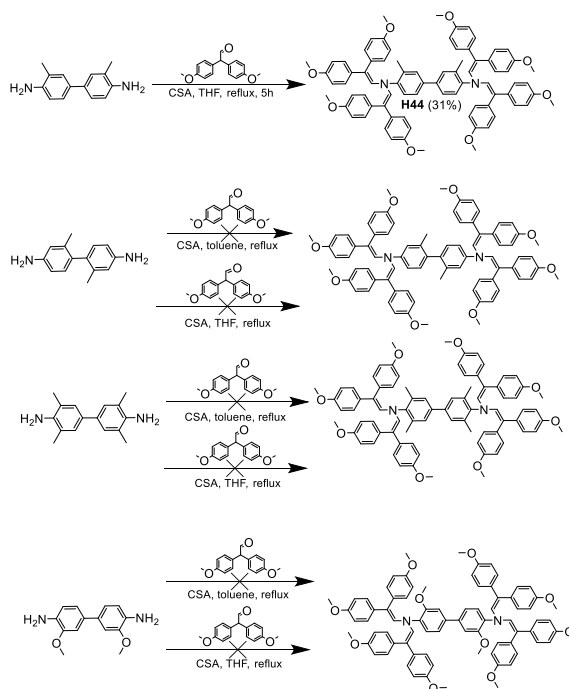
Scheme 3.27. Synthesis of enamines **H37** and **H38**

Biphenyl derivatives **H39-H43** were synthesized by condensing the corresponding biphenyls with diphenylacetaldehyde via CSA catalyzed reaction (Scheme 3.28).



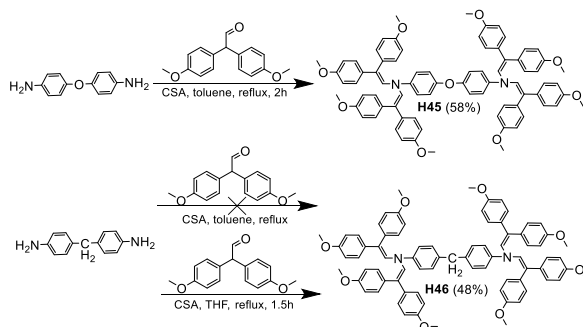
Scheme 3.28. Synthesis of biphenyl derivatives **H39-H43**

The condensation of *o*-tolidine and 2,2-bis(4-methoxyphenyl)acetaldehyde in toluene was unsuccessful; therefore, the solvent was changed to THF to give biphenyl-based enamine **H44**. The reactions of *m*-tolidine, 3,3',5,5'-tetramethylbenzidine, *o*-dianisidine with the aforementioned aldehyde containing methoxy groups did not yield the desired product (Scheme 3.29) due to side reactions taking place between the reactants in methylbenzene.



Scheme 3.29. Condensation reactions of biphenyl derivatives with 2,2-bis(4-methoxyphenyl)acetaldehyde

Synthesis of oxydianiline-based enamine **H45** was conducted by reacting 2,2-bis(4-methoxyphenyl)acetaldehyde with 4,4'-oxydianiline in the presence of CSA in toluene (Scheme 3.30).



Scheme 3.30. Synthesis of enamines **H45** and **H46**

The usage of methylbenzene as the solvent for the condensation of 4,4'-methylenedianiline with the above mentioned methoxy aldehyde did not yield the appropriate enamine **H46** as the product. However, similarly to **H44**, aniline derivative **H46** was obtained by changing the solvent to THF (Scheme 3.30).

3.5.2. Thermal properties

The thermal stability of the materials was measured by using thermogravimetric analysis (TGA), and the results are listed in Table 3.13. For the comparison of properties, a known biphenyl derivative 4,4'-oxybis[*N,N*-bis(2,2-diphenylethenyl)aniline] (OBDA) [249] was also added to Table 3.13. With the exception of **H44**, all the tested HTMs showed a 5% weight loss at temperatures higher than 300 °C, thereby proving that they are sufficiently thermally stable for application in PSCs. Furthermore, materials **H37**, **H40**, **H41** and **H42** demonstrated rapid weight loss, which suggests that they show potential for application in vacuum deposited devices (Figure 3.40).

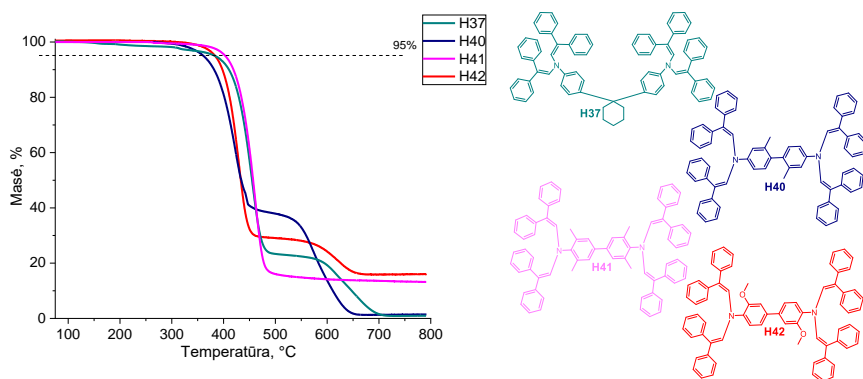


Figure 3.40. TGA curves of enamines **H37**, **H40**, **H41** and **H42**

The peculiar case of a relatively low stability of **H44** could be explained by the spatial restraints due to the presence in the close proximity of large bis(4-methoxyphenyl)ethenyl substituents and the methyl groups of the biphenyl core that, when heated, might limit the movement of the separate parts of its molecule, thereby causing bond breaking strains. More than 20% mass loss observed in Figure 3.41 roughly coincides with a single bis(4-methoxyphenyl)ethenyl fragment.

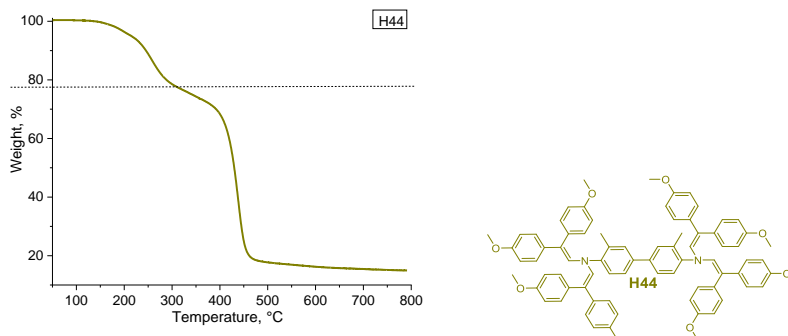


Figure 3.41. TGA curve of **H44**

Cyclohexane derivative **H37** during the 1st heating crystallizes at 202 °C and melts at 315 °C; however, after cooling, it becomes completely amorphous, and only T_g of 156 °C is observed in the second heating (Figure 3.42). The addition of methoxy groups to **H37** eliminates the crystalline phase thus making **H38** purely amorphous (Figure 3.42). This could be explained by the less orderly structure of **H38** due to the steric hindrances introduced by the alkoxy substituents.

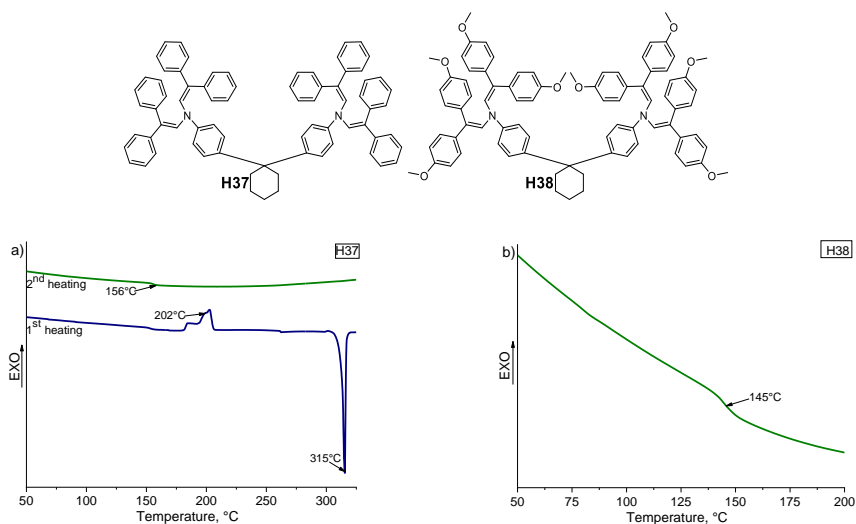


Figure 3.42. a) DSC heating curves of compound **H37**. b) DSC second heating curve of **H38**

The DSC curves of biphenyl enamines **H39-H42** can be observed in Figure 3.43. Aniline derivative **H39** is a fully amorphous compound with a T_g value of 103 °C. Interestingly, the change of the position of methyl groups from *ortho* to *meta* has a significant effect on the thermal properties of compound **H40**, thus making it fully crystalline. This could be explained by the limited rotation around the bond connecting phenyl rings in the biphenyl fragment. The limitation is caused by methyl groups in the *meta* position together with diphenylethenyl substituents in **H40**, thereby making the molecule more rigid and hence leading to a higher tendency to crystallize.

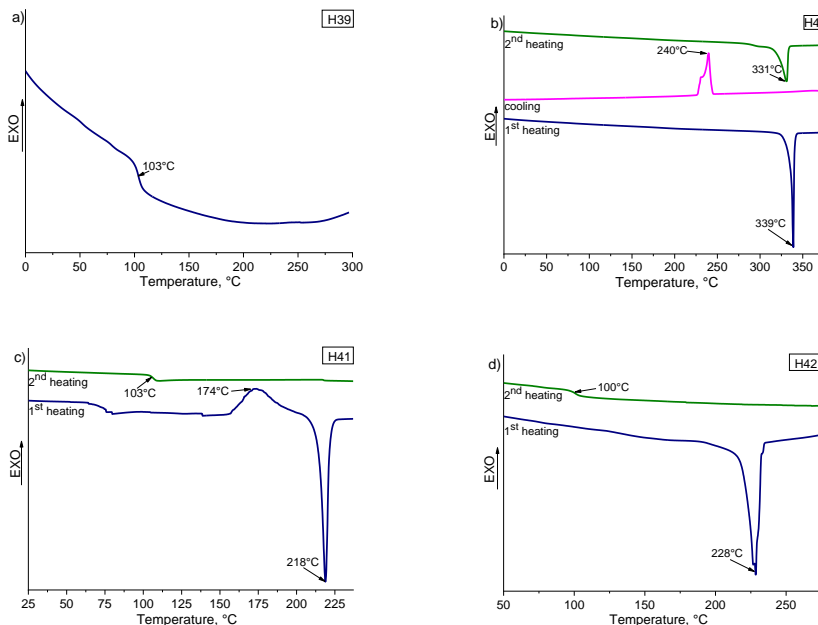
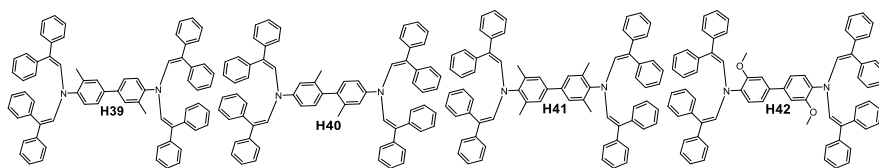


Figure 3.43. a) DSC second heating curve of **H39** b) DSC heating and cooling curves of compound **H40** c) DSC heating curves of **H41** d) DSC heating curves of **H42**

The addition of two extra methyl groups in the structure of **H41** leads to a similar outcome as in case of **H40**, although not as strongly pronounced. These materials have some tendency to crystallize; however, a stable amorphous state can also be observed at 103 °C (Figure 3.43c). This could be due to more steric hindrances slightly limiting the movement of different parts of molecules making them moderately more orderly. Similarly to the previously mentioned biphenyl derivative, changing the methyl substituents to methoxy in **H42** also results in material with a stronger tendency to crystallize (Figure 3.43d), although the slightly bulkier methoxy groups do not form as orderly structures, and one can also observe the formation of the amorphous state during rapid cooling.

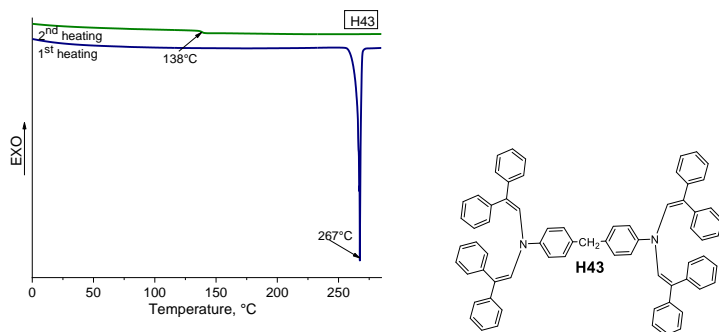


Figure 3.44. a) DSC heating curves of **H43**

DSC curves of **H43** can be seen in Figure 3.44. The compound can exist in the crystalline as well as in the amorphous state as melting of the crystals can be seen during the first heating, and only T_g is observed during the second heating. In comparison, a known biphenyl derivative OBDA, whereas the methylene linker is replaced by oxygen compared to **H43**, has a similar T_g value – around 140 °C – but a roughly 30 °C higher T_m value (Table 3.13).

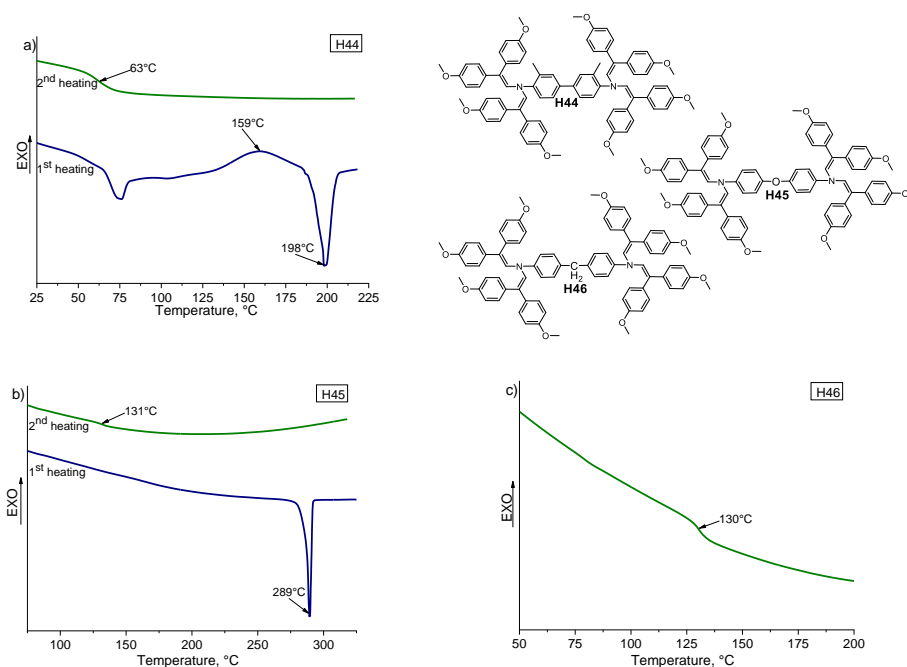


Figure 3.45. a) DSC heating curves of **H44** b) DSC heating curves of compound **H45** c) DSC second heating curve of **H46**

The phase changes of compounds **H44-H46** can be observed in Figure 3.45. Biphenyl derivative **H44**, as it was obtained after synthesis and purification, is a

mixture of amorphous and crystalline materials; however, during the 2nd heating only T_g is seen (Figure 3.45a). The separation of conjugation by an oxygen atom in **H45** gives a material that can be either purely crystalline or a molecular glass (Figure 3.45b). Interestingly, changing the linker from oxygen to methyl leads to a fully amorphous compound (Figure 3.45c). This might be due to the less rigid nature of the **H46** molecule compared to **H45**.

Table 3.13. Thermal properties of compounds **H37-H46**

| Compound | $T_g^{a,}$ °C | $T_m^{b,}$ °C | $T_{cr}^{c,}$ °C | $T_{dec}^{d,}$ °C |
|------------|---------------|---------------|------------------|-------------------|
| H37 | 156 | 315 | - | 383 |
| H38 | 145 | - | - | 385 |
| H39 | 103 | - | - | 327 |
| H40 | - | 339 | 240 | 361 |
| H41 | 106 | 218 | 174 | 382 |
| H42 | 100 | 228 | - | 383 |
| H43 | 138 | 267 | - | 350 |
| OBDA | 139 | 295 | 244 | 405 |
| H44 | 63 | 198 | 159 | 215 |
| H45 | 131 | 289 | - | 361 |
| H46 | 130 | - | - | 366 |

a) Determined by DSC: scan rate = 10 °C min⁻¹, N₂ atmosphere; second run; b) Determined by DSC: scan rate = 10 °C min⁻¹, N₂ atmosphere; first run; c) Determined by DSC: scan rate = 10 °C min⁻¹, N₂ atmosphere; d) Onset of decomposition determined by TGA: heating rate = 10 °C min⁻¹, N₂ atmosphere

To sum up, the best choice as HTM for PSC based on thermal analysis would be **H39**, **H40** and **H46** due to the fact that they are fully amorphous and have a relatively high T_g , while **H40** is also a possible option if properly crystallized during device fabrication [233]. Materials **H37**, **H41-H43**, **H45** and **H46** display only the amorphous state after the 2nd heating and could also be considered as candidates for applications in PSCs, while the low T_g of **H44** would be problematic for the long term thermal stability of the device [250].

3.5.3. Optical properties

The light absorption spectra of cyclohexane derivatives **H37** and **H38** can be seen in Figure 3.46. In THF absorption maxima for **H37** peaks at around 343 nm; despite the addition of donoric methoxy groups, π - π^* electron transition for **H38** is also observed at the same wavelength. Interestingly, methoxy substituted enamine **H38** has a significantly more pronounced absorption peak at around 260 nm, and it corresponds to n - σ^* electron transitions in the proximity of oxygen atoms in methoxy substituents. Virtually no change is observed when comparing the spectra in a solution and on a glass substrate, which indicates very little interaction between molecules in the solid state.

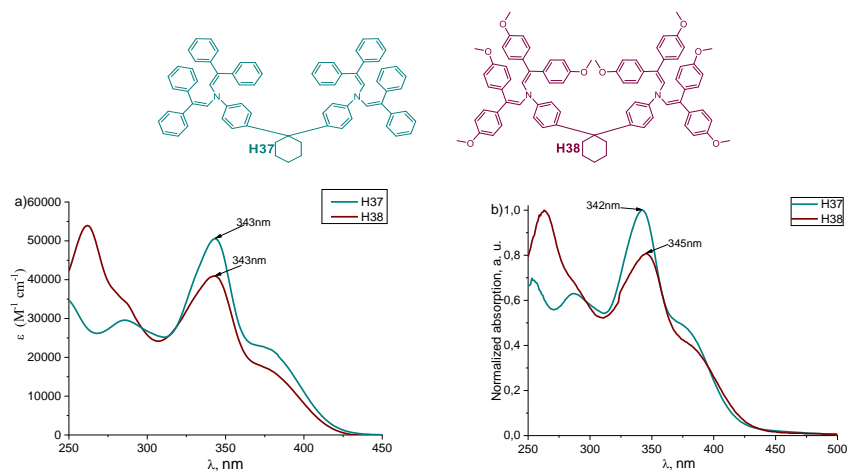


Figure 3.46 a) UV-Vis absorption spectra of **H37**, **H38** in THF and b) thin films on glass

The absorption spectra of biphenyl derivatives **H39-H42** were recorded and are presented in Figure 3.47. In the solution, the $\pi \rightarrow \pi^*$ transition for **H39** peaks at 364 nm, while the change of the position of the methyl groups from *ortho* to *meta* in **H40** blueshifts the absorption maximum by 17 nm. **H41** with additional methyl substituents in the *ortho* position exhibits a hypsochromic shift compared to **H39**, but to a smaller extent compared to **H40**. Changing the methyl groups in the *ortho* position of **H39** to methoxy in **H42** causes a slight bathochromic shift due to the stronger donoric properties of the methoxy substituents. The shifts in the absorption maxima of biphenyl derivatives **H40**, **H41** could be explained by out-of-plane twisting of the phenyl rings of the biphenyl moiety when the methyl groups are in the *meta* position or stronger steric hindrances occurring when there are more than two substituents in the *ortho* position.

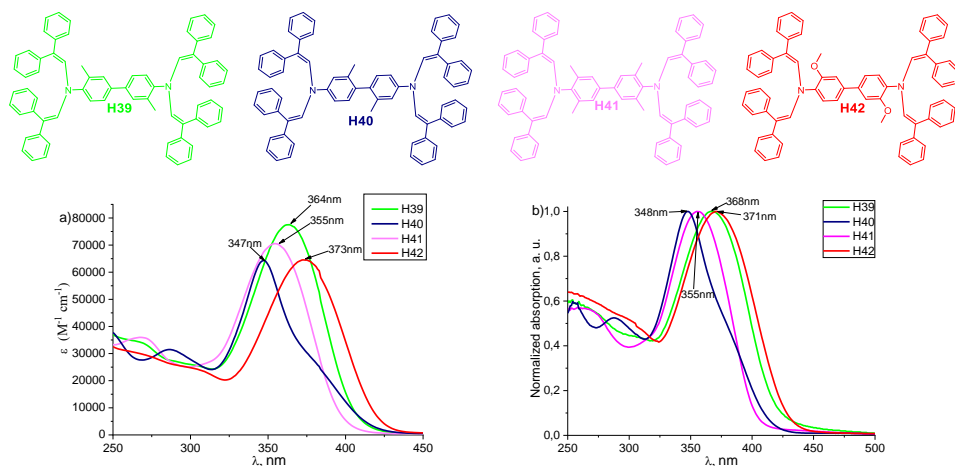


Figure 3.47 a) UV-Vis absorption spectra of **H39-H42** in THF and b) thin films on glass

When comparing the absorption spectra in a solution and on the glass substrate, the most notable change is the 4 nm redshift for **H39**, while **H40** and **H41** peak at virtually the same wavelength as before. This could back up the previously mentioned suggestion that **H39** has less steric hindrances than **H40** or **H41** and shows some indications for more orderly orientation of the molecules in the film.

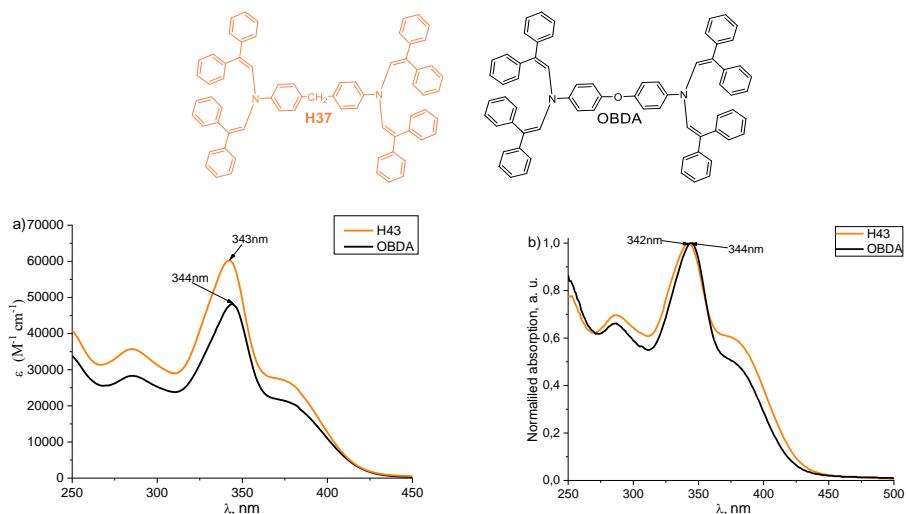


Figure 3.48 a) UV-Vis absorption spectra of **H43**, OBDA in THF and b) thin films on glass

The light absorption properties of **H43** were recorded and compared with known compound OBDA (Figure 3.48). Despite having a different linker, the π - π^* electron transition for both compounds can be seen at around 344 nm in a solution and on the glass substrate. The only difference between the spectra of these compounds is the slightly more intensive absorption of **H43** in THF, assumedly due to the change in the electron distribution within the molecule compared to OBDA.

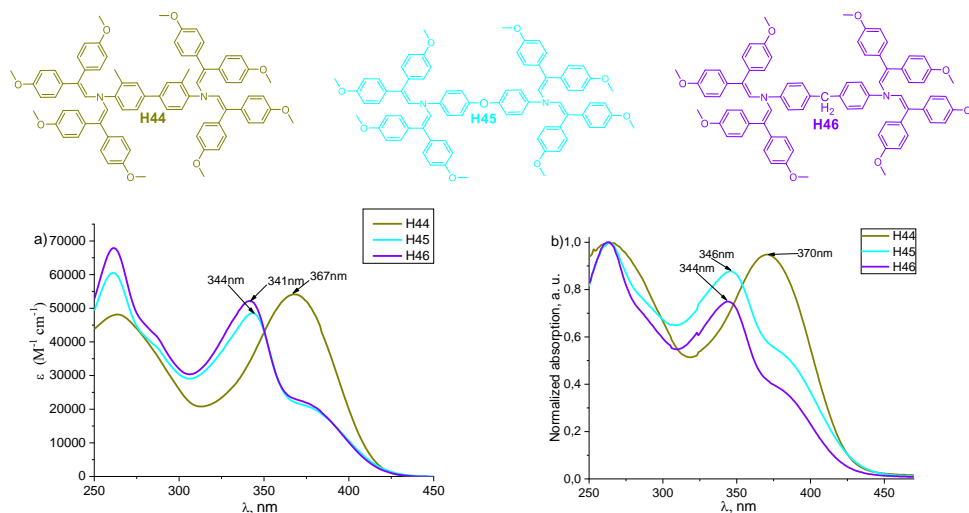


Figure 3.49. a) UV-Vis absorption spectra of **H44**, **H45** and **H46** in THF and b) thin films on glass

The UV-Vis absorption spectra of methoxy substituted aniline derivatives **H34-H46** are presented in Figure 3.49. In a solution and on the glass substrate, the π - π^* electron transition of compound **H44** peaks at around 370 nm, while, in comparison, the other two materials display hypsochromic shifts of more than 20 nm. This could be explained by the breaking of conjugation by the oxygen or else by the methyl linker in **H45** and **H46** respectively. It is also worth noting that all three compounds have a strong absorption peak at around 250 nm which could correspond to n - σ^* electron transitions in the proximity of oxygen atoms in methoxy substituents.

3.5.4. Photophysical properties

To evaluate the electrochemical stability of the synthesized compounds, CV measurements in DCM were carried out. All the researched materials demonstrated reversible oxidation, examples of the cyclic voltammograms of the tested HTMs are shown in Figure 3.50.

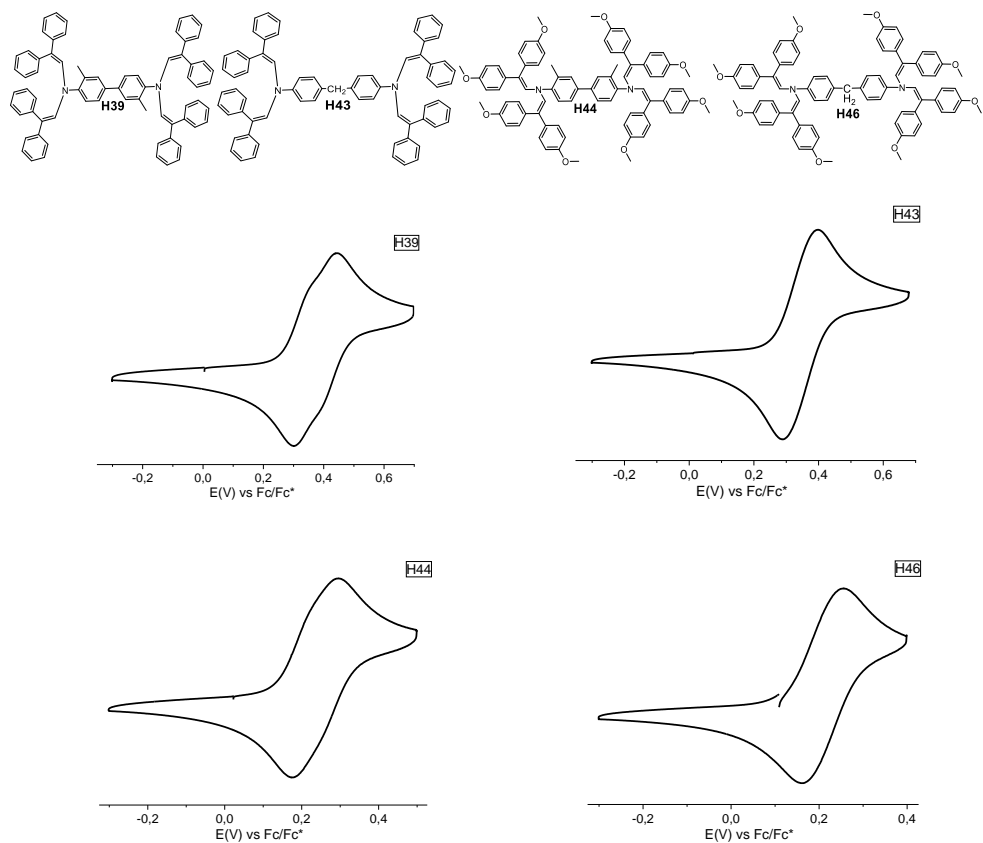


Figure 3.50. Voltammograms of **H39**, **H43**, **H44** and **H46**

The data acquired from CV measurements together with the optical band gaps (E_g^{opt1}) estimated from the edges of electronic absorption spectra in a solution were used to calculate the HOMO and LUMO energies (Table 3.14). After analyzing the results, a trend was observed that materials containing 2,2-bis(4-methoxyphenyl)ethenyl fragments tend to have lower HOMO and LUMO energies in comparison to their respective derivatives which have diphenylacetaldehyde moieties.

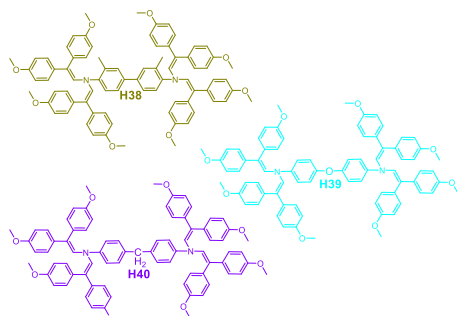
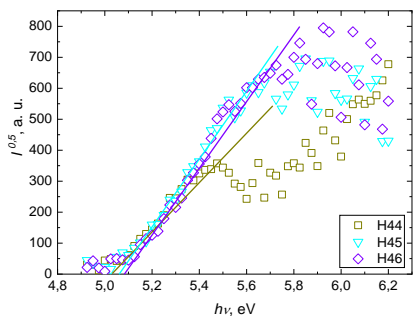


Figure 3.51. I_p measurements of compounds **H44**, **H45**, and **H46**

The ionization energies of the investigated *p*-type semiconductors **H37-H46** were measured by photoemission spectroscopy in air. An example of an I_p graph is presented in Figure 3.51. The solid state I_p values of the tested materials follow the same trend as E_{HOMO} measured from solutions – the presence of stronger electron donating 2,2-bis(4-methoxyphenyl)ethenyl fragments leads to a lower I_p value compared to their respective derivatives which have diphenylacetaldehyde moieties (Table 3.14).

As a separate case, it is worth analyzing the change in I_p among compounds **H39-H42**. Biphenyl derivative **H39** has a ionization potential value of 5.16 eV, while the change of the position of methyl groups from *ortho* to *meta* for **H40** increases the I_p value by 0.16 eV. Additional methyl substituents in **H41** also increase the I_p in a similar manner, while the change from the methyl groups to methoxy in **H42** has no effect on the ionization energy. This could be explained by the different spatial configuration of the molecules having an effect on the conjugation between the separate aniline fragments.

Table 3.14. Energy level and hole mobility data for **H37-H46** ^a

| Compound | E_{HOMO} , eV ^b | $E_{\text{g}}^{\text{opt1}}$, eV ^c | E_{LUMO} , eV ^d | I_{p} , eV ^e | $E_{\text{g}}^{\text{opt2}}$, eV ^f | EA , eV ^g | μ_{o} , $\text{cm}^2 \text{V}^{-1} \text{s}^{-1}$ ^h | μ_{h} , $\text{cm}^2 \text{V}^{-1} \text{s}^{-1}$ ⁱ |
|------------|--|---|--|-------------------------------------|---|---------------------------|--|--|
| H37 | -5.27 | 2.94 | -2.33 | 5.37 | 2.94 | 2.43 | $1.5 \cdot 10^{-4}$ | $1 \cdot 10^{-2}$ |
| H38 | -5.09 | 2.95 | -2.14 | 5.19 | 2.87 | 2.32 | $2 \cdot 10^{-5}$ | $2.3 \cdot 10^{-3}$ |
| H39 | -5.27 | 3.00 | -2.27 | 5.16 | 2.90 | 2.26 | $2.1 \cdot 10^{-3}$ | $1.2 \cdot 10^{-2}$ |
| H40 | -5.30 | 3.12 | -2.18 | 5.32 | 3.06 | 2.26 | $2.4 \cdot 10^{-3}$ | $7 \cdot 10^{-3}$ |
| H41 | -5.27 | 3.06 | -2.21 | 5.33 | 3.05 | 2.28 | $3.6 \cdot 10^{-4}$ | $6.5 \cdot 10^{-3}$ |
| H42 | -5.20 | 2.90 | -2.30 | 5.16 | 2.86 | 2.30 | $2 \cdot 10^{-4}$ | $2 \cdot 10^{-2}$ |
| H43 | -5.24 | 2.93 | -2.31 | 5.37 | 2.86 | 2.51 | $7.5 \cdot 10^{-6*}$ | $5.5 \cdot 10^{-5*}$ |
| OBDA | -5.20 | 2.92 | -2.28 | 5.26 | 2.88 | 2.38 | $8 \cdot 10^{-7*}$ | $1.9 \cdot 10^{-5*}$ |
| H44 | -5.13 | 2.96 | -2.17 | 5.03 | 2.88 | 2.15 | $1.6 \cdot 10^{-5}$ | $4.5 \cdot 10^{-4}$ |
| H45 | -5.08 | 2.92 | -2.16 | 5.06 | 2.84 | 2.22 | $2 \cdot 10^{-6}$ | $8 \cdot 10^{-5}$ |
| H46 | -5.10 | 2.94 | -2.16 | 5.09 | 2.85 | 2.24 | $5 \cdot 10^{-5}$ | $8.8 \cdot 10^{-4}$ |

a) The CV measurements were carried out at a glassy carbon electrode in dichloromethane solutions containing 0.1 M tetrabutylammonium hexafluorophosphate as electrolyte and Ag/AgNO₃ as the reference electrode. Each measurement was calibrated with ferrocene (Fc). Potentials measured vs. Fc+/Fc. b) Conversion factors: ferrocene in DCM vs. SCE 0.46 [219], SCE vs. SHE: 0.244 [220], SHE vs. vacuum: 4.43 [221]. c) The optical band gaps $E_{\text{g}}^{\text{opt1}}$ estimated from the edges of the electronic absorption spectra in solution. d) E_{LUMO} was calculated from the equation $E_{\text{LUMO}} = E_{\text{HOMO}} - E_{\text{g}}^{\text{opt1}}$. e) Solid-state ionization potential (I_{p}) was measured by the photoemission in the air method from films. f) The optical band gaps $E_{\text{g}}^{\text{opt2}}$ were estimated from the edges of electronic absorption spectra in the solid state. g) EA was calculated from the equation $EA = I_{\text{p}} - E_{\text{g}}^{\text{opt2}}$ h) Mobility value at zero field strength. i) Mobility value at $6.4 \times 10^5 \text{ V cm}^{-1}$ field strength. * drift carrier mobility measured with PC-Z

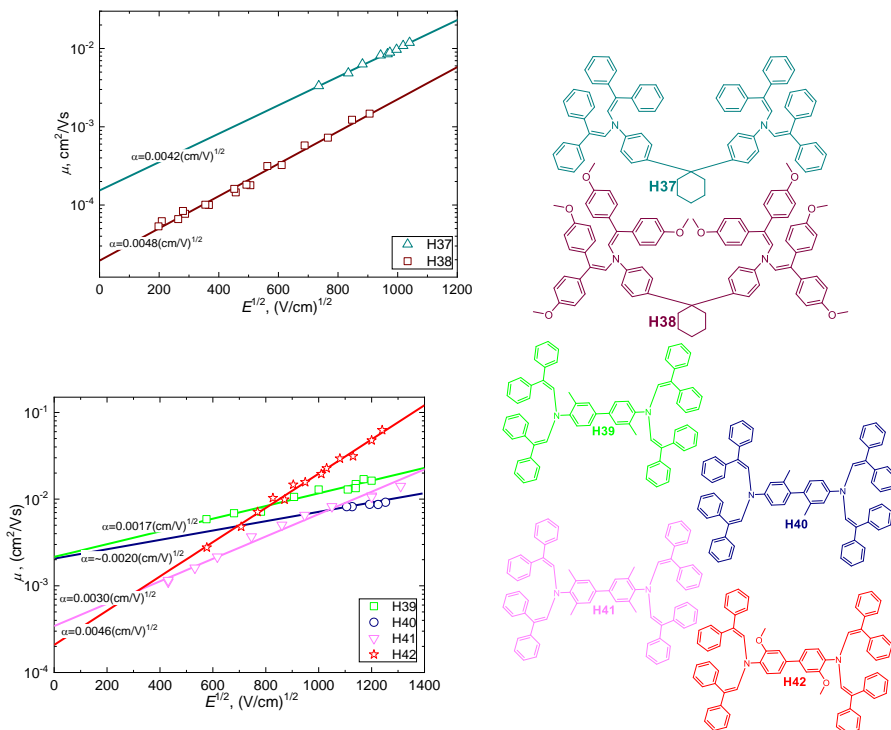


Figure 3.52. Charge carrier mobility of HTMs **H37-H42**

The charge transport properties of HTMs were measured from films by the xerographic time-of-flight (XTOF) method. Examples of charge carrier mobility graphs of tested materials are presented in Figure 3.52. The values of the charge mobility defining parameters: zero field mobility (μ_0) and the mobility at the electric field of $6.4 \times 10^5 \text{ V cm}^{-1}$ for compounds **H37-H46** are given in Table 3.14. The lowest mobility values belong to compound **H43**; due to a poor quality level of the film it had to be mixed with PC-Z at a weight ratio 1:1 to obtain uniform layers. Therefore, the absolute mobility results for **H43** are lower (by approximately one order of magnitude) due to the presence of a large portion of a nonconductive polymer.

After analyzing the mobility data of the tested materials, a trend can be seen: methoxy groups tend to lower the value of drift carrier mobility. For example, **H37** demonstrates one order of magnitude higher results than **H38** containing methoxy groups. The same applies for the pair of **H39** and **H44**. The decrease in mobility is most likely caused by the less tight packing occurring due to the addition of methoxy groups, which, in turn, leads to longer distances between charge hopping sites, thus slowing the charge transport.

3.5.5. Results of perovskite solar cells

Enamines **H37** and **H40** were tested in vacuum deposited PSCs with the structure of ITO/MoO₃/H31/MAPI/C₆₀/BCP/Ag (p-i-n), and their J-V curves are shown in Figure 3.53. Both materials demonstrate similar *V*_{oc} and *J*_{sc} values, however, **H40** reaches 14.3% PCE, while **H37** is 1.1 percentage point less efficient. The reason for this becomes obvious when Figure 3.47a is examined more thoroughly: a pronounced kink in the *J*-*V* curve under illumination is observed for **H37**, which results in reduced FF leading to the lower PCE of the device.

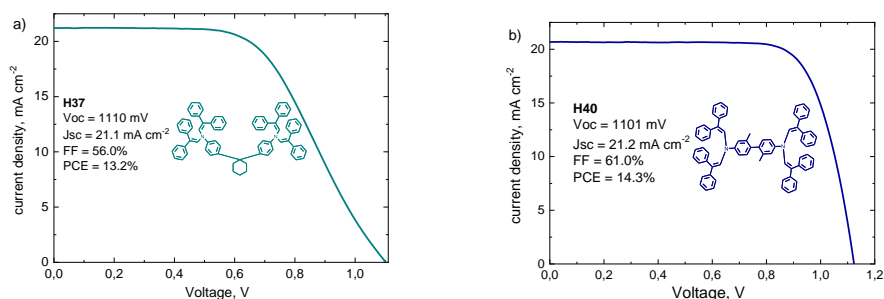


Figure 3.53. p-i-n architecture PSC J-V curves of a) **H37** and b) **H40**

Methoxy substituted enamines **H44-H46** were preliminarily tested in n-i-p PSCs with the structure of FTO/SnO₂ (NPs)/PCBM/FA_{0.83}Cs_{0.17}Pb(I_{0.9}Br_{0.1})₃/HTM/Au. All HTMs were doped with 50 mol% of LiTFSI (respectively to each compound) and 33 μl *t*BP; their photovoltaic characteristics in comparison to spiro-MeOTAD can be observed in Figure 3.54.

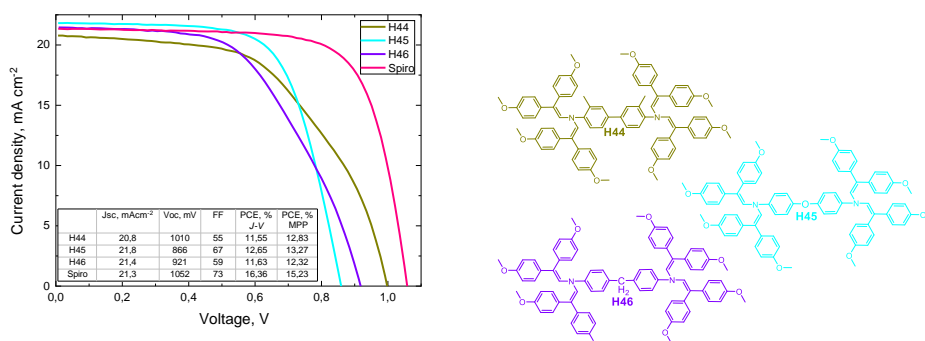


Figure 3.54. Current density-voltage characteristics of best performing perovskite solar cells with **H44**, **H45**, **H46** and spiro-OMeTAD as hole transporting materials

Despite the structural similarities, solar cell parameters of biphenyl derivatives somewhat differ. The short circuit voltage varies in the range of 20.8–21.8 mA/cm², whereas *V_{oc}* ranges in between 866–1010 mV, while *FF* varies by 12 percentage points. Best performing biphenyl derivative **H44**, compared to spiro-MeOTAD, demonstrates about 3.5% lower PCE. However, this might be due to the unoptimized doping procedure which, in this case, is specifically tuned to suite spiro-MeOTAD. Doping times and concentrations are especially important in this case as spiro-MeOTAD is denoted by a lower ionization potential (5.0 eV) compared with the investigated HTMs (around 5.1 eV), therefore, is it easier to produce oxidized species of spiro than those of **H44-H46**.

3.5.6. Conclusion of Chapter 3.5

Every aniline derivative described in this chapter displayed suitable energy levels to be used in PSCs. Furthermore, all the materials displayed electrochemical and, with the exception of **H44** (Table 3.13), great thermal stability. HTMs **H37**, **H40** were tested in fully vacuum deposited devices with the p-i-n configuration and demonstrated respectable performance, 13.2% power conversion efficiency for cyclohexane derivative **H37** and 14.3% for **H40**. Methoxy groups containing materials **H44-H46** were applied in n-i-p architecture PSCs with more modest results; however, it is still worth noting that biphenyl derivatives **H44-H46** were used under conditions that are tuned for spiro-MeOTAD, and therefore further testing and optimization is needed in order to fulfill the full potential of HTMs. Lastly, enamines **H38**, **H39**, **H41** and **H42** should be mentioned as very promising candidates HTMs for applications in PSCs due to their high mobility and overall great properties.

4. EXPERIMENTAL PART

4.1. Instrumentation

Measurements

The ^1H and ^{13}C NMR spectra were taken on *Bruker Avance III 400* (400 MHz) and *Bruker Avance III 700* (700 MHz) spectrometers at room temperature. The chemical shifts, expressed in δ (ppm), are relative to the $(\text{CH}_3)_4\text{Si}$ (TMS, 0 ppm) internal standard. The compounds were dissolved in deuterated solvents as indicated for each compound. All the experiments were performed at 25 °C.

The course of the reaction products was monitored by TLC on *ALUGRAM SIL G/UV254* plates and developed with I_2 or UV light. Silica gel (grade 62, 60–200 mesh, 150 Å, *Aldrich*) was used for column chromatography.

The elemental analysis was performed with an *Exeter Analytical CE-440 Elemental*.

The melting points were determined in capillary tubes by using *Electrothermal MEL-TEMP* and *DigiMelt MPA 161* capillary melting point apparatus.

Differential scanning calorimetry (DSC) was performed on a *Q10* calorimeter (*TA Instruments*) at a scan rate of 10 K min^{-1} in the nitrogen atmosphere. The glass transition temperatures for the investigated compounds were determined during the second heating scan.

Thermogravimetric analysis (TGA) was performed on a *Q50* thermogravimetric analyzer (*TA Instruments*) at a scan rate of 10 K min^{-1} in the nitrogen atmosphere.

FT-IR spectra were recorded by using a *Perkin-Elmer Frontier* spectrophotometer with a single reflectance horizontal ATR (Attenuated Total Reflectance) cell equipped with a diamond crystal and the *Perkin Elmer Spectrum BX II FT-IR System* using KBr pellets. The data were recorded in the spectral range from 650 to 4000 cm^{-1} by accumulating 5 scans with a resolution of 4 cm^{-1} .

The absorption spectra of the dilute THF solutions were recorded on a UV-VIS-NIR spectrophotometer *Lambda 950* (*Perkin Elmer*). Microcells with an internal width of 1 mm were used.

Cyclic voltammetry (CV) measurements were carried out by a three-electrode assembly cell from a *Bio-Logic SAS* potentiostat-galvanostat. The measurements were carried out at a glassy carbon electrode in dichloromethane solutions containing 0.1 M tetrabutylammonium hexafluorophosphate as an electrolyte, Pt as the reference, and counter electrodes at a scan rate of 50 mV s^{-1} . Each measurement was calibrated with ferrocene (Fc). The oxidation potential was obtained as an average value between the anodic and cathodic potentials: $E_{1/2}^{\text{red/ox}} = 1/2(E_{\text{pc}} + E_{\text{pa}})$.

The fluorescence of the investigated compounds in PS (polystyrene) or neat films was initiated by a light-emitting diode ($\lambda = 365 \text{ nm}$; *Nichia NSHU590-B*) and measured by using a back-thinned charge-coupled device (CCD) spectrophotometer *PMA-11* (*Hamamatsu*). For these measurements, dilute

solutions of the investigated compounds were prepared by dissolving them in spectral-grade tetrahydrofuran ($c=10^{-6}$ M). PS films (with concentrations that ranged from 1 wt%) were prepared by mixing the dissolved compound with a solution of PS in tetrahydrofuran at the appropriate ratio and casted on glass substrates under ambient conditions. Drop casting from solutions in tetrahydrofuran ($c=10^{-3}$ M) was also employed to prepare neat films of the compounds. Aggregated particles were formed by the precipitation method, by mixing the H₂O/THF solution, ratio 10:1, with the researched materials dissolved in THF. The size was estimated with a *ZetaSizer* instrument. The QY values of the solutions were estimated by comparing the wavelength-integrated PL intensity of the compound solution to that of quinine sulfate in a 0.1 M aqueous solution of H₂SO₄ (QY=53%) as a reference. The optical densities of the reference and sample solutions were kept below 0.05 so that to avoid reabsorption effects. Estimated quantum yields of the investigated compound solutions were verified by using the integrated sphere method.

Photoelectrical measurements

The solid state ionization potential (I_p) of the layers of the synthesized compounds was measured by the electron photoemission in the air method at the Institute of Chemical Physics, Vilnius University. The samples for the ionization energy measurement were prepared by dissolving materials in THF, and these solutions were coated on Al plates that were pre-coated with a ~ 0.5 μm thick methylmethacrylate and methacrylic acid copolymer adhesive layer. The thickness of the transporting material layer was 0.5–1 μm . Usually, photoemission experiments are carried out in vacuum, and high vacuum is one of the main requirements for these measurements. If the vacuum is not high enough, the sample surface oxidation and gas adsorption influence the measurement results. In this case, however, the organic materials that were investigated were stable enough to oxygen, and the measurements could be carried out in the air. The samples were illuminated with monochromatic light from the quartz monochromator with a deuterium lamp. The power of the incident light beam was $(2-5)\cdot 10^{-8}$ W. The negative voltage of -300 V was supplied to the sample substrate. The counter-electrode with the 4.5×15 mm² slit for illumination was placed at an 8 mm distance from the sample surface. The counter-electrode was connected to the input of the BK2-16 type electrometer working in the open input regime for the photocurrent measurement. The 10^{-15} – 10^{-12} A strong photocurrent was flowing in the circuit under illumination. Photocurrent I is strongly dependent on the incident light photon energy $h\nu$. The $I^{0.5} = f(h\nu)$ dependence chart was plotted. Usually, the dependence of the photocurrent on the incident light quanta energy is well described by the linear relationship between $I^{0.5}$ and $h\nu$ near the threshold [251, 252]. The linear part of this dependence was extrapolated to the $h\nu$ axis, and the I_p value was determined as the photon energy at the interception point.

The hole drift mobility was measured by the xerographic time of flight technique (XTOF) [253, 254] at the Institute of Chemical Physics, Vilnius University. The samples for the hole mobility measurements were prepared by

spin-coating the solutions of the synthesized compounds or compositions of the synthesized compounds with bisphenol-Z polycarbonate (PC-Z) (*Iupilon Z-200* from *Mitsubishi Gas Chemical Co.*) at weight ratio 1:1 on polyester films with a conductive Al layer. The layer thickness was in the range of 5–11 μm . The electric field was created by positive corona charging. The charge carriers were generated at the layer surface by illumination with pulses of a nitrogen laser (the pulse duration was 2 ns, the wavelength was 337 nm). The layer surface potential decreases as a result of pulse illumination that was up to 1–5 % of the initial potential before the illumination. The capacitance probe that was connected to the wide frequency band electrometer measured the speed of the surface potential decrease dU/dt . The transit time t_t was determined by the kink on the curve of the dU/dt transient in the double logarithmic scale. The drift mobility was calculated by the formula $\mu = d^2/U_0 t_t$, where d is the layer thickness, and U_0 is the surface potential at the moment of illumination.

Regular Architecture Perovskite Device Fabrication and Measurements

Substrate preparation. FTO values on glass substrates (TEC 7, sheet resistance 7~8 ohms per square) were etched with zinc powder with 2 M hydrochloric acid (HCl) in order to produce device patterns. The substrates were cut into 28×28 mm square pieces. The substrates were subsequently sonicate-cleaned with 1 vol% (in deionized water) solution of *Decon 90* cleaning agent, and then, deionized water, acetone, and isopropanol for 10 minutes each. The substrates were dried with dry nitrogen. Then, the substrates were treated with oxygen-plasma cleaning for 15 minutes before use.

Tin oxide electron transport layer. SnOx nanocrystals in H₂O 15% colloidal dispersion were purchased from Alfa Aesar and diluted to 2% vol in de-ionized water. The solution was spin-coated onto FTO/glass at a spin rate of 4000 rpm for 30 sec. The substrates were annealed at 180 °C for 30 min. Before spinning the perovskite layer, the substrates were treated with UV-ozone for 10 minutes.

FACs perovskite layer. 1.45 M FA_{0.83}CS_{0.17}Pb(I_{0.9}Br_{0.1})₃ precursor solution was made by dissolving 64 mg CsI (*Alfa Aesar*), 80 mg PbBr₂ (TCI), 207 mg FAI (*Dyesol*), and 568 mg PbI₂ (TCI) into a 1 mL 4:1 ratio DMF:DMSO solvent mixture. The precursor solution was heated and stirred on a hotplate at 70 °C for 15 min under nitrogen atmosphere before use. Room temperature precursor solution 35 μL was deposited on FTO/SnO₂ substrate in a dry box at a spin speed of 6000 rpm for 35 sec (with a ramp speed of 2000 rpm/sec). 100 μL anisole was dropped at the center 10 sec before the end of spinning. Then, the samples were annealed on a hotplate at 100 °C for 15 min. The perovskite layer was deposited at approximately 5% relative humidity.

Hole transport layer and electrode deposition. The HTM 2,2',7,7'-tetrakis(*N,N'*-di-*p*-methoxyphenylamine)-9,9'-spirobifluorene (spiro-OMeTAD) was prepared by dissolving 85 mg of spiro-OMeTAD in 1 mL anhydrous chlorobenzene along with 20 μL Li-TFSI solution (500 mg/mL in acetonitrile) and 33 μL *t*BP. 50 μL of spiro-OMeTAD solution was dynamically spin-coated at 2500 rpm for 30 sec.

H32, H44-H46 solutions were prepared by dissolving 25 mg of HTM in 1 mL anhydrous chlorobenzene along with 20 μL Li-TFSI solution (129.2 mg/mL) to achieve 50 mol% Li-TFSI with respect to **H32** ($M_w=1760.15$ g/mol), **H44** ($M_w=1165.44$ g/mol), **H45** ($M_w=1153.39$ g/mol) and **H46** ($M_w=1151.41$ g/mol). 33 μL tBP was added to each solution. The solutions were stirred and heated at $\sim 60^\circ\text{C}$ overnight until the solute had completely dissolved. Then, the solutions were passed through a 0.22 μL polytetrafluoroethylene (PTFE) syringe filter. 50 μL of each solution was dynamically deposited onto the respective samples at 2500 rpm for 30 sec.

H33 and **H34** solutions were prepared by dissolving 25 mg of HTM in 1 mL anhydrous chlorobenzene along with 20 μL Li-TFSI solution (64.6 mg/mL) to achieve 25 mol% Li-TFSI with respect to **H33** ($M_w=1388.67$ g/mol) and **H34** ($M_w=1206.49$ g/mol). 33 μL tBP was added to each solution. The solutions were stirred and heated at $\sim 60^\circ\text{C}$ overnight until the solute had completely dissolved. Then, the solutions were passed through a 0.22 μL PTFE syringe filter. 50 μL of each solution was dynamically deposited onto the respective samples at 2500 rpm for 30 sec. The dopant-free solutions of these HTMs were prepared in a similar way only without the use of Li-TFSI and tBP.

Inverted Architecture Perovskite Device Fabrication and Measurements

Photolithographically patterned ITO-coated glass substrates were used as substrates. MoO_3 and 2,9-dimethyl-4,7-diphenyl-1,10-phenanthroline (BCP) were purchased from *Lumtec*, and fullerene (C_{60}) was purchased from *Sigma Aldrich*. $\text{CH}_3\text{NH}_3\text{I}$ (MAI) and PbI_2 were purchased from *Lumtec*. All materials were used as received.

ITO-coated glass substrates were subsequently cleaned with soap, water and isopropanol in an ultrasonic bath, followed by UV-ozone treatment. They were transferred to a vacuum chamber integrated into a nitrogen-filled glovebox (H_2O and $\text{O}_2 < 0.1$ ppm) and evacuated to a pressure of 10–6 mbar. The vacuum chamber used to sublime HTMs, ETL and MAPI was equipped with six temperature-controlled evaporation sources (*Creaphys*) fitted with ceramic crucibles. The sources were directed upward with an angle of approximately 90° with respect to the bottom of the evaporator. The substrate holder to evaporation source distance was approximately 20 cm. Three quartz crystal microbalance (QCM) sensors were used: two monitoring the deposition rate of each evaporation source and a third one close to the substrate holder monitoring the total deposition rate. The materials were sublimed, and the evaporation rate was controlled by separate QCM sensors obtaining precisely the deposited thickness. For the perovskite deposition, MAI and PbI_2 were coevaporated by measuring the deposition rate of each material in a different sensor and obtaining the total perovskite thickness in the third one, leading to a 500 nm-thick film. MoO_3 and Ag were evaporated in a third vacuum chamber by using tantalum boats and applying currents ranging from 2.0 to 4.8 \AA .

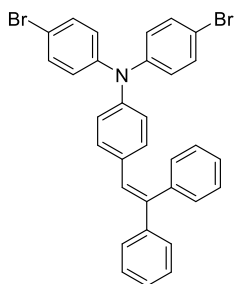
The J - V curves of the solar cells were recorded by using a *Keithley 2612A Source-Meter* with 0.01 V steps and integrating the signal for 20 ms after a 10 ms

delay, corresponding to a speed of about 0.3 V s^{-1} . The devices were illuminated under a *Wavelabs Sinus 70* LED solar simulator. The light intensity was calibrated before every measurement by using a calibrated Si reference diode. Solar cell stability measurements were recorded by using a maximum power point tracking system, with a white LED light source at 1 sun equivalent, developed by *Candlelight*. During the stability measurements, the encapsulated devices were exposed to a flow of N_2 gas; temperature was stabilized at 300 K during the entire measurement by using a water-circulating cooling system controlled by a Peltier element; J - V curves were recorded every 10 min.

4.2. Materials

The anhydrous solvents, later used for reactions, were prepared by standard procedures. Chemicals were purchased from *Sigma-Aldrich* and *TCI Europe* and used as received without further purification. Synthesis of compounds **H1**, **H4** and **H7** was conducted in a *CEM Discover Synthesis Unit* (*CEM Corp.*, Matthews NC) microwave reactor (MWR). OBDA was synthesized according to the procedure reported earlier [249]. The course of the reactions was monitored by TLC (thin layer chromatography) on *ALUGRAM SIL G/UV254* plates and developed with UV light. Silica gel (grade 9385, 230–400 mesh, 60 Å, *Aldrich*) was used for column chromatography.

4-bromo-N-(4-bromophenyl)-N-[4-(2,2-diphenylethenyl)phenyl]aniline (1)



A mixture of 4,4'-dibromotriphenylamine (5 g, 12.4 mmol), diphenylacetaldehyde (2.92 g, 14.9 mmol) and camphor-10-sulfonic acid (β) (2.28 g, 12.4 mmol) was dissolved in toluene (30 ml + the volume of the Dean-Stark trap). The mixture was heated for 16 hours at reflux. At the end of the reaction (TLC control *n*-hexane), the mixture was cooled to room temperature, diluted with water and extracted three times with ethyl acetate ($3 \times 250 \text{ mL}$). The organic layer was dried over anhydrous Na_2SO_4 , filtered, and the solvent was removed. The crude

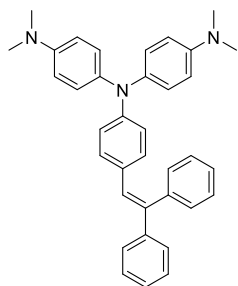
product was purified by column chromatography (*n*-hexane) to give **1** as a yellow amorphous powder. Yield: 3.6 g (50%).

$^1\text{H NMR}$ (CDCl_3 , 400MHz): δ 7.39–7.18 (m, 14H, Ph), 6.93–6.85 (m, 7H, Ph), 6.78 (d, $J = 8.7 \text{ Hz}$, 2H, Ph).

$^{13}\text{C NMR}$ (CDCl_3 , 101MHz): δ 146.18, 145.40, 143.34, 141.52, 140.51, 132.45, 132.38, 130.61, 130.20, 128.85, 128.25, 127.52, 127.42, 127.39, 127.26, 125.79, 123.12, 115.78.

Anal. calcd. for $\text{C}_{32}\text{H}_{23}\text{NBr}_2$, %: C 66.05; H 3.96; N 2.41, found, %: 65.82; H 4.11; N 2.29.

*N*¹-[4-(dimethylamino)phenyl]-*N*¹-[4-(2,2-diphenylethenyl)phenyl]-*N*⁴,*N*⁴-dimethylbenzene-1,4-diamine (**H1**)



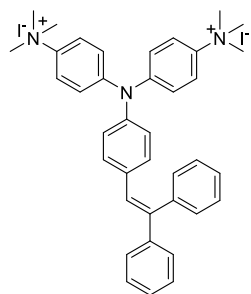
A mixture of **1** (0.3 g, 0.52 mmol), dimethyl amine hydrochloride (0.126 g, 1.5 mmol), XPhos-Pd-G2 precatalyst (0.005 g, 0.0063 mmol) and sodium *tert*-butoxide (0.3 g, 3.12 mmol) was dissolved in anhydrous dioxane (3.5 ml) under argon atmosphere. The reaction was conducted in a microwave reactor for 3 hours (130 °C, power 200 W, pressure 3 atm.). At the end of the reaction (TLC control 1/49 v/v THF/*n*-hexane), the reaction mixture was cooled to room temperature and filtered through a layer of celite. The crude product was purified by column chromatography (1/49 v/v THF/*n*-hexane) to give **H1** as bright yellow crystals (m. p. 165–167 °C). Yield: 0.11 g (43%).

¹H NMR (DMSO-*d*₆, 700MHz): δ 7.41 (t, *J* = 7.6 Hz, 2H, Ph), 7.34 (t, *J* = 7.4 Hz, 1H, Ph), 7.32–7.27 (m, 2H, Ph), 7.24 (d, *J* = 7.4 Hz, 2H, Ph), 7.22 (d, *J* = 7.2 Hz, 1H, Ph), 7.15 (d, *J* = 6.9 Hz, 2H, Ph), 6.95–6.86 (m, 6H, Ph), 6.70 (d, *J* = 8.9 Hz, 2H, Ph), 6.68 (d, *J* = 9.0 Hz, 3H, Ph), 6.37 (d, *J* = 8.9 Hz, 2H, Ph), 2.85 (s, 12H, CH₃).

¹³C NMR (DMSO-*d*₆, 176MHz): δ 151.45, 147.96, 147.60, 142.77, 140.56, 139.16, 137.73, 135.72, 129.99, 129.67, 129.04, 128.25, 128.01, 127.43, 127.32, 127.02, 126.85, 126.77, 126.46, 124.89, 116.08, 113.44, 30.41.

Anal. calcd. for C₃₆H₃₅N₃, %: C 84.75; H 6.87; N 8.38, found, %: C 84.46; H 6.99; N 8.55.

4,4'-[[4-(2,2-diphenylethenyl)phenyl]azanediyl]bis(*N,N,N*-trimethylanilinium) diiodide (**H2**)



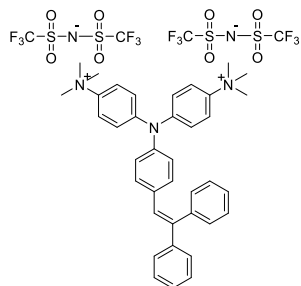
Tertiary amine **H1** (0.58 g, 1.14 mmol) and methyl iodide (0.165 g, 1.14 mmol) were dissolved in anhydrous DMF (3 ml). The reaction was conducted at room temperature for 24 hours. Afterwards (TLC control 1/4 v/v THF/methanol), the reaction mixture was poured into 60 ml of diethyl ether and was cooled to -5 °C for 1 hour, forming crystals which later on were filtered, giving **H2** as white crystals (m. p. 182–184 °C). Yield: 0.7 g (78%)

¹H NMR (mixture of CDCl₃ & Methanol-*d*₄ 1:1, 700 MHz): δ 7.79 (d, *J* = 9.2 Hz, 4H, Ph), 7.38 (t, *J* = 7.3 Hz, 2H, Ph), 7.36 – 7.27 (m, 6H, Ph), 7.23 (d, *J* = 8.6 Hz, 6H, Ph), 7.04 (d, *J* = 8.5 Hz, 2H, Ph), 6.98 (s, 1H, CH), 6.89 (d, *J* = 8.4 Hz, 2H, Ph), 3.70 (s, 18H, CH₃).

¹³C NMR (mixture of CDCl₃ & Methanol-*d*₄ 1:1, 176MHz): δ 152.12, 147.61, 147.04, 146.87, 145.07, 144.20, 139.10, 135.04, 133.94, 132.66, 132.04, 131.47, 131.22, 130.42, 129.25, 128.01, 127.98, 125.23, 125.12, 61.10, 34.10.

Anal. calcd. for C₃₈H₄₁N₃I₂, %: 57.46; H 5.17; N 5.29, found, %: 57.31; H 5.33; N 5.43.

4,4'-[[4-(2,2-diphenylethenyl)phenyl]azanediyl]bis(*N,N,N*-trimethylanilinium) bis[bis(trifluoromethanesulfonyl)azanide] (**H3**)



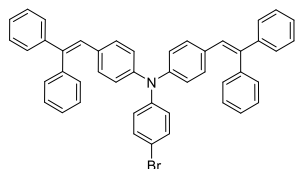
Iodine salt **H2** (0.45 g, 0.57 mmol) and LiTFSI (0.2 g, 0.68 mmol) were dissolved in a mixture of DCM (2 ml) and methanol (0.4 ml). The reaction was conducted at room temperature for 16 hours. At the end of the reaction (TLC control 1/4 v/v THF/methanol), the mixture was diluted with distilled water and extracted three times with DCM (3 × 50 mL), the solvent was removed giving pure product **H3** as a white amorphous powder (0.35 g, 56%).

¹H NMR (mixture of CDCl₃ & Methanol-d₄ 1:1, 700 MHz): δ 7.71 (d, *J* = 9.4 Hz, 4H, Ph); 7.38 (t, *J* = 7.3 Hz, 3H, Ph), 7.35–7.31 (m, 5H, Ph), 7.22 (d, *J* = 9.4 Hz, 6H, Ph), 7.04 (d, *J* = 8.6 Hz, 2H, Ph), 6.98 (s, 1H, CH), 6.89 (d, *J* = 8.6 Hz, 2H, Ph), 3.64 (s, 18H, CH₃).

¹³C NMR (mixture of CDCl₃ & Methanol-d₄ 1:1, 176MHz): δ 152.18, 147.61, 147.03, 146.88, 145.04, 144.21, 139.09, 135.03, 133.95, 132.64, 132.04, 131.46, 131.22, 130.44, 130.42, 129.19, 128.00, 124.95, 124.61, 122.79, 60.87.

Anal. calcd. for C₄₂H₄₁N₅F₁₂S₄O₈, %: C 45.81; H 3.73; N 6.36, found, %: 46.05; H 3.88; N 6.12.

4-bromo-*N,N*-bis[4-(2,2-diphenylethenyl)phenyl]aniline (**2**)



A mixture of 4-bromotriphenylamine (5 g, 15.4 mmol), diphenylacetaldehyde (6.66 g, 34 mmol) and camphor-10-sulfonic acid (β) (3.58 g, 15.4 mmol) was dissolved in toluene (30 ml + the volume of the Dean-Stark trap). The mixture was heated for 18 hours at reflux. After reaction was terminated (TLC control *n*-hexane), the

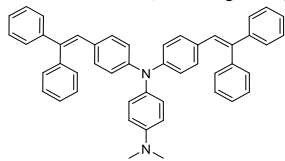
mixture was cooled to room temperature, diluted with water and extracted three times with ethyl acetate (3 × 300 mL). The organic layer was dried over anhydrous Na₂SO₄, filtered, and the solvent was removed. The crude product was purified by column chromatography (*n*-hexane) to give **2** as a yellowish amorphous powder. Yield: 4.47 g (39%).

¹H NMR (700 MHz, CDCl₃) δ 7.35–7.33 (m, 4H, Ph), 7.31–7.27 (m, 12H, Ph), 7.25–7.21 (m, 6H, Ph), 6.89–6.85 (m, 8H, Ph), 6.76 (d, *J* = 8.7 Hz, 4H, Ph).

¹³C NMR (176 MHz, CDCl₃) δ 146.27, 145.51, 143.38, 141.28, 140.54, 132.18, 130.45, 130.19, 128.77, 128.18, 127.41, 127.34, 127.30, 125.89, 123.24, 115.47.

Anal. calcd. for C₄₆H₃₄BrN, %: C 81.17; H 5.03; N 2.06, found, %: C 81.33; H 5.14; N 1.89.

*N*¹,*N*¹-bis[4-(2,2-diphenylethenyl)phenyl]-*N*⁴,*N*⁴-dimethylbenzene-1,4-diamine (**H4**)



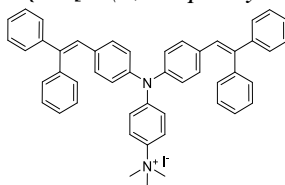
A mixture of **2** (0.3 g, 0.44 mmol), dimethyl amine hydrochloride (0.054 g, 0.66 mmol), XPhos-Pd-G2 precatalyst (0.007 g, 0.0088 mmol) and sodium *tert*-butoxide (0.123 g, 1.32 mmol) was dissolved in anhydrous dioxane (3.5 ml) under argon atmosphere. The reaction was conducted in a microwave reactor for 3 hours (130 °C, power 200 W, pressure 3 atm.). Afterwards (TLC control 1/49 v/v THF/*n*-hexane), the reaction mixture was cooled to room temperature and filtered through a layer of celite. The crude product was purified by column chromatography (1/49 v/v THF/*n*-hexane) to give **H4** as a yellowish amorphous powder. Yield: 0.12 g (42%).

¹H NMR (700 MHz, DMSO-*d*₆) δ 7.42 (dd, *J* = 10.3, 4.6 Hz, 4H, Ph), 7.38–7.35 (m, 2H, Ph), 7.34–7.30 (m, 4H, Ph), 7.28–7.24 (m, 6H, Ph), 7.16–7.15 (m, 4H, Ph), 6.99 (s, 2H, CH), 6.87–6.86 (m, 2H, Ph), 6.82 (d, *J* = 8.8 Hz, 4H, Ph), 6.69–6.68 (m, 2H, Ph), 6.61 (d, *J* = 8.8 Hz, 4H, Ph), 2.87 (s, 6H, CH₃).

¹³C NMR (176 MHz, DMSO-*d*₆) δ 148.61, 146.47, 143.06, 140.73, 139.93, 135.09, 130.62, 130.46, 130.10, 129.54, 128.78, 128.37, 127.97, 127.67, 127.59, 127.16, 121.18, 113.92, 40.67.

Anal. calcd. for C₄₈H₄₀N₂, %: C 89.40; H 6.25; N 4.34, found, %: C 89.65; H 6.13; N 4.22.

4-{bis[4-(2,2-diphenylethenyl)phenyl]amino}-*N,N,N*-trimethylanilinium iodide



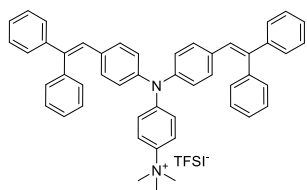
(**H5**) Tertiary amine **H4** (0.32 g, 0.5 mmol) and methyl iodide (0.142 g, 1 mmol) were dissolved in anhydrous DMF (6 ml). The reaction was conducted at room temperature for 24 hours. Afterwards (TLC control 1/4 v/v THF/methanol), the reaction mixture was poured into 60 ml of diethyl ether and was cooled to -5 °C for 1 hour, forming crystals which later on were filtered, giving yellow crystals (m. p. 143–145 °C). Yield: 0.38 g (98.3%).

¹H NMR (700 MHz, CDCl₃) δ 7.65 (d, *J* = 9.4 Hz, 2H, Ph), 7.36 (t, *J* = 7.3 Hz, 4H, Ph), 7.33–7.29 (m, 10H, Ph), 7.28–7.26 (m, 2H, Ph), 7.23–7.22 (m, 4H, Ph), 7.06 (d, *J* = 9.4 Hz, 2H, Ph), 6.92–6.90 (m, 6H, Ph), 6.80 (d, *J* = 8.6 Hz, 4H, Ph), 3.95 (s, 9H, CH₃).

¹³C NMR (176 MHz, CDCl₃) δ 149.12, 144.34, 143.23, 142.21, 140.35, 139.70, 133.86, 130.79, 130.17, 128.84, 128.23, 127.54, 127.50, 127.43, 127.04, 124.63, 122.20, 120.51, 57.93.

Anal. calcd. for C₄₉H₄₃IN₂, %: C 74.80; H 5.51; N 3.56, found, %: C 74.59; H 5.38; N 3.70.

4-{bis[4-(2,2-diphenylethenyl)phenyl]amino}-*N,N,N*-trimethylanilinium
bis(trifluoromethanesulfonyl)azanide (**H6**)



H5 (0.28 g, 0.36 mmol) and LiTFSI (0.123 g, 0.43 mmol) were dissolved in a mixture of DCM (2 ml) and methanol (2 ml). The reaction was conducted at room temperature for 16 hours. Afterwards (TLC control 1/4 v/v THF/methanol), the mixture was diluted with water and extracted three times with DCM (3×50 mL), the solvent was removed giving the pure product

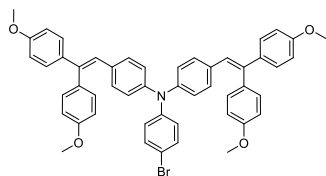
H6 as a yellow amorphous powder (0.31 g, 94%).

$^1\text{H NMR}$ (700 MHz, CDCl_3) δ 7.38–7.29 (m, 18H, Ph), 7.22–7.21 (m, 4H, Ph), 7.05–7.03 (m, 2H, Ph), 6.94–6.91 (m, 6H, Ph), 6.81 (d, $J = 8.6$ Hz, 4H, Ph), 3.59 (s, 9H, CH_3).

$^{13}\text{C NMR}$ (176 MHz, CDCl_3) δ 144.19, 143.19, 142.34, 140.33, 134.03, 130.81, 130.16, 128.82, 128.24, 127.55, 127.43, 127.00, 124.68, 124.60, 122.10, 119.81, 57.71.

Anal. calcd. for $\text{C}_{51}\text{H}_{43}\text{F}_6\text{N}_3\text{O}_4\text{S}_2$, %: C 65.16; H 4.61; N 4.47, found, %: C 64.94; H 4.49; N 4.66.

4-[2,2-bis(4-methoxyphenyl)ethenyl]-*N*-{4-[2,2-bis(4-methoxyphenyl)ethenyl]phenyl}-*N*-(4-bromophenyl)aniline (**3**)



4-bromo-*N,N*-diphenylaniline (5 g, 15.4 mmol), 2,2-bis(4-methoxyphenyl)acetaldehyde (8.69 g, 33.9 mmol) and camphor-10-sulfonic acid (β) (3.58 g, 15.4 mmol) were dissolved in toluene (40 ml + the volume of the Dean-Stark trap). The mixture was heated for 24 hours at reflux. Afterwards (TLC

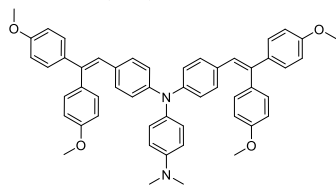
control 2/23 v/v acetone/*n*-hexane) the mixture was cooled to room temperature, diluted with water and extracted three times with ethyl acetate (3×400 mL). The organic layer was dried over anhydrous Na_2SO_4 , filtered, and the solvent was removed. The crude product was purified by column chromatography (2/23 v/v acetone/*n*-hexane) to give **3** as a yellowish green amorphous powder. Yield: 4.94 g (40%).

$^1\text{H NMR}$ (700 MHz, $\text{DMSO}-d_6$) δ 7.52–7.36 (m, 2H, Ph), 7.28–7.12 (m, 4H, Ph), 7.10–6.78 (m, 21H, Ph), 6.76–6.69 (m, 2H, Ph), 6.68 (d, $J = 8.6$ Hz, 1H, Ph), 3.79–3.70 (m, 12H, OCH_3).

$^{13}\text{C NMR}$ (176 MHz, $\text{DMSO}-d_6$) δ 159.26, 159.03, 145.08, 140.41, 135.91, 131.30, 130.91, 130.66, 128.64, 125.99, 125.90, 125.86, 125.76, 123.56, 114.84, 114.16, 55.60, 55.47.

Anal. calcd. for $\text{C}_{50}\text{H}_{42}\text{BrNO}_4$, %: C 74.99; H 5.29; N 1.75, found, %: C 75.28; H 5.16; N 1.62.

*N*¹,*N*¹-bis{4-[2,2-bis(4-methoxyphenyl)ethenyl]phenyl}-*N*⁴,*N*⁴-dimethylbenzene-1,4-diamine (**H7**)



Compound **3** (0.3 g, 0.38 mmol), dimethyl amine hydrochloride (0.046 g, 0.56 mmol), XPhos-Pd-G2 precatalyst (0.006 g, 0.0075 mmol) and sodium *tert*-butoxide (0.108 g, 1.32 mmol) were dissolved in anhydrous dioxane (3 ml) under argon atmosphere.

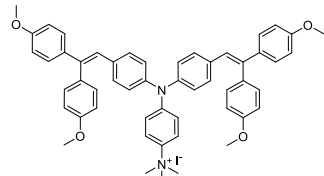
The reaction was conducted in a microwave reactor for 3 hours (130 °C, power 200 W, pressure 3 atm.). Afterwards (TLC control 1/4 v/v THF/*n*-hexane), the reaction mixture was cooled to room temperature and filtered through a layer of celite. The crude product was purified by column chromatography (1/4 v/v THF/*n*-hexane) to give **H7** as a yellowish powder. Yield: 0.115 g (40%).

¹H NMR (700 MHz, DMSO-*d*₆) δ 7.19–7.17 (m, 2H, Ph), 7.06–7.04 (m, 5H, Ph), 6.98–6.95 (m, 5H, Ph), 6.90–6.82 (m, 12H, Ph), 6.76–6.68 (m, 4H, Ph), 6.62 (d, *J* = 8.7 Hz, 2H, Ph), 3.78–3.75 (m, 12H, OCH₃), 2.89–2.88 (m, 6H, CH₃).

¹³C NMR (176 MHz, DMSO-*d*₆) δ 159.12, 158.96, 146.13, 139.37, 136.05, 132.84, 131.46, 131.33, 130.97, 130.81, 130.33, 128.50, 128.29, 125.59, 121.23, 114.86, 114.16, 55.61, 55.49, 49.07.

Anal. calcd. for C₅₂H₄₈N₂O₄, %: C 81.65; H 6.32; N 3.66, found, %: C 81.39; H 6.24; N 3.75.

4-(bis{4-[2,2-bis(4-methoxyphenyl)ethenyl]phenyl}amino)-*N,N,N*-trimethylanilinium iodide (**H8**)



A mixture of triphenylamine derivative **H7** (0.36 g, 0.47 mmol) and methyl iodide (0.233 g, 1.65 mmol) was dissolved in anhydrous DMF (6.5 ml). The reaction was conducted at room temperature for 18 hours. Afterwards (TLC control 1/4 v/v THF/methanol), the reaction mixture was poured into

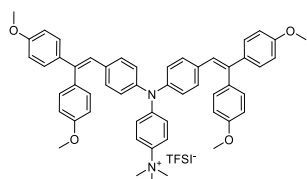
65 ml of diethyl ether and was cooled to -5 °C for 1 hour, forming crystals which were filtered giving yellowish crystals (m. p. 128–130 °C). Yield: 0.42 g (99.3%).

¹H NMR (700 MHz, CDCl₃) δ 7.29–7.21 (m, 5H, Ph), 7.17–7.09 (m, 6H, Ph), 7.06 (d, *J* = 9.3 Hz, 1H, Ph), 6.98–6.92 (m, 5H, Ph), 6.90–6.76 (m, 13H, Ph), 3.99–3.91 (m, 9H, CH₃), 3.85–3.80 (m, 12H, OCH₃).

¹³C NMR (176 MHz, CDCl₃) δ 162.54, 159.26, 159.00, 149.27, 143.94, 141.48, 139.43, 136.26, 134.41, 132.70, 131.57, 131.41, 130.75, 130.66, 130.58, 128.71, 125.15, 124.72, 121.94, 120.38, 114.19, 113.59, 57.92, 55.34, 55.29, 55.24, 55.18.

Anal. calcd. for C₅₃H₅₁IN₂O₄, %: C 70.19; H 5.67; N 3.09, found, %: C 70.01; H 5.42; N 3.24.

4-(bis[4-[2,2-bis(4-methoxyphenyl)ethenyl]phenyl]amino)-N,N,N-trimethylanilinium bis(trifluoromethanesulfonyl)azanide (H9)



Iodine salt **H9** (0.2 g, 0.22 mmol) and LiTFSI (0.076 g, 0.264 mmol) were dissolved in a mixture of DCM (3 ml) and methanol (3 ml). The reaction was conducted at room temperature for 24 hours. Afterwards (TLC control 1/4 v/v THF/methanol), the mixture was diluted with water and extracted three

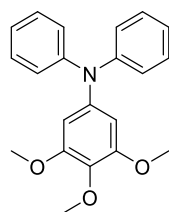
times with DCM (3 × 50 mL), the solvent was removed thus giving pure product **H9** as a dark green amorphous powder. Yield: 0.21 g (90%).

¹H NMR (700 MHz, CDCl₃) δ 7.37–7.34 (m, 2H, Ph), 7.14–7.11 (m, 5H, Ph), 7.02–7.01 (m, 3H, Ph), 7.00–6.94 (m, 6H, Ph), 6.90–6.87 (m, 6H, Ph), 6.86–6.80 (m, 6H, Ph), 6.70–6.66 (m, 2H, Ph), 3.83–3.80 (m, 12H, OCH₃), 3.64–3.60 (m, 9H, CH₃).

¹³C NMR (176 MHz, CDCl₃, ppm) δ 159.30, 159.03, 149.64, 149.54, 143.75, 141.65, 136.21, 134.64, 132.67, 131.55, 131.40, 130.76, 130.66, 130.62, 128.72, 125.08, 124.80, 121.79, 119.70, 114.17, 113.61, 57.77, 55.34, 55.24, 55.18.

Anal. calcd. for C₅₆H₅₁F₆N₃O₈S₂, %: C 62.50; H 5.15; N 3.90, found, %: C 62.38; H 5.02; N 4.00.

3,4,5-trimethoxy-N,N-diphenylaniline (4)



A mixture of diphenylamine (1 g, 5.0 mmol), 5-bromo-1,2,3-trimethoxybenzene (1.48 g, 6.0 mmol), palladium(II) acetate (0.056 g, 0.25 mmol), tri-*tert*-butylphosphonium tetrafluoroborate (0.217 g, 0.75 mmol) and sodium *tert*-butoxide (1.44 g, 15.0 mmol) was dissolved in anhydrous toluene (7 ml) under argon atmosphere. The mixture was heated for 3 hours at reflux (TLC control 7/18 v/v diethyl ether/*n*-hexane). Afterwards, the reaction

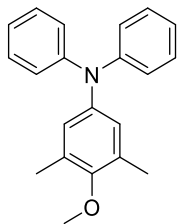
mixture was cooled to room temperature and filtered through a layer of celite. The crude product was purified by column chromatography (7/18 v/v diethyl ether/*n*-hexane) to give **4** as white crystals (m. p. 117–119 °C). Yield: 1.14 g (68%).

¹H NMR (400 MHz, Acetone-*d*₆) δ 7.28 (t, *J* = 7.8 Hz, 4H, Ph), 7.11–6.94 (m, 6H, Ph), 6.39 (s, 2H, Ph), 3.73 (s, 3H, OCH₃), 3.68 (s, 6H, OCH₃).

¹³C NMR (101 MHz, Acetone-*d*₆) δ 154.15, 147.90, 143.50, 135.09, 129.16, 123.39, 122.41, 103.20, 59.77, 55.50.

Anal. calcd. for C₂₁H₂₁NO₃, %: C 75.20; H 6.31; N 4.18, found, %: C 75.33; H 6.42; N 3.94.

4-methoxy-3,5-dimethyl-*N,N*-diphenylaniline (**5**)



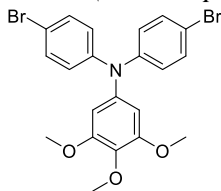
A mixture of diphenylamine (0.3 g, 1.5 mmol), 4-bromo-2,6-dimethylanisole (0.35 g, 1.6 mmol), palladium(II) acetate (0.017 g, 0.07 mmol), tri-*tert*-butylphosphonium tetrafluoroborate (0.065 g, 0.22 mmol) and sodium *tert*-butoxide (0.43 g, 4.5 mmol) was dissolved in anhydrous toluene (5 ml) under argon atmosphere. The mixture was heated for 5 hours at reflux (TLC control 3/22 v/v diethyl ether/*n*-hexane). Afterwards, the reaction mixture was cooled to room temperature and filtered through a layer of celite. The crude product was purified by column chromatography (3/22 v/v diethyl ether/*n*-hexane) to give **5** as white crystals (m. p. 113–115 °C). Yield: 0.32 g (71%).

¹H NMR (400 MHz, CDCl₃) δ 7.26 (dd, *J* = 15.4, 7.0 Hz, 4H, Ph), 7.07 (d, *J* = 7.7 Hz, 4H, Ph), 6.99 (t, *J* = 7.3 Hz, 2H, Ph), 6.79 (s, 2H, Ph), 3.75 (s, 3H, OCH₃), 2.23 (s, 6H, CH₃).

¹³C NMR (101 MHz, CDCl₃) δ 153.17, 148.16, 143.10, 131.67, 129.07, 125.61, 123.43, 122.00, 59.84, 16.18.

Anal. calcd. for C₂₁H₂₁NO, %: C 83.13; H 6.98; N 4.62, found, %: C 83.41; H 6.85; N 4.47.

N,N-bis(4-bromophenyl)-3,4,5-trimethoxyaniline (**6**)



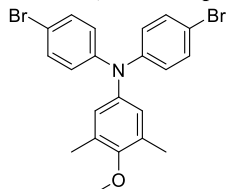
A mixture of **4** (0.3 g, 0.9 mmol) and *N*-bromosuccinimide (0.32 g, 1.8 mmol) was dissolved in DCM (3 ml). The mixture reacted for 12 hours at room temperature (TLC control 1/9 v/v diethyl ether/*n*-hexane). Afterwards (TLC control 1/9 v/v diethyl ether/*n*-hexane), the reaction mixture was diluted with water and extracted three times with DCM (3 × 50 mL). The organic layer was dried over anhydrous Na₂SO₄, filtered, and the solvent was removed. The crude product was purified by column chromatography (1/9 v/v diethyl ether/*n*-hexane) to give **6** as a greenish solid. Yield: 0.36 g (81%).

¹H NMR (400 MHz, DMSO-*d*₆) δ 7.44 (d, *J* = 8.7 Hz, 4H, Ph), 6.94 (d, *J* = 8.7 Hz, 4H, Ph), 6.38 (s, *J* = 9.1 Hz, 2H, Ph), 3.68–3.62 (m, 9H, OCH₃).

¹³C NMR (101 MHz, DMSO-*d*₆) δ 154.21, 146.63, 142.32, 135.44, 132.67, 125.06, 114.66, 104.08, 60.56, 56.40.

Anal. calcd. for C₂₁H₁₉Br₂NO₃, %: C 51.14; H 3.88; N 2.84, found, %: C 51.26; H 4.01; N 2.61.

N,N-bis(4-bromophenyl)-4-methoxy-3,5-dimethylaniline (**7**)



A mixture of **5** (0.1 g, 0.3 mmol) and *N*-bromosuccinimide (0.12 g, 0.7 mmol) was dissolved in DCM (3 ml). The mixture reacted for 12 hours at room temperature (TLC control 1/49 v/v THF/*n*-hexane). Afterwards, the reaction mixture was diluted with water and extracted three times with DCM (3 × 50 mL). The organic layer was dried over

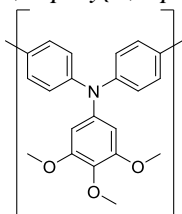
anhydrous Na₂SO₄, filtered, and the solvent was removed. The crude product was purified by column chromatography (1/49 v/v THF/*n*-hexane) to give **7** as a greenish solid. Yield: 0.13 g (85%).

¹H NMR (400 MHz, Acetone-*d*₆) δ 7.44–7.37 (m, 4H, Ph), 6.98 – 6.91 (m, 4H, Ph), 6.81 (s, 2H, Ph), 3.73 (s, 3H, OCH₃), 2.21 (s, 6H, CH₃).

¹³C NMR (101 MHz, Acetone-*d*₆) δ 154.26, 147.03, 142.02, 132.22, 132.17, 126.18, 124.70, 114.21, 59.08, 15.35.

Anal. calcd. for C₂₁H₁₉Br₂NO, %: C 54.69; H 4.15; N 3.04, found, %: C 54.92; H 4.03; N 2.93.

α, ω-poly{1,4-phenylene[(3,4,5-trimethoxyphenyl)azanediyl]-1,4-phenylene} (**H10**)

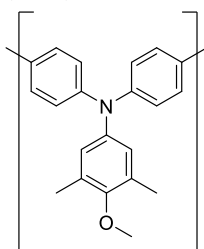


NiCl₂ (0.002 g, 0.02 mmol), zinc powder (0.16 g, 2.4 mmol), 2,2'-bipyridine (0.003 g, 0.02 mmol) and triphenylphosphine (0.15 g, 0.57 mmol) were dispersed in anhydrous and degassed DMA (2 ml) under argon atmosphere. The mixture was stirred for 1 h; during this time, the color changed from grey to brown. Monomer **6** (0.4 g, 0.8 mmol) was added, and the mixture was heated at 80 °C for 14 hours. Afterwards, chlorobenzene (1 ml)

was added, and stirring was continued for another 2 hours. After the termination of the reaction, the solution was diluted with water and extracted three times with chloroform (3 × 100 mL), the organic layer was dried over anhydrous Na₂SO₄, filtered, the solvent was removed, and the residue was filtered through a short (5 cm) silica gel column. The polymer was precipitated from THF to 10-fold excess of methanol 3 times to give **H1** as a yellow solid. Yield 0.01 g (4%).

\overline{Mn} =380 g/mol; \overline{Mw} =1611 g/mol; $\overline{Mw}/\overline{Mn}$ =4.24

α, ω-poly{1,4-phenylene[(4-methoxy-3,5-dimethylphenyl)azanediyl]-1,4-phenylene} (**H11**)

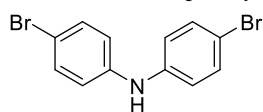


NiCl₂ (0.012 g, 0.09 mmol), zinc powder (0.26 g, 4.0 mmol), 2,2'-bipyridine (0.023 g, 0.15 mmol) and triphenylphosphine (0.24 g, 0.9 mmol) were dispersed in anhydrous and degassed DMF (2 ml) under argon atmosphere. The mixture was stirred for 1 h; during this time, the color changed from grey to brown. Monomer **7** (0.3 g, 0.65 mmol) was added, and the mixture was heated at 80 °C for 14 hours. Afterwards, chlorobenzene (1 ml) was added, and stirring was continued for another 2 hours.

After the termination of the reaction, the solution was diluted with water and extracted three times with chloroform (3 × 100 mL), the organic layer was dried over anhydrous Na₂SO₄, filtered, the solvent was removed, and the residue was filtered through a short (5 cm) silica gel column. The polymer was precipitated from THF to 10-fold excess of methanol 3 times to give **H11** as a yellow solid. Yield: 0.011 g (5%).

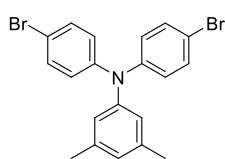
\overline{Mn} =1101 g/mol; \overline{Mw} =3630 g/mol; $\overline{Mw}/\overline{Mn}$ =3.23

4,4'-Dibromodiphenylamine (**8**)



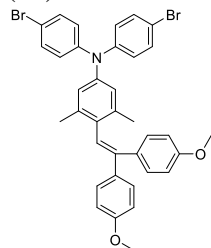
Was synthesized according to an earlier reported procedure [255].

N,N-bis(4-bromophenyl)-3,5-dimethylaniline (**9**)



Was synthesized according to an earlier reported procedure [18].

4-[2,2-bis(4-methoxyphenyl)ethenyl]-*N,N*-bis(4-bromophenyl)-3,5-dimethylaniline (**10**)



A mixture of **9** (0.1 g, 0.23 mmol), 2,2-bis(4-methoxyphenyl)acetaldehyde (0.07 g, 0.26 mmol), and camphor-10-sulfonic acid (0.054 g, 0.23 mmol) was dissolved in toluene (3 ml + the volume of the Dean-Stark trap). The mixture was heated for 8 hours at reflux (TLC control 1/9 v/v acetone/*n*-hexane). Afterwards, the reaction mixture was cooled to room temperature, diluted with water and extracted three times with ethyl acetate

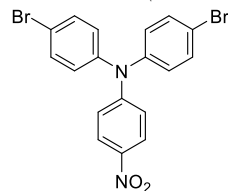
(3 × 50 mL). The organic layer was dried over anhydrous Na₂SO₄, filtered, and the solvent was removed. The crude product was purified by column chromatography (1/9 v/v acetone/*n*-hexane) to give **10** as a yellowish solid. Yield: 0.07 g (47%).

¹H NMR (400 MHz, CDCl₃) δ 7.42–7.23 (m, 6H, Ph), 7.03–6.97 (m, 5H, Ph), 6.93–6.83 (m, 4H, Ph), 6.81 (s, 2H, Ph), 6.70 (d, *J* = 8.8 Hz, 2H, Ph), 3.80 (d, *J* = 12.8 Hz, 6H, OCH₃), 1.94 (s, 6H, CH₃).

¹³C NMR (101 MHz, CDCl₃) δ 159.02, 158.44, 146.64, 145.64, 138.15, 136.76, 135.31, 133.85, 132.32, 130.48, 129.58, 126.90, 125.96, 125.26, 124.23, 115.12, 113.95, 113.57, 55.33, 55.21, 19.96.

Anal. calcd. for C₃₆H₃₁Br₂NO₂, %: C 64.59; H 4.67; N 2.09, found, %: C 64.83; H 4.56; N 1.97.

4-bromo-*N*-(4-bromophenyl)-*N*-(4-nitrophenyl)aniline (**11**)



A mixture of 4,4'-dibromotriphenylamine (0.5 g, 1.2 mmol) and Cu(NO₃)₂ (0.12 g, 0.6 mmol) was dissolved in acetic anhydride (10 ml). The mixture reacted for 2 hours at room temperature (TLC control 4/21 v/v acetone/*n*-hexane). Afterwards, the reaction mixture was diluted with distilled water and DCM (7:1) and stirred overnight. After that, the mixture was filtered and washed with distilled water to give **8** as an orange powder

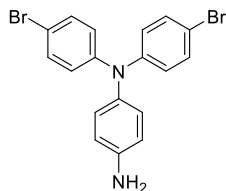
(m. p. 219–221 °C). Yield: 0.5 g (90%).

^1H NMR (400 MHz, CDCl_3) δ 8.07 (d, $J = 9.2$ Hz, 2H, Ph), 7.48 (d, $J = 8.6$ Hz, 4H, Ph), 7.09–6.88 (m, 6H, Ph).

^{13}C NMR (101 MHz, CDCl_3) δ 152.56, 144.55, 141.21, 133.18, 127.65, 125.56, 119.29, 118.86.

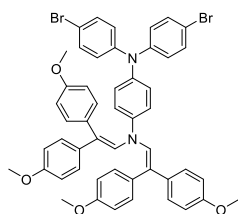
Anal. calcd. for $\text{C}_{18}\text{H}_{12}\text{Br}_2\text{N}_2\text{O}_3$, %: C 48.25; H 2.70; N 6.25, found, %: C 48.41; H 2.59; N 6.12.

4-Amino-4',4''-dibromotriphenylamine (**12**)



Was synthesized according to an earlier reported procedure [256].

N^1, N^1 -bis[2,2-bis(4-methoxyphenyl)ethenyl]- N^4, N^4 -bis(4-bromophenyl)benzene-1,4-diamine (**13**)



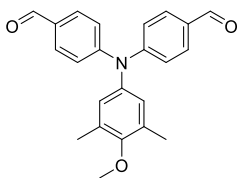
A mixture of **12** (0.1 g, 0.24 mmol), 2,2-bis(4-methoxyphenyl)acetaldehyde (0.14 g, 0.5 mmol), and camphor-10-sulfonic acid (0.06 g, 0.24 mmol) was dissolved in toluene (3 ml + the volume of the Dean-Stark trap). The mixture was heated for 4 hours at reflux (TLC control 2/23 v/v THF/*n*-hexane). Afterwards, the reaction mixture was cooled to room temperature, diluted with water and extracted three times with ethyl acetate (3 \times 50 mL). The organic layer was dried over anhydrous Na_2SO_4 , filtered, and the solvent was removed. The crude product was purified by column chromatography (1/4 v/v acetone/*n*-hexane) to give **13** as a yellow solid. Yield: 0.12 g (56%).

^1H NMR (400 MHz, CDCl_3) δ 7.83–7.74 (m, 2H, Ph), 7.38–7.19 (m, 4H, Ph), 7.04–6.78 (m, 14H, Ph), 6.65 (d, $J = 8.8$ Hz, 4H, Ph), 6.50 (d, $J = 8.8$ Hz, 4H, Ph), 5.77 (s, 2H, CH), 3.91–3.71 (m, 12H, OCH_3).

^{13}C NMR (101 MHz, CDCl_3) δ 158.98, 158.72, 146.71, 134.35, 132.59, 132.22, 130.79, 130.65, 130.52, 128.83, 127.76, 126.85, 126.65, 124.52, 118.09, 114.70, 113.84, 113.48, 113.05, 55.49, 55.44, 55.30, 55.25.

Anal. calcd. for $\text{C}_{50}\text{H}_{42}\text{Br}_2\text{N}_2\text{O}_4$, %: C 67.12; H 4.73; N 3.13, found, %: C 67.39; H 4.58; N 3.03.

4,4'-[(4-methoxy-3,5-dimethylphenyl)azanediyl]dibenzaldehyde (**14**)



Phosphorus oxychloride (1.77 g, 11.5 mmol) was dropwise added to DMF (1.33 ml), cooled to 0 $^\circ\text{C}$, then **5** (0.7 g, 2.3 mmol) was added to the reaction mixture, the temperature was gradually raised to 85 $^\circ\text{C}$ and left to react for 10 hours (TLC control 6/19 v/v THF/*n*-hexane). Afterwards, the reaction mixture was quenched with

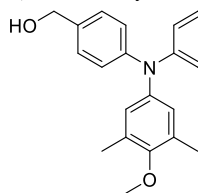
saturated solution of K_2CO_3 in water and extracted three times with ethyl acetate (3×300 mL). The organic layer was dried over anhydrous Na_2SO_4 , filtered, and the solvent was removed. The crude product was purified by column chromatography (6/19 v/v THF/*n*-hexane) to give **14** as a yellow amorphous solid. Yield: 0.51 g (61%).

1H NMR (400 MHz, Acetone- d_6) δ 9.92 (s, 2H, CHO), 7.84 (d, $J = 8.7$ Hz, 4H, Ph), 7.21 (d, $J = 8.6$ Hz, 4H, Ph), 6.95 (s, 2H, Ph), 3.77 (s, 3H, OCH_3), 2.26 (s, $J = 7.2$ Hz, 6H, CH_3).

^{13}C NMR (101 MHz, Acetone- d_6) δ 190.16, 155.64, 152.03, 140.77, 132.88, 131.35, 130.95, 127.81, 122.22, 59.15, 15.33.

Anal. calcd. for $C_{23}H_{21}NO_3$, %: C 76.86; H 5.89; N 3.90, found, %: C 76.61; H 6.02; N 4.02.

[[4-methoxy-3,5-dimethylphenyl)azanediy]di(4,1-phenylene)]dimethanol (15)



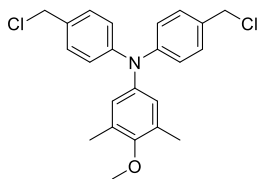
A mixture of **14** (0.2 g, 0.55 mmol) and sodium borohydride (0.12 g, 1.1 mmol) was dissolved in a mixture of ethanol and THF (2ml v/v 1/1). The mixture was heated for 2 hours at 40 °C (TLC control 6/19 v/v THF/*n*-hexane). Afterwards, the reaction mixture was diluted with water and extracted three times with ethyl acetate (3×50 mL). The organic layer was dried over anhydrous Na_2SO_4 , filtered, and the solvent was removed. The crude product was purified by column chromatography (6/19 v/v THF/*n*-hexane) to give **12** as greenish amorphous mass. Yield: 0.198 g (98%).

1H NMR (400 MHz, Acetone- d_6) δ 7.25 (d, $J = 8.4$ Hz, 4H, Ph), 6.96 (d, $J = 8.5$ Hz, 4H, Ph), 6.75 (s, 2H, Ph), 4.58 (d, $J = 5.9$ Hz, 4H, CH_2), 4.16–4.01 (m, 2H, OH), 3.71 (s, 3H, OCH_3), 2.19 (s, 6H, CH_3).

^{13}C NMR (101 MHz, Acetone- d_6) δ 153.56, 148.27, 137.16, 131.74, 129.46, 127.78, 125.68, 121.98, 63.50, 59.06, 15.38.

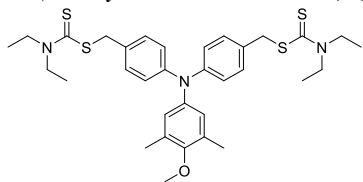
Anal. calcd. for $C_{23}H_{25}NO_3$, %: C 76.01; H 6.93; N 3.85, found, %: C 75.78; H 7.05; N 3.96.

N,N-bis[4-(chloromethyl)phenyl]-4-methoxy-3,5-dimethylaniline (16)



A 0.7 M solution of thionyl chloride (0.17 g, 1.5 mmol) in THF (2.1 ml) was added dropwise to a solution cooled to 0 °C of **15** (0.18 g, 0.5 mmol) in THF (1 ml). The mixture reacted for 1 hour at room temperature (TLC control 1/4 v/v THF/*n*-hexane). Afterwards, the reaction mixture was quenched with saturated Na_2CO_3 solution in water and extracted three times with ethyl acetate (3×100 mL), the organic layer was dried over anhydrous Na_2SO_4 , filtered, and the solvent was removed. The crude product was used in the next step without further purification due to its high reactivity.

[(4-methoxy-3,5-dimethylphenyl)azanediyl]bis[(4,1-phenylene)methylene]bis(diethylcarbamoedithioate) (17)



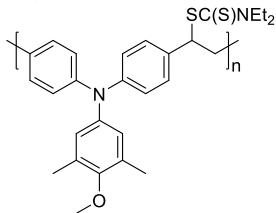
A mixture of **16** (0.18 g, 0.45 mmol) and sodium diethyldithiocarbamate trihydrate (0.4 g, 1.8 mmol) was dissolved in a mixture of ethanol and THF (4 ml v/v 1/1). The mixture reacted for 2.5 hours at room temperature (TLC control 4/21 v/v THF/*n*-hexane). Afterwards, the reaction mixture was diluted with water and extracted three times with ethyl acetate (3 × 100 mL). The organic layer was dried over anhydrous Na₂SO₄, filtered, and the solvent was removed. The crude product was purified by column chromatography (4/21 v/v THF/*n*-hexane) to give **17** as a yellowish amorphous solid. Yield: 0.12 g (43%).

¹H NMR (400 MHz, DMSO-*d*₆) δ 7.26 (d, *J* = 8.5 Hz, 4H, Ph), 6.86 (d, *J* = 8.5 Hz, 4H, Ph), 6.73 (s, *J* = 32.4 Hz, 2H, Ph), 4.42 (s, 4H, CH₂), 3.97 (q, *J* = 6.9 Hz, 4H, CH₂CH₃), 3.73 (q, *J* = 6.9 Hz, 4H, CH₂CH₃), 3.65 (s, 3H, OCH₃), 2.15 (s, 6H, CH₃), 1.19 (s, 12H, CH₂CH₃).

¹³C NMR (101 MHz, DMSO-*d*₆) δ 194.09, 153.77, 147.11, 142.54, 132.11, 130.77, 129.84, 126.24, 123.01, 59.80, 49.45, 46.97, 41.15, 16.34, 12.89, 11.84.

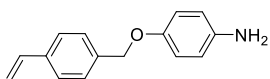
Anal. calcd. for C₃₃H₄₃N₃OS₄, %: C 63.32; H 6.92; N 6.71, found, %: C 63.57; H 6.78; N 6.60.

α,ω-dimethylpoly{1,4-phenylene[(4-methoxy-3,5-dimethylphenyl)azanediyl]-1,4-phenylene[1-(((diethyl-λ~5~-azanyliidyne)-λ~6~-sulfanyliidyne)methyl)sulfanyl]ethane-1,2-diyl]} (18)



A 1 M solution of sodium bis(trimethylsilyl)amide (0.059 g, 0.32 mmol) in THF (0.3 ml) was dropwise added to **17** (0.1 g, 0.16 mmol) in argon atmosphere. The mixture reacted for 12 hours at room temperature (TLC control 7/18 v/v THF/*n*-hexane). Afterwards, the reaction mixture was poured into ice cold water, quenched with 10% HCl solution and extracted three times with chloroform (3 × 50 mL). The crude product was used in the next step without further purification.

4-[(4-ethenylphenyl)methoxy]aniline (19)



A mixture of 4-aminophenol (0.3 g, 2.7 mmol), 4-vinylbenzyl chloride (0.39 g, 2.5 mmol), and sodium hydride (0.165 g, 4.1 mmol, 60% mixture in oil) was dissolved in ice-cold anhydrous DMF (5 ml) under argon atmosphere. The mixture reacted for 3 hours at room temperature (TLC control 11/39 v/v THF/*n*-hexane). Afterwards, the reaction mixture was diluted with water and extracted three times with ethyl acetate (3 × 100 mL). The organic layer was dried over anhydrous Na₂SO₄, filtered, and the solvent was removed. The crude product was purified by

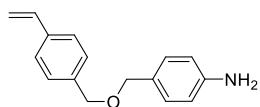
column chromatography (13/37 v/v THF/*n*-hexane) to give **19** as a white powder. Yield: 0.5 g (81%).

^1H NMR (400 MHz, DMSO- d_6) δ 7.47 (d, J = 8.0 Hz, 2H, Ph), 7.38 (d, J = 8.0 Hz, 2H, Ph), 6.80–6.66 (m, 3H, CHCH_2 , Ph), 6.51 (d, J = 8.7 Hz, 2H, Ph), 5.83 (d, J = 17.7 Hz, 1H, CHCH_2), 5.26 (d, J = 10.9 Hz, 1H, CHCH_2), 4.94 (s, 2H, NH_2), 4.62 (s, 2H, CH_2).

^{13}C NMR (101 MHz, DMSO- d_6) δ 150.07, 143.11, 137.99, 136.90, 136.82, 128.27, 126.56, 116.23, 115.34, 114.73, 70.02.

Anal. calcd. for $\text{C}_{15}\text{H}_{15}\text{NO}$, %: C 79.97; H 6.71; N 6.22, found, %: C 79.73; H 6.84; N 6.33.

4-[[4-ethenylphenyl)methoxy]methyl]aniline (**20**)



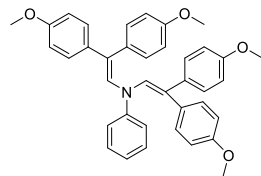
A mixture of 4-aminobenzyl alcohol (0.5 g, 4.0 mmol), 4-vinylbenzyl chloride (0.56 g, 3.6 mmol), and sodium hydride (0.244 g, 6.1 mmol, 60% mixture in oil) was dissolved in cooled anhydrous DMF (6 ml) under argon atmosphere. The mixture reacted for 4 hours at room temperature. Afterwards (TLC control 13/37 v/v THF/*n*-hexane), the reaction mixture was extracted three times with ethyl acetate (3×200 mL). The organic layer was dried over anhydrous Na_2SO_4 , filtered, and the solvent was removed. The crude product was purified by column chromatography (13/37 v/v THF/*n*-hexane) to give **20** as a white powder. Yield: 0.51 g (53%).

^1H NMR (400 MHz, DMSO- d_6) δ 7.45 (d, J = 8.0 Hz, 2H, Ph), 7.30 (d, J = 8.0 Hz, 2H, Ph), 7.01 (d, J = 8.2 Hz, 2H, Ph), 6.73 (dd, J = 17.7, 10.9 Hz, 1H, CH), 6.55 (d, J = 8.2 Hz, 2H, Ph), 5.82 (d, J = 17.7 Hz, 1H, CHCH_2), 5.25 (d, J = 11.0 Hz, 1H, CHCH_2), 5.06 (s, 2H, NH_2), 4.43 (s, 2H, CH_2), 4.32 (s, 2H, CH_2).

^{13}C NMR (101 MHz, DMSO- d_6) δ 148.74, 138.94, 136.88, 136.65, 129.73, 128.19, 126.49, 125.49, 114.50, 114.04, 72.24, 70.87.

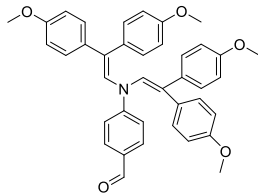
Anal. calcd. for $\text{C}_{16}\text{H}_{17}\text{NO}$, %: C 80.30; H 7.16; N 5.85, found, %: C 80.17; H 7.31; N 5.73.

N,N-bis[2,2-bis(4-methoxyphenyl)vinyl]aniline (**21**)



Was synthesized according to an earlier reported procedure [20].

4-{bis[2,2-bis(4-methoxyphenyl)ethenyl]amino}benzaldehyde (**22**)



Phosphorus oxychloride (3.23 g, 21.0 mmol) was dropwise added to DMF (2.4 ml) and cooled to 0 °C, then **21** (0.6 g, 1.0 mmol) was added to the reaction mixture, the temperature was gradually raised to 85 °C and left to react for 132 hours (TLC control 6/19 v/v THF/*n*-hexane).

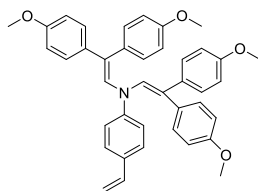
Afterwards, the reaction mixture was quenched with saturated solution of K₂CO₃ in water and extracted three times with ethyl acetate (3 × 400 mL). The organic layer was dried over anhydrous Na₂SO₄, filtered, and the solvent was removed. The crude product was purified by column chromatography (6/19 v/v THF/*n*-hexane) to give **22** as a yellow amorphous solid. Yield: 0.036 g (6%).

¹H NMR (400 MHz, DMSO-*d*₆) δ 9.85 (s, 1H, CHO), 7.84 (d, *J* = 8.6 Hz, 2H, Ph), 7.19–6.78 (m, 12H, Ph), 6.74–6.62 (m, 4H, Ph), 6.38 (d, *J* = 8.7 Hz, 2H, Ph), 5.80 (s, 2H, CH), 3.89–3.63 (m, 12H, OCH₃).

¹³C NMR (101 MHz, DMSO-*d*₆) δ 191.37, 159.51, 159.25, 139.66, 133.44, 133.10, 131.99, 131.94, 130.52, 129.04, 125.84, 125.38, 115.94, 114.63, 113.64, 55.79, 55.55.

Anal. calcd. for C₃₉H₃₅NO₅, %: C 78.37; H 5.90; N 2.34, found, %: C 78.25; H 6.08; N 2.23.

N,N-bis[2,2-bis(4-methoxyphenyl)ethenyl]-4-ethenylaniline (**23**)



A mixture of **22** (0.036 g, 0.06 mmol), methyltriphenylphosphonium bromide (0.032 g, 0.09 mmol), and sodium hydride (0.01 g, 0.27 mmol, 60% mixture in oil) was dissolved in cooled anhydrous THF (1 ml) under argon atmosphere. The mixture reacted for 72 hours at room temperature (TLC control 6/19 v/v THF/*n*-hexane). Afterwards, the reaction mixture was

diluted with water and extracted three times with ethyl acetate (3 × 50 mL). The organic layer was dried over anhydrous Na₂SO₄, filtered, and the solvent was removed. The crude product was purified by column chromatography (6/19 v/v THF/*n*-hexane) to give **23** as a yellow solid. Yield: 0.015 g (41%).

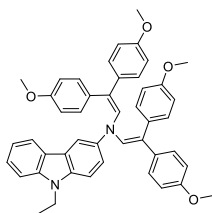
¹H NMR (400 MHz, DMSO-*d*₆) δ 7.71 (d, *J* = 8.6 Hz, 1H, Ph), 7.42 (d, *J* = 8.3 Hz, 1H, Ph), 7.20–6.54 (m, 16H, Ph), 6.37 (d, *J* = 8.5 Hz, 3H, CHCH₂, Ph), 5.75–5.60 (m, 3H, NCH; CHCH₂), 5.12 (d, *J* = 11.0 Hz, 1H, CHCH₂), 3.91–3.61 (m, 12H, OCH₃).

¹³C NMR (101 MHz, DMSO-*d*₆) δ 163.01, 159.25, 158.95, 145.69, 136.60, 133.96, 132.31, 132.28, 131.03, 130.56, 130.49, 128.83, 127.76, 126.45, 116.64, 114.46, 114.24, 113.56, 55.98, 55.75, 55.50, 55.26.

Anal. calcd. for C₄₀H₃₇N₂O₄, %: C 80.65; H 6.26; N 2.35, found, %: C 80.89; H 6.15; N 2.24.

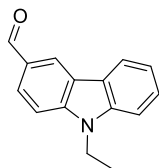
9-ethyl-3-{N,N-bis[2,2-bis(4-methoxyphenyl)vinyl]amino}-9H-carbazole (24)

Was synthesized according to an earlier reported procedure [140].

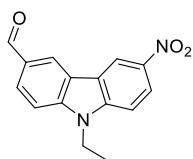


9-ethyl-9H-carbazole-3-carbaldehyde (25)

Was synthesized according to an earlier reported procedure [257].



9-ethyl-6-nitro-9H-carbazole-3-carbaldehyde (26)



A mixture of **25** (0.3 g, 1.3 mmol) and $\text{Cu}(\text{NO}_3)_2$ (0.13 g, 0.67 mmol) was dissolved in acetic anhydride (8 ml). The mixture reacted for 2 hours at room temperature (TLC control 1/4 v/v THF/*n*-hexane). Afterwards, the reaction mixture was quenched with water and extracted three times with DCM (3 ×

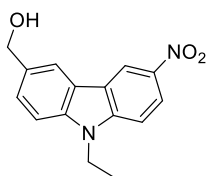
50 mL). The organic layer was dried over anhydrous Na_2SO_4 , filtered, and the solvent was removed. The crude product was purified by column chromatography (1/4 v/v THF/*n*-hexane) to give **26** as a yellow powder (m. p. 246–248 °C). Yield: 0.16 g (44%).

^1H NMR (400 MHz, $\text{DMSO}-d_6$) δ 10.08 (s, 1H, CHO), 9.26 (d, $J = 2.1$ Hz, 1H, Ht), 8.98 (s, 1H, Ph), 8.41–8.35 (m, 1H, Ph), 8.08 (d, $J = 8.6$ Hz, 1H, Ph), 7.88 (dd, $J = 8.8, 5.6$ Hz, 2H, Ph), 4.61–4.49 (m, 2H, CH_2), 1.40–1.30 (m, 3H, CH_3).

^{13}C NMR (101 MHz, $\text{DMSO}-d_6$) δ 192.38, 144.84, 144.11, 141.35, 130.07, 128.30, 125.71, 122.82, 122.62, 122.56, 118.31, 111.25, 110.71, 38.51, 14.19.

Anal. calcd. for $\text{C}_{15}\text{H}_{12}\text{N}_2\text{O}_3$, %: C 67.16; H 4.51; N 10.44, found, %: C 67.02; H 4.39; N 10.68.

(9-ethyl-6-nitro-9H-carbazol-3-yl)methanol (27)



A mixture of **26** (0.1 g, 0.37 mmol) and sodium borohydride (0.02 g, 0.47 mmol) was dissolved in a mixture of ethanol and THF (2 ml v/v 1/1). The mixture was heated for 2 hours at 40 °C. Afterwards (TLC control 9/41 v/v THF/*n*-hexane), the reaction mixture was extracted three times with ethyl acetate (3 × 50 mL). The organic layer was dried over

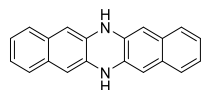
anhydrous Na₂SO₄, filtered, and the solvent was removed. The crude product was purified by column chromatography (9/41 v/v acetone/*n*-hexane) to give **27** as a yellow powder (m. p. 159–161 °C). Yield: 0.07 g (71%).

¹H NMR (400 MHz, Acetone-*d*₆) δ 9.05 (d, *J* = 1.9 Hz, 1H, Ht), 8.39–8.26 (m, 2H, Ph), 7.66 (dt, *J* = 13.4, 8.8 Hz, 3H, Ph), 4.84 (s, 2H, CH₂), 4.56 (q, *J* = 7.2 Hz, 2H, CH₂CH₃), 4.25 (s, 1H, OH), 1.45 (t, *J* = 7.2 Hz, 3H, CH₃).

¹³C NMR (101 MHz, Acetone-*d*₆) δ 143.29, 140.57, 140.49, 135.20, 126.79, 122.64, 122.47, 121.05, 119.29, 116.85, 109.63, 108.76, 64.12, 37.82, 13.18.

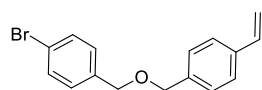
Anal. calcd. for C₁₅H₁₄N₂O₃, %: C 66.66; H 5.22; N 10.36, found, %: C 66.51; H 5.11; N 10.57.

6,13-dihydro-6,13-diazapentacene (**28**)



was synthesized according to an earlier reported procedure [258].

1-bromo-4-[(4-ethenylphenyl)methoxy]methylbenzene (**29**)



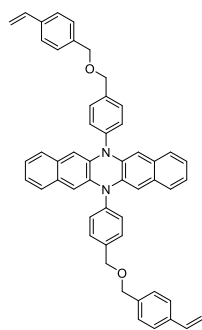
A mixture of 4-bromobenzyl alcohol (1 g, 5.3 mmol), 4-vinylbenzyl chloride (0.75 g, 4.8 mmol), and sodium hydride (0.32 g, 8.0 mmol, 60 % mixture in oil) was dissolved in anhydrous DMF (6 ml) under argon atmosphere. The mixture reacted for 1.5 hours at room temperature (TLC control 1/249 v/v acetone/*n*-hexane). Afterwards, the reaction mixture was diluted with water and extracted three times with ethyl acetate (3 × 250 mL), the organic layer was dried over anhydrous Na₂SO₄, filtered, and the solvent was removed. The crude product was purified by column chromatography (1/249 v/v acetone/*n*-hexane) to give **29** as a white powder (m. p. 45–47 °C). Yield: 1.23 g (76%).

¹H NMR (400 MHz, DMSO-*d*₆) δ 7.56 (d, *J* = 8.4 Hz, 2H, Ph), 7.47 (d, *J* = 8.1 Hz, 2H, Ph), 7.33 (dd, *J* = 8.1, 4.2 Hz, 4H, Ph), 6.74 (dd, *J* = 17.7, 10.9 Hz, 1H, CH), 5.83 (dd, *J* = 17.7, 0.6 Hz, 1H, CHCH₂), 5.27 (d, *J* = 11.0 Hz, 1H, CHCH₂), 4.51 (d, *J* = 7.9 Hz, 4H, CH₂).

¹³C NMR (101 MHz, DMSO-*d*₆) δ 138.40, 138.33, 136.87, 136.84, 131.67, 130.09, 128.29, 126.56, 120.96, 114.66, 71.69, 71.00.

Anal. calcd. for C₁₆H₁₅BrO, %: C 63.38; H 4.99, found, %: C 63.53; H 4.87.

6,13-bis(4-[[4-ethenylphenyl)methoxy]methyl]phenyl)-6,13-dihydrodibenzo[*b,i*]phenazine (**H12**)

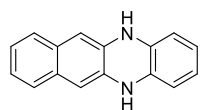


A mixture of **28** (0.1 g, 0.35 mmol), **29** (0.21 g, 0.7 mmol), XPhos-Pd-G2 (0.014 g, 0.018 mmol) and sodium *tert*-butoxide (0.1 g, 1.1 mmol) was dissolved in anhydrous dioxane (5 ml) under argon atmosphere. The mixture was heated for 3 hours at reflux (TLC control 9/41 v/v THF/*n*-hexane). Afterwards, the reaction mixture was cooled to room temperature and filtered through a layer of celite. The crude product was purified by column chromatography (9/41 v/v THF/*n*-hexane) to give **H12** as yellowish crystals (m. p. 234–236 °C). Yield: 0.1 g (39%).

¹H NMR (400 MHz, CDCl₃) δ 7.73 (d, *J* = 5.3 Hz, 4H, Ph), 7.55 – 7.34 (m, 12H, Ph), 7.11 (dd, *J* = 5.6, 3.2 Hz, 4H, Ph), 6.99 (d, *J* = 8.0 Hz, 4H, Ph), 6.75 (dd, *J* = 17.6, 10.9 Hz, 2H, CHCH₂), 5.99 (s, 4H, Ph), 5.78 (d, *J* = 17.6 Hz, 2H, CHCH₂), 5.27 (d, *J* = 10.9 Hz, 2H, CHCH₂), 4.73 (d, *J* = 2.9 Hz, 8H, CH₂).
¹³C NMR (101 MHz, CDCl₃) δ 139.08, 137.57, 137.31, 136.53, 135.79, 130.77, 128.21, 126.44, 125.55, 123.89, 114.04, 107.86, 72.74, 71.71.

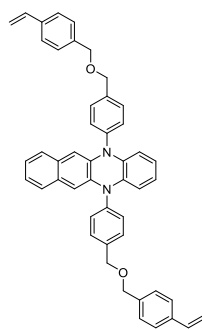
Anal. Calcd. for C₅₂H₄₂N₂O₂, %: C 85.92; H 5.82; N 3.85, found, %: C 85.69; H 5.93; N 3.96.

5,12-Dihydrobenzo[*b*]phenazine (**30**)



Was synthesized according to an earlier reported procedure [259].

5,12-bis(4-[[4-ethenylphenyl)methoxy]methyl]phenyl)-5,12-dihydrobenzo[*b*]phenazine (**H13**)



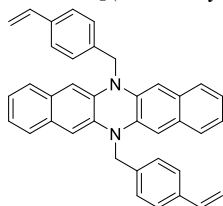
A mixture of **30** (0.1 g, 0.4 mmol), **29** (0.26 g, 0.9 mmol), XPhos-Pd-G2 (0.017 g, 0.021 mmol) and sodium *tert*-butoxide (0.12 g, 1.3 mmol) was dissolved in anhydrous dioxane (4 ml) under argon atmosphere. The mixture was heated for 1.5 hours at reflux (TLC control 2/23 v/v THF/*n*-hexane). Afterwards, the reaction mixture was cooled to room temperature and filtered through a layer of celite. The crude product was purified by column chromatography (2/23 v/v THF/*n*-hexane) to give **H13** as yellowish crystals (m. p. 160–162 °C). Yield: 0.13 g (45%).

¹H NMR (400 MHz, Toluene-*d*₈) δ 7.39 (d, *J* = 7.9 Hz, 4H, Ph), 7.29–7.13 (m, 12H, Ph), 6.91 (dd, *J* = 5.7, 3.4 Hz, 2H, Ph), 6.83 (dd, *J* = 6.0, 3.2 Hz, 2H, Ph), 6.58 (dd, *J* = 17.6, 10.9 Hz, 2H, CHCH₂), 6.33 (dd, *J* = 5.5, 3.5 Hz, 2H, Ph), 6.09 (s, 2H, Ph), 5.92 (dd, *J* = 5.4, 3.7 Hz, 2H, Ph), 5.62 (d, *J* = 17.6 Hz, 2H, CHCH₂), 5.09 (d, *J* = 10.9 Hz, 2H, CHCH₂), 4.36 (d, *J* = 19.8 Hz, 8H, CH₂).

^{13}C NMR (101 MHz, Toluene- d_8) δ 139.13, 139.11, 138.05, 137.11, 136.95, 136.72, 135.01, 131.05, 130.88, 130.15, 127.70, 126.26, 125.67, 123.78, 120.90, 113.19, 113.03, 107.57, 72.15, 71.24.

Anal. calcd. for $\text{C}_{48}\text{H}_{40}\text{N}_2\text{O}_2$, %: C 85.18; H 5.96; N 4.14, found, %: C 84.89; H 6.09; N 4.28.

6,13-bis[(4-ethenylphenyl)methyl]-6,13-dihydrodibenzo[*b,i*]phenazine (H14)



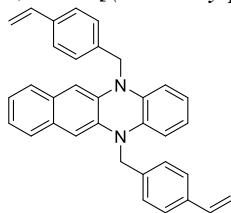
A mixture of **28** (0.2 g, 0.7 mmol), 4-vinylbenzyl chloride (0.211 g, 1.4 mmol) and sodium hydride (0.04 g, 2.1 mmol, 60% mixture in oil) was dissolved in anhydrous DMF (3 ml) under argon atmosphere and stirred for 15 minutes at room temperature (TLC control 2/23 v/v THF/*n*-hexane). Afterwards, the reaction mixture was cooled and poured into 30 ml of ethyl acetate giving yellowish solid that was filtered and then washed with ethyl acetate and methanol (1/4 v/v) to give **H14**. Yield: 0.17 g (47%).

^1H NMR (400 MHz, CDCl_3) δ 7.51–7.35 (m, 8H, Ph), 7.30 (dd, $J = 5.8, 3.2$ Hz, 4H, Ph), 7.07 (dd, $J = 5.7, 2.9$ Hz, 4H, Ph), 6.74 (dd, $J = 17.6, 10.9$ Hz, 2H, CH), 6.57 (s, 4H, Ph), 5.77 (d, $J = 17.6$ Hz, 2H, CHCH_2), 5.26 (d, $J = 10.9$ Hz, 2H, CHCH_2), 5.11 (s, 4H, CH_2).

^{13}C NMR (101 MHz, CDCl_3) δ 136.65, 136.37, 135.44, 135.32, 130.39, 126.92, 126.59, 125.96, 124.01, 113.94, 107.21, 51.54.

Anal. calcd. for $\text{C}_{38}\text{H}_{30}\text{N}_2$, %: C 88.68; H 5.88; N 5.44, found, %: C 88.94; H 5.76; N 5.30.

5,12-bis[(4-ethenylphenyl)methyl]-5,12-dihydrobenzo[*b*]phenazine (H15)



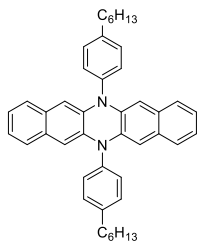
A mixture of **30** (0.1 g, 0.4 mmol), 4-vinylbenzyl chloride (0.125 g, 0.8 mmol) and sodium hydride (0.05 g, 1.3 mmol, 60% mixture in oil) was dissolved in anhydrous DMF (1 ml) under argon atmosphere and stirred for 15 minutes at room temperature (TLC control 1/24 v/v THF/*n*-hexane). Afterwards, the reaction mixture was extracted three times with ethyl acetate (3×50 mL), the organic layer was dried over anhydrous Na_2SO_4 , filtered, and the solvent was removed. The crude product was purified by column chromatography (1/24 v/v THF/*n*-hexane) to give **H15** as a brownish solid. Yield: 0.07 g (35%).

^1H NMR (400 MHz, THF- d_8) δ 7.43 (dd, $J = 29.2, 8.1$ Hz, 8H, Ph), 7.21 (dd, $J = 5.9, 3.3$ Hz, 2H, Ph), 6.96 (dd, $J = 6.1, 3.2$ Hz, 2H, Ph), 6.77 (dd, $J = 17.6, 10.9$ Hz, 2H, CH), 6.57–6.42 (m, 4H, Ph), 6.36–6.26 (m, 2H, Ph), 5.79 (d, $J = 17.6$ Hz, 2H, CHCH_2), 5.22 (d, $J = 10.9$ Hz, 2H, CHCH_2), 4.99 (s, 4H, CH_2).

^{13}C NMR (101 MHz, THF- d_8) δ 137.07, 136.65, 136.46, 136.33, 135.15, 131.04, 126.51, 126.47, 125.47, 123.30, 121.12, 112.60, 111.96, 106.06, 50.28.

Anal. calcd. for $\text{C}_{34}\text{H}_{28}\text{N}_2$, %: C 87.90; H 6.07; N 6.03, found, %: C 87.65; H 6.18; N 6.17.

6,13-bis(4-hexylphenyl)-6,13-dihydrodibenzo[*b,i*]phenazine (**H16**)



A mixture of **28** (0.2 g, 0.7 mmol), 1-bromo-4-hexylbenzene (0.358 g, 1.5 mmol), XPhos-Pd-G2 (0.028 g, 0.035 mmol) and sodium *tert*-butoxide (0.2 g, 2.1 mmol) was dissolved in anhydrous dioxane (7 ml) under argon atmosphere. The mixture was heated for 1.5 hours at reflux (TLC control *n*-hexane). Afterwards, the reaction mixture was cooled to room temperature and filtered through a layer of celite. The crude product was purified by column chromatography (*n*-hexane) to

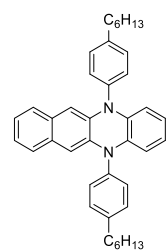
give **H16** as greenish yellow crystals (m. p.182–184 °C). Yield: 0.24 g (57%).

¹H NMR (400 MHz, THF-*d*₈) δ 7.63 (d, *J* = 7.8 Hz, 4H, Ph), 7.43 (d, *J* = 7.7 Hz, 4H, Ph), 7.08 (dd, *J* = 5.6, 3.3 Hz, 4H, Ph), 6.93 (dd, *J* = 5.9, 3.1 Hz, 4H, Ph), 6.03 (s, 4H, Ph), 2.85 (t, *J* = 7.8 Hz, 4H, CH₂), 1.91–1.77 (m, 4H, CH₂), 1.60–1.36 (m, 12H, CH₂), 0.99 (t, *J* = 6.5 Hz, 6H, CH₃).

¹³C NMR (101 MHz, THF-*d*₈) δ 143.56, 137.41, 135.26, 131.35, 130.34, 130.27, 125.41, 123.30, 107.69, 35.63, 31.73, 31.31, 29.08, 22.55, 13.47.

Anal. calcd. for C₄₄H₄₆N₂, %: C 87.66; H 7.69; N 4.65, found, %: C 87.89; H 7.57; N 4.54.

5,12-bis(4-hexylphenyl)-5,12-dihydrobenzo[*b*]phenazine (**H17**)



A mixture of **30** (0.1 g, 0.4 mmol), 1-bromo-4-hexylbenzene (0.218 g, 0.9 mmol), XPhos-Pd-G2 (0.017 g, 0.02 mmol) and sodium *tert*-butoxide (0.124 g, 1.3 mmol) was dissolved in anhydrous dioxane (4 ml) under argon atmosphere. The mixture was heated for 1.5 hours at reflux (TLC control *n*-hexane). Afterwards, the reaction mixture was cooled to room temperature and filtered through a layer of celite. The crude product was purified by column chromatography (*n*-hexane) to give **H17** as

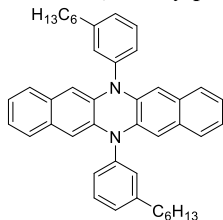
greenish yellow crystals (m. p.116–118 °C). Yield: 0.09 g (39%).

¹H NMR (400 MHz, THF-*d*₈) δ 7.56 (d, *J* = 7.3 Hz, 4H, Ph), 7.36 (d, *J* = 7.6 Hz, 4H, Ph), 6.97 (dd, *J* = 5.6, 3.3 Hz, 2H, Ph), 6.86 (s, 2H, Ph), 6.29 (s, 2H, Ph), 5.96–5.61 (m, 4H, Ph), 2.85–2.75 (m, 4H, CH₂), 1.85–1.69 (m, 4H, CH₂), 1.56–1.30 (m, 12H, CH₂), 1.05–0.87 (m, 6H, CH₃).

¹³C NMR (101 MHz, THF-*d*₈) δ 143.28, 131.21, 130.70, 130.13, 129.67, 125.56, 125.13, 123.15, 120.27, 119.53, 112.55, 106.86, 35.59, 31.73, 31.39, 29.09, 22.53, 13.46.

Anal. calcd. for C₄₀H₄₄N₂, %: C 86.91; H 8.02; N 5.07, found, %: C 87.17; H 7.88; N 4.95.

6,13-bis(3-hexylphenyl)-6,13-dihydrodibenzo[*b,i*]phenazine (H18)



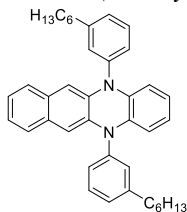
A mixture of **28** (0.2 g, 0.7 mmol), 1-bromo-3-hexylbenzene (0.358 g, 1.5 mmol), XPhos-Pd-G2 (0.028 g, 0.035 mmol) and sodium *tert*-butoxide (0.2 g, 2.1 mmol) was dissolved in anhydrous dioxane (7 ml) under argon atmosphere. The mixture was heated for 6 hours at reflux (TLC control *n*-hexane). Afterwards, the reaction mixture was cooled to room temperature and filtered through a layer of celite. The crude product was purified by column chromatography (*n*-hexane) to give **H18** as greenish yellow crystals (m. p. 164–166 °C). Yield: 0.3 g (71%).

¹H NMR (400 MHz, THF-*d*₈) δ 7.67 (t, *J* = 7.7 Hz, 2H, Ph), 7.45 (d, *J* = 7.6 Hz, 2H, Ph), 7.38–7.27 (m, 4H, Ph), 7.04 (dd, *J* = 5.7, 3.3 Hz, 4H, Ph), 6.89 (dd, *J* = 5.9, 3.1 Hz, 4H, Ph), 6.01 (s, 4H, Ph), 2.79 (t, *J* = 7.6 Hz, 4H, CH₂), 1.83–1.65 (m, 4H, CH₂), 1.49–1.21 (m, 12H, CH₂), 0.88 (t, *J* = 6.6 Hz, 6H, CH₃).

¹³C NMR (101 MHz, THF-*d*₈) δ 144.89, 137.95, 133.28, 129.33, 128.55, 128.42, 126.88, 125.84, 123.56, 121.46, 105.85, 33.66, 29.81, 29.29, 26.93, 20.67, 11.59.

Anal. calcd. for C₄₄H₄₆N₂, %: C 87.66; H 7.69; N 4.65, found, %: C 87.92; H 7.55; N 4.53.

5,12-bis(3-hexylphenyl)-5,12-dihydrobenzo[*b*]phenazine (H19)



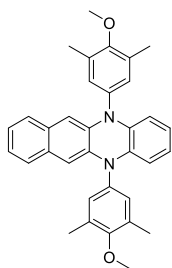
A mixture of **30** (0.1 g, 0.4 mmol), 1-bromo-3-hexylbenzene (0.218 g, 0.9 mmol), XPhos-Pd-G2 (0.017 g, 0.02 mmol) and sodium *tert*-butoxide (0.124 g, 1.3 mmol) was dissolved in anhydrous dioxane (4 ml) under argon atmosphere. The mixture was heated for 3 hours at reflux (TLC control *n*-hexane). Afterwards, the reaction mixture was cooled to room temperature and filtered through a layer of celite. The crude product was purified by column chromatography (*n*-hexane) to give **H19** as greenish yellowish crystals (m. p. 105–107 °C). Yield: 0.1 g (42%).

¹H NMR (400 MHz, THF-*d*₈) δ 7.64 (t, *J* = 7.7 Hz, 2H, Ph), 7.41 (d, *J* = 7.6 Hz, 2H, Ph), 7.32 (s, *J* = 10.9 Hz, 2H, Ph), 7.27 (d, *J* = 7.8 Hz, 2H, Ph), 6.98 (dd, *J* = 5.8, 3.3 Hz, 2H, Ph), 6.87 (dd, *J* = 5.9, 3.2 Hz, 2H, Ph), 6.29 (dd, *J* = 5.7, 3.5 Hz, 2H, Ph), 5.84 (s, 2H, Ph), 5.74 (dd, *J* = 5.6, 3.6 Hz, 2H, Ph), 2.78 (t, *J* = 7.6 Hz, 4H, CH₂), 1.83–1.68 (m, 4H, CH₂), 1.50–1.24 (m, 12H, CH₂), 0.92 (t, *J* = 6.6 Hz, 6H, CH₃).

¹³C NMR (101 MHz, THF-*d*₈) δ 146.62, 139.92, 136.70, 134.71, 131.04, 130.70, 130.61, 128.42, 127.90, 125.17, 123.16, 120.33, 112.58, 106.89, 35.52, 31.66, 31.19, 28.82, 22.52, 13.44.

Anal. calcd. for C₄₀H₄₄N₂, %: C 86.91; H 8.02; N 5.07, found, %: C 87.19; H 7.90; N 4.91.

*5,12-bis(4-methoxy-3,5-dimethylphenyl)-5,12-dihydrobenzo[*b*]phenazine (H20)*



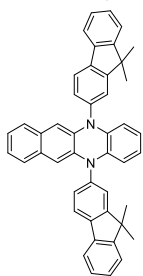
A mixture of **30** (0.1 g, 0.43 mmol), 4-bromo-2,6-dimethylanisole (0.2 g, 0.94 mmol), palladium(II) acetate (0.01 g, 0.04 mmol), tritert-butylphosphonium tetrafluoroborate (0.04 g, 0.13 mmol) and sodium *tert*-butoxide (0.124 g, 1.3 mmol) was dissolved in anhydrous toluene (5 ml) under argon atmosphere. The mixture was heated for 5 hours at reflux (TLC control 1/24 v/v THF/*n*-hexane). Afterwards, the reaction mixture was cooled to room temperature and filtered through a layer of celite. The crude product was purified by column chromatography (1/24 v/v THF/*n*-hexane) to give **H20** as yellow crystals (m. p. 281–283 °C). Yield: 0.32 g (67%).

¹H NMR (400 MHz, Acetone-*d*₆) δ 7.26–6.92 (m, 8H, Ph), 5.73 (s, 6H, Ph), 3.87 (s, 6H, OCH₃), 2.40 (s, 12H, CH₃).

¹³C NMR (101 MHz, Acetone-*d*₆) δ 157.19, 157.15, 157.13, 157.12, 134.32, 134.30, 134.27, 134.25, 134.23, 134.19, 122.76, 118.10, 59.24, 15.52.

Anal. calcd. for C₃₄H₃₂N₂O₂, %: C 81.57; H 6.44; N 5.60, found, %: C 81.31; H 6.58; N 5.71.

*5,12-bis(9,9-dimethyl-9H-fluoren-2-yl)-5,12-dihydrobenzo[*b*]phenazine (H21)*



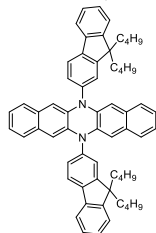
A mixture of **30** (0.1 g, 0.4 mmol), 2-bromo-9,9-dimethylfluorene (0.26 g, 0.9 mmol), XPhos-Pd-G2 (0.017 g, 0.018 mmol) and sodium *tert*-butoxide (0.12 g, 1.3 mmol) was dissolved in anhydrous dioxane (4 ml) under argon atmosphere. The mixture was heated for 3 hours at reflux (TLC control 3/47 v/v THF/*n*-hexane). Afterwards, the reaction mixture was cooled to room temperature and filtered through a layer of celite. The crude product was purified by column chromatography (3/47 v/v THF/*n*-hexane) to give **H21** as yellow crystals (m. p. 361–363 °C). Yield: 0.95 g (38%).

¹H NMR (400 MHz, THF-*d*₈) δ 8.14 (d, *J* = 7.9 Hz, 2H, Ph), 7.90 (d, *J* = 6.9 Hz, 2H, Ph), 7.66 (s, 2H, Ph), 7.58 (d, *J* = 7.1 Hz, 2H, Ph), 7.49–7.32 (m, 6H, Ph), 7.00 (dd, *J* = 5.6, 3.4 Hz, 2H, Ph), 6.86 (dd, *J* = 5.9, 3.1 Hz, 2H, Ph), 6.33 (dd, *J* = 5.4, 3.7 Hz, 2H, Ph), 5.98 (s, 2H, Ph), 5.9–5.83 (m, 2H, Ph), 1.60 (s, 12H, CH₃).

¹³C NMR (101 MHz, THF-*d*₈) δ 157.22, 154.04, 139.51, 138.97, 138.38, 136.94, 134.99, 130.78, 129.63, 127.61, 127.06, 125.25, 125.18, 123.25, 122.61, 122.49, 120.49, 120.15, 112.72, 107.07, 47.00, 26.35.

Anal. calcd. for C₄₆H₃₆N₂, %: C 89.58; H 5.88; N 4.54, found, %: C 89.84; H 5.76; N 4.40.

6,13-bis(9,9-dibutyl-9H-fluoren-2-yl)-6,13-dihydrodibenzo[*b,i*]phenazine (H22)



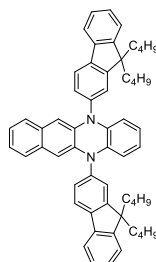
A mixture of **28** (0.1 g, 0.35 mmol), 2-bromo-9,9-dibutylfluorene (0.28 g, 0.8 mmol), XPhos-Pd-G2 (0.014 g, 0.018 mmol) and sodium *tert*-butoxide (0.1 g, 1.1 mmol) was dissolved in anhydrous dioxane (5 ml) under argon atmosphere. The mixture was heated for 3 hours at reflux (TLC control 3/47 v/v THF/*n*-hexane). Afterwards, the reaction mixture was cooled to room temperature and filtered through a layer of celite. The crude product was purified by column chromatography (3/47 v/v THF/*n*-hexane) to give **H22** as greenish yellow crystals (m. p. 362–364 °C). Yield: 0.15 g (52%).

¹H NMR (400 MHz, CDCl₃) δ 8.08 (s, 2H, Ph), 7.84 (d, *J* = 7.6 Hz, 2H, Ph), 7.57–7.30 (m, 10H, Ph), 7.11–6.77 (m, 8H, Ph), 6.09 (s, 4H, Ph), 2.14–1.94 (m, 8H, CH₂), 1.19–0.97 (m, 8H, CH₂), 0.80–0.60 (m, 20H, CH₂CH₃).

¹³C NMR (101 MHz, CDCl₃) δ 154.26, 151.12, 141.77, 140.30, 127.77, 127.71, 127.13, 125.55, 123.92, 123.03, 122.74, 122.65, 120.12, 107.86, 68.00, 55.49, 40.22, 30.34, 29.73, 26.29, 25.63, 23.06, 14.00.

Anal. calcd. for C₆₂H₆₂N₂, %: C 89.16; H 7.48; N 3.35, found, %: C 89.41; H 7.37; N 3.22.

5,12-bis(9,9-dibutyl-9H-fluoren-2-yl)-5,12-dihydrobenzo[*b*]phenazine (H23)



A mixture of **30** (0.1 g, 0.4 mmol), 2-bromo-9,9-dibutylfluorene (0.34 g, 0.9 mmol), XPhos-Pd-G2 (0.017 g, 0.018 mmol) and sodium *tert*-butoxide (0.12 g, 1.3 mmol) was dissolved in anhydrous dioxane (4 ml) under argon atmosphere. The mixture was heated for 2 hours at reflux (TLC control 2/23 v/v THF/*n*-hexane). Afterwards, the reaction mixture was cooled to room temperature and filtered through a layer of celite. The crude product was purified by column chromatography (2/23 v/v THF/*n*-hexane) to give **H23** as yellowish crystals (m. p. 304–306 °C). Yield: 0.11 g

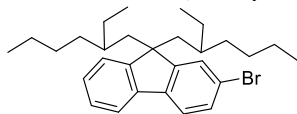
(33%).

¹H NMR (400 MHz, THF-*d*₈) δ 8.12 (d, *J* = 7.9 Hz, 2H, Ph), 7.89 (d, *J* = 6.9 Hz, 2H, Ph), 7.56 (s, 2H, Ph), 7.50 (d, *J* = 7.1 Hz, 2H, Ph), 7.45–7.35 (m, 6H, Ph), 6.98–6.91 (m, 2H, Ph), 6.85 (dd, *J* = 5.9, 3.1 Hz, 2H, Ph), 6.38–6.25 (m, 2H, Ph), 5.95 (s, 2H, Ph), 5.89 (dd, *J* = 5.0, 4.1 Hz, 2H, Ph), 2.27–1.96 (m, 8H, CH₂), 1.24–1.04 (m, 8H, CH₂), 0.85–0.64 (m, 20H, CH₂CH₃).

¹³C NMR (101 MHz, THF-*d*₈) δ 154.09, 150.92, 141.62, 140.47, 138.73, 137.04, 134.95, 130.79, 129.34, 127.51, 126.97, 125.53, 125.10, 123.29, 122.80, 122.33, 120.42, 119.91, 112.64, 107.04, 55.26, 39.89, 26.20, 22.91, 13.30.

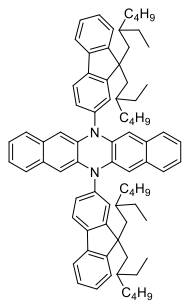
Anal. calcd. for C₅₈H₆₀N₂, %: C 88.73; H 7.70; N 3.57, found, %: C 88.97; H 7.57; N 3.46.

2-bromo-9,9-di(2-ethylhexyl)-9H-fluorene (**31**)



Was synthesized according to an earlier reported procedure [260].

6,13-bis[9,9-bis(2-ethylhexyl)-9H-fluoren-2-yl]-6,13-dihydrodibenzo[*b,i*]phenazine (**H24**)



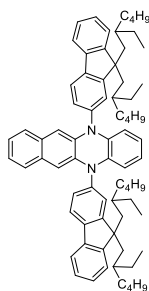
A mixture of **28** (0.1 g, 0.35 mmol), **31** (0.37 g, 0.8 mmol), XPhos-Pd-G2 (0.014 g, 0.018 mmol) and sodium *tert*-butoxide (0.1 g, 1.1 mmol) was dissolved in anhydrous dioxane (5 ml) under argon atmosphere. The mixture was heated for 3 hours at reflux (TLC control 1/24 v/v THF/*n*-hexane). Afterwards, the reaction mixture was cooled to room temperature and filtered through a layer of celite. The crude product was purified by column chromatography (1/24 v/v THF/*n*-hexane) to give **H24** as a yellow solid. Yield: 0.08 g (21%).

^1H NMR (400 MHz, THF- d_8) δ 8.21 (d, $J = 7.9$ Hz, 2H, Ph), 7.94 (d, $J = 7.3$ Hz, 2H, Ph), 7.68 (s, 2H, Ph), 7.62–7.34 (m, 8H, Ph), 7.10–6.98 (m, 4H, Ph), 6.92 (dd, $J = 5.9, 3.0$ Hz, 4H, Ph), 6.14 (t, $J = 7.6$ Hz, 4H, Ph), 2.23–2.08 (m, 8H, aliph), 1.13–0.81 (m, 40H, aliph), 0.60 (m, 20H, CH_2CH_3).

^{13}C NMR (101 MHz, THF- d_8) δ 154.35, 151.07, 142.05, 140.54, 140.40, 138.46, 138.41, 138.39, 135.31, 135.28, 135.25, 130.28, 129.42, 129.39, 127.09, 127.04, 127.00, 126.95, 126.91, 126.33, 126.30, 126.26, 125.49, 125.40, 125.33, 125.31, 124.22, 123.37, 123.33, 123.29, 122.54, 122.50, 120.01, 107.91, 55.27, 55.17, 55.09, 44.70, 44.64, 44.52, 44.48, 35.01, 34.98, 34.72, 34.67, 34.12, 33.44, 33.40, 33.36, 29.67, 28.47, 28.46, 28.42, 28.41, 28.14, 28.11, 26.97, 26.06, 26.01, 22.76, 22.62, 13.38, 13.29, 9.69, 9.67, 9.64, 9.45, 9.42.

Anal. calcd. for $\text{C}_{78}\text{H}_{94}\text{N}_2$, %: C 88.42; H 8.94; N 2.64, found, %: C 88.54; H 9.09; N 2.37.

5,12-bis[9,9-bis(2-ethylhexyl)-9H-fluoren-2-yl]-5,12-dihydrobenzo[*b*]phenazine (**H25**)



A mixture of **30** (0.1 g, 0.4 mmol), **31** (0.44 g, 0.9 mmol), XPhos-Pd-G2 (0.017 g, 0.018 mmol) and sodium *tert*-butoxide (0.12 g, 1.3 mmol) was dissolved in anhydrous dioxane (4 ml) under argon atmosphere. The mixture was heated for 3 hours at reflux (TLC control 1/49 v/v THF/*n*-hexane). Afterwards, the reaction mixture was cooled to room temperature and filtered through a layer of celite. The crude product was purified by column chromatography (1/49 v/v THF/*n*-hexane) to give **H25** as a yellow resin. Yield: 0.15 g (35%).

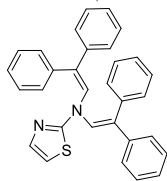
^1H NMR (400 MHz, THF- d_8) δ 8.14 (d, $J = 7.9$ Hz, 2H, Ph), 7.90 (d, $J = 7.3$ Hz, 2H, Ph), 7.62 (s, 2H, Ph), 7.56 (d, $J = 7.2$ Hz, 2H, Ph), 7.48–7.33 (m, 6H, Ph),

7.00–6.77 (m, 4H, Ph), 6.34 (s, 2H, Ph), 6.01–5.74 (m, 4H, Ph), 2.26–2.04 (m, 8H, aliph), 1.14–0.44 (m, 60H, aliph).

^{13}C NMR (101 MHz, THF- d_8) δ 154.36, 154.33, 154.30, 154.23, 154.20, 154.08, 151.01, 150.92, 150.86, 141.81, 141.79, 141.78, 140.70, 140.59, 140.48, 130.73, 127.05, 126.94, 126.91, 126.87, 124.20, 124.16, 124.13, 123.19, 122.35, 119.93, 112.80, 107.15, 107.10, 107.04, 55.26, 55.17, 55.08, 44.77, 44.70, 44.64, 44.59, 44.55, 34.85, 34.70, 34.66, 34.21, 33.35, 33.33, 28.66, 28.62, 28.59, 28.02, 27.19, 27.17, 27.15, 26.02, 22.78, 22.62, 13.41, 9.91, 9.88, 9.85, 9.34, 9.31.

Anal. calcd. for $\text{C}_{74}\text{H}_{92}\text{N}_2$, %: C 88.04; H 9.19; N 2.77, found, %: C 88.15; H 9.34; N 2.51.

N,N-bis(2,2-diphenylethenyl)-1,3-thiazol-2-amine (**H26**)



A mixture of 2-aminothiazole (0.3 g, 3.0 mmol), diphenylacetaldehyde (1.4 g, 7.2 mmol) and camphor-10-sulfonic acid (0.696 g, 3.0 mmol) was dissolved in THF (4 ml + the volume of the Dean-Stark trap), and 3 Å molecular sieves were added. The mixture was heated for 6 hours at reflux (TLC control 2/23 v/v diethyl ether/*n*-hexane). Afterwards, the reaction mixture was

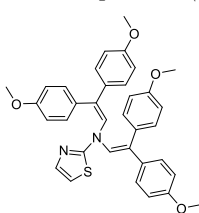
cooled to room temperature, diluted with water and extracted three times with ethyl acetate (3 × 150 mL). The organic layer was dried over anhydrous Na_2SO_4 , filtered, and the solvent was removed. The crude product was purified by column chromatography (2/23 v/v diethyl ether/*n*-hexane) to give **H26** as a yellow amorphous material. Yield: 0.31 g (23%).

^1H NMR (400 MHz, CDCl_3) δ 7.47–7.40 (m, 4H, Ht, Ph), 7.40–7.27 (m, 10H, Ph), 7.24–7.14 (m, 8H, Ph), 7.08 (s, 2H, CH).

^{13}C NMR (101 MHz, CDCl_3) δ 165.07, 140.39, 139.42, 137.34, 130.18, 129.39, 128.41, 127.83, 126.49, 126.40, 123.88, 121.37, 108.17.

Anal. calcd. for $\text{C}_{31}\text{H}_{24}\text{N}_2\text{S}$, %: C 81.54; H 5.30; N 6.14, found, %: C 81.31; H 5.41; N 6.27.

N,N-bis[2,2-bis(4-methoxyphenyl)ethenyl]-1,3-thiazol-2-amine (**H27**)



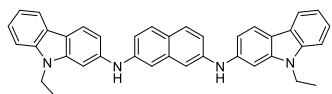
A mixture of 2-aminothiazole (0.3 g, 3.0 mmol), 2,2-bis(4-methoxyphenyl)acetaldehyde (1.8 g, 7.2 mmol) and camphor-10-sulfonic acid (0.696 g, 3.0 mmol) was dissolved in THF (6 ml + the volume of the Dean-Stark trap), 3 Å molecular sieves were added. The mixture was heated for 6 hours at reflux (TLC control 9/16 v/v diethyl ether/*n*-hexane). Afterwards, the reaction mixture was cooled to room temperature, diluted with

water and extracted three times with ethyl acetate (3 × 150 mL). The organic layer was dried over anhydrous Na_2SO_4 , filtered, and the solvent was removed. The crude product was purified by column chromatography (9/16 v/v diethyl ether/*n*-hexane) to give **H27** as a red amorphous material. Yield: 0.2 g (12%).

^1H NMR (400 MHz, Acetone- d_6) δ 7.83–7.73 (m, 2H, Ht), 7.48–6.61 (m, 18H, Ph), 3.96–3.73 (m, 12H, OCH_3).

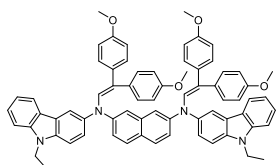
^{13}C NMR (101 MHz, Acetone- d_6) δ 162.97, 131.85, 131.68, 131.43, 129.75, 128.44, 127.55, 127.22, 114.37, 114.22, 113.69, 113.60, 113.50, 55.02, 54.61.
Anal. calcd. for $\text{C}_{35}\text{H}_{32}\text{N}_2\text{O}_4\text{S}$, %: C 72.89; H 5.59; N 4.86, found, %: C 72.62; H 5.74; N 4.98.

N,N'-di(9-ethyl-9H-carbazolyl)-2,7-diaminonaphthalene (**32**)



Was synthesized according to an earlier reported procedure [261].

*N*²,*N*⁷-bis[2,2-bis(4-methoxyphenyl)ethenyl]-*N*²,*N*⁷-bis(9-ethyl-9H-carbazol-3-yl)naphthalene-2,7-diamine (**H28**)

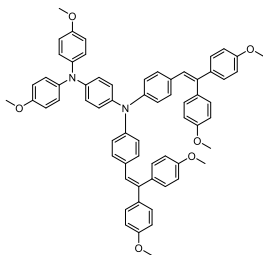


A mixture of **32** (0.3 g, 0.5 mmol), 2,2-bis(4-methoxyphenyl)acetaldehyde (0.31 g, 1.2 mmol), and camphor-10-sulfonic acid (0.13 g, 0.5 mmol) was dissolved in toluene (4 ml + the volume of the Dean-Stark trap). The mixture was heated for 1.5 hours at reflux (TLC control 4/21 v/v THF/*n*-hexane). Afterwards, the reaction mixture was cooled to room temperature, diluted with water and extracted three times with ethyl acetate (3 \times 75 mL). The organic layer was dried over anhydrous Na_2SO_4 , filtered, and the solvent was removed. The crude product was purified by column chromatography (4/21 v/v acetone/*n*-hexane) to give **H28** as a dark blue amorphous material. Yield: 0.23 g (41%).

^1H NMR (400 MHz, $\text{DMSO}-d_6$) δ 8.36–6.10 (m, 38H, Ar), 4.32 (m, 4H, CH_2), 3.88–3.49 (m, 12H, OCH_3), 1.32–1.13 (m, 6H, CH_3).

^{13}C NMR (101 MHz, $\text{DMSO}-d_6$) δ 158.40, 158.12, 151.95, 140.62, 140.43, 139.67, 136.72, 130.19, 130.08, 128.52, 125.39, 123.20, 123.17, 122.84, 122.41, 120.92, 118.92, 118.87, 118.81, 114.02, 113.51, 109.81, 109.51, 55.39, 55.36, 34.85, 14.21.
Anal. calcd. for $\text{C}_{70}\text{H}_{60}\text{N}_4\text{O}_4$, %: C 82.33; H 5.92; N 5.49, found, %: C 82.47; H 6.04; N 5.23.

*N*¹,*N*¹-bis{4-[2,2-bis(4-methoxyphenyl)ethenyl]phenyl}-*N*⁴,*N*⁴-bis(4-methoxyphenyl)benzene-1,4-diamine (**H29**)



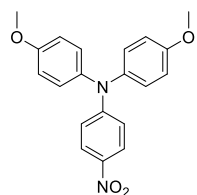
A mixture of **3** (0.5 g, 0.6 mmol), diphenylamine (0.172 g, 0.7 mmol), XPhos-Pd-G2 (0.005 g, 0.006 mmol) and sodium *tert*-butoxide (0.09 g, 0.9 mmol) was dissolved in anhydrous dioxane (5 ml) under argon atmosphere. The mixture was heated for 8 hours at reflux (TLC control 4/21 v/v acetone/*n*-hexane). Afterwards, the reaction mixture was cooled to room temperature and filtered through a layer of celite. The crude product was purified by column chromatography (4/21 v/v acetone/*n*-hexane) to give **H29** as a yellow amorphous material. Yield: 0.29 g (49%).

^1H NMR (400 MHz, $\text{DMSO-}d_6$) δ 7.21–7.10 (m, 4H, Ph), 7.08–6.58 (m, 34H, Ph), 3.80–3.64 (m, 18H, OCH_3).

^{13}C NMR (101 MHz, $\text{DMSO-}d_6$) δ 159.16, 158.97, 145.79, 139.66, 136.04, 131.55, 131.45, 131.33, 130.45, 128.56, 127.19, 126.88, 126.79, 125.38, 115.38, 114.85, 114.15, 113.95, 55.67, 55.60, 55.47.

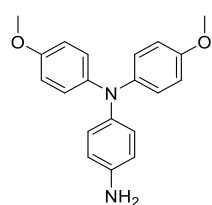
Anal. calcd. for $\text{C}_{64}\text{H}_{56}\text{N}_2\text{O}_6$, %: C 80.99; H 5.95; N 2.95, found, %: C 80.74; H 6.09; N 3.06.

4-Nitro-4',4''-dimethoxytriphenylamine (**33**)



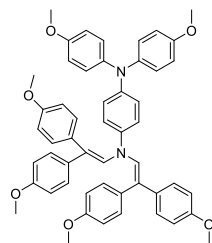
Was synthesized according to an earlier reported procedure [262].

4-Amino-4',4''-dimethoxytriphenylamine (**34**)



Was synthesized according to an earlier reported procedure [262].

N^1,N^1 -bis[2,2-bis(4-methoxyphenyl)ethenyl]- N^4,N^4 -bis(4-methoxyphenyl)benzene-1,4-diamine (**H30**)



A mixture of **34** (0.8 g, 2.5 mmol), 2,2-bis(4-methoxyphenyl)acetaldehyde (1.4 g, 5.5 mmol), and camphor-10-sulfonic acid (0.58 g, 2.5 mmol) was dissolved in toluene (12 ml + the volume of the Dean-Stark trap). The mixture was heated for 3.5 hours at reflux (TLC control 1/4 v/v acetone/*n*-hexane). Afterwards, the reaction mixture was cooled to room temperature, diluted with water and extracted three times with ethyl acetate (3 \times 250 mL). The organic layer was dried over

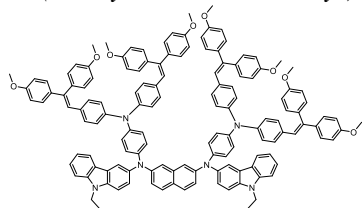
anhydrous Na_2SO_4 , filtered, and the solvent was removed. The crude product was purified by column chromatography (1/4 v/v acetone/*n*-hexane) to give **H30** as yellow crystals (m. p. 185–187 $^\circ\text{C}$). Yield: 0.7 g (35%).

^1H NMR (400 MHz, CDCl_3) δ 7.10–6.74 (m, 22H, Ph), 6.66–6.58 (m, 4H, Ph), 6.48 (d, $J = 8.0$ Hz, 4H, Ph), 3.89–3.70 (m, 18H, OCH_3).

^{13}C NMR (101 MHz, CDCl_3) δ 132.25, 131.44, 130.80, 130.68, 130.09, 128.81, 123.68, 117.94, 114.57, 114.22, 114.07, 113.81, 113.48, 113.00, 55.52, 55.43, 55.24.

Anal. calcd. for C₅₂H₄₈N₂O₆, %: C 78.37; H 6.07; N 3.52, found, %: C 78.14; H 6.19; N 3.63.

*N*²,*N*⁷-bis[4-(bis{4-[2,2-bis(4-methoxyphenyl)ethenyl]phenyl}amino)phenyl]-*N*²,*N*⁷-bis(9-ethyl-9H-carbazol-3-yl)naphthalene-2,7-diamine (**H31**)



A mixture of **32** (0.2 g, 0.4 mmol), **3** (0.647 g, 0.8 mmol), XPhos-Pd-G2 (0.003 g, 0.004 mmol) and sodium *tert*-butoxide (0.106 g, 1.1 mmol) was dissolved in anhydrous dioxane (4 ml) under argon atmosphere. The mixture was heated for 16 hours at reflux (TLC control 1/4 v/v THF/*n*-hexane).

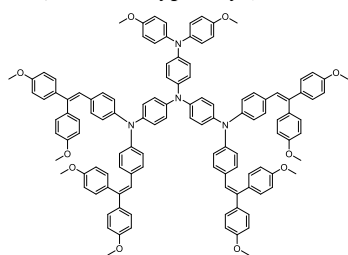
Afterwards, the reaction mixture was cooled to room temperature and filtered through a layer of celite. The crude product was purified by column chromatography (1/4 v/v THF/*n*-hexane) to give **H31** as a dark yellow amorphous material. Yield: 0.32 g (44%).

¹H NMR (400 MHz, DMSO-*d*₆) δ 7.85 (s, 4H, Ar), 7.60–7.31 (m, 8H, Ar), 7.21–6.50 (m, 68H, Ph), 3.78–3.52 (m, 24H, OCH₃), 3.78–3.52 (m, 4H, CH₂), 1.21–1.15 (m, 6H, CH₃).

¹³C NMR (101 MHz, DMSO-*d*₆) δ 159.17, 159.13, 158.96, 158.95, 158.91, 158.89, 158.87, 151.94, 146.14, 143.19, 139.70, 139.67, 136.01, 132.74, 132.72, 132.05, 131.46, 131.42, 131.41, 131.39, 131.29, 131.28, 130.82, 130.81, 130.58, 130.48, 130.37, 130.25, 128.55, 128.52, 125.39, 114.76, 114.10, 113.89, 55.55, 55.51, 55.41, 55.35, 34.86, 30.89.

Anal. calcd. for C₁₃₈H₁₁₄N₆O₈, %: C 83.52; H 5.79; N 4.23, found, %: C 83.78; H 5.68; N 4.08.

*N*¹,*N*¹-bis[4-(bis{4-[2,2-bis(4-methoxyphenyl)ethenyl]phenyl}amino)phenyl]-*N*⁴,*N*⁴-bis(4-methoxyphenyl)benzene-1,4-diamine (**H32**)



A mixture of **34** (0.3 g, 0.9 mmol), **3** (1.58 g, 2.0 mmol), XPhos-Pd-G2 (0.14 g, 0.18 mmol) and sodium *tert*-butoxide (0.212 g, 2.1 mmol) was dissolved in anhydrous dioxane (10 ml) under argon atmosphere. The mixture was heated for 16 hours at reflux (TLC control 7/18 v/v THF/*n*-hexane). Afterwards, the reaction mixture was cooled to room temperature and filtered through a layer of

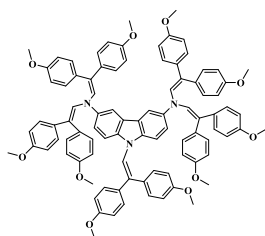
celite. The crude product was purified by column chromatography (7/18 v/v THF/*n*-hexane) to give **H32** yellow solid. Yield: 0.66 g (40%).

¹H NMR (400 MHz, CDCl₃) δ 7.79–6.36 (m, 72H, Ph), 4.15–3.42 (m, 30H, OCH₃).

¹³C NMR (101 MHz, CDCl₃) δ 159.17, 159.16, 158.80, 141.46, 135.87, 131.40, 130.24, 130.20, 130.17, 128.68, 128.63, 128.61, 128.59, 128.56, 128.50, 128.46, 128.42, 128.40, 128.39, 126.89, 126.14, 120.48, 118.03, 114.05, 113.85, 113.83, 113.81, 113.67, 113.66, 55.33, 55.20, 55.16.

Anal. calcd. for C₁₂₀H₁₀₂N₄O₁₀, %: C 81.89; H 5.84; N 3.18, found, %: C 82.01; H 5.99; N 2.91.

N^3 , N^3 , N^6 , N^6 , 9-pentakis[2,2-bis(-methoxyphenyl)ethenyl]-9H-carbazole-3,6-diamine (**H33**)



A mixture of 9H-carbazole-3,6-diamine (0.5 g, 2.5 mmol), 2,2-bis(4-methoxyphenyl)acetaldehyde (4.06 g, 15.8 mmol) and camphor-10-sulfonic acid (0.59 g, 2.5 mmol) was dissolved in THF (10 ml + the volume of the Dean-Stark trap), 3 Å molecular sieves were added. The mixture was heated under argon for 8 hours at reflux (TLC control 7/18 v/v acetone/*n*-hexane). Afterwards, the reaction mixture was cooled to room temperature and

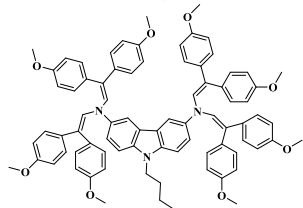
poured into 200 ml of ethanol. The precipitate was filtered and washed with 200 ml of ethanol and then crystallized from acetone giving **H33** as yellow crystals (m. p. 187–189 °C). Yield: 2.05 g (58%).

^1H NMR (700 MHz, CDCl_3) δ 7.69 (s, 2H, Ht), 7.38 (d, 8.7 Hz, 2H, Ht), 7.18–7.10 (m, 4H, Ar), 7.06 (d, J = 8.6 Hz, 2H, Ar), 7.02 (d, J = 8.3 Hz, 8H, Ph), 6.97–6.88 (m, 2H, Ar), 6.86–6.75 (m, 8H, Ph), 6.70–6.55 (m, 11H, CH, Ph), 6.53–6.42 (m, 8H, Ph), 5.81 (s, 4H, CH), 3.89–3.69 (m, 30H, OCH_3).

^{13}C NMR (176 MHz, CDCl_3) δ 159.78, 158.87, 158.85, 158.50, 136.58, 134.61, 133.63, 133.00, 131.14, 130.80, 130.66, 130.15, 129.94, 129.68, 128.81, 127.68, 124.24, 117.27, 114.39, 113.80, 113.74, 112.97, 110.98, 108.74, 55.40, 55.40, 55.19.

Anal. calcd. for $\text{C}_{92}\text{H}_{81}\text{N}_3\text{O}_{10}$, %: C 79.57; H 5.88; N 3.03, found, %: C 79.31; H 6.01; N 3.16.

N^3 , N^3 , N^6 , N^6 , 9-tetrakis[2,2-bis(-methoxyphenyl)ethenyl]-9-butyl-9H-carbazole-3,6-diamine (**H34**)



A mixture of 9-butyl-9H-carbazole-3,6-diamine (1 g, 3.9 mmol), 2,2-bis(4-methoxyphenyl)acetaldehyde (5.0 g, 19.7 mmol) and camphor-10-sulfonic acid (0.9 g, 3.9 mmol) was dissolved in toluene (10 ml + the volume of the Dean-Stark trap ml). The mixture was heated for 1 hour at reflux (TLC control 1/4 v/v acetone/*n*-hexane). Afterwards, the reaction mixture

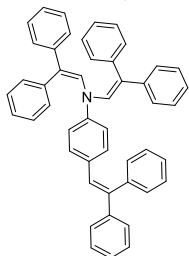
was cooled to room temperature, diluted with water and extracted three times with ethyl acetate (3 × 350 mL). The organic layer was dried over anhydrous Na_2SO_4 , filtered, and the solvent was removed. The crude product was washed with hot ethanol giving green crystals, which then were recrystallized from a mixture of THF and ethanol (1:1) giving **H34** as yellowish crystals (247–249 °C). Yield: 2.31 g (49%).

^1H BMR (400 MHz, CDCl_3 δ): 7.76 (s, 2H, Ht), 7.35–7.26 (m, 4H, Ht), 7.06 (d, J = 8.7 Hz, 8H, Ph), 6.82 (d, J = 8.2 Hz, 8H, Ph), 6.63 (d, J = 8.2 Hz, 8H, Ph), 6.49 (d, J = 8.7 Hz, 8H, Ph), 5.86 (s, 4H, CH), 4.27 (s, 2H, NCH_2), 3.84–3.81 (m, 12H, OCH_3), 3.77–3.74 (m, 12H, OCH_3), 1.87–1.83 (m, 2H, CH_2), 1.44–1.39 (m, 2H, CH_2), 0.96 (t, J = 7.3 Hz, 3H, CH_3).

^{13}C BMR (100 MHz, CDCl_3 δ): 158.9, 158.6, 147.9, 143.7, 134.9, 133.2, 130.8, 128.9, 126.7, 117.6, 113.9, 113.1, 111.5, 109.0, 89.6, 84.5, 55.6, 55.4, 23.0, 20.7, 16.7, 14.1.

Anal. calcd. for $\text{C}_{80}\text{H}_{75}\text{N}_3\text{O}_8$, %: C 79.64; H 6.27; N 3.48, found, %: C 79.41; H 6.39; N 3.59.

N,N,4-tris(2,2-diphenylethenyl)aniline (H35)



A mixture of aniline (0.5 g, 5.4 mmol), diphenylacetaldehyde (3.45 g, 20.1 mmol) and camphor-10-sulfonic acid (1.24 g, 5.4 mmol) was dissolved in THF (10 ml + the volume of the Dean-Stark trap), 3 Å molecular sieves were added. The mixture was heated for 6 hours at reflux (TLC control 2/23 toluene/*n*-hexane). At the end of the reaction, the mixture was cooled to room temperature, diluted with water and extracted three times with ethyl acetate (3×200 mL). The organic layer was dried

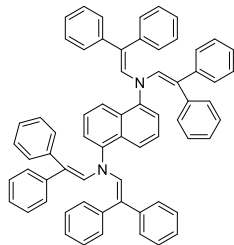
over anhydrous Na_2SO_4 , filtered, and the solvent was removed. The crude product was dissolved in 17 ml THF and poured into 250 ml ethanol to remove the excess amount of aldehyde. The acquired powder was purified by column chromatography (2/23 toluene/*n*-hexane) to give **H35** as yellow crystals (m. p. 230–232 °C). Yield: 1.4 g (42%).

^1H NMR (CDCl_3 , 400MHz, ppm): δ 7.40–7.21 (m, 16H, Ph); 7.14–7.01 (m, 10H, Ph); 6.97 (d, $J = 8.6$ Hz, 3H, NCH, Ph), 6.87 (d, $J = 8.6$ Hz, 2H, Ph), 6.42 (d, $J = 7.5$ Hz, 4H, Ph), 5.81 (s, 2H, NCH).

^{13}C NMR (CDCl_3 , 101 MHz, ppm) δ 144.33; 143.46; 141.26; 140.74; 140.57; 140.00; 132.37; 131.12; 130.59; 130.25; 129.54; 128.91; 128.61; 128.55; 128.21; 127.73; 127.63; 127.47; 127.44; 127.29; 127.21; 126.77; 116.45.

Anal. calcd. for $\text{C}_{48}\text{H}_{37}\text{N}$, %: C 91.83; H 5.94; N 2.23, found, %: C 91.97; H 5.67; N 2.36.

N¹,N¹,N⁵,N⁵-tetrakis(2,2-diphenylethenyl)naphthalene-1,5-diamine (H36)



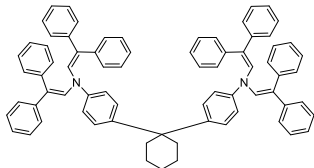
A mixture of 1,5-naphthalenediamine (0.25 g, 1.6 mmol), 2,2-bis(4-methoxyphenyl)acetaldehyde (1.4 g, 7.1 mmol), and camphor-10-sulfonic acid (0.13 g, 1.6 mmol) was dissolved in toluene (6 ml + the volume of the Dean-Stark trap). The mixture was heated for 4 hours at reflux (TLC control 4/21 v/v acetone/*n*-hexane). Afterwards, the reaction mixture was cooled to room temperature and poured into 60 ml of methanol. The precipitate was filtered, dried and then crystallized from acetone to give **H36** as dark yellow crystals (m. p. 201–203 °C). Yield: 0.43 g (31%).

^1H NMR (400 MHz, CDCl_3) δ 8.03 (d, $J = 8.4$ Hz, 2H, Ph), 7.21–6.98 (m, 36H, Ph), 6.76 (dd, $J = 6.1, 3.1$ Hz, 8H, Ph), 6.25 (s, 4H, CH).

^{13}C NMR (101 MHz, CDCl_3) δ 142.23, 142.15, 139.28, 132.65, 130.19, 130.10, 129.85, 127.82, 127.76, 127.35, 126.58, 126.29, 126.21, 124.83, 121.19, 121.09.

Anal. calcd. for C₆₆H₅₀N₂, %: C 91.00; H 5.79; N 3.21, found, %: C 90.76; H 5.91; N 3.33.

*N*¹,*N*¹,*N*³,*N*³-*tetrakis*(2,2-diphenylethenyl)-2³,2⁴,2⁵,2⁶-tetrahydro-2²H-[1¹,2¹:2¹,3¹-terphenyl]-1⁴,3⁴-diamine (**H37**)



A mixture of 1,1-bis(4-aminophenyl)cyclohexane (1.2 g, 4.5 mmol), diphenylacetaldehyde (4.4 g, 22.5 mmol) and camphor-10-sulfonic acid (1.04 g, 4.5 mmol) was dissolved in THF (9 ml + the volume of the Dean-Stark trap), 3 Å molecular sieves were added. The mixture was heated for 4 hours at reflux

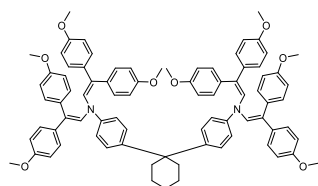
(TLC control 2/23 v/v diethyl ether/*n*-hexane). Afterwards, the reaction mixture was cooled and poured into 180 ml of methanol giving a yellow amorphous solid that was filtered and then washed with methanol. The crude product was purified by column chromatography (2/23 v/v diethyl ether/*n*-hexane) to give **H37** as yellow crystals (m. p. 314–316 °C). Yield: 1.8 g (41%).

¹H NMR (CDCl₃, 400MHz): δ 7.32–7.26 (m, 12H, Ph); 7.24–7.20 (m, 4H, Ph); 7.14–7.00 (m, 24H, Ph), 6.48–6.44 (m, 8H, Ph), 5.88 (s, 4H, CH), 2.27 (s, 4H, CH₂) 1.62–1.48 (m, 6H, CH₂).

¹³C NMR (CDCl₃, 101 MHz) δ 143.15, 142.45, 141.57, 140.11, 131.39, 129.64, 129.00, 128.48, 127.86, 127.70, 127.60, 127.06, 126.56, 117.20, 45.32, 37.30, 22.93.

Anal. calcd. for C₇₄H₆₂N₂, %: C 90.76; H 6.38; N 2.86, found, %: C 90.63; H 6.24; N 3.13.

*N*¹,*N*¹,*N*³,*N*³-*tetrakis*[2,2-bis(4-methoxyphenyl)ethenyl]-2³,2⁴,2⁵,2⁶-tetrahydro-2²H-[1¹,2¹:2¹,3¹-terphenyl]-1⁴,3⁴-diamine (**H38**)



A mixture of 1,1-bis(4-aminophenyl)cyclohexane (0.5 g, 1.9 mmol), 2,2-bis(4-methoxyphenyl)acetaldehyde (2.3 g, 9.0 mmol) and camphor-10-sulfonic acid (0.43 g, 1.9 mmol) was dissolved in toluene (9 ml + the volume of the Dean-Stark trap). The mixture was heated for 3 hours at reflux (TLC control 12/13 v/v diethyl ether/*n*-hexane).

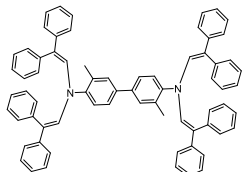
Afterwards, the reaction mixture was cooled to room temperature, diluted with water and extracted three times with ethyl acetate (3 × 250 mL). The organic layer was dried over anhydrous Na₂SO₄, filtered, and the solvent was removed. The crude product was purified by column chromatography (12/13 v/v diethyl ether/*n*-hexane) to give **H38** as a white amorphous material. Yield: 1.0 g (44%).

¹H NMR (400 MHz, DMSO-*d*₆) δ 7.48 (d, *J* = 8.5 Hz, 2H, Ph), 7.27–7.08 (m, 6H, Ph), 6.92–6.72 (m, 16H, Ph), 6.64–6.47 (m, 8H, Ph), 6.35 (d, *J* = 8.5 Hz, 8H, Ph), 5.61 (s, 4H, NCH), 3.90–3.47 (m, 24H, OCH₃), 2.27–2.04 (m, 4H, CH₂), 1.53–1.28 (m, 6H, CH₂).

^{13}C NMR (101 MHz, DMSO- d_6) δ 159.11, 158.79, 143.28, 134.20, 132.34, 130.58, 130.13, 128.74, 128.11, 127.94, 127.56, 126.72, 119.58, 116.61, 114.33, 113.46, 55.70, 55.45, 45.05, 36.65, 26.81, 22.95.

Anal. calcd. for $\text{C}_{82}\text{H}_{78}\text{N}_2\text{O}_8$, %: C 80.76; H 6.45; N 2.30, found, %: C 80.98; H 6.33; N 2.20.

N^4, N^4, N^4, N^4 -tetrakis(2,2-diphenylethenyl)-3,3'-dimethyl[1,1'-biphenyl]-4,4'-diamine (**H39**)



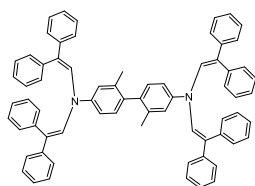
A mixture of *o*-tolidine (0.5 g, 2.3 mmol), diphenylacetaldehyde (2.22 g, 11.3 mmol) and camphor-10-sulfonic acid (0.55 g, 2.3 mmol) was dissolved in toluene (7 ml + the volume of the Dean-Stark trap). The mixture was heated for 1 hour at reflux (TLC control 2/23 v/v chloroform/*n*-hexane). Afterwards, toluene was removed, and the remaining amorphous solid was dissolved in THF and poured into methanol. The precipitate was filtered, dried and purified by column chromatography (2/23 v/v chloroform/*n*-hexane) to give **H39** as an amorphous yellow solid. Yield: 0.61 g (28%).

^1H NMR (400 MHz, CDCl_3) δ 7.21–7.00 (m, 36H, Ph), 6.97 (s, 2H, Ph), 6.87–6.79 (m, 8H, Ph), 6.25 (s, 4H, NCH), 2.28 (s, 6H, CH_3).

^{13}C NMR (101 MHz, CDCl_3) δ 143.53, 142.24, 139.15, 137.40, 132.79, 132.36, 130.16, 129.74, 128.95, 128.59, 128.54, 128.47, 127.80, 127.11, 126.53, 126.42, 126.14, 126.02, 125.23, 124.65, 25.64.

Anal. calcd. for $\text{C}_{70}\text{H}_{56}\text{N}_2$, %: C 90.87; H 6.10; N 3.03, found, %: C 90.98; H 6.23; N 2.79.

N^4, N^4, N^4, N^4 -tetrakis(2,2-diphenylethenyl)-2,2'-dimethyl[1,1'-biphenyl]-4,4'-diamine (**H40**)



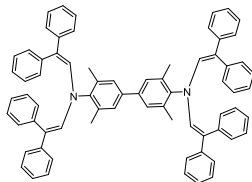
A mixture of *m*-tolidine (0.6 g, 2.8 mmol), diphenylacetaldehyde (2.66 g, 13.6 mmol) and camphor-10-sulfonic acid (0.66 g, 2.8 mmol) was dissolved in toluene (7 ml + the volume of the Dean-Stark trap). The mixture was heated for 3 hours at reflux (TLC control 1/24 v/v diethyl ether/*n*-hexane). Afterwards, the reaction mixture was cooled and poured into 130 ml of ethyl acetate giving **H40** as yellow crystals (m. p. 338–339 °C) that were filtered and then washed with ethyl acetate and ethanol (1/4 v/v). Yield: 0.94 g (36%).

^1H NMR (CDCl_3 , 400MHz, ppm): δ 7.40–7.27 (m, 14H, Ph); 7.16–7.04 (m, 22H, Ph); 7.02–6.96 (m, 4H, Ph), 6.52–6.47 (m, 6H, Ph), 5.95 (s, 4H, NCH), 2.11 (s, 6H, CH_3).

^{13}C NMR (CDCl_3 , 101 MHz, ppm) δ 144.66, 141.57, 140.17, 137.45, 135.25, 131.64, 130.67, 129.67, 129.20, 129.06, 128.55, 127.66, 127.15, 126.67, 118.41, 114.62, 20.34.

Anal. calcd. for $C_{70}H_{56}N_2$, %: C 90.87; H 6.10; N 3.03, found, %: C 90.76; H 5.98; N 3.26.

$N^4,N^4,N^{4'},N^{4'}$ -tetrakis(2,2-diphenylethenyl)-3,3',5,5'-tetramethyl[1,1'-biphenyl]-4,4'-diamine (**H41**)



A mixture of 3,3',5,5'-tetramethylbenzidine (0.6 g, 2.5 mmol), diphenylacetaldehyde (2.35 g, 12.0 mmol) and camphor-10-sulfonic acid (0.66 g, 2.5 mmol) was dissolved in THF (6 ml + the volume of the Dean-Stark trap), 3 Å molecular sieves were added. The mixture was heated for 3 hours at reflux (TLC control 3/22 v/v diethyl ether/*n*-hexane).

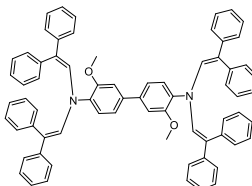
Afterwards, the mixture was cooled to room temperature, diluted with water and extracted three times with ethyl acetate (3 × 250 mL). The organic layer was dried over anhydrous Na_2SO_4 , filtered, and the solvent was removed. Then, the amorphous solid was dissolved in THF and poured into methanol. The precipitate was filtered, dried and purified by column chromatography (3/22 v/v diethyl ether/*n*-hexane) to give **H41** as yellowish crystals (m. p. 217–219 °C). Yield: 0.93 g (39%).

1H NMR (400 MHz, $CDCl_3$) δ 7.17–7.03 (m, 32H, Ph), 6.88 (d, $J = 7.3$ Hz, 8H, Ph), 6.73 (s, 4H, Ph), 6.45 (s, 4H, NCH), 2.20 (s, 12H, CH_3).

^{13}C NMR (101 MHz, $CDCl_3$) δ 142.56, 142.45, 139.16, 138.78, 135.78, 132.97, 130.14, 127.91, 127.66, 126.81, 126.43, 126.10, 125.58, 121.42, 19.59.

Anal. calcd. for $C_{72}H_{60}N_2$, %: C 90.72; H 6.34; N 2.94, found, %: C 90.97; H 6.22; N 2.81.

$N^4,N^4,N^{4'},N^{4'}$ -tetrakis(2,2-diphenylethenyl)-3,3'-dimethoxy[1,1'-biphenyl]-4,4'-diamine (**H42**)



A mixture of *o*-dianisidine (0.5 g, 2.0 mmol), diphenylacetaldehyde (1.93 g, 9.8 mmol) and camphor-10-sulfonic acid (0.47 g, 2.0 mmol) was dissolved in toluene (9 ml + the volume of the Dean-Stark trap). The mixture was heated for 3 hours at reflux (TLC control 4/21 v/v diethyl ether/*n*-hexane). Afterwards, the reaction mixture

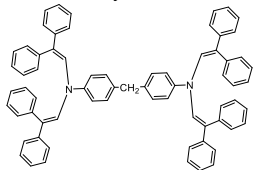
was cooled and poured into 150 ml of methanol. The precipitate was filtered, dried and purified by column chromatography (1/9 v/v DCM/*n*-hexane) to give **H42** as yellow crystals (m. p. 227–229 °C). Yield: 0.96 g (49%).

1H NMR (400 MHz, $CDCl_3$) δ 7.21–7.05 (m, 34H, Ph), 6.84 (d, $J = 8.1$ Hz, 2H, Ph), 6.79–6.72 (m, 8H, Ph), 6.69 (s, 2H, Ph), 6.13 (s, 4H, NCH), 3.76 (s, 6H, OCH_3).

^{13}C NMR (101 MHz, $CDCl_3$) δ 153.50, 142.44, 139.71, 138.59, 133.48, 132.30, 130.27, 127.82, 127.69, 127.35, 126.33, 125.94, 125.84, 125.48, 119.06, 110.46, 55.74.

Anal. calcd. for $C_{70}H_{56}N_2O_2$, %: C 87.83; H 5.90; N 2.93, found, %: C 88.07; H 5.77; N 2.82.

4,4'-methylenebis[*N,N*-bis(2,2-diphenylethenyl)aniline] (**H43**)



A mixture of 4,4'-methylenedianiline (0.6 g, 3.0 mmol), diphenylacetaldehyde (2.85 g, 14.5 mmol) and camphor-10-sulfonic acid (0.7 g, 3.0 mmol) was dissolved in toluene (5 ml + the volume of the Dean-Stark trap). The mixture was heated for 2 hours at reflux (TLC control 7/18 v/v diethyl ether/*n*-hexane). Afterwards, the reaction mixture

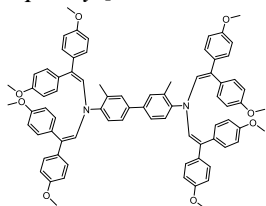
was cooled and poured into 120 ml of ethyl acetate giving **H43** as yellow crystals (m. p. 266–268 °C) which were filtered and then washed with ethyl acetate and ethanol (1/4 v/v). Yield: 1.16 g (39%).

$^1\text{H NMR}$ (400 MHz, CDCl_3) δ 7.39–7.20 (m, 12H, Ph), 7.20–6.97 (m, 28H, Ph), 6.46 (d, $J = 7.2$ Hz, 8H, Ph), 5.87 (s, 4H, NCH), 3.94 (s, 2H, CH_2).

$^{13}\text{C NMR}$ (101 MHz, CDCl_3) δ 144.00, 141.43, 140.12, 135.15, 131.81, 129.60, 129.58, 128.97, 128.53, 127.71, 127.62, 127.13, 126.64, 117.34, 40.58.

Anal. calcd. for $\text{C}_{69}\text{H}_{54}\text{N}_2$, %: C 90.96; H 5.97; N 3.07, found, %: C 91.25; H 5.86; N 2.89.

N^d, N^d, N^d, N^d tetrakis[2,2-bis(4-methoxyphenyl)ethenyl]-3,3'-dimethyl[1,1'-biphenyl]-4,4'-diamine (**H44**)



A mixture of *o*-tolidine (0.5 g, 2.3 mmol), 2,2-bis(4-methoxyphenyl)acetaldehyde (2.89 g, 11.3 mmol) and camphor-10-sulfonic acid (0.55 g, 2.3 mmol) was dissolved in THF (7 ml + the volume of the Dean-Stark trap), 3 Å molecular sieves were added. The mixture was heated for 5 hours at reflux (TLC control 7/18 v/v diethyl ether/*n*-hexane). Afterwards, the reaction mixture was

cooled to room temperature, diluted with water and extracted three times with ethyl acetate (3 × 250 mL). The organic layer was dried over anhydrous Na_2SO_4 , filtered, and the solvent was removed. The crude product was purified by column chromatography

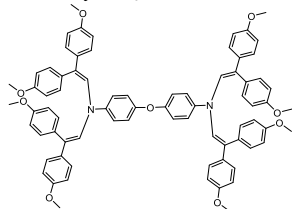
(7/18 v/v diethyl ether/*n*-hexane) to give **H44** as yellow crystals (m. p. 204–206 °C). Yield: 0.85 g (31%).

$^1\text{H NMR}$ (400 MHz, $\text{DMSO}-d_6$) δ 7.16–7.04 (m, 6H, Ph), 6.96 (d, $J = 8.5$ Hz, 8H, Ph), 6.78–6.67 (m, 24H, Ph), 6.00 (s, 4H, NCH), 3.72–3.63 (m, 24H, OCH_3), 2.24 (s, 6H, CH_3).

$^{13}\text{C NMR}$ (101 MHz, $\text{DMSO}-d_6$) δ 158.32, 143.70, 139.66, 136.46, 135.13, 132.21, 131.65, 131.14, 130.51, 129.66, 128.33, 128.21, 125.68, 125.38, 124.59, 124.27, 113.73, 55.49, 55.46, 25.60.

Anal. calcd. for $\text{C}_{78}\text{H}_{72}\text{N}_2\text{O}_8$, %: C 80.39; H 6.23; N 2.40, found, %: C 80.14; H 6.36; N 2.52.

4,4'-oxybis{N,N-bis[2,2-bis(4-methoxyphenyl)ethenyl]aniline} (**H45**)



A mixture of 4,4'-oxydianiline (0.6 g, 3.0 mmol), 2,2-bis(4-methoxyphenyl)acetaldehyde (3.69 g, 14.4 mmol) and camphor-10-sulfonic acid (0.7 g, 3.0 mmol) was dissolved in toluene (8 ml + the volume of the Dean-Stark trap). The mixture was heated for 2 hours at reflux (TLC control 1/4 v/v acetone/*n*-hexane). Afterwards, the reaction mixture was cooled and poured into 100 ml of

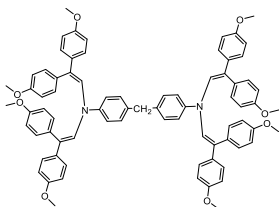
ethyl acetate giving **H45** as white crystals (m. p. 288–290 °C) which were filtered and then washed with ethyl acetate and ethanol (1/4 v/v). Yield: 2.01 g (58%).

¹H NMR (400 MHz, CDCl₃) δ 7.14–6.89 (m, 16H, Ph), 6.83 (d, *J* = 8.6 Hz, 8H, Ph), 6.63 (d, *J* = 8.6 Hz, 8H, Ph), 6.48 (d, *J* = 8.6 Hz, 8H, Ph), 5.76 (s, 4H, NCH), 3.88–3.70 (m, 24H, OCH₃).

¹³C NMR (101 MHz, CDCl₃) 159.01, 158.96, 158.66, 152.64, 141.80, 134.44, 132.74, 132.71, 132.25, 131.44, 131.43, 130.62, 130.34, 130.29, 130.17, 128.81, 128.52, 127.08, 119.40, 118.06, 118.02, 114.42, 113.86, 113.03, 55.43, 55.34, 55.31, 55.24.

Anal. calcd. for C₇₆H₆₈N₂O₉, %: C 79.14; H 5.94; N 2.43, found, %: C 79.03; H 6.17; N 2.31.

4,4'-methylenebis{N,N-bis[2,2-bis(4-methoxyphenyl)ethenyl]aniline} (**H46**)



A mixture of 4,4'-methylenedianiline (0.6 g, 3.0 mmol), 2,2-bis(4-methoxyphenyl)acetaldehyde (2.89 g, 11.3 mmol) and camphor-10-sulfonic acid (0.70 g, 3.0 mmol) was dissolved in THF (7 ml + the volume of the Dean-Stark trap), 3 Å molecular sieves were added. The mixture was heated for 2 hours at reflux (TLC control 7/18 v/v THF/*n*-hexane). Afterwards, the

reaction mixture was cooled to room temperature, diluted with water and extracted three times with ethyl acetate (3 × 250 mL). The organic layer was dried over anhydrous Na₂SO₄, filtered, and the solvent was removed. The crude product was purified by column chromatography (7/18 v/v THF/*n*-hexane) to give **H46** as yellow crystals (m. p. 204–206 °C). Yield: 1.39 g (40%).

¹H NMR (400 MHz, CDCl₃) δ 7.16 (d, *J* = 8.3 Hz, 4H, Ph), 7.04 (d, *J* = 8.3 Hz, 4H, Ph), 6.98 (d, *J* = 8.6 Hz, 8H, Ph), 6.82 (d, *J* = 8.6 Hz, 8H, Ph), 6.63 (d, *J* = 8.7 Hz, 8H, Ph), 6.45 (d, *J* = 8.6 Hz, 8H, Ph), 5.75 (s, 4H, NCH), 3.92 (s, 2H, CH₂), 3.87–3.69 (m, 24H, OCH₃).

¹³C NMR (101 MHz, CDCl₃) δ 158.98, 158.66, 144.34, 134.68, 134.43, 132.80, 130.63, 130.63, 129.54, 128.81, 127.03, 116.93, 113.87, 113.01, 68.00, 55.44, 55.24.

Anal. calcd. for C₇₇H₇₀N₂O₈, %: C 80.32; H 6.13; N 2.43, found, %: C 80.11; H 6.25; N 2.54.

5. MAIN RESULTS AND CONCLUSIONS

- 1) Triphenylamine quaternary ammonium compounds were thoroughly studied. It has been found that:
 - Quaternary ammonium compounds containing iodine anions have low thermal stability.
 - Due to very low conductivity, quaternary ammonium compounds do not function well in perovskite solar cells.
 - All of the tested ionic materials exhibited aggregation induced emission enhancement in the solid state due to suppressed molecular torsions.
 - Precursors to organic quaternary ammonium compounds overall demonstrated better performance than their respective salts and have potential to be used as multifunctional charge transport and emissive materials.

- 2) Cross-linkable monomers **H12-H15** were successfully synthesized. It was determined that:
 - All of the compounds are electrochemically stable.
 - The shift in the absorption of diazacenes **H12-H15** in thin films suggests that the molecules can pack in a more orderly way in the solid state.
 - The energy levels of said materials are suitable for applications in lead-based PSCs as they fall in the range of 5.0–5.6 eV.
 - All the monomers cross-link at temperatures higher than 200 °C, which makes them suitable to use only in inverted p-i-n architecture PSCs.

- 3) HTMs containing the diazacene central core were obtained, and their investigation has revealed that:
 - All of the compounds are thermally and electrochemically stable.
 - The thermal analysis of HTMs **H16-H20** and **H23** reveals rapid weight loss at elevated temperatures, which indicates potential for application in vacuum deposited PSCs.
 - The energy levels of the tested materials are suitable for applications in lead-based PSCs as they fall in the range of 5.0–5.6 eV.
 - Due to the more orderly arrangement in the solid state, diazapentacene **H16** reaches high hole mobility reaching $2.5 \cdot 10^{-3} \text{ cm}^2 \text{ V}^{-1} \text{ s}^{-1}$ at zero field strength and $1.1 \cdot 10^{-2} \text{ cm}^2 \text{ V}^{-1} \text{ s}^{-1}$ at stronger fields.

- 4) New compounds containing diphenylethenyl moieties were successfully synthesized and studied. It has been found that:
 - Low decomposition temperatures of materials **H26-H28** and **H31** make them questionable for applications in optoelectronics.
 - The energy levels of the tested materials are suitable for applications in lead-based PSCs as they fall in the range of 5.0–5.6 eV.

- Due to their great overall properties, carbazole enamines **H33** and **H34** demonstrated almost 17% efficiency in regular configuration PSC (vs. 18.14% reached with doped spiro-OMeTAD) without any additives, which is important to the longevity of the device.
 - High mobility and good thermal properties allowed aniline derivative **H35** to achieve more than 18% PCE in a fully vacuum deposited p-i-n perovskite solar cell thus rivalling the highest reported result for vacuum-processed inverted devices.
- 5) Aniline based hole transporting materials were successfully synthesized, and their investigation has revealed that:
- The energy levels of the tested materials are suitable for applications in lead-based PSCs as they fall in the range of 5.0–5.6 eV.
 - Aniline derivatives **H39** and **H40** demonstrate high hole mobility up to $2.4 \cdot 10^{-3} \text{ cm}^2 \text{ V}^{-1} \text{ s}^{-1}$ at zero field strength and $1.2 \cdot 10^{-2} \text{ cm}^2 \text{ V}^{-1} \text{ s}^{-1}$ at a stronger field, which is beneficial for applications in optoelectronics.
 - Due to their rapid evaporation determined by TGA, HTMs **H37**, **H40** tested in fully vacuum deposited devices with the p-i-n configuration and demonstrated 13.2% and 14.3% PCE, respectively.
 - The modest performance of enamines **H44-H46** in n-i-p architecture PSCs could be attributed to the unoptimized doping procedure which, if improved, could still yield better results.

6. SANTRAUKA

Įvadas

Mokslo ir technologijų pažanga leido panaudoti organines medžiagas įvairiuose optoelektroniniuose prietaisuose, pavyzdžiui: šviesos dioduose, fotoelektriniuose prietaisuose, lauko tranzistoriuose, fotoreceptoriuose ir fotorefraktoriuose [1]. Organinių puslaidininkių naudojimas yra patrauklus dėl galimybės juos apdoroti žemoje temperatūroje, lengvo sluoksnio formavimo ir pritaikymo lanksčių prietaisų gamyboje. Verta paminėti, jog organinių puslaidininkių tyrimai lėmė daugiafunkcinių įtaisų, tokių kaip organinių šviesą skleidžiančių tranzistorių, kurie išnaudoja minėtų junginių krūvininkų pernašos ir emisijos savybes, sukūrimą [2].

Šiuo metu viena perspektyviausių naujų technologijų, naudojančių organinius puslaidininkius, yra perovskitiniai saulės elementai. Šių prietaisų gamyba yra palyginti paprasta [3, 4] ir dažnu atveju naudoja organines skyles pernešančias medžiagas [5], o kartais ir organinius elektronus pernešančius junginius [6]. Lengvai reguliuojami perovskito energetiniai lygmenys [7] leidžia naudoti įvairius *p*-tipo organinius puslaidininkius, bandant pasiekti geriausią įmanomą našumą. Turint tai omenyje nenuostabu, jog perovskitiniai saulės elementai, naudojantys organines skyles pernešančias medžiagas, vis gerina rekordinį efektyvumą, kuris šiuo metu viršija 25 % [8]. Nepaisant puikių rezultatų, minėti prietaisai vis dar susiduria su problemomis, dėl kurių kol kas negali būti gaminami komerciškai. Šie trūkumai susiję su prietaiso gamybos kaina ir ilgalaikiu stabilumu. Pagrindiniai veiksniai, lemiantys perovskitų degradavimą, yra higroskopiskumas, terminis nestabilumas ir jonų migracija [9]. Pirmieji du gali būti išspręsti keičiant perovskitą ir modifikuojant prietaiso konfigūraciją [10, 11, 12], o jonų migraciją galima sušvelninti specialiai modifikuojant skyles pernešančias medžiagas [13, 14] arba keičiant legiravimo procedūrą, kuri paprastai yra naudojama norint pagerinti organinio puslaidininkio elektrines savybes [15, 16]. Nagrinėjant perovskitinio saulės elemento savikainą verta atkreipti dėmesį, jog santykinai didelę jos dalį sudaro dažniausiai naudojami organiniai *p*-tipo puslaidininkiai 2,2',7,7'-tetrakis-(*N,N*-di-*p*-metoksifenilaminas)-9,9'-spirobifluorenas (spiro-MeOTAD) ir poli[bis(4-fenil)(2,4,6-trimetilfenil)aminas] (PTAA) [17], todėl jiems pakeisti ieškoma pigesnių, bet panašų efektyvumą demonstruojančių alternatyvų.

Šio darbo tikslas – susintetinti ir ištirti įvairius lengvai gaunamus *p*-tipo organinius puslaidininkius, skirtus perovskitiniams saulės elementams.

Disertacijos tikslui pasiekti išsikelti šie **uždaviniai**:

1. Ištirti trifenilamino ketvirtinių amonio junginių pritaikymą optoelektronikoje.

2. Mažamolekulinių *p*-tipo puslaidininkių, turinčių dihidrodiazatetraceno ar dihidrodiazapentaceno centrinį fragmentą, sintezė ir tyrimas.

3. Optimaliausios sistemos skylių pernašai paieška, keičiant centrinį fragmentą, prie kurio prijungti difeniletlenilo dariniai.

4. Per vieną stadiją gaunamų enaminų, skirtų pernešti skyles, sintezė ir tyrimas.

Darbo mokslinis naujumas

Per daugiau nei dešimtmetį buvo sukurta daug įvairių organinių skyles pernešančių medžiagų, skirtų perovskitiniams saulės elementams, tačiau dauguma jų yra brangios, reikalauja kelių pakopų sintezės. Du dažniausiai naudojami *p*-tipo puslaidininkiai spiro-MeOTAD ir PTAA nėra šios taisyklės išimtis. Verta paminėti, jog dėl naudojamų priedų, kurie yra būtini norint pasiekti puikų šios spiro-MeOTAD veikimą, kyla įrenginių stabilumo problemų. Šioje daktaro disertacijoje aprašyta įvairių *p*-tipo puslaidininkių, sukurtų tikintis pašalinti bent vieną dažniausiai naudojamų skyles pernešančių medžiagų trūkumą, sintezė ir tyrimai.

Nepaisant nepastovaus atsikartojamumo, polimerai sudaro geros kokybės plonus sluoksnius, kurie puikiai tinka naudoti perovskitiniuose saulės elementuose. Turint tai omenyje buvo bandomi keli skirtingi polimerizacijos metodai, siekiant susintetinti konjuguotus polimerus.

Dihidrodiazaacenaai yra medžiagų grupė dar neišbandyta perovskitiniuose saulės elementuose. Jų struktūroje esančios aminogrupės, suteikia galimybę įvairioms modifikacijoms, o palyginti plokščia šių junginių struktūra gali būti naudinga efektyviam krūvininkų transportavimui. Šiame darbe aprašyti diazaacenaai lengvai sintetinami, pasižymi tinkamais energetiniais lygmenimis bei santykinai aukštu skylių judriu, siekiančiu $2,5 \cdot 10^{-3} \text{ cm}^2 \text{ V}^{-1} \text{ s}^{-1}$ esant nuliniam lauko stipriui, dalis jų gali būti padengti vakuuminio nusodinimo būdu. Visos minėtos savybės daro juos patrauklia alternatyva anksčiau minėtiesiems komerciniams junginiams.

Difeniletlenilo fragmentų turintys junginiai yra žinomi dėl savo santykinai aukšto skylių judrio, ši savybė daro juos patrauklius pritaikymui optoelektronikoje. Difeniletlenildariniai buvo prijungti prie įvairių centrinių fragmentų siekiant surasti sistemas, tinkančias naudoti perovskitiniuose saulės elementuose. Karbazolo enaminai pasirodė vieni perspektyviausių *p*-tipo puslaidininkių. Saulės elementai, naudojantys šiuos junginius, ne tik pasiekė beveik 17 % našumą, tačiau tai pavyko padaryti nenaudojant jokių priedų. Savo ruožtu anilino darinys, turintis tris difeniletlenil- fragmentus, pasiekė daugiau nei 18 % visiškai vakuuminiu būdu padengtame invertuotame perovskitiniame saulės elemente, kas yra vienas geriausių rezultatų tokio tipo prietaisuose.

Anilino enaminai gauti atlikus lengvą vieno etapo sintezę, nenaudojant brangių pereinamųjų metalų katalizatorių. Dalis šių *p*-tipo puslaidininkių buvo išbandyti perovskitiniuose saulės elementuose, tačiau aukšto našumo pasiekta nebuvo. Nepaisant to daugeliui medžiagų būdingas palyginti didelis krūvininkų judris, siekiantis $2,4 \cdot 10^{-3} \text{ cm}^2 \text{ V}^{-1} \text{ s}^{-1}$ esant nuliniam lauko stipriui, tinkami energetiniai lygmenys ir dažnu atveju aukšta stiklėjimo temperatūra. Tai palieka vilčių, jog parinkus tinkamos struktūros perovskitinį saulės elementą, su šiomis medžiagomis galėtų būti pasiektas aukštas efektyvumas.

Pagrindiniai ginamieji disertacijos teiginiai:

1. Gauti monomerai, turintys keletą vinilgrupių, gali būti sutinklinti kietoje būsenoje.

2. Susintetinti nauji diazaaceno centrinį fragmentą turintys skyles pernešantys junginiai. Dalis jų pasižymi aukštu skylių judriu, siekiančiu $2,5 \cdot 10^{-3} \text{ cm}^2 \text{ V}^{-1} \text{ s}^{-1}$ esant nuliniam lauko stipriui. Be to, dauguma jų greitai garuoja aukštose temperatūrose, kas yra naudinga pritaikymui perovskitiniuose saulės elementuose, konstruojamuose vakuminio nusodinimo būdu.

3. Puikios karbazolo ir anilino enaminų, savo struktūroje turinčių difeniletendarinius, fotoelektrinės ir terminės savybės leido sukonstruoti aukšto našumo perovskitinius saulės elementus.

4. Anilino enaminai gauti naudojant paprastą vieno etapo sintezę, nenaudojant brangių pereinamųjų metalų katalizatorių. Junginiai pasižymėjo aukšta stiklėjimo ar kristalų lydymosi temperatūra, be to, buvo pasiektas santykinai aukštas $2,4 \cdot 10^{-3} \text{ cm}^2 \text{ V}^{-1} \text{ s}^{-1}$ krūvininkų judris, kas daro šiuos junginius labai perspektyvius naudoti perovskitiniuose saulės elementuose.

1. Skyles pernešantys polimeriniai puslaidininkiniai skirti perovskitiniams saulės elementams

Vienas didžiausių iššūkių siekiant sukurti aukšto našumo prietaisus yra efektyvių krūvininkus pernešančių medžiagų kūrimas [194, 195]. Organinė chemija gali padėti išspręsti šią problemą, kadangi ji suteikia galimybę susintetinti begales įvairių junginių, kurie gali būti paruošti naudojant paprastus bei pigius metodus [3, 196]. Mažamolekulinės skyles pernešančios medžiagos turi daug privalumų lyginant su polimerinėmis medžiagomis, pavyzdžiui: tiksli molekulinė masė, struktūrinis universalumas ir gana lengvas gryninimas kristalizacijos, chromatografijos ar vakuuminės sublimacijos būdais [197, 198]. Deja, daugelis šių krūvį pernešančių junginių pasižymi santykinai žemomis stiklėjimo temperatūromis (T_g) [131, 196, 199], dėl ko gali įvykti virsmas stiklas–skystis, pabloginantis prietaiso veikimą ir ilgaamžiškumą [200, 201]. Be to, kai kurios mažamolekulinės skyles pernešančios medžiagos nesudaro kokybiškų, vientisų sluoksnių, todėl gali įvykti krūvininkų rekombinacija [202–204], kuri lemia mažesnę saulės elementų našumą [203].

Skyles pernešantys polimerai turi atitikti daugumą tų pačių reikalavimų, kaip ir mažamolekuliniai analogai: energetiniai lygmenys turi būti suderinti su perovskito, geras skylių judris ir nebrangi sintezė [205]. Iš esmės yra dvejų rūšių polimerai, naudojami kaip skyles pernešančios medžiagos: D–A tipo kopolimerai ir homopolimerai. Dauguma jų yra konjuguoti, tačiau esama ir išimčių [167].

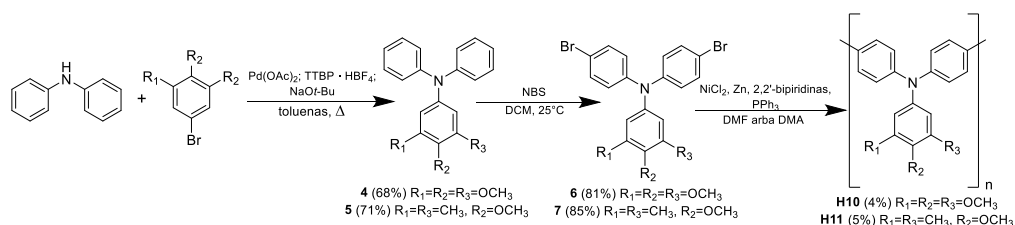
Nemažas kiekis D–A konjuguotų kopolimerų gali suformuoti kokybiškas plėveles, pasižymi tinkamais energijos lygmenimis ir dideliu krūvininkų judrumu nenaudojant priedų [205]. Nepaisant minėtų pranašumų, šio tipo polimerai nėra praktiški, jų sintezė dažnai yra sudėtinga, todėl žymiai išauga galutinio produkto savikaina [206–208].

Viena didžiausių puslaidininkinių polimerų grupių yra trifenilamino (TPA) dariniai. Iš jų plačiausiai naudojamas poli[bis(4-fenil)(2,4,6-trimetilfenil)aminas] (PTAA), pasiekiantis panašų našumą kaip populiariausias perovskitiniuose saulės elementuose naudojamas skyles pernešantis junginys spiro-OMeTAD [209]. Nepaisant to, kad PTAA nereikalauja priedų bei pasižymi sąlyginai geru stabilumu aukštoje temperatūroje, jo kaina yra per didelė komerciniam naudojimui [81]. Kita vertus, T. Matsui atliktame tyrime [18] pristatyti trys nauji pigūs triarilamino pagrindu susintetinti polimerai, iš kurių geriausias perovskitiniame saulės elemente stabiliai veikė daugiau nei 140 valandų ir pademonstravo 12,3 % našumą. Nors pasiekti neblogi rezultatai, 12,3 % efektyvumas yra per mažas komerciniam pritaikymui.

Kita polimerinių sluoksnių gavimo strategija yra kurti monomerus, turinčius daugiau nei vieną aktyvią grupę (pvz., vinilgrupę ar metakrilgrupę), kurios galėtų reaguoti tarpusavyje kaitinant arba švitinant šviesa. Tokiu būdu gaunami nekonjuguoti polimerai, tačiau jiems nereikalingi priedai tam, kad pasiektų aukštą efektyvumą [210]. Šis skyrelis skirtas TPA grupės polimerų ir kelias aktyvias grupes turinčių monomerų sintezei ir tyrimams.

1.1. Trifenilamino polimerų ir monomerų su vinilgrupėmis sintezė

3,4,5-Trimetoksi-*N,N*-difenilamino (**4**) sintezė buvo vykdoma Buchwald-Hartwig kryžminimo kopuliavimo būdu, reaguojant difenilaminui ir 1,2,3-trimetoksibenzenui, dalyvaujant paladžio organometaliniam junginiui kaip katalizatoriui. Tos pačios sąlygos buvo taikomos difenilaminui reaguojant su 4-brom-2,6-dimetilanizoliu, gaunant 4-metoksi-3,5-dimetil-*N,N*-difenilamino (**5**) (1 schema).



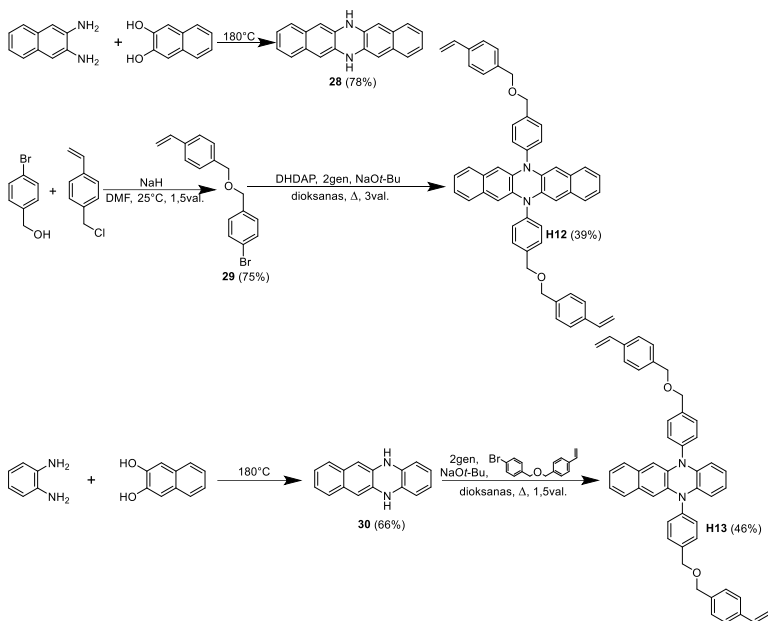
1 schema. Polimerų **H10** ir **H11** sintezė

Trifenilaminai **4** ir **5** buvo brominti *N*-bromosukcinimidu (NBS) naudojant DCM kaip tirpiklį, gaunant atitinkamai *N,N*-bis(4-bromfenil)-3,4,5-trimetoksianiliną (**6**) ir *N,N*-bis(4-bromfenil)-4-metoksi-3,5-dimetilaniliną (**7**). Abu TPA dariniai buvo naudojami Yamamoto homopolimerizacijoje dalyvaujant trifenilfosfinui (TPP), Zn, 2,2'-bipiridinui ir NiCl₂ argono atmosferoje, susidarant polimerams **H10** ir **H11** (1 schema). Remiantis I. Colon, V. Percec ir G. T. Kwiatkowski darbais, buvo bandyta optimizuoti minėtą polimerizacijos reakciją, tačiau nesėkmingai (1 lentelė) [211–213]. Prieš gilinant į 1 lentelės rezultatus, verta paminėti, jog šios reakcijos yra ypač jautrios deguoniui ir drėgmei [211–213], net mažiausi jų kiekiai gali daryti reikšmingą įtaką reakcijos išeigai. Kad būtų sumažinta minėta rizika, kolbos buvo dešimt minučių kaitintos 180 °C temperatūroje ir ilgiau nei valandą leistos argono dujos.

1 lentelė. Junginio H11 Yamamoto polimerizacijos eksperimentai

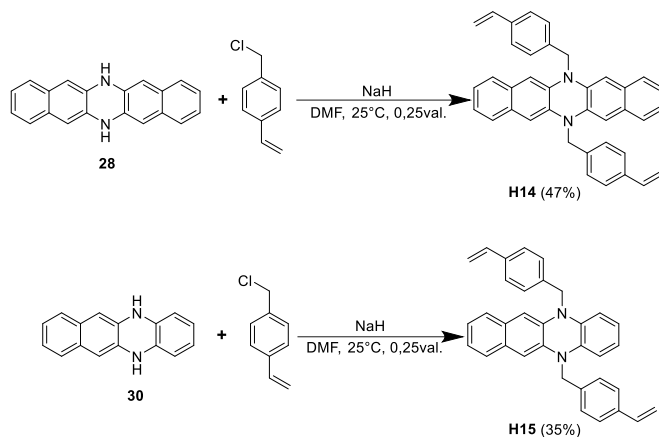
| Bandymo nr. | Monomeras, mmol | NiCl ₂ , mmol | Zn, mmol | 2,2'-bipiridinas, mmol | TPP, mmol | Tirpiklis, ml | T, °C | t, h | Išei-ga, % |
|-------------|-----------------|--------------------------|----------|------------------------|-----------|---------------|-------|------|------------|
| 1 | 0,65 | 0,047 | 2,05 | 0,07 | 0,47 | DMA, 2 | 80 | 6 | 0 |
| 2 | 0,65 | 0,047 | 2,05 | 0,07 | 0,47 | DMF, 2 | 80 | 6 | 2 |
| 3 | 0,65 | 0,047 | 2,05 | 0,07 | 0,47 | DMF, 2 | 80 | 14 | 3 |
| 4 | 0,65 | 0,047 | 2,05 | 0,07 | 0,47 | DMF, 2 | 80 | 48 | 3 |
| 5 | 0,65 | 0,047 | 2,05 | 0,07 | 0,47 | DMF, 2 | 140 | 14 | 3 |
| 6 | 0,65 | 0,01 | 4,0 | 0,01 | 0,9 | DMF, 2 | 80 | 14 | 2 |
| 7 | 0,65 | 0,01 | 4,0 | 0,01 | 0,9 | DMF, 1 | 80 | 14 | 2 |
| 8 | 0,65 | 0,01 | 4,0 | 0,01 | 0,9 | DMF, 4 | 80 | 14 | 2 |
| 9 | 0,65 | 0,01 | 4,0 | 0,01 | 1,37 | DMF, 2 | 80 | 14 | 2 |
| 10 | 0,65 | 0,09 | 4,0 | 0,15 | 0,9 | DMF, 2 | 80 | 14 | 5 |
| 11 | 0,65 | 0,18 | 4,0 | 0,15 | 0,9 | DMF, 2 | 80 | 14 | 3 |
| 12 | 0,65 | 0,09 | 4,0 | 0,09 | 0,9 | DMF, 2 | 80 | 14 | 5 |

Kadangi monomerai turi būti visiškai ištirpę, reakcijas galima atlikti tik dipoliniuose aprotiniuose tirpikliuose, pvz., DMA ir DMF. Pirmųjų bandymų metu produktas buvo gautas tik DMF, kas lėmė jo naudojimą tolesniuose eksperimentuose. Bandymais nr. 3 ir 4 buvo nustatyta, kad optimali reakcijos trukmė turėtų būti apie 14 valandų, o 5-tu eksperimentu pademonstruota, jog neverta viršyti 80 °C temperatūros. Savo tyrime I. Colon ir kt. teigė, jog norint gauti didelę išei-gą NiCl₂ santykis su monomeru turėtų būti mažesnis nei 2 mol %, o 2,2'-bipiridino neturėtų viršyti nikelio molinio kiekio 1,25 kartus, savo ruožtu TPP koncentracija tirpale turėtų būti bent 0,25 M [211]. Atsižvelgiant į tai buvo atlikti bandymai nr. 6–12, siekiant rasti geriausią pusiausvyrą tarp visų junginių, deja, šių eksperimentų metu buvo pasiekta tik 5 % išei-ga.



2 schema. Vinilo grupes turinčių junginių **H12** ir **H13** sintezė

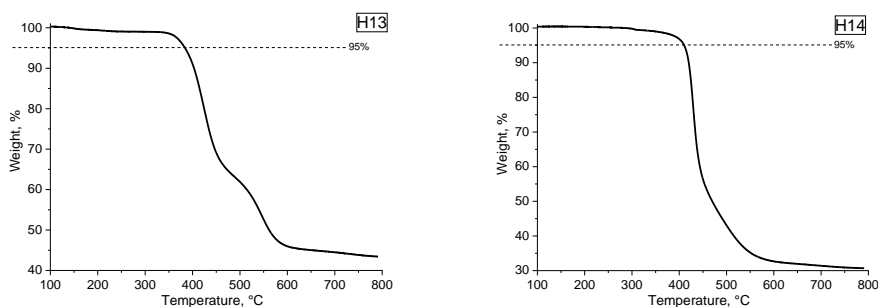
Prieš tai minėti nesėkmingi bandymai paskatino sukurti molekules, kurios galėtų būti sutinkintos sluoksnyje. Tam buvo susintetinti monomerai su dviem vinilgrupėmis. Iš pradžių tarpinis junginys 1-brom-4-[[4-(etenilfenil) metoksi] metil]benzenas (**29**) buvo gautas Williamsono eterio sintezės būdu iš 4-brombenzilo alkoholio ir 4-vinilbenzilchlorido, naudojant natrio hidridą kaip bazę, o DMF kaip tirpiklį. Gautas junginys buvo naudojamas kartu su dihidrodiazapentacenu (DHDAP) **28** Buchwald-Hartwig kryžminio kopuliavimo reakcijoje, argono atmosferoje, naudojant sausą dioksaną susidarant monomerui **H12**. Tos pačios reakcijos sąlygos buvo taikomos gaunant **H13** iš eterio (**29**) ir dihidrodiazatetraceno (DHDAT) (**30**) (2 schema). Savo ruožtu DHDAT buvo gautas kondensuojant 1,2-fenilendiaminą su 2,3-dihidroksinaftalenu nenaudojant jokio tirpiklio.



Norint rasti kuo tinkamesnę kandidatą perovskitiniams saulės elementams, buvo susintetinti dar du junginiai su dviem vinilgrupėmis. Reakcijos metu tarp **28** ir 4-vinilbenzilchlorido, esant natrio hidridui DMF tirpiklyje, susidarė monomeras **H14**, o esant toms pačioms sąlygoms sujungus **30** su 4-vinilbenzilchloridu gautas **H15** (3 schema).

1.2. Susintetintų junginių terminės savybės

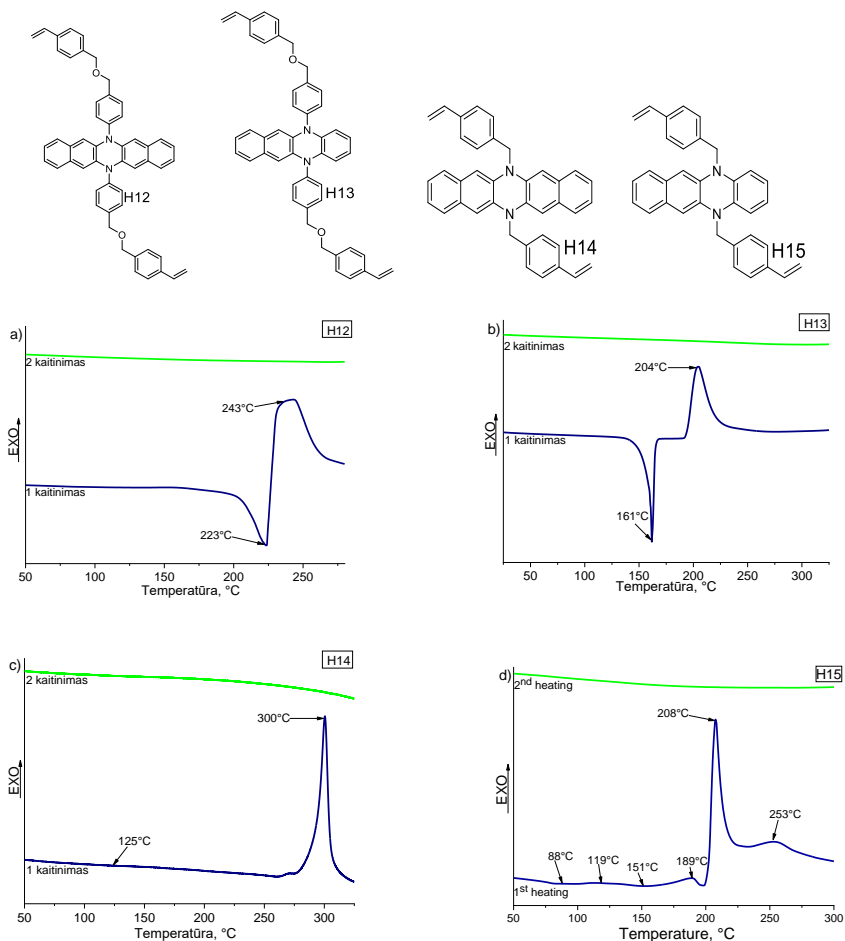
Norint įvertinti medžiagų terminį stabilumą ir jų tinkamumą terminiam tinkimui, buvo atlikti diferencinės skenuojamosios kalorimetrijos (DSC) ir termogravimetrinės analizės (TGA) tyrimai. TGA kreivių pavyzdžius galima pamatyti 1 pav., o visų junginių šiluminės savybės galima rasti 2 lentelėje. Visų bandytų medžiagų terminis stabilumas po polimerizacijos viršijo 350 °C.



1 pav. Junginių H13 ir H14 terminio stabilumo grafikai

Pirmojo DSC kaitinimo metu DHDAP darinio **H12** lydimosi temperatūra užfiksuota ties 223 °C, po kurios sekė egzoterminis procesas esant 243 °C, žymintis terminę polimerizaciją (2a pav.). Antrojo kaitinimo metu fazių perėjimų nebuvo pastebėta, kas patvirtina tinklinio polimero susidarymą. Panašūs pokyčiai

žemesnėje temperatūroje stebėti ir DHDAT darinio **H13** atveju – kristalai lydosi esant 161 °C, o polimerizacija vyksta 204 °C (2b pav.).



2 pav. DSC kreivės junginių: a) **H12**, b) **H13**, c) **H14**, d) **H15**

Savo ruožtu diazapentacenas **H14** polimerizuojasi 300 °C temperatūroje, ši smailė tokia intensyvi, jog praktiškai užgožia T_g , kuri vos matoma ties 125 °C (2c pav.). Daug fazinių virsmų stebima DHDAT darinio **H15** pirmojo kaitinimo metu, todėl sunku pasakyti, kuris iš jų nurodo T_g , tačiau galima teigti, jog 208 °C temperatūroje vyksta kristalizacija, o ties 253 °C – polimerizacija (2d pav.).

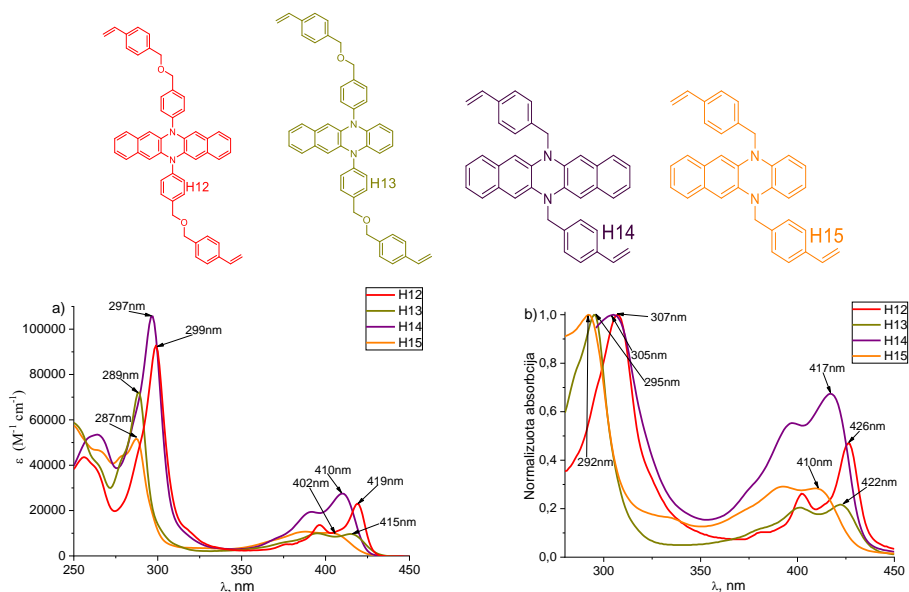
2 lentelė. Terminės junginių **H12–H15** savybės

| Junginys | $T_g^a, ^\circ\text{C}$ | $T_m^b, ^\circ\text{C}$ | $T_{cr}^c, ^\circ\text{C}$ | $T_{poly}^c, ^\circ\text{C}$ | $T_{dec}^d, ^\circ\text{C}$ |
|------------|-------------------------|-------------------------|----------------------------|------------------------------|-----------------------------|
| H12 | - | 223 | - | 243 | 360* |
| H13 | - | 161 | - | 204 | 384* |
| H14 | 125 | - | - | 300 | 410* |
| H15 | 88 | 151 | 119, 189, 208 | 253 | 371* |

a) Nustatyta taikant DSC: kaitinimo greitis 10 K/min; N₂ atmosfera; antrasis kaitinimas. b) Lydimosi temperatūra užfiksuota tik pirmojo kaitinimo metu, 10 K/min. c) Nustatyta taikant DSC: kaitinimo greitis 10 K/min; N₂ atmosfera. d) Skilimo pradžia nustatyta TGA metodu: kaitinimo greitis 10 K/min; N₂ atmosfera. * junginių terminis stabilumas po terminės polimerizacijos.

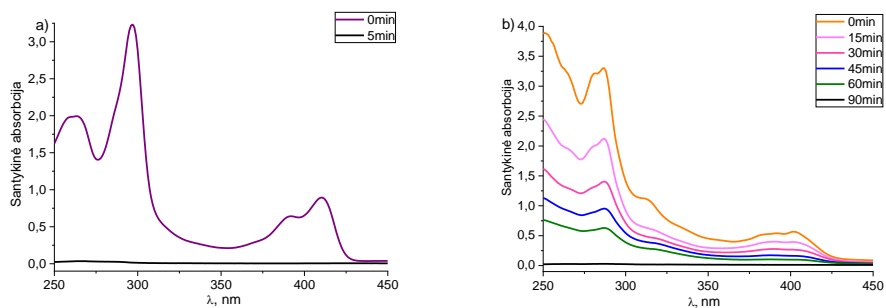
1.3. Optinės susintetintų junginių savybės

UV-Vis absorbcijos spektrai buvo išmatuoti THF tirpaluose ir ant stiklo. Tirpale diazaacenų $n-\pi^*$ elektronų perėjimai matomi 400–420 nm diapazone, o minėtų junginių absorbcijos maksimumai stebimi nuo 287 nm iki 299 nm (3 pav.). Taip pat verta paminėti, jog papildomas fenilo žiedas diazapentacenuose **H12** ir **H14** lemia 10 nm bathochrominį poslinkį, lyginant su atitinkamais DHDAT dariniais **H13**, **H15**.



3 pav. a) UV-Vis absorbcijos spektrai junginių **H12–H15** THF tirpaluose ir b) plėvelių ant stiklo

Lyginant diazaacenų absorbcijos maksimumus tirpale ir plėvelėje matomas maždaug 8 nm bathochrominis poslinkis DHDAP darinių **H12**, **H14** ir maždaug 6 nm diazatetracenų **H13**, **H15**. Tai rodo, kad medžiagos gali tvarkingiau išsidėstyti kietame būvyje [191, 217].



4 pav. UV-Vis absorbcijos spektrai tirpaluose po kaitinimo ir plovimo THF tirpikliu a) **H14**, b) **H15**

Junginių **H12–H15** plėvelės buvo kaitinamos jų polimerizacijos temperatūroje (2 lentelė) ir įvairiais intervalais plaunamos 3 ml THF. Po plovimo buvo išmatuoti surinktų tirpalų absorbcijos spektrai tam, kad būtų nustatytas laikas, per kurį medžiaga susipolimerina (4 pav.). Diazaacenu tinklinimo trukmė (t_{poly}) svyruoja nuo 5 iki 210 min (3 lentelė).

3 lentelė. Junginių **H12–H15** optinės savybės bei polimerizacijos trukmė

| Junginys | $\lambda_{\text{max}}^{\text{abs}}$, nm ^a | t_{poly} , min ^b |
|------------|--|---|
| H12 | 307 | 210 |
| H13 | 295 | 120 |
| H14 | 305 | 5 |
| H15 | 292 | 90 |

a) Plėvelių UV-Vis absorbcijos maksimumai.

b) Polimerizacijos trukmė.

1.4. Fotoelektrinės savybės

Junginių energijos viršmai ir elektronų pernaša tirpaluose, siekiant apskaičiuoti junginių E_{LUMO} ir E_{HOMO} , buvo matuojama taikant ciklinės voltamperometrijos (CV) metodą. Šios vertės neatspindi absoliučios kietosios būsenos arba dujų fazės jonizacijos energijų, tačiau gali būti naudojamos panašiams junginiams palyginti tarpusavyje (4 lentelė).

Norint įvertinti medžiagų energetinius lygius kietame būvyje jonizacijos potencialas (I_p) buvo išmatuotas fotoelektronų spektroskopijos ore metodu (PESA) (5 pav.). Šio metodo paklaida 0,03 eV. Visos 4 lentelėje pateiktos I_p vertės yra tinkamos naudoti perovskitiniuose saulės elementuose, kadangi švino pagrindo perovskito valentinė juosta yra tarp 5,0 ir 5,6 eV [125].

4 lentelė. Junginių H12–H15 energetinių lygmenų duomenys^a

| Junginys | E_{HOMO} , eV ^b | E_g^{opt1} , eV ^c | E_{LUMO} , eV ^d | I_p , eV ^e | E_g^{opt2} , eV ^f | EA , eV ^g |
|------------|--|--|--|----------------------------|--|---------------------------|
| H12 | -5,17 | 2,88 | -2,29 | 5,36 | 2,79 | 2,57 |
| H13 | -5,11 | 2,86 | -2,25 | 5,23 | 2,78 | 2,45 |
| H14 | -5,16 | 2,91 | -2,25 | 5,31 | 2,84 | 2,47 |
| H15 | -5,33 | 2,89 | -2,44 | 5,23 | 2,84 | 2,39 |

a) CV matavimai atlikti su stiklo elektrodu dichlormetano tirpaluose, naudojant 0,1 M tetrabutilamonio heksafluorofosfatą kaip elektrolitą ir Ag/AgNO₃ kaip palyginamąjį elektrodą. Kiekvienas matavimas buvo kalibruotas naudojant feroceną (Fc). Potencialai apskaičiuoti plg. su Fc⁺/Fc. b) Konversijos koeficientai: ferocenas DCM-SCE: 0,46 [219], SCE-SHE: 0,244 [220], SHE-vakuumas: 4,43 [221]. c) Optinės draustinės juostos E_g^{opt1} apskaičiuotos iš tirpalų absorbcijos spektrų. d) E_{LUMO} apskaičiuota pagal lygtį $E_{\text{LUMO}} = E_{\text{HOMO}} - E_g^{\text{opt1}}$. e) Kietosios būsenos junginių jonizacijos potencialas (I_p) buvo matuojamas fotoemisijos ore metodu iš plėvelių. f) Optinės draustinės juostos E_g^{opt2} apskaičiuotos iš plėvelių absorbcijos spektrų. g) Elektronų giminingumas (EA) apskaičiuotas pagal lygtį $EA = E_{\text{HOMO}} - E_g^{\text{opt2}}$.

1.5. Skyriaus išvados

Po daugybės nesėkmingų bandymų gauti konjuguotus polimerus buvo nuspręsta susintetinti monomerus **H12–H15**, kurie po kaitinimo galėtų suformuoti nekonjuguotas makromolekules. Visi gauti junginiai yra termiškai ir elektrochemiškai stabilūs, pasižymi tinkamais energetiniais lygmenimis, gali būti sutinkinti bei pakuoti kietoje būsenoje. Dėl santykinai aukštos polimerizacijos temperatūros medžiagas **H12–H14** galima naudoti tik invertuotuose perovskitiniuose saulės elementuose, tuo tarpu kaitinant **H15** susidaro lašeliai, o ne vientisa plėvelė, todėl jis yra netinkamas naudoti optoelektroniniuose įtaisuose.

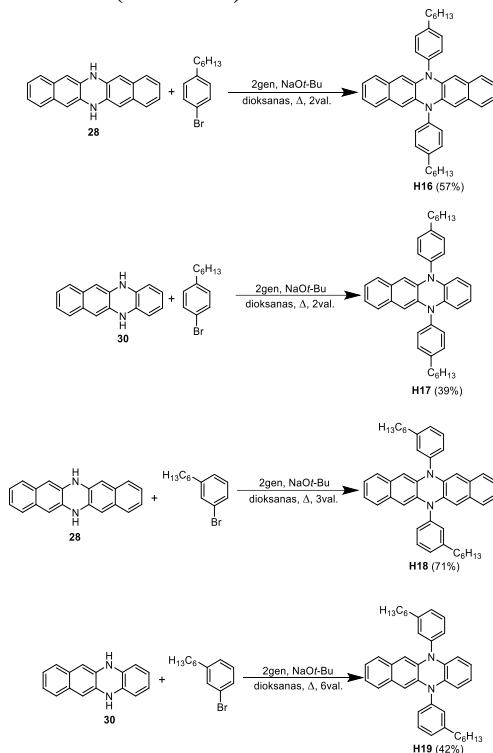
2. Mažamolekuliniai diazaacenu dariniai

Kaip minėta ankstesniame skyriuje, mažamolekuliniai organiniai skyles pernešantys junginiai turi daug privalumų lyginant su polimerais. Kuriant naujus junginius, galima sustiprinti tam tikras savybes (pvz., judrį) padidinant tarpmolekulinę sąveiką kietajame būvyje [191, 222, 223]. Tam pasiekti dažniausiai naudojama plokščių struktūrų, tokių kaip trukseno [224], pireno [225], tetratioantraceno [226] ir kitų policiklinių aromatinių angliavandenilių [227] įterpimas, siekiant pagerinti π - π sąveiką. Deja, tokie junginiai dažnai susiduria su tirpumo ir didelio kristališkumo problemomis [5].

Dihidroazaacenu (DHDA) yra įdomi medžiagų grupė, kuri dar nėra išbandyta perovskitiniuose saulės elementuose. Struktūriškai jie labai panašūs į plokščius acenus [228, 229], tačiau antriniai aminai esantys DHDA struktūroje atveria daug galimybių įvairioms modifikacijoms. Šis skyrius skirtas lengvai susintetinamiems dihidroazaacenu dariniams su pakaitais, gerinančiais tirpumą ir krūvio pernašos savybes.

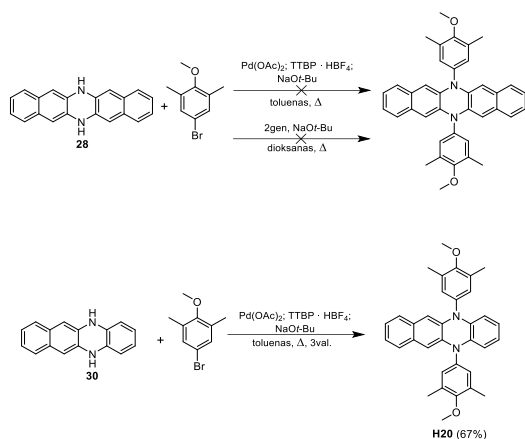
2.1. Dihydrodiazapentaceno ir dihidrodiazatetraceno darinių sintezė

DHDAP ir DHDAT dariniai **H16–H19** buvo susintetinti Buchwald-Hartwig kryžminio kopuliavimo reakcijos metu tarp atitinkamo brominto heksilbenzeno darinio ir junginio **28** arba **30** (4 schema).



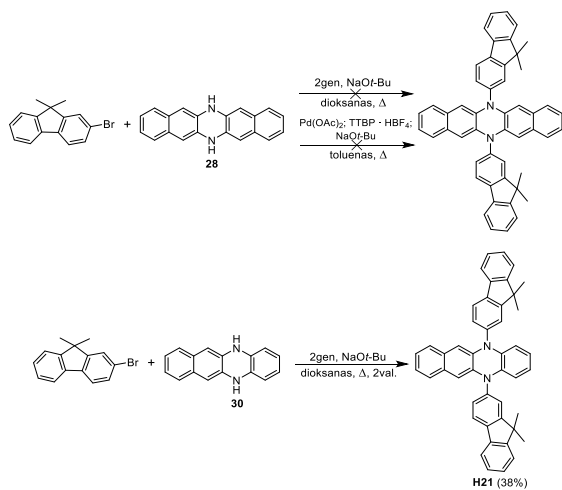
4 schema. Diazaacenu **H16–H19** sintezė

Paladžio katalizuojamos kryžminio sujungimo reakcijos metu tarp diazatetraceno **30** ir 4-brom-2,6-dimetilanizolo inertinėje argono atmosferoje naudojant sausą dioksaną kaip tirpiklį gautas DHDAT darinys **H20** (5 schema). Taikant tas pačias sąlygas jungiant **28** su 4-brom-2,6-dimetilanizolu produktas gautas nebuvo, tad nuspręsta pakeisti paladžio katalizatorių ir tirpiklį, tačiau tai neturėjo jokios įtakos reakcijos rezultatams (5 schema).



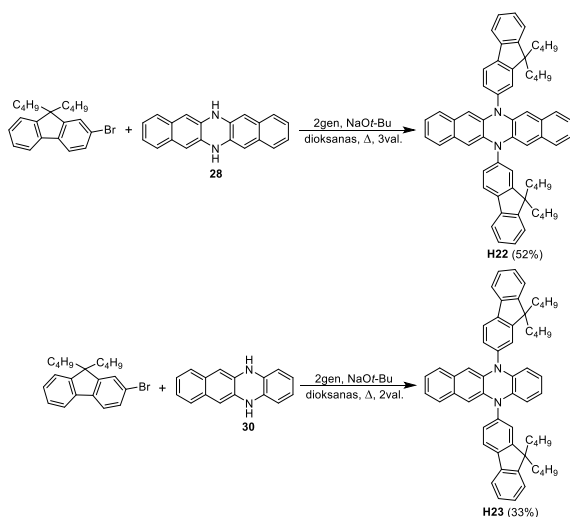
5 schema. Diazatetraceno H20 sintezė

Buchwald-Hartwig kryžminio kopuliavimo reakcijos metu tarp pentaceno analogo **28** ir 2-brom-9,9-dibutilfluoreno buvo gautos netirpios nuosėdos, iš kurių nepavyko išskirti norimo produkto (6 schema). Iš kitos pusės, paladžio katalizuojama reakcija tarp diazatetraceno **30** ir 2-brom-9,9-dimetilfluoreno vyko sklandžiai, jos metu gautas junginys **H21** (6 schema).



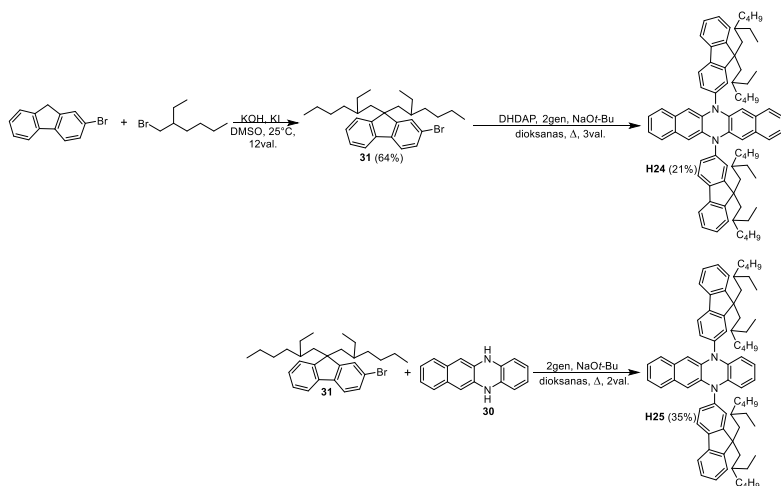
6 schema. Diazaaceno H21 sintezė

Norint pagerinti DHDAP ir DHDAT darinių su fluoreno fragmentais tirpumą, buvo naudojamos pradinės medžiagos, turinčios butilo pakaitus, kas lėmė junginių **H22** ir **H23** sintezę (7 schema).



7 schema. Diazaacenu **H22** ir **H23** sintezė

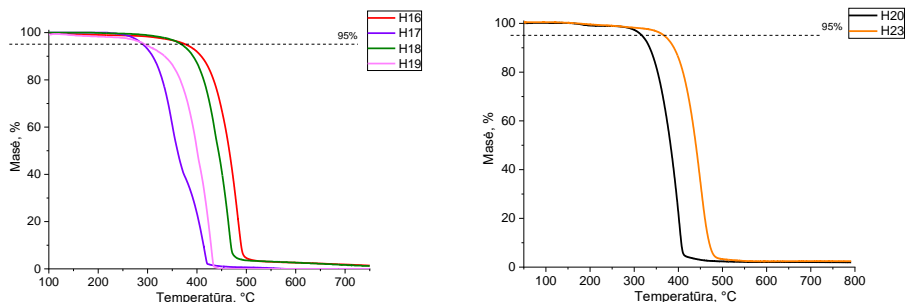
Norint dar labiau pagerinti DHDAP ir DHDAT darinių tirpumą, 2-brom-9,9-di(2-etilheksil)-9H-fluorenas (**31**) buvo susintetintas alkilinant 2-brom-9,9-dibutilfluoreną 2-etilheksilbromidu naudojant kalio hidroksidą kaip bazę. Gautas junginys buvo panaudotas reakcijose su diazaacenaais **28** ir **30** susidarant atitinkamai diazapentacenui **H24** ir diazatetracenui **H25** (8 schema).



8 schema. Diazaacenu **H24** ir **H25** sintezė

2.2. Terminės savybės

Vieni iš pagrindinių optoelektroninių prietaisų gamybos reikalavimų yra terminis stabilumas ir galimybė formuoti geros kokybės amorfinės arba retais atvejais kristalines plėveles [233]. Šiam tikslui pasiekti organiniai puslaidininkiai turi pasižymėti gan aukšta T_g arba T_m .



5 pav. Diazaacenu H16–H20 ir H23 TGA kreivės

Diazaacenu H16–H25 terminis stabilumas buvo matuojamas naudojant TGA, rezultatus galima pamatyti 5 lentelėje ir 5 pav. Visi testuoti junginiai prarado 5 % masės esant aukštesnei nei 290 °C temperatūrai, tai įrodo, jog jie yra pakankamai termiškai stabilūs, kad juos būtų galima naudoti perovskitiniuose saulės elementuose. Verta paminėti, jog greitas masės kitimas 5 pav. leidžia tikėtis, kad medžiagos H16–H20 ir H23 galės būti padengiamos vakuuminio nusodinimo būdu.

5 lentelė. Terminės junginių H16–H25 savybės

| Junginys | $T_g^a, ^\circ\text{C}$ | $T_m^b, ^\circ\text{C}$ | $T_{cr}^c, ^\circ\text{C}$ | $T_{dec}^d, ^\circ\text{C}$ |
|----------|-------------------------|-------------------------|----------------------------|-----------------------------|
| H16 | 35 | 164, 183 | 71, 166 | 377 |
| H17 | 11 | 117 | - | 291 |
| H18 | 25 | 165 | - | 367 |
| H19 | 0 | 102, 106 | - | 295 |
| H20 | 118 | 272 | 177 | 318 |
| H21 | - | 359 | 233 | 367 |
| H22 | 127 | 363 | 177 | 400 |
| H23 | - | 293 | 197 | 368 |
| H24 | 64 | - | - | 369 |
| H25 | 48 | - | - | 366 |

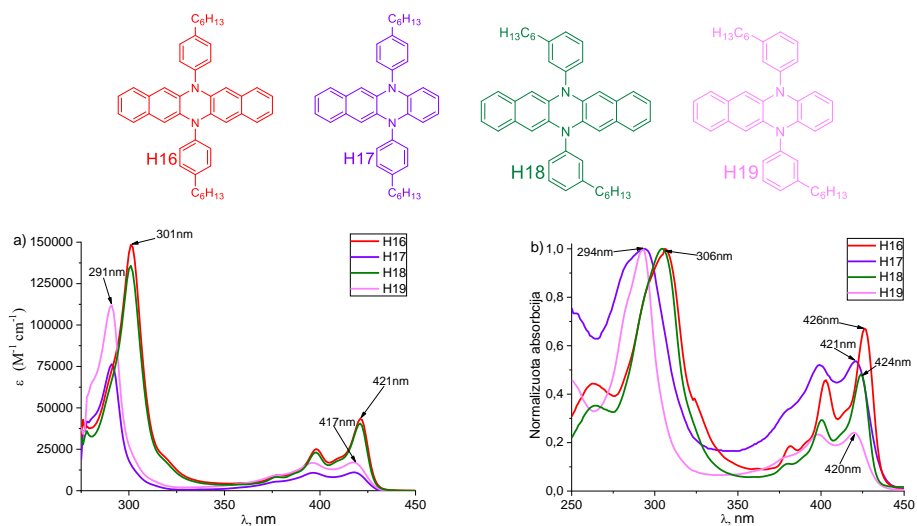
a) Nustatyta taikant DSC: kaitinimo greitis 10 K/min; N₂ atmosfera; antrasis kaitinimas. b) Lydymosi temperatūra užfiksuota tik pirmojo kaitinimo metu, 10 K/min. c) Nustatyta taikant DSC: kaitinimo greitis 10 K/min; N₂ atmosfera. d) Skilimo pradžia nustatyta TGA metodu: kaitinimo greitis 10 K/min; N₂ atmosfera.

Iš visos serijos junginių H20–H23 turi tinkamiausias termines savybes (aukštą T_g , T_m ir T_{dec}), reikalingas perovskitiniams saulės elementams. Greitas diazatetracenu H20 ir H23 garavimas aukštose temperatūrose suteikia jiems papildomo pranašumo saulės celių gamyboje, kadangi minėtieji junginiai gali būti padengti ne tik iš tirpalų, bet ir vakuuminio garinimo būdu.

2.3. Optinės savybės

Norint įvertinti konjuguotos sistemos pokyčius ir junginių galimybę tvarkingai išsidėstyti kietoje būsenoje, UV-Vis absorbcijos spektrai buvo matuoti iš

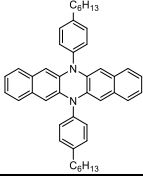
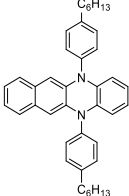
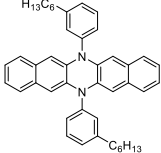
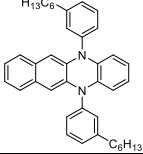
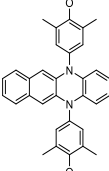
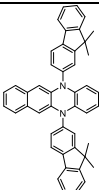
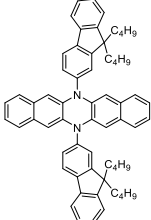
tolueno arba THF tirpalų ir plėvelių ant stiklo (6 pav.). Visiems bandytiems junginiams būdingas $n-\pi^*$ elektronų perėjimas ties maždaug 420 nm. DHDAT darinių **H17** ir **H19** $\pi-\pi^*$ absorbcijos maksimumai stebimi ties 291 nm, o diazapentacenų **H16**, **H18** – 301 nm (6a pav.). Lyginant su tetraceno analogais **H17**, **H19**, 10 nm batochrominis DHDAP darinių poslinkis gali būti paaikšintas didesne konjuguota sistema, kurią lemia papildomas fenilo žiedas diazapentacenuose **H16** ir **H18**.



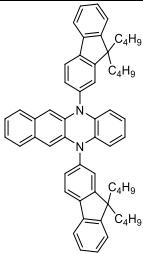
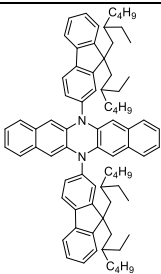
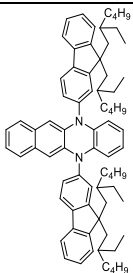
6 pav. a) UV-Vis absorbcijos spektrai junginių **H16–H19** toluene ir b) plėvelių ant stiklo

Lyginant absorbcijos spektrus toluene ir ant stiklo, galima pastebėti, jog kietoje būsenoje DHDAP ir DHDAT darinių absorbcijos maksimumai pasislinkę į trumpesnių bangų pusę atitinkamai per maždaug 5 nm ir 3 nm. Visų diazaacenų absorbcijos spektrų maksimumus galima matyti 6 lentelėje.

6 lentelė. Junginių **H16–H25** optinės savybės

| Nr. | Struktūra | $\lambda_{\text{max}}^{\text{abs}}$, nm ^a | $\lambda_{\text{max}}^{\text{abs}}$, nm ^b |
|------------|---|--|--|
| H16 |  | 301 | 306 |
| H17 |  | 292 | 295 |
| H18 |  | 300 | 305 |
| H19 |  | 291 | 294 |
| H20 |  | 289 | 293 |
| H21 |  | 290 | 294 |
| H22 |  | 300 | 304 |

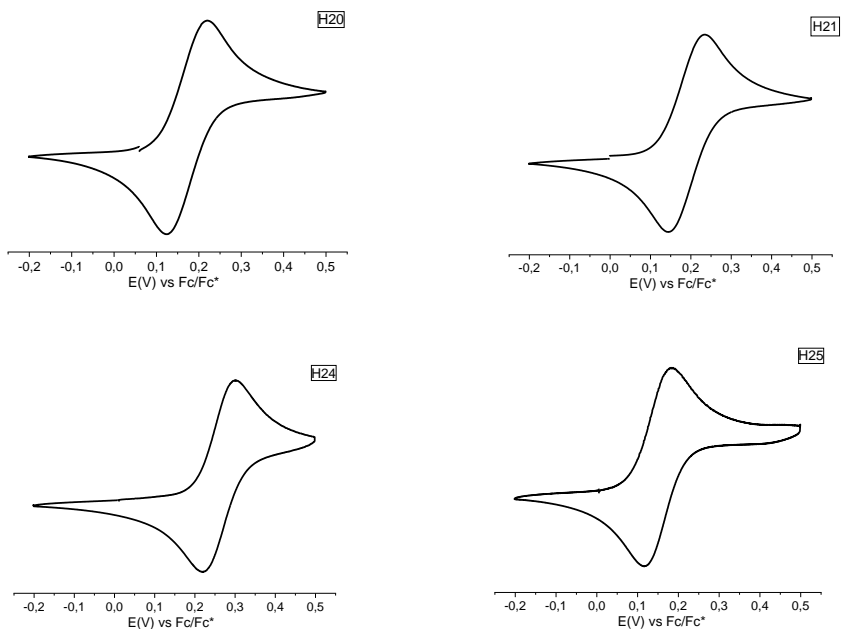
6 lentelės tęsinys. Junginių **H16–H25** optinės savybės

| | | | |
|------------|--|-----|-----|
| H23 |  | 290 | 293 |
| H24 |  | 300 | 304 |
| H25 |  | 290 | 293 |

a) Tirpalų UV-Vis absorbcijos maksimumai. b) Plėvelių UV-Vis absorbcijos maksimumai.

2.4. Fotoelektrinės savybės

Norint įvertinti elektrocheminį junginių **H16–H25** stabilumą buvo atlikti CV matavimai, voltamogramų pavyzdžiai matomi 7 pav. Duomenys, gauti šių matavimų metu, buvo panaudoti E_{LUMO} ir E_{HOMO} skaičiavimams (7 lentelė).



7 pav. Junginių **H20**, **H21**, **H24** ir **H25** CV voltamogramos

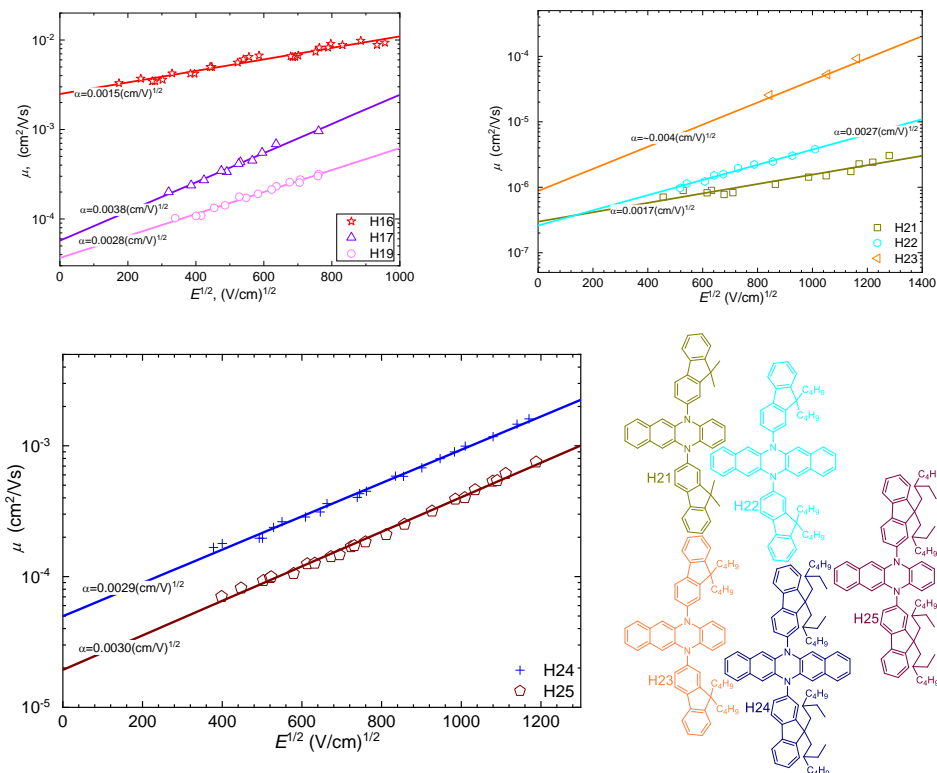
Norint įvertinti medžiagų energetinius lygius kietame būvyje I_p buvo išmatuotas PESA metodu (7 lentelė). Nepaisant papildomo fenilo žiedo diazapentacenų struktūroje, DHDAP darinio **H16** ir tetraceno analogo **H17** I_p vertės praktiškai vienodos, tačiau pakeitus heksilpakaitą iš parapozicijos į metajonizacijos potencialo vertės kinta netolygiai – pentaceno analogo **H18** stipriai padidėja, o diazatetraceno **H19** nežymiai sumažėja. Tai galima paaiškinti skirtinga diazaacenų simetrija: diazapentacenai dėl savo simetrijos yra mažiau lankstūs erdvėje nei DHDAP dariniai, todėl heksilpakaitai metapozicijoje sukelia daugiau erdvinį trikdžių pastariesiems, kas lemia skirtingas I_p vertes.

7 lentelė. Junginių H16–H25 energetiniai lygmenys ir judriai ^a

| Junginys | E_{HOMO} , eV ^b | E_g^{opt1} , eV ^c | E_{LUMO} , eV ^d | I_p , eV ^e | E_g^{opt2} , eV ^f | EA , eV ^g | $\frac{\mu_0}{h}$ $\text{cm}^2 \text{V}^{-1} \text{s}^{-1}$ | $\frac{\mu_h}{h}$ $\text{cm}^2 \text{V}^{-1} \text{s}^{-1}$ |
|------------|--|--|--|----------------------------|--|---------------------------|--|--|
| H16 | -5,13 | 2,87 | -2,26 | 5,07 | 2,83 | 2,24 | $2,5 \cdot 10^{-3}$ | $1,1 \cdot 10^{-2}$ |
| H17 | -5,06 | 2,86 | -2,20 | 5,12 | 2,82 | 2,30 | $5,8 \cdot 10^{-5}$ | $1,15 \cdot 10^{-3}$ |
| H18 | -5,16 | 2,87 | -2,29 | 5,31 | 2,84 | 2,47 | - | - |
| H19 | -5,04 | 2,86 | -2,18 | 5,06 | 2,84 | 2,22 | $3,7 \cdot 10^{-5}$ | $3,5 \cdot 10^{-4}$ |
| H20 | -5,11 | 2,86 | -2,25 | 4,98 | 2,83 | 2,15 | - | - |
| H21 | -5,13 | 2,80 | -2,33 | 5,18 | 2,78 | 2,40 | $3 \cdot 10^{-7*}$ | $1,6 \cdot 10^{-6*}$ |
| H22 | -5,15 | 2,83 | -2,32 | 5,28 | 2,83 | 2,45 | $2,7 \cdot 10^{-7*}$ | $3,8 \cdot 10^{-6*}$ |
| H23 | -5,10 | 2,79 | -2,31 | 5,19 | 2,79 | 2,40 | $9 \cdot 10^{-7}$ | $5 \cdot 10^{-5}$ |
| H24 | -5,20 | 2,85 | -2,35 | 5,31 | 2,84 | 2,47 | $5 \cdot 10^{-5}$ | $9,3 \cdot 10^{-4}$ |
| H25 | -5,09 | 2,82 | -2,27 | 5,23 | 2,78 | 2,45 | $2 \cdot 10^{-5}$ | $4 \cdot 10^{-4}$ |

a) CV matavimai atlikti su stiklo elektrodu dichlormetano tirpaluose, naudojant 0,1 M tetrabutilamonio heksafluorofosfatą kaip elektrolitą ir Ag/AgNO₃ kaip palyginamąjį elektrodą. Kiekvienas matavimas buvo kalibruotas naudojant feroceną (Fc). Potencialai apskaičiuoti plg. su Fc⁺/Fc. b) Konversijos koeficientai: ferocenas DCM-SCE: 0,46 [219], SCE-SHE: 0,244 [220], SHE-vakuumas: 4,43 [221]. c) Optinės draustinės juostos E_g^{opt1} apskaičiuotos iš tirpalų absorbcijos spektrų. d) E_{LUMO} apskaičiuota pagal lygtį $E_{\text{LUMO}} = E_{\text{HOMO}} - E_g^{\text{opt1}}$. e) Kietosios būsenos junginių jonizacijos potencialas (I_p) buvo matuojamas fotoemisijos ore metodu iš plėvelių. f) Optinės draustinės juostos E_g^{opt2} apskaičiuotos iš plėvelių absorbcijos spektrų. g) Elektronų giminingumas (EA) apskaičiuotas pagal lygtį $EA = E_{\text{HOMO}} - E_g^{\text{opt2}}$. h) Dreifinio judrio vertė esant nuliniam lauko stipriui. i) Judrio vertė, kai lauko stipris yra $6,4 \cdot 10^5 \text{ V cm}^{-1}$. * Junginio judrio vertės buvo išmatuotos iš jo ir PC-Z mišinio (1 : 1).

Heksilgrupių pakeitimas metoksi ir metilo grupėmis junginyje **H20** lemia I_p vertės sumažėjimą iki mažiau nei 5,00 eV. Savo ruožtu fluoreno pakaitai su skirtingo ilgio alifatinėmis grandinėmis, įvesti vietoje heksilbenzeno, diazaacenuose **H21–H25** lemia I_p padidėjimą. Verta paminėti, jog alifatinių grandinių ilgis beveik nedaro jokios įtakos I_p vertei (7 lentelė).



8 pav. Junginių **H16**, **H17**, **H19** ir **H21–H25** judriai

Susintetintų junginių **H16–H25** krūvininkų pernašos savybės buvo tirtos kserografiniu lėkio trukmės metodu, diazaacenų judrio grafikus galima matyti 8 pav. Pagrindiniai parametrai gaunami šiuo metodu yra dreifinis judris esant nuliniam lauko stipriui ir judris esant lauko stipriui $6,4 \cdot 10^5 \text{ V cm}^{-1}$. Junginių **H18** ir **H20** dreifinių judrių išmatuoti nepavyko atitinkamai dėl didelio kristališkumo ir prastos kokybės plėvelės. Iš visų bandytų medžiagų DHDAP darinys **H16** pasižymėjo didžiausiomis krūvininkų judrio vertėmis, pasiekdamas $2,5 \cdot 10^{-3} \text{ cm}^2 \text{ V}^{-1} \text{ s}^{-1}$ esant nuliniam lauko stipriui ir $1,1 \cdot 10^{-2} \text{ cm}^2 \text{ V}^{-1} \text{ s}^{-1}$ esant stipresniam laukui. Visų junginių dreifinių judrių vertės pateiktos 7 lentelėje.

2.5. Skyriaus išvados

Visos šiame skyrelyje aprašytos medžiagos yra elektrochemiškai ir termiškai stabilios, dauguma iš jų yra arba gali būti kristalinės išskyrus **H24** ir **H25**, kurios yra amorfinės dėl labai ilgų etilheksilgrandinėlių, prijungtų prie fluoreno pakaitų. Visų medžiagų energetiniai lygmenys tinkami naudojimui perovskitiniuose saulės elementuose, o diazaaceni **H16**, **H17**, **H19**, **H24** ir **H25** taip pat pasižymi sąlyginai geru krūvininkų transportu. Dažniausiai renkantis medžiagas minėtiems saulės elementams vieno puikaus parametro neužtenka, tad reikia atsižvelgti į junginius, turinčius geriausias savybių rinkinius. Atsižvelgiant į tai junginiai **H16**,

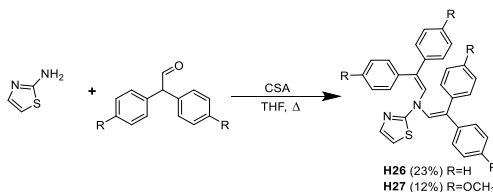
H17 ir **H19** atrodo kaip daugiausiai žadantys *p*-tipo puslaidininkiai. Šie diazaacenaai gali išsidėstyti šiek tiek tvarkingiau plėvelėje, turi tinkamus energijos lygmenis ir santykinai aukštus judrius, tačiau dėl mažo T_g jie prietaise turėtų būti naudojami tik kristališkajame būvyje. Savo ruožtu junginiai **H24** ir **H25** dėl savo žemų stiklėjimo temperatūrų negali būti naudojami perovskitiniuose saulės elementuose, o prastos krūvio pernašos savybės kelia abejonę dėl likusių junginių panaudojimo optoelektronikoje.

3. Naujų sistemų, turinčių difeniletetilfragmentų, tyrimas

Per pastarąjį dešimtmetį perovskitiniuose saulės elementuose naudojant brangias skyles pernešančias medžiagas spiro-MeOTAD ir PTAA, buvo pasiektas didesnis nei 25 % našumas [8]. Nepaisant aukšto efektyvumo šie *p*-tipo puslaidininkiai yra per brangūs komerciniam naudojimui, todėl ieškoma pigesnių, tačiau panašų našumą demonstruojančių medžiagų. Vienas iš būdų tai pasiekti yra sintetinti junginius iš pigių komerciškai prieinamų medžiagų naudojant sudėtingų sąlygų nereikalaujančias reakcijas. Iš literatūros žinoma, jog prijungus feniletetilardinius galima pagerinti junginių stiklėjimo temperatūras ir terminį stabilumą [237] bei kai kuriais atvejais ir dreifinį judrį [191, 236, 237]. Todėl šis skyrelis skirtas tirti įvairias sistemas, turinčias feniletetilfragmentų.

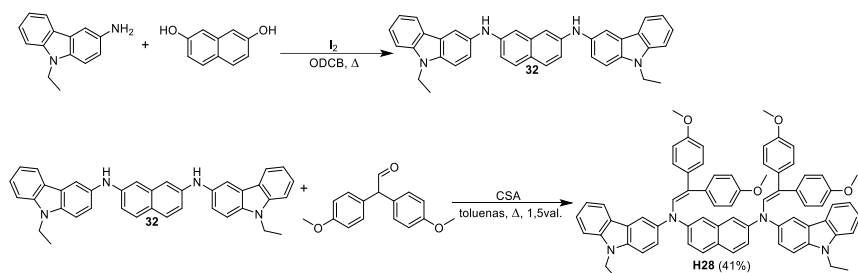
3.1. Junginių su keliais difeniletetilardiniais sintezė

N,N-bis(2,2-difeniletetil)-1,3-tiazol-2-aminas (**H26**) buvo susintetintas kamparo sulfoninės rūgšties (CSA) katalizuojamoje kondensacijos reakcijoje tarp 2-aminotiazolo ir difenilacetaldehido THF. Tokios pat sąlygos taikytos kondensuojant 2,2-bis(4-metoksifenil)acetaldehidą su minėtu aminu, gaunant enaminą **H27** (9 schema).



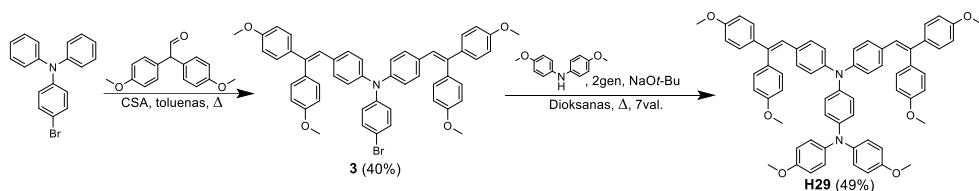
9 schema. Tiazolo darinių **H26** ir **H27** sintezė

Dešimtmečiais karbazolas dėl gero cheminio stabilumo, lengvo modifikavimo ir gerų fotoelektrinių savybių buvo naudojamas kaip vienas pagrindinių junginių sintetinant medžiagas, skirtas naudoti optoelektronikoje [140, 236]. Atsižvelgiant į tai buvo susintetintas karbazolo darinys **32**, kuris toliau buvo kondensuotas su 2,2-bis(4-metoksifenil)acetaldehidu toluene esant CSA, gaunant enaminą **H28** (10 schema).



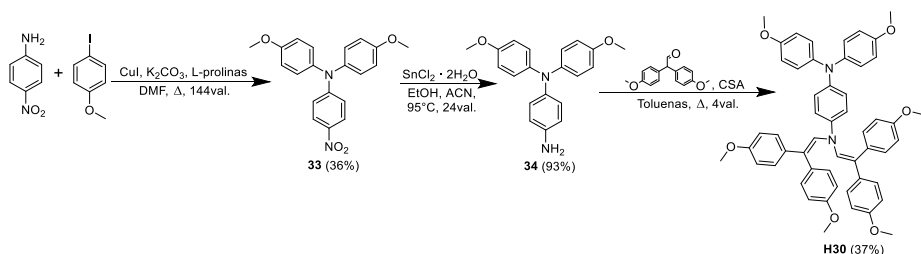
10 schema. Enamino **H28** sintezė

Trifenilamino dariniai taip pat yra dažnai naudojami optoelektronikoje, todėl ieškant optimalios chromoforinės sistemos reikėtų įtraukti ir juos. Sukondensavus TPA ir 2,2-bis(4-metoksifenil)acetaldehidą susintetintas dipakeistas TPA tarpinis junginys **3**, kuris kartu su 4,4'-dimetoksidifenilaminu buvo panaudotas Buchwald-Hartwig kryžmininio kopuliavimo reakcijoje gaunant TPA darinį **H29** (11 schema).



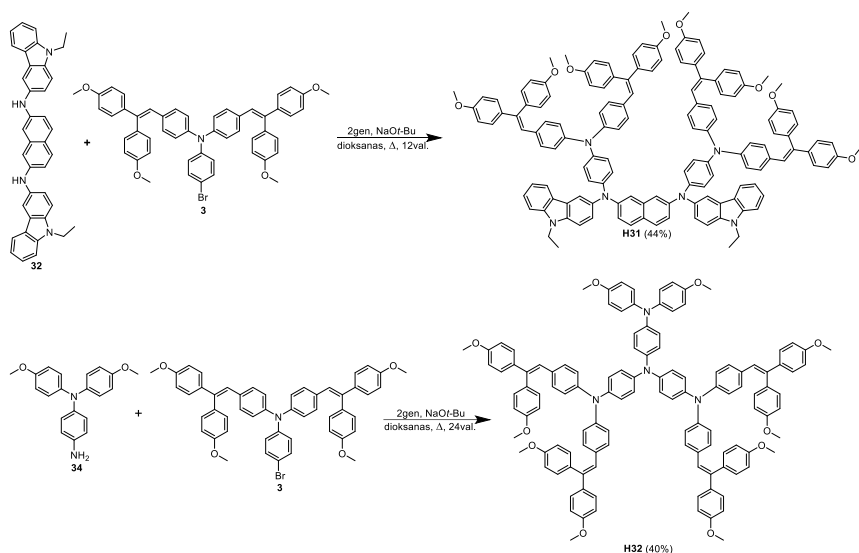
11 schema. TPA darinio **H29** sintezė

p-Nitroanilinas ir *p*-jodoanizolis buvo sujungti naudojant Ulmano tipo reakciją argono atmosferoje, bevandeniame DMF, gaunant 4-nitro-4',4'-dimetoksitrifenilaminą (**33**). Nitro grupės redukcija buvo atlikta naudojant alavo chlorido dihidratą etanolio ir acetonitrilo mišinyje, gaunant aminą **34**, kuris paskesnėje reakcijoje sukondensuotas su 2,2-bis(4-metoksifenil)acetaldehidu, esant CSA, susintetinant enamina **H30** (12 schema).



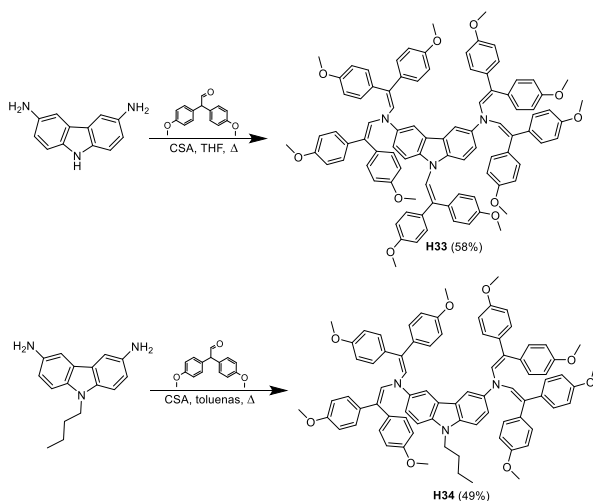
12 schema. Enamino **H30** sintezė

TPA dariniai **H31** ir **H32** buvo susintetinti reaguojant bromintam trifenilaminui **3** su atitinkamai aminu **32** arba **34** paladžio katalizuojamoje reakcijoje, argono atmosferoje, bevandeniame dioksane (13 schema).



13 schema. TPA darinių **H31** ir **H32** sintezė

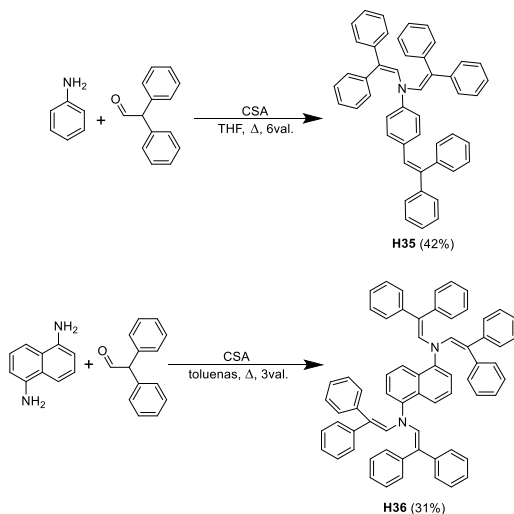
Norint geriau įvertinti karbazolo įtaką junginių savybėms buvo nuspręsta susintetinti enaminus **H33** ir **H34** CSA katalizuojamomis kondensacijos reakcijomis tarp atitinkamų karbazolo darinių ir 2,2-bis (4-metoksifenil)acetaldehido (14 schema).



14 schema. Karbazolo enaminų **H33** ir **H34** sintezė

Neseniai buvo įrodyta, kad nebrangūs junginiai, tokie kaip anilinas, gali būti panaudoti kaip pradinės medžiagos sintetinant skyles pernešančius junginius [20], kas paskatino enaminų **H35** ir **H36** sintezę. Rūgštimi katalizuojamos reakcijos tarp anilino ir difenilacetaldehido metu gautas anilino darinys **H35**. Beveik

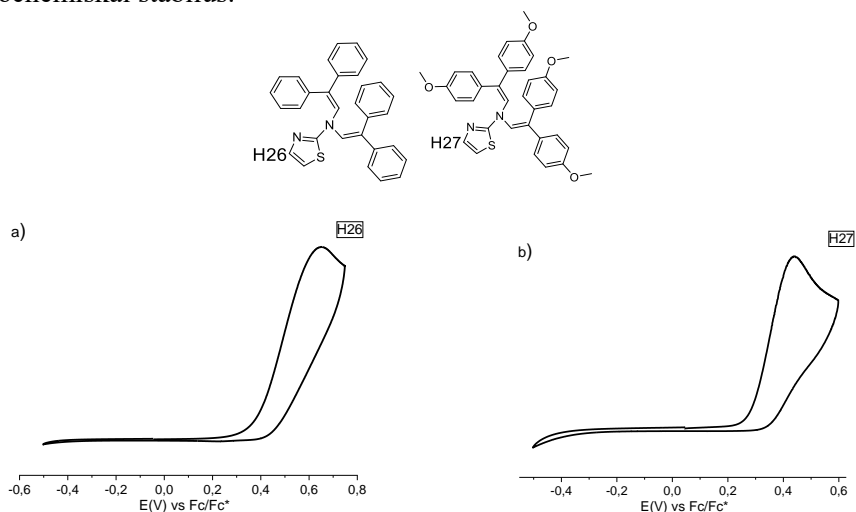
identiškomis sąlygomis iš 1,5-naftalendiamino buvo susintetintas enaminas **H36** (15 schema).



15 schema. Junginių **H35** ir **H36** sintezė

3.2. Fotoelektrinės savybės

Tikrinant junginių stabilumą CV metodu buvo pastebėta, jog tiazolo dariniai **H26** ir **H27** oksiduojasi negrįžtamai (9 pav.). Kiti tirti junginiai buvo elektrochemiškai stabilūs.

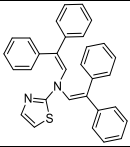
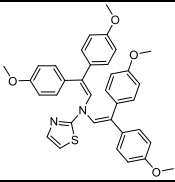
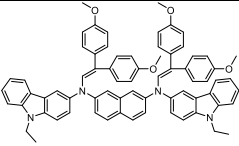
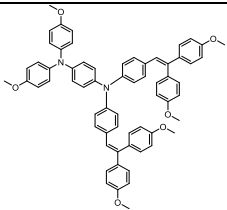
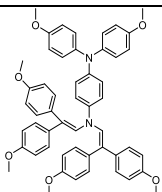
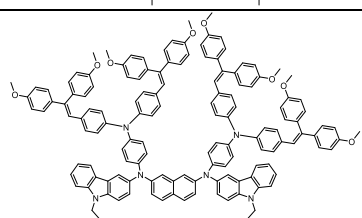


9 pav. CV voltamogramos junginių a) **H26**, b) **H27**

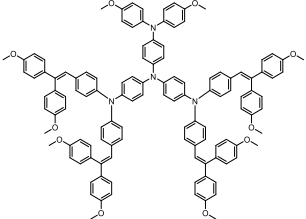
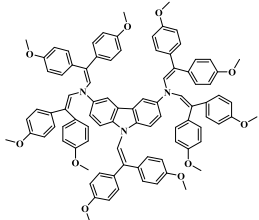
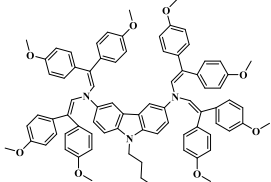
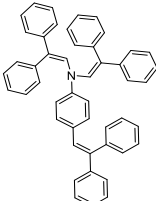
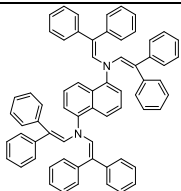
Jonizacijos potencialo ir dreifinio judrio rezultatai matomi 8 lentelėje. Išanalizavus duomenis matyti, jog didžiausios I_p vertės priklauso tiazolo dariniams

H26 ir **H21**, o mažiausios – metoksigrupes turintiems enaminamas **H28**, **H30**, **H33**, **H34** bei dideles konjuguotas sistemas turintiems TPA dariniams **H31** ir **H32**. Geriausius krūvininkų judrius pademonstravo karbazolo junginiai **H33** ir **H34** bei anilino enaminas **H35**. Verta paminėti, jog nepavyko išmatuoti medžiagų **H28** ir **H36** dreifinių judrių atitinkamai dėl labai silpnų krūvio transportavimo savybių ar prastos kokybės plėvelės, o junginių **H31** ir **H32** judrius pavyko nustatyti tik sumaišius juos su PC-Z santykiu 1 : 1.

8 lentelė. Junginių **H26–H36** jonizacijos potencialai ir judriai

| Nr. | Struktūra | I_p , eV ^a | μ_0 , cm ² V ⁻¹ s ⁻¹ b | μ_h , cm ² V ⁻¹ s ⁻¹ c |
|------------|---|----------------------------|--|--|
| H26 |  | 5,52 | 1·10 ⁻¹¹ | 8·10 ⁻⁹ |
| H27 |  | 5,40 | 4·10 ⁻¹⁰ | 1,2·10 ⁻⁷ |
| H28 |  | 5,00 | - | - |
| H29 |  | 5,21 | 5·10 ⁻⁷ | 4,5·10 ⁻⁵ |
| H30 |  | 5,06 | 6·10 ⁻⁷ | 1,1·10 ⁻⁴ |
| H31 |  | 5,00 | 3·10 ^{-8*} | 4,4·10 ^{-7*} |

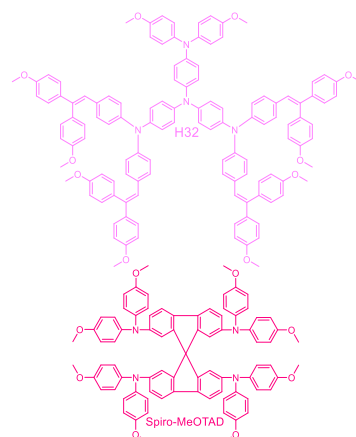
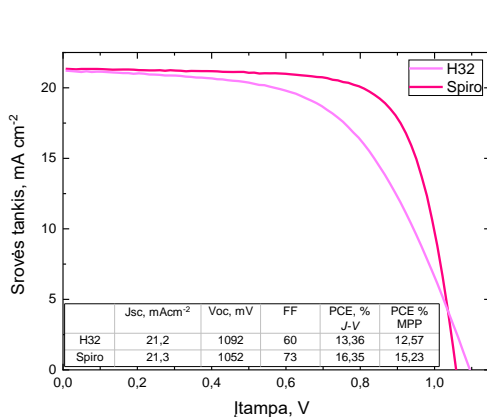
8 lentelės tęsinys. Junginių **H26–H36** jonizacijos potencialai ir jūdriai

| | | | | |
|------------|---|------|---------------------|-----------------------|
| H32 |  | 5,00 | $3 \cdot 10^{-8}$ * | $1,2 \cdot 10^{-6}$ * |
| H33 |  | 5,01 | $3,7 \cdot 10^{-5}$ | $7,8 \cdot 10^{-4}$ |
| H34 |  | 4,96 | $1,2 \cdot 10^{-4}$ | $1,1 \cdot 10^{-3}$ |
| H35 |  | 5,31 | $6 \cdot 10^{-4}$ | $2,5 \cdot 10^{-2}$ |
| H36 |  | 5,31 | - | - |

a) Kietosios būsenos junginių jonizacijos potencialas (I_p) buvo matuojamas fotoemisijos ore metodu iš plėvelių. b) Dreifinio jūdrio vertė esant nuliniam lauko stipriui. c) Jūdrio vertė, kai lauko stipris yra $6,4 \cdot 10^5 \text{ V cm}^{-1}$. * Junginio jūdrio vertės buvo išmatuotos iš jo mišinio su PC-Z santykiu 1 : 1.

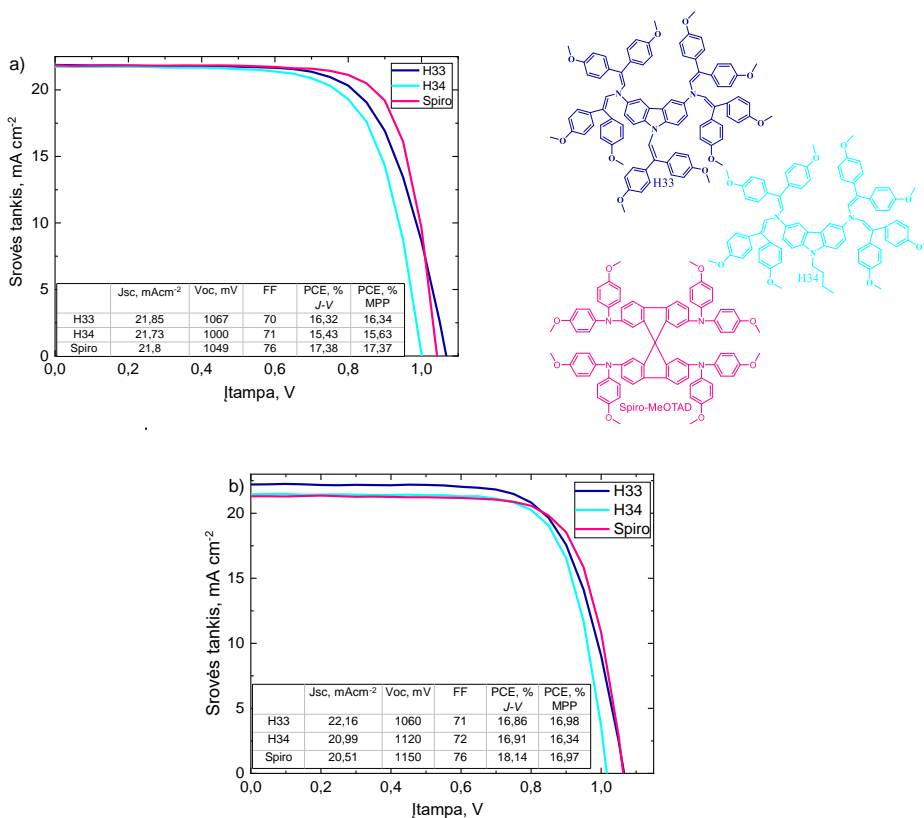
3.3. Perovskitinių saulės elementų rezultatai

TPA darinys **H32** buvo išbandytas įprastos architektūros (n-i-p) perovskitiniuose saulės elementuose, kuriuos sudarė fluoru legiruotas alavo oksidas (FTO), SnO_2 nanodalelės, fenil-C61-sviesto rūgšties metilesteris (PCBM), perovskito sluoksnis $\text{FA}_{0,83}\text{Cs}_{0,17}\text{Pb}(\text{I}_{0,9}\text{Br}_{0,1})_3$, skyles pernešanti medžiaga ir aukso elektrodas. Visi matavimai buvo atlikti naudojant standartinį AM 1,5 G apšvietimą, p-tipo puslaidininkiai naudoti su LiTFSI ir 4-*tert*-butilpiridino (tBP) priedais.



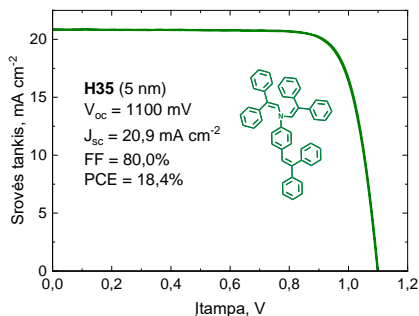
10 pav. Geriausiai veikiančių perovskitinių saulės elementų, kuriuose junginiai **H32** ir spiro-OMeTAD naudojami kaip skyles pernešančios medžiagos, charakteristikos

Geriausiai veikiantis saulės elementas, pagamintas naudojant **H32** kaip skyles pernešančią medžiagą, pasiekė 13,36 % energijos konversijos efektyvumą (PCE). Išmatuotas prietaiso srovės tankis buvo (J_{sc}) 21,2 mA cm⁻², atvirosios grandinės įtampa (V_{oc}) – 1092 mV, užpildymo faktorius (FF) – 60 %. Lyginant su plačiai naudojamu spiro-MeOTAD, **H32** demonstruoja panašias J_{sc} ir V_{oc} vertes, tačiau ženkliai mažesnis FF lemia beveik 3 % mažesnę našumą (10 pav.). Šiems rezultatams gali daryti įtaką priedų koncentracijos, kurios yra pritaikytos spiro-MeOTAD, tačiau gali visiškai netikti junginiui **H32** [128, 129, 240].



11 pav. Geriausiai veikiančių perovskitinių saulės elementų charakteristikos naudojant a) **H33**, **H34** ir spiro-OMeTAD su priedais, b) be priedų **H33**, **H34** ir spiro-OMeTAD su priedais

Karbazolo enaminai **H33**, **H34** buvo išbandyti tokio pat tipo ir struktūros prietaisuose kaip ir **H32**. Pirminiai bandymai buvo atlikti naudojant LiTFSI ir *t*BP priedus. Saulės elementai su šiais junginiais pasiekė apie 16 % našumą (11a pav.), tačiau tolesni bandymai atskleidė, jog minėtiems enaminams priedų nereikia tam, kad pasiektų gerus rezultatus. Prietaisai buvo optimizuoti sumažinant **H33** ir **H34** sluoksnių storį iki 45~55 nm (spiro-MeOTAD reikalingas 200 nm storis), kas ir leido atsikratyti LiTFSI ir *t*BP. Saulės elementai su skylių transportinėmis medžiagomis **H33** ir **H34** be priedų pasiekė beveik 17 % našumą, nusileidžiantį tik 1 % spiro-MeOTAD, kuris buvo naudotas su LiTFSI ir *t*BP (11b pav.). Verta paminėti, jog priedų nenaudojimas kenkia prietaiso ilgaamžiškumui [109, 243], todėl karbazolo dariniai **H33** ir **H34** tampa realiais kandidatais pakeisti spiro-MeOTAD kaip skylių pernešantys *p*-tipo puslaidininkiai.



12 pav. Saulės elemento charakteristikos naudojant 5 nm storio **H35** sluoksnį

Anilino darinys **H35** panaudotas perovskitiniame saulės elemente, kurio visi sluoksniai buvo padengti naudojant vakuuminio nusodinimo metodą. Prietaiso struktūra buvo tokia: ant stiklo padengtas ITO, MoO_3 , **H35**, perovskitas MAPI, elektronus pernešanti medžiaga C_{60} , batokuproinas (BCP) ir sidabro elektrodas. Minėtasis saulės elementas pasiekė 18,4 % našumą (12 pav.), šis rezultatas yra vienas geriausių tokio tipo prietaisuose [245, 246].

3.4. Skyriaus išvados

Perovskitiniuose saulės elementuose buvo išbandyti geriausių savybių rinkinį turintys junginiai. TPA darinys **H32**, nepaisant žemo judrio, pademonstravo neblogus rezultatus saulės elementuose, kas teikia vilties, jog optimizavus priedų kiekius bandinyje, **H32** galės konkuruoti su spiro-MeOTAD. Savo ruožtu karbazolo enaminai **H33** ir **H34** pasiekė beveik 17 % našumą nenaudojant jokių priedų, todėl jie tampa patrauklia alternatyva minėtam spiro junginiui. Paskutinis *p*-tipo puslaidininkis, išbandytas perovskitiniuose saulės elementuose, buvo anilino darinys **H35**, kuris pademonstravo didesnę nei 18 % efektyvumą invertuotame prietaise, kurio visi sluoksniai buvo padengti vakuuminio nusodinimo būdu. Šis rezultatas yra vienas geriausių tokio tipo saulės elementuose [245, 246] ir nulėmė tolesniame skyrelyje aprašytų junginių sintezę bei tyrimus.

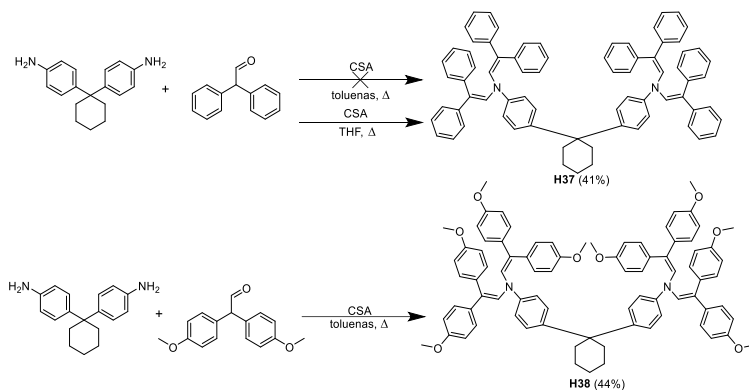
4. Anilino dariniai kaip skyles pernešančios medžiagos

Anilinas, vienas plačiausiai chemijos pramonėje naudojamų junginių, yra labai pigus ir gaminamas didžiuliu mastu [247]. Nenuostabu, kad anilinas taip pat naudojamas puslaidininkinių medžiagų, skirtų naudojimui optoelektronikoje [20, 248], sintezėje. Atsižvelgiant į praeito skyrelio rezultatus buvo nuspręsta sintetinti krūvininkus pernešančius enaminus giminingus anilinui, pasitelkiant vieno žingsnio reakcijas, nenaudojant brangių pereinamųjų metalų grupės katalizatorių.

4.1. Anilino darinių, turinčių difeniletetilfragmentų, sintezė

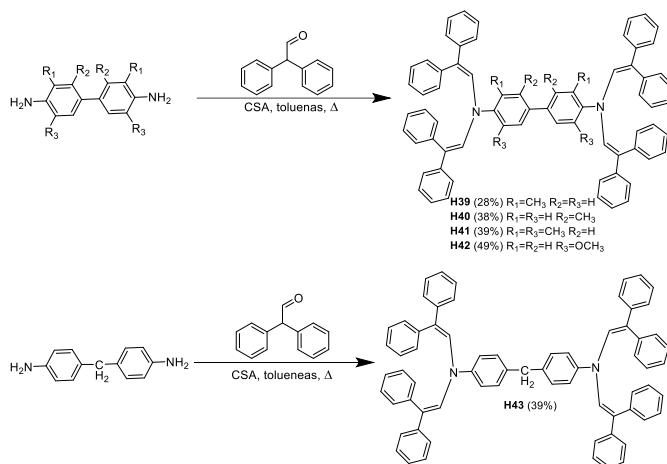
Kondensacijos reakcija tarp 1,1-bis(4-aminofenil)cikloheksano ir difenilacetaldehido, naudojant CSA kaip katalizatorių, buvo nesėkmingai vykdoma toluene, tačiau pakeitus tirpiklį į THF, gautas enaminas **H37**. Savo ruožtu

metoksigrupes turintis enaminas **H38** buvo sėkmingai gautas toluene kondensuojant 1,1-bis(4-aminofenil)cikloheksaną su 2,2-bis(4-metoksifenil)acetaldehidu, esant rūgštiniam katalizatoriui (16 schema).



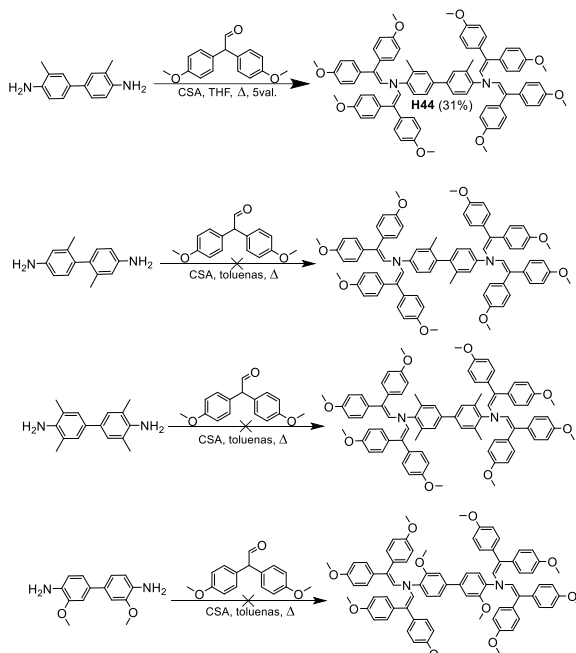
16 schema. Junginių **H37** ir **H38** sintezė

Bifenilo dariniai **H39–H43** buvo sintetinami kondensuojant atitinkamus bifenilo darinius su difenilacetaldehidu CSA katalizuojamoje reakcijoje (17 schema).



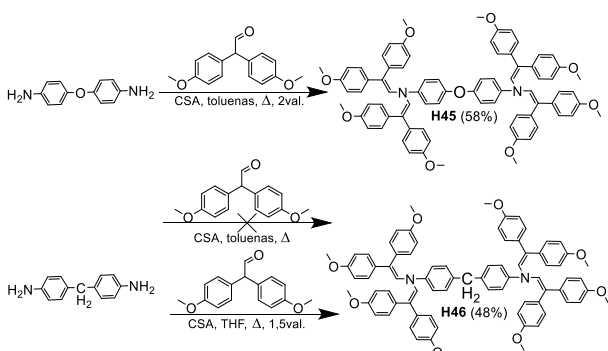
17 schema. Enaminų **H39–H43** sintezė

o-Tolidino ir 2,2-bis(4-metoksifenil)acetaldehido kondensavimas toluene buvo nesėkmingas, tai lėmė tirpiklio pakeitimą į THF, dėl to gautas bifenilo darinys **H44**. *m*-Tolidino, 3,3',5,5'-tetrametilbenzidino ir *o*-dianizidino reakcijų su minėtu metoksigrupes turinčiu aldehidu metu norimas produktas gautas nebuvo (18 schema). Tai gali būti dėl šalutinių reakcijų vykstančių tarp reagentų metilbenzene.



18 schema. Bifenilų kondensacijos reakcijos su 2,2-bis(4-metoksifenil)acetaldehidais

Oksidianilino darinys **H45** buvo gautas reaguojant 2,2-bis(4-metoksifenil)acetaldehidui su 4,4'-oksidianilinu toluene esant rūgštiniam katalizatoriui. Naudojant metilbenzeną kaip tirpiklį 4,4'-metilendianilino kondensacijai su minėtu metoksialdehidu enaminas **H46** susintetintas nebuvo, tačiau panašiai kaip ir **H44** atveju junginys **H46** buvo gautas pakeitus tirpiklį į THF (19 schema).

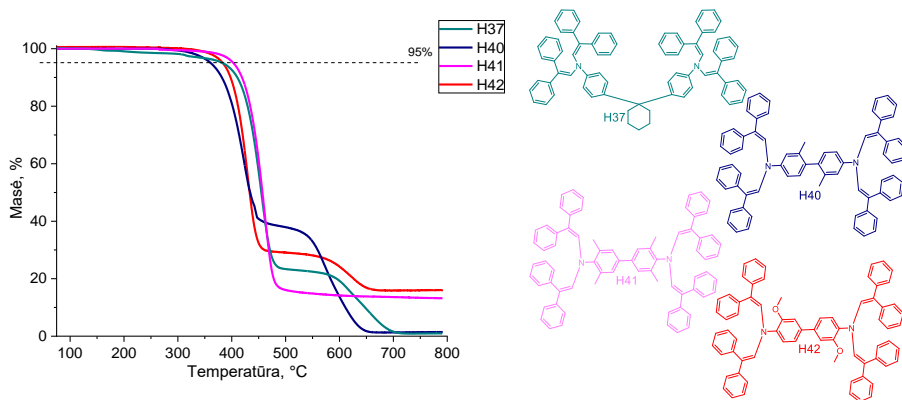


19 schema. Enaminų **H45** ir **H46** sintezė

4.2. Terminės savybės

Medžiagų terminis stabilumas buvo išmatuotas naudojant TGA, rezultatai matomi 9 lentelėje. Visi tirti junginiai, išskyrus **H44**, prarado 5 % masės

aukštesnėje nei 300 °C temperatūroje pademonstruodami, kad jie yra pakankamai termiškai stabilūs naudoti perovskitiniuose saulės elementuose. Verta paminėti, jog greitas masės praradimas matomas enaminų **H37**, **H40–H42** TGA grafikuose (13 pav.) rodo, kad juos galima padengti vakuuminio nusodinimo būdu.



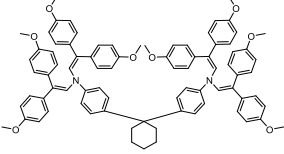
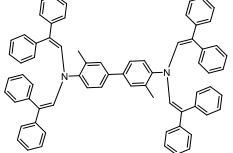
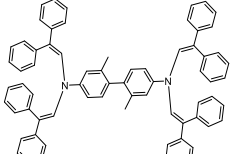
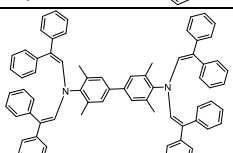
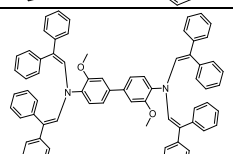
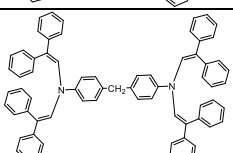
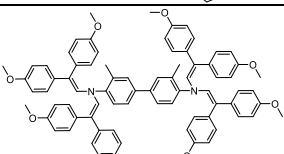
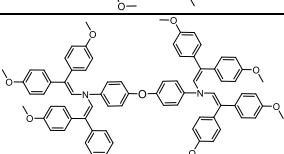
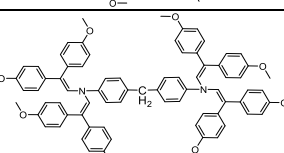
13 pav. Enaminų **H37**, **H40–H42** TGA kreivės

Trumpai apžvelgiant 9 lentelę galima pastebėti, jog bifenilo dariniai, turintys metoksigrupių savo struktūroje, pasižymi žemesnėmis stiklėjimo ir lydymosi temperatūromis nei atitinkami analogai be metoksigrupių, o enaminų **H38** ir **H46** atveju alkoksigrupių įvedimas lemia tai, jog junginiai tampa amorfiniai. Remiantis tik terminėmis savybėmis perspektyviausi enaminai perovskitiniams saulės elementams būtų **H39**, **H40** ir **H46**, nes jie yra visiškai amorfiniai ir turi palyginti aukštą T_g , o **H40** yra kristalinis ir tinkamai paruoštas taip pat galėtų būti panaudotas prietaisuose [233]. Verta paminėti, jog dėl savo žemos T_g ir prasto terminio stabilumo mažiausiai vilčių teikia bifenilo darinys **H44**, kurio panaudojimas kaip skyles pernešančios medžiagos keltų daug klausimų ilgalaikiam prietaiso stabilumui [250].

9 lentelė. Terminės junginių **H37–H46** savybės

| Nr. | Struktūra | T_g^a , °C | T_m^b , °C | T_{cr}^c , °C | T_{dec}^d , °C |
|------------|-----------|--------------|--------------|-----------------|------------------|
| H37 | | 156 | 315 | - | 383 |

9 lentelės tęsinys. Terminės junginių H37–H46 savybės

| | | | | | |
|------------|---|-----|-----|-----|-----|
| H38 |  | 145 | - | - | 385 |
| H39 |  | 103 | - | - | 327 |
| H40 |  | - | 339 | - | 361 |
| H41 |  | 106 | 218 | 174 | 382 |
| H42 |  | 100 | 228 | - | 383 |
| H43 |  | 138 | 267 | - | 350 |
| H44 |  | 63 | 198 | 159 | 215 |
| H45 |  | 131 | 289 | - | 361 |
| H46 |  | 130 | - | - | 366 |

a) Nustatyta taikant DSC: kaitinimo greitis 10 K/min; N₂ atmosfera; antrasis kaitinimas. b) Lydymosi temperatūra užfiksuota tik pirmojo kaitinimo metu, 10 K/min. c) Nustatyta taikant DSC: kaitinimo greitis 10 K/min; N₂ atmosfera. d) Skilimo pradžia nustatyta TGA metodu: kaitinimo greitis 10 K/min; N₂ atmosfera.

4.3. Fotoelektrinės savybės

Junginių **H37–H46** elektrocheminis stabilumas ir energetiniai lygmenys tirpale buvo įvertinti pasitelkus CV metodą, jonizacijos potencialas ir dreifinis judris išmatuoti iš minėtų *p*-tipo puslaidininkių plėvelių atitinkamai PESA ir kserografiniu lėkio trukmės metodais (10 lentelė). Visų enaminų oksidacija buvo grįžtama kas įrodo, jog jie yra elektrochemiškai stabilūs.

10 lentelė. Junginių **H37–H46**^a energetiniai lygmenys ir dreifiniai judriai

| Junginys | E_{HOMO} , eV ^b | $E_{\text{g}}^{\text{opt1}}$, eV ^c | E_{LUMO} , eV ^d | I_p , eV ^e | $E_{\text{g}}^{\text{opt2}}$, eV ^f | EA , eV ^g | μ_0 , cm ² V ⁻¹ s ⁻¹ h | μ_h , cm ² V ⁻¹ s ⁻¹ i |
|------------|--|---|--|----------------------------|---|---------------------------|--|--|
| H37 | -5,27 | 2,94 | -2,33 | 5,37 | 2,94 | 2,43 | $1,5 \cdot 10^{-4}$ | $1 \cdot 10^{-2}$ |
| H38 | -5,09 | 2,95 | -2,14 | 5,19 | 2,87 | 2,32 | $2 \cdot 10^{-5}$ | $2,3 \cdot 10^{-3}$ |
| H39 | -5,27 | 3,00 | -2,27 | 5,16 | 2,90 | 2,26 | $2,1 \cdot 10^{-3}$ | $1,2 \cdot 10^{-2}$ |
| H40 | -5,30 | 3,12 | -2,18 | 5,32 | 3,06 | 2,26 | $2,4 \cdot 10^{-3}$ | $7 \cdot 10^{-3}$ |
| H41 | -5,27 | 3,06 | -2,21 | 5,33 | 3,05 | 2,28 | $3,6 \cdot 10^{-4}$ | $6,5 \cdot 10^{-3}$ |
| H42 | -5,20 | 2,90 | -2,30 | 5,16 | 2,86 | 2,30 | $2 \cdot 10^{-4}$ | $2 \cdot 10^{-2}$ |
| H43 | -5,24 | 2,93 | -2,31 | 5,37 | 2,86 | 2,51 | $7,5 \cdot 10^{-6*}$ | $5,5 \cdot 10^{-5*}$ |
| H44 | -5,13 | 2,96 | -2,17 | 5,03 | 2,88 | 2,15 | $1,6 \cdot 10^{-5}$ | $4,5 \cdot 10^{-4}$ |
| H45 | -5,08 | 2,92 | -2,16 | 5,06 | 2,84 | 2,22 | $2 \cdot 10^{-6}$ | $8 \cdot 10^{-5}$ |
| H46 | -5,10 | 2,94 | -2,16 | 5,09 | 2,85 | 2,24 | $5 \cdot 10^{-5}$ | $8,8 \cdot 10^{-4}$ |

a) CV matavimai atlikti su stiklo elektrodu dichlormetano tirpaluose, naudojant 0,1 M tetrabutilamonio heksafluorofosfatą kaip elektrolitą ir Ag/AgNO₃ kaip palyginamąjį elektrodą. Kiekvienas matavimas buvo kalibruotas naudojant feroceną (Fc). Potencialai apskaičiuoti plg. su Fc⁺/Fc. b) Konversijos koeficientai: ferocenas DCM-SCE: 0,46 [219], SCE-SHE: 0,244 [220], SHE-vakuumas: 4,43 [221]. c) Optinės draustinės juostos $E_{\text{g}}^{\text{opt1}}$ apskaičiuotos iš tirpalų absorbcijos spektrų. d) E_{LUMO} apskaičiuota pagal lygtį $E_{\text{LUMO}} = E_{\text{HOMO}} - E_{\text{g}}^{\text{opt1}}$. e) Kietosios būsenos junginių jonizacijos potencialas (I_p) buvo matuojamas fotoemisijos ore metodu iš plėvelių. f) Optinės draustinės juostos $E_{\text{g}}^{\text{opt2}}$ apskaičiuotos iš plėvelių absorbcijos spektrų. g) Elektronų giminingumas (EA) apskaičiuotas pagal lygtį $EA = E_{\text{HOMO}} - E_{\text{g}}^{\text{opt2}}$. h) Dreifinio judrio vertė esant nuliniam lauko stipriui. i) Judrio vertė, kai lauko stipris yra $6,4 \cdot 10^5$ V cm⁻¹. * Junginio judrio vertės buvo išmatuotos iš jo mišinio su PC-Z santykiu 1 : 1.

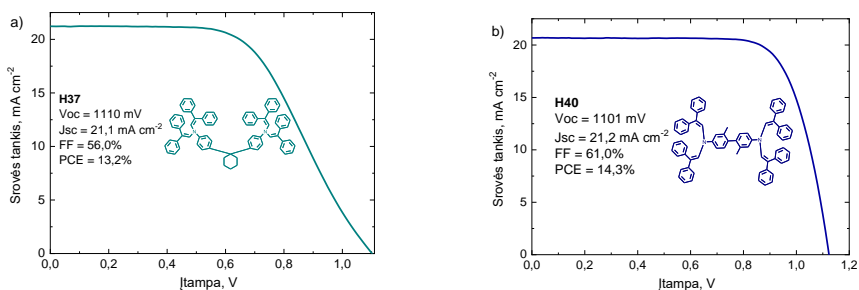
Panaši tendencija stebima tarp tirtų medžiagų kietos fazės I_p ir energetinių lygmenų nustatytų iš tirpalų – esant stipresniems donoriniams 2,2-bis(4-metoksifenil)etenilo fragmentams I_p , E_{HOMO} ir E_{LUMO} yra linę mažėti lyginant su atitinkamais dariniais, turinčiais difeniletetilfragmentus (10 lentelė). Kaip atskirą atvejį verta išanalizuoti junginių **H39–H42** I_p pokytį. Bifenilo darinio **H39** jonizacijos potencialo vertė yra 5,16 eV, tuo tarpu enamino **H40** metilgrupių padėties pokytis iš *orto* į *meta* lemia I_p padidėjimą per 0,16 eV. Įvesti papildomi metilpakaitai junginyje **H41** taip pat padidina I_p , panašiai kaip ir anksčiau minėtu atveju, o metilpakaitų pakeitimas į metoksipakaitus neturi įtakos bifenilo darinio

H42 jonizacijos potencialui. Šiuos pokyčius galima paaiškinti skirtinga molekulių erdvine konfigūracija, turinčia įtakos konjugacijai tarp atskirų anilino fragmentų.

Atlikus enaminų **H37–H46** judrių analizę, galima pastebėti, jog metoksigrupės daro neigiamą įtaką minėtam parametrai. Pavyzdžiui, **H37** demonstruoja beveik 10 kartų geresnius rezultatus nei alkoksigrupes turintis **H38**. Tą patį galima pasakyti ir apie bifenilus **H39** ir **H44**, tik šiuo atveju judris skiriasi daugiau nei 100 kartų. Tokį sumažėjimą greičiausiai lemia erdviniai trukdžiai, atsirandantys dėl metoksipakaitų.

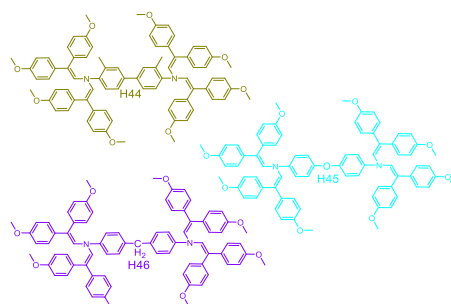
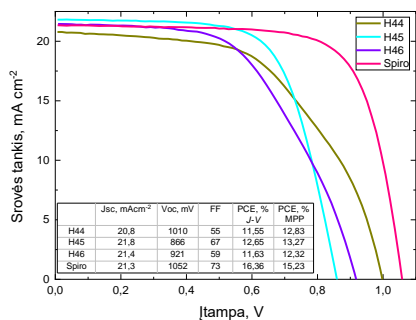
4.4. Perovskitinių saulės elementų rezultatai

Enaminai **H37** ir **H40** buvo išbandyti invertuotuose p-i-n saulės elementuose, kurių struktūra identiška aprašytiems 3.3 skyrelyje, o rezultatai matomi 14 pav. Abi medžiagos pademonstravo aukštas V_{oc} ir J_{sc} reikšmes, tačiau žemas FF lėmė, jog nė viena medžiaga neviršijo 14,5 % našumo.



14 pav. Invertuotų saulės elementų rezultatai a) **H37**, b) **H40**

Metoksipakaitus turintys bifenilo dariniai **H44–H46** buvo išbandyti n-i-p perovskitiniuose saulės elementuose, kurių struktūra buvo FTO/ SnO_2 (nanodalelės)/PCBM/ $\text{FA}_{0.83}\text{Cs}_{0.17}\text{Pb}(\text{I}_{0.9}\text{Br}_{0.1})_3$ /HTM/Au. Įskaitant palyginimui naudojamą spiro-MeOTAD, visi p-tipo puslaidininkiai buvo naudoti su priedais, prietaisų rezultatus galima matyti 15 pav. Nors testuoti enaminai stipriai nusileidžia spiro-MeOTAD, tačiau priedų koncentracijos, naudotos paruošiant skylių transportinius sluoksnius, buvo pritaikytos būtent minėta spiro junginiui, kas galėjo padaryti didelę įtaką rezultatams.



15 pav. Saulės elementų rezultatai naudojant enaminus **H44–H46** ir spiro-OMeTAD kaip skyles pernešančias medžiagas

4.5. Skyriaus išvados

Kiekvienas šiame skyriuje aprašytas anilino darinys pasižymi tinkamais energetiniais lygmenimis bei yra elektrochemiškai ir išskyrus **H44** (9 lentelė) termiškai stabilūs. Skyles pernešantys junginiai **H37**, **H40** buvo išbandyti garintuose p-i-n konfigūracijos saulės elementuose ir atitinkamai pademonstravo 13,2 % ir 14,3 % našumus. Metoksigrupių turinčios medžiagos **H44–H46** buvo išbandytos n-i-p tipo prietaisuose, tačiau kol kas neparodė gerų rezultatų, našiausias saulės elementas šiek tiek viršijo 12 %. Nors enaminų **H44–H46** pasiektas efektyvumas žemas, vilties suteikia tai, jog jie buvo bandyti su priedais, pritaikytais spiro-MeOTAD, todėl tik papildomi eksperimentai padės nustatyti šių medžiagų tinkamumą saulės elementams. Be to, dėl savo puikių savybių enaminai **H38**, **H39**, **H41** ir **H42** turėtų būti išskirti kaip perspektyvūs skyles pernešantys junginiai.

Pagrindiniai rezultatai ir išvados

1) Trifenilamino ketvirtinio amonio junginiai buvo ištirti. Nustatyta, kad:

- jodo anijonų turintys ketvirtinio amonio junginiai nėra stabilūs aukštose temperatūrose,
- dėl labai žemo laidumo ketvirtiniai amonio junginiai blogai veikia perovskitiniuose saulės elementuose,
- dėl sumažėjusio molekulių judėjimo visoms tirtoms joninėms medžiagoms būdingas šviesos emisijos padidėjimas kietoje būsenoje,
- organinių ketvirtinių amonio junginių pirmtakai pasižymėjo geresnėmis savybėmis nei atitinkamos jų druskos, todėl juos potencialiai būtų galima naudoti kaip daugiavertines krūvį pernešančias ir šviesą emituojančias medžiagas.

2) Susintetinti monomerai **H12–H15**, buvo nustatyta kad:

- visi junginiai yra elektrochemiškai stabilūs,

- absorbcijos pokytis plėvelėse lyginant su tirpalu leidžia teigti, jog diazaaceni **H12–H15** gali tvarkingai išsidėstyti kietoje būsenoje,
- minėtų medžiagų energetiniai lygmenys yra tinkami naudoti švinu pagrįstuose perovskitiniuose saulės elementuose, kadangi patenka į 5,0–5,6 eV ribą,
- visi monomerai sutinklinami esant aukštesnei nei 200 °C temperatūrai, todėl juos galima naudoti tik invertuotuose perovskitiniuose saulės elementuose.

3) Gauti junginiai, turintys centrinį diazaaceno fragmentą, jų tyrimas parodė, kad:

- visos medžiagos yra termiškai ir elektrochemiškai stabilios,
- termogravimetrinė analizė parodė, jog diazaaceni **H16–H20** ir **H23** greitai garuoja aukštose temperatūrose, kas teikia vilčių, kad jie galės būti panaudojami vakuuminio būdu padengiamuose perovskitiniuose saulės elementuose,
- išbandytų medžiagų energetiniai lygmenys yra tinkami naudoti švinu pagrįstuose perovskitiniuose saulės elementuose, kadangi patenka į 5,0–5,6 eV ribą,
- tvarkingas išsidėstymas plėvelėje lemia, jog diazapentacenas **H16** pasižymi aukštu skylių judriu, kuris pasiekia $2,5 \cdot 10^{-3} \text{ cm}^2 \text{ V}^{-1} \text{ s}^{-1}$, esant nuliniam lauko stipriui, ir $1,1 \cdot 10^{-2} \text{ cm}^2 \text{ V}^{-1} \text{ s}^{-1}$ stipriuose laukuose.

4) Nauji junginiai, turintys difeniletetilfragmentų buvo susintetinti ir ištirti. Nustatyta kad:

- santykinai žemos medžiagų **H26–H28** ir **H31** skilimo temperatūros kelia abejonių dėl jų panaudojimo optoelektronikoje,
- išbandytų medžiagų energetiniai lygmenys tinkami naudoti švinu pagrįstuose perovskitiniuose saulės elementuose, kadangi patenka į 5,0–5,6 eV ribą,
- puikios karbazolo enaminų **H33** ir **H34** savybės leido pasiekti beveik 17 % efektyvumą įprastos konfigūracijos PSC (palyginti su 18,14 % pasiekė su legiruotu spiro-OMeTAD) nenaudojant jokių priedų, kas yra labai svarbu prietaiso ilgaamžiškumui,
- anilino darinio **H35** aukštas judris ir santykinai geros terminės savybė leido jį panaudoti vakuuminio nusodinimo būdu suformuotame p-i-n perovskitiniame saulės elemente, kuris pasiekė didesnę nei 18 % našumą. Šis rezultatas yra vienas geriausių tokio tipo prietaisuose.

5) Anilino darinių skylių transportinės medžiagos buvo susintetintos, jų tyrimas parodė, kad:

- enamino **H44** erdvinė konfigūracija gali lemti jo santykinai prastą terminį stabilumą, savo ruožtu visos kitos medžiagos yra termiškai ir elektrochemiškai stabilios,
- išbandytų medžiagų energetiniai lygmenys tinkami naudoti švinu pagrįstuose perovskitiniuose saulės elementuose, kadangi patenka į 5,0–5,6 eV ribą,

- anilino dariniai **H39** ir **H40** pasižymi aukštu skylių judriu, siekiančiu iki $2,4 \cdot 10^{-3} \text{ cm}^2 \text{ V}^{-1} \text{ s}^{-1}$ esant nuliniam lauko stipriui ir $1,2 \cdot 10^{-2} \text{ cm}^2 \text{ V}^{-1} \text{ s}^{-1}$ stipriuose laukuose, kas daro juos patraukliais *p*-tipo puslaidininkiais panaudojimui optoelektronikoje,

- dėl TGA analizės metu stebėto intensyvaus garavimo aukštoje temperatūroje, junginiai **H37**, **H40**, išbandyti vakuuminio nusodinimo būdu suformuotuose perovskitiniuose p-i-n konfigūracijos saulės elementuose ir pasiekė atitinkamai 13,2 % ir 14,3 % našumus,

- medžiagos **H44–H46**, testuotos n-i-p struktūros perovskitiniuose saulės elementuose, nepasiekė aukštų rezultatų, tačiau optimizavus priedų koncentracijas ir panaudojimo procedūrą būtų galima gerokai pagerinti prietaisų našumą.

7. REFERENCES

1. OSTROVERKHOVA, Oksana. Organic optoelectronic materials: mechanisms and applications. *Chemical reviews*. 2016. Vol. 116, no. 22, p. 13279–13412.
2. CHAUDHRY, Mujeeb Ullah, MUHIEDDINE, Khalid, WAWRZINEK, Robert, SOBUS, Jan, TANDY, Kristen, LO, Shih-Chun, NAMDAS, Ebinazar B. Organic Light-Emitting Transistors: Advances and Perspectives. *Adv. Funct. Mater.* 2020. Vol. 30, no. 20, p. 1905282.
3. SHI, Zhengqi and JAYATISSA, Ahalapitiya H. Perovskites-based solar cells: a review of recent progress, materials and processing methods. *Materials* [online]. 2018. Vol 11, no. 5, p. 729. DOI: 10.3390/ma11050729. Available from: <https://www.ncbi.nlm.nih.gov/pmc/articles/PMC5978106/>.
4. WHITAKER, James B., KIM, Dong Hoe, LARSON, Bryon W., ZHANG, Fei, BERRY, Joseph J, VAN HEST, Maikel F. A. M. and ZHU, Kai. Scalable slot-die coating of high performance perovskite solar cells. *Sustainable Energy Fuels*. 2018. Vol. 2, no. 11, p. 2442-2449.
5. URIETA-MORA, Javier, GARCIA-BENITO, Ines, MOLINA-ONTORIA, Agustin and MARTIN, Nazario. Hole transporting materials for perovskite solar cells: a chemical approach. *Chem. Soc. Rev.* 2018. Vol. 47, no. 23, p. 8541-8571.
6. MENG, Xiangyue, BAI, Yang, XIAO, Shuang, ZHANG, Teng, HU, Chen, YANG Yinglong, ZHENG, Xiaoli and YANG, Shihe. Designing new fullerene derivatives as electron transporting materials for efficient perovskite solar cells with improved moisture resistance. *Nano Energy*. 2016. Vol. 30, p. 341-346.
7. SALIBA, Michael, CORREA-BAENA, Juan-Pablo, GRATZEL, Michael, HAGFELDT, Anders and ABATE Antonio. Perovskite solar cells: from the atomic level to film quality and device performance. *Angew. Chem. Int. Ed.* 2017. Vol. 57, no. 10, p. 2554-2569.
8. GREEN, Martin A., DUNLOP, Ewan D., HOHL-EBINGER, Jochen, YOSHITA, Masahiro, KOPIDAKIS, Nikos and HAO, Xiaojing. Solar cell efficiency tables (version 56). *Progress in Photovoltaics*. 2020. Vol. 28, no. 7, p. 629-638.
9. MENG, Lei, YOU, Jingbi and YANG, Yang. Addressing the stability issue of perovskite solar cells for commercial applications. *Nat. Commun* [online]. 2018. Vol. 9. DOI: 10.1038/s41467-018-07255-1. Available from: <https://www.nature.com/articles/s41467-018-07255-1>.
10. HU, Zhaosheng, LIN, Zhenhua, SU, Jie, ZHANG, Jincheng, CHANG, Jingjing and HAO, Yue. A review on energy band-gap engineering for perovskite photovoltaics. *Sol. RRL*. 2019. Vol. 3, no. 12, p. 1900304. DOI: 10.1002/solr.201900304. Available from: <https://onlinelibrary.wiley.com/doi/abs/10.1002/solr.201900304>.
11. Pengyang Wang, Xingwang Zhang, Yuqin Zhou, Qi Jiang, Qiufeng Ye, Zema Chu, Xingxing Li, Xiaolei Yang, Zhigang Yin & Jingbi You. Solvent-controlled growth of inorganic perovskite films in dry environment for efficient and stable solar cells. *Nat. Commun* [online]. 2018. Vol. 9. DOI: 10.1038/s41467-018-04636-4. Available from: <https://www.nature.com/articles/s41467-018-04636-4>.

12. POLI, Isabella, ESLAVA, Salvador and CAMERON, Petra. Tetrabutylammonium cations for moisture-resistant and semitransparent perovskite solar cells. *J. Mater. Chem. A*. 2017. Vol. 5, no. 42, p. 22325-22333.
13. AL-ASHOURI, Amran, MAGOMEDOV, Artiom, ROß, Marcel, JOŠT, Marko, TALAIKIS, Martynas, CHISTIANKOVA, Ganna, BERTRAM, Tobias, MARQUEZ, José A., KOHNENE, Eike, KASPARAVIČIUS, Ernestas, LEVCENCO, Sergiu, GIL-ESCRIG, Lidón, HAGES, Charles J., SCHLATMANN, Rutger, RECH, Bernd, MALINAUSKAS, Tadas, UNOLD, Thomas, KAUFMANN, Christian A., KORTE, Lars, NIAURA, Gediminas, GETAUTIS, Vytautas and ALBRECHT, Steve. Conformal monolayer contacts with lossless interfaces for perovskite single junction and monolithic tandem solar cells. *Energy Environ. Sci.* 2019. Vol. 12, no. 11, p. 3356-3369.
14. ABUDULIMU, Abasi, LANG, Liu, GUILIN, Liu, AIMAITI, Nijiati, REZEK, Bohuslav and CHEN, Qi. Crucial role of charge transporting layers on ion migration in perovskite solar cells. *J. Energy Chem.* 2020. Vol. 47, p. 132-137.
15. CHANG, Chih-Yu, TSAI, Bo-Chou and HSIAO, Yu-Cheng. Efficient and stable vacuum-free-processed perovskite solar cells enabled by a robust solution-processed hole transport layer. *ChemSusChem*. 2017. Vol. 10, no. 9, p. 1981-1988.
16. SCHLOEMER, Tracy H., GEHAN, Timothy S., CHRISTIANS, Jeffrey A., MITCHELL, Deborah G., DIXON, Alex, LI, Zhen, ZHU, Kai, BERRY, Joseph J., LUTHER, Joseph M. and Alan Sellinger. Thermally Stable Perovskite Solar Cells by Systematic Molecular Design of the Hole-Transport Layer. *ACS Energy Lett.* 2019. Vol. 4, no. 2, p. 473-482.
17. SALIBA, Michael, CORREA-BAENA, Juan-Pablo, WOLFF, Christian M., STOLTERFOHT, Martin, PHUNG, Nga, ALBRECHT, Steve, NEHER, Dieter and ABATE, Antonio. How to make over 20% efficient perovskite solar cells in regular (n-i-p) and inverted (p-i-n) architectures. *Chem. Mater.* 2018. Vol. 30, no. 13, p. 4193-4201.
18. MATSUI, Taisuke, PETRIKYTE, Ieva, MALINAUSKAS, Tadas, DOMANSKI, Konrad Domanski, DASKEVICIENE, Maryte, STEPONAITIS Matas, GRATIA, Paul, TRESS, Wolfgang, CORREA-BAENA, Juan-Pablo, ABATE, Antonio, HAGFELDT, Anders, GRATZEL, Michael, NAZEERUDDIN, Mohammad Khaja, GETAUTIS, Vytautas, SALIBA, Michael. Additive-free transparent triarylamine-based polymeric hole-transport materials for stable perovskite solar cells. *ChemSusChem*. 2016. Vol. 9, no. 18, p. 2567-2571.
19. YAO, Ze-Fan, WANG, Jie-Yu, and PEI, Jian. Control of π - π stacking via crystal engineering in organic conjugated small molecule crystals. *Cryst. Growth Des.* 2018. Vol. 18, no. 1, p. 7-15.
20. VAITUKAITYTE, Deimante, WANG, Zhiping, MALINAUSKAS, Tadas, MAGOMEDOV, Artiom, BUBNIENE, Giedre, JANKAUSKAS, Vyngintas, GETAUTIS, Vytautas and SNAITH Henry J. Efficient and stable perovskite solar cells using low-cost aniline-based enamine hole-transporting materials. *Adv. mater.* 2018. Vol. 30, no. 45, p. 1803735.
21. BRAUKYLA, Titas, XIA, Rui, DASKEVICIENE, Maryte, MALINAUSKAS, Tadas, GRUODIS, Alytis, JANKAUSKAS, Vyngintas, FEI, Zhaofu,

- MOMBLONA, Cristina, ROLDN-CARMONA, Cristina, DYSON, Paul J., GETAUTIS, Vytautas and NAZEERUDDIN, Mohammad Khaja. Inexpensive hole-transporting materials derived from trçgers base afford efficient and stable perovskite solar cells. *Angew. Chem. Int. Ed.* 2019. Vol. 58, no. 33, p. 11266-11272.
22. CHEETHAM, Anthony K. and RAO C. N. R. There's Room in the Middle. *Science*. 2017. Vol. 318, no. 5847, p. 58-59.
23. Golschmidt, V. M. Die gesetze der krystallochemie. *Naturwissenschaften*. 1926. Vol. 21, p. 477-485.
24. TRAVIS, W., GLOVER, E. N. K., BRONSTEIN, H., SCANLOBC, D. O. and PALGRAVE, R. G. On the application of the tolerance factor to inorganic and hybrid halide perovskites: a revised system. *Chem. Sci.* 2016. Vol. 7, no. 7, p. 4548-4556.
25. LI, Chonghe, SOH, Kitty Chi Kwan and WU, Ping. Formability of ABO_3 perovskites. *J. Alloys Compd.* 2004. Vol. 372, no. 1, p. 40-48.
26. MITZI, D.B., FEILDT, C.A., SCHLESINGER Z. and LAIBOWITZ, R.B. Transport, optical, and magnetic properties of the conducting halide perovskite $CH_3NH_3SnI_3$. *J. Solid State Chem.* 1995. Vol. 114, no. 1, p. 159-163.
27. KAGAN, C. R., MITZI, D. B. and DIMITRAKOPOULOS C. D. Organic-inorganic hybrid materials as semiconducting channels in thin-film field-effect transistors. *Science*. 1999. Vol. 286, no. 5441, p. 945-947.
28. KOJIMA, Akihiro, TESHIMA, Kenjiro, SHIRAI, Yasuo and MIYASAKA, Tsutomu. Organometal halide perovskites as visible-light sensitizers for photovoltaic cells. *J. Am. Chem. Soc.* 2009. Vol. 131, no. 17, p. 6050-6051.
29. LIU, Mingzhen, JOHNSTON, Michael B. and SNAITH, Henry J. Efficient planar heterojunction perovskite solar cells by vapour deposition. *Nature*. 2013. Vol. 501, no. 7467, p. 395-398.
30. AL-ASHOURI, Amran, KOHNEN, Eike, LI, Bor, MAGOMEDOV, Artiom, HEMPEL, Hannes, CAPRIOGLIO, Pietro, MARQUEZ, José A., VILCHES, Anna Belen Morales, KASPARAVICIUS, Ernestas, SMITH, Joel A., PHUNG, Nga, MENZEL, Dorothee, GRISCHEK, Max, KEGELMANN, Lukas, SKROBLIN, Dieter, GOLLWITZER, Christian, MALINAUSKAS, Tadas, JOŠT, Marko, MATIĆ, Gašper, RECH, Bernd, SCHLATMANN, Rutger, TOPIĆ, Marko, KORTE, Lars, ABATE, Antonio, STANNOWSKI, Bernd, NEHER, Dieter, STOLTERFOHT Martin, UNOLD, Thomas, GETAUTIS, Vytautas and ALBRECHT, Steve. Monolithic perovskite/silicon tandem solar cell with >29% efficiency by enhanced hole extraction. *Science*. 2020. Vol. 370, no. 6522, p. 1300-1309.
31. BRENNER, Thomas M., EGGER, David A., KRONIK, Leor, HODES, Gary and CAHEN, David. Hybrid organic-inorganic perovskites: lowcost semiconductors with intriguing charge-transport properties. *Nat. Rev. Mater* [online]. 2016. Vol. 1, no. 1, p. 15007. DOI: 10.1038/natrevmats.2015.7. Available from: <https://www.nature.com/articles/natrevmats20157>.
32. JUNG, Hyun Suk and PARK, Nam-Gyu. Perovskite solar cells: from materials to devices. *Small*. 2015. Vol. 11, no. 1, p. 10-25.

33. SHOCKLEY, William and QUEISSER, Hans J. Detailed balance limit of efficiency of p-n junction solar cells. *J. Appl. Phys.* 1961. Vol. 32, no. 3, p. 510-519.
34. HAO, Feng, STOUMPOS, Constantinos C., CAO, Duyen Hanh, CHANG, Robert P. H. and KANATZIDIS, Mercouri G. Lead-free solid-state organic-inorganic halide perovskite solar cells. *Nature Photonics*. 2014. Vol 8, no. 6, p. 489-494.
35. LIN, Qianqian, ARMIN, Ardanan, NAGIRI, Ravi Chandra Raju, BURN, Paul L. and MEREDITH, Paul. Electro-optics of perovskite solar cells. *Nat. Photon.* 2015. Vol. 9, no. 2, p. 106-112.
36. MIYATA, Atsuhiko, MITIOGLU, Anatolie, PLOCHOCKA, Paulina, PORTUGALL, Oliver, WANG, Jacob Tse-Wei, STRANKS, Samuel D., SNAITH, Henry J. and NICHOLAS, Robin J. Direct measurement of the exciton binding energy and effective masses for charge carriers in organic-inorganic tri-halide perovskites. *Nat. Phys.* 2015. Vol. 11, no. 7, p. 582-587.
37. STRANKS, Samuel D., EPERON, Giles E., GRANCINI, Giulia, MENELAOU, Christopher, ALCOGER, Marcelo J. P., LEIJTENS, Tomas, HERZ, Laura M., PETROZZA, Annamaria, SNAITH, Henry J. Electron-hole diffusion lengths exceeding 1 micrometer in an organometal trihalide perovskite absorber. *Science*. 2013. Vol. 342, no. 6156, p. 341-344.
38. XING, Guichuan, MATHEWS, Nripan, SUN, Shuangyong, LIM, Swee Sien, LAM, Yeng Ming, GRATZEL, Michael, MHAISALKAR, Subodh and SUM, Tze Chien. Long-range balanced electron- and hole-transport lengths in organic-inorganic $\text{CH}_3\text{NH}_3\text{PbI}_3$. *Science*. 2013. Vol. 342, no. 6156, p. 344-347.
39. GIL-ESCRIG, Lidón, DREESSEN, Chris, KAYA, Ismail Cihan, KIM, Beom-Soo, PALAZON, Francisco, SESSOLO, Michele, and BOLINK, Henk J. Efficient vacuum-deposited perovskite solar cells with stable cubic $\text{FA}_{1-x}\text{MA}_x\text{PbI}_3$. *ACS Energy Lett.* 2020. Vol. 5, no. 9, 3053-3061.
40. LEE, Michael M, TEUSCHER, Joël, MIYASAKA, Tsutomu, MURAKAMI, Takuro N. and SNAITH, Henry J. Efficient hybrid solar cells based on meso-superstructured organometal halide perovskites. *Science*. 2012. Vol. 338, no. 6107, p. 643-647.
41. ADNAN, Muhammad and LEE, Jae Kwan. All sequential dip-coating processed perovskite layers from an aqueous lead precursor for high efficiency perovskite solar cells. *Sci. Rep* [online]. 2018. Vol. 8, p. 2168. DOI: 10.1038/s41598-018-20296-2. Available from: <https://www.nature.com/articles/s41598-018-20296-2>.
42. BARROWS, Alexander T., PEARSON, Andrew J., KWAK, Chan Kyu, DUNBAR, Alan D. F., BUCKLEY, Alastair R. and LIDZEY, David G. Efficient planar heterojunction mixed-halide perovskite solar cells deposited via spray-deposition. *Energy Environ. Sci.* 2014. Vol. 7, no. 9, p.2944-2950.
43. SEO, Seongrok, JEONG, Seonghwa, PARK, Hyoungmin, SHIN, Hyunjung and PARK, Nam-Gyu. Atomic layer deposition for efficient and stable perovskite solar cells. *Chem. Commun.* 2019. Vol. 55, no. 17, p. 2403-2416.

44. PENG, Xiaojin, YUAN, Jian, SHEN, Shirley, GAO, Mei CHESMAN, Anthony S. R., YIN, Hong, CHENG, Jinshu, ZHANG, Qi and ANGMO, Dechan. Perovskite and organic solar cells fabricated by inkjet printing: progress and prospects. *Adv. Funct. Mater.* 2017. Vol. 27, no. 41, p. 1703704.
45. MITZI, David B. Templating and structural engineering in organic-inorganic perovskites. *J. Chem. Soc., Dalton Trans.* 2001. No. 1, p. 1-12.
46. SAPAROV, Bayrammurad and MITZI, David B. Organic-inorganic perovskites: structural versatility for functional materials design. *Chem. Rev.* 2016. Vol. 116, no. 7, p. 4558-4596.
47. GANGADHARAN, Deepak Thirithamarassery and MA, Dongling. Searching for stability at lower dimensions: current trends and future prospects of layered perovskite solar cells. *Energy Environ. Sci.* 2019. Vol. 12, no. 10, p. 2860-2889.
48. YANG, Shuang, WANG, Yun, LIU, Porun, CHENG, Yi-Bing, ZHAO, Hui Jun and YANG, Hua Gui. Functionalization of perovskite thin films with moisture-tolerant molecules. *Nat. Energy.* 2016. Vol. 1, p. 15016. DOI: 10.1038/NENERGY.2015.16. Available from: <https://www.nature.com/articles/nenergy201516>.
49. ZHANG, Fei, LU, Haipeng, TONG, Jinhui, BERRY, Joseph J., BEARD, Matthew C. and ZHU, Kai. Advances in two-dimensional organic-inorganic hybrid perovskites. *Energy Environ. Sci.* 2020. Vol. 13, no. 4, p. 1154-1186.
50. YUAN, Mingjian, QUAN, Li Na, COMIN, Riccardo, WALTERS, Grant, SABATINI, Randy, VOZNYI, Oleksandr, HOOGLAND, Sjoerd, ZHAO, Yongbiao, BEAUREGARD, Eric M., KANJANABOOS, Pongsakorn, LU, Zhenghong, KIM, Dong Ha and SARGENT, Edward H. Perovskite energy funnels for efficient light-emitting diodes. *Nat. Nanotechnol.* 2016. Vol. 11, no. 10, p. 872-877.
51. ZHOU, Ning, SHEN, Yiheng, LI, Liang, TAN, Shunquan, LIU, Na, ZHENG, Guan haojie, CHEN, Qi, and ZHOU, Huanping. Exploration of crystallization kinetics in quasi two-dimensional perovskite and high performance solar cells. *J. Am. Chem. Soc.* 2018. Vol. 140, no. 1, p. 459-465.
52. PARITMONGKOL, Watcharaphol, DAHOD, Nabeel S., STOLLMANN, Alexia, MAO, Nannan, SETTENS, Charles, ZHENG, Shao-Liang, and TISDALE, William A. Synthetic variation and structural trends in layered two-dimensional alkylammonium lead halide perovskites. *Chem. Mater.* 2019. Vol. 31, no. 15, p. 5592-5607.
53. LI, Xiaotong, KE, Weijun, TRAORE, Boubacar, GUO, Peijun, HADAR, Ido, KEPENEKIAN, Mikaël, EVEN, Jacky, KATAN, Claudine, STOUMPOS, Constantinos C., SCHALLER, Richard D. and KANATZIDIS, Mercouri G. Two-dimensional Dion-Jacobson hybrid lead iodide perovskites with aromatic diammonium cations. *J. Am. Chem. Soc.* 2019. Vol. 141, no. 32, p.12880-12890.
54. MAO, Lingling, KE, Weijun, PEDESSEAU, Laurent, WU, Yilei, KATAN, Claudine, EVEN, Jacky, WASIELEWSKI, Michael R., STOUMPOS, Constantinos C. and KANATZIDIS, Mercouri G. Hybrid Dion-Jacobson 2D lead iodide perovskites. *J. Am. Chem. Soc.* 2018. Vol. 140, no. 10, p. 3775-3783.

55. Organic-inorganic perovskite precursors. Available from: <https://www.tcichemicals.com/US/en/c/12969>, accessed 24/02/2021.
56. AHMAD, Sajjad, FU, Ping, YU, Shuwen, YANG, Qing, LIU, Xuan, WANG, Xuchao, WANG, Xiuli, GUO, Xin and LI, Can. Dion-Jacobson phase 2D layered perovskites for solar cells with ultrahigh stability. *Joule*. 2019. Vol. 3, no. 3, p. 794-806.
57. MAO, Lingling, STOUUMPOS, Constantinos C., and KANATZIDIS, Mercuri G. Two-dimensional hybrid halide perovskites: principles and promises. *J. Am. Chem. Soc.* 2019. Vol. 141, no. 3, p. 1171-1190.
58. REN, Hui, YU, Shidong, CHAO, Lingfeng, XIA, Yingdong, SUN, Yuanhui, ZUO, Shouwei, LI, Fan, NIU, Tingting, YANG, Yingguo, JU, Huanxin, LI, Bixin, DU, Haiyan, GAO, Xingyu, ZHANG, Jing, WANG, Jianpu, ZHANG, Lijun, CHEN, Yonghua and HUANG, Wei. Efficient and stable Ruddlesden–Popper perovskite solar cell with tailored interlayer molecular interaction. *Nat. Photonics* [online]. 2020. Vol. 14, p. 154–163. DOI: 10.1038/s41566-019-0572-6. Available from: <https://www.nature.com/articles/s41566-019-0572-6>.
59. LERMER, Claudia, BIRKHOLO, Susanne T., MOUDRAKOVSKI, Igor L., MAYER, Peter, SCHOOP, Leslie M., SCHMIDT-MENDE Lukas and LOTSCH, Bettina V. Toward fluorinated spacers for MAPI-derived hybrid perovskites: synthesis, characterization, and phase transitions of $(\text{FC}_2\text{H}_4\text{NH}_3)_2\text{PbCl}_4$. *Chem. Mater.* 2016. Vol., 28, no. 18, p. 6560–6566.
60. MERCIER, Nicolas. $(\text{HO}_2\text{C}(\text{CH}_2)_3\text{NH}_3)_2(\text{CH}_3\text{NH}_3)\text{Pb}_2\text{I}_7$: a predicted non-centrosymmetrical structure built up from carboxylic acid supramolecular synthons and bilayer perovskite sheets. *CrystEngComm*. 2005. Vol. 7, no. 70, p. 429-432.
61. BILLING, David G. and LEMMERER, Andreas. Inorganic–organic hybrid materials incorporating primary cyclic ammonium cations: The lead iodide series. *CrystEngComm*. 2007. Vol. 9, no. 3, p. 236-244.
62. BILLINGA, David G. and LEMMERER, Andreas. Poly[bis--[2-(1-cyclo-hexen-yl)ethyl-ammonium] di- μ -iodo-diodo-plumbate(II)]. *Acta Crystallographica Section C*. 2006. Vol. 62, no. 7, p. m269-m271.
63. KAMMINGA, Machteld E., FANG, Hong-Hua, FILIP, Marina R., GIUSTINO, Feliciano, BAAS, Jacob, BLAKE, Graeme R., LOI, Maria Antonietta and PALSTRA, Thomas T. M. Confinement effects in low-dimensional lead iodide perovskite hybrids. *Chem. Mater.* 2016. Vol. 28, no. 13, p. 4554–4562.
64. HU, Jun, OSWALD, Iain W. H., HU, Huamin, STUARD, Samuel J., NAHID, Masrur Morshed, YAN, Liang, CHEN, Zheng, ADE, Harald, NEILSON, James R. and YOU, Wei. Aryl-perfluoroaryl interaction in two-dimensional organic–inorganic hybrid perovskites boosts stability and photovoltaic efficiency. *ACS Materials Lett.* 2019. Vol. 1, no. 1, p. 171–176.
65. PARK, In-Hyeok, CHU, Leiqliang, LENG, Kai, CHOY, Yu Fong, LIU, Wei, ABDELWAHAB, Ibrahim, ZHU, Ziyu, MA, Zhirui, CHEN, Wei, XU, Qing-Hua EDA, Goki and LOH, Kian Ping. Highly stable two-dimensional tin (II) iodide hybrid organic–inorganic perovskite based on stilbene derivative. *Adv. Funct. Mater.* 2019. Vol. 29, no. 39, p. 1904810.

66. DU, Ke-zhao, TU, Qing, ZHANG, Xu, HAN, Qiwei, LIU, Jie Liu, ZAUSCHER, Stefan and MITZI, David B. Two-dimensional lead(II) halide-based hybrid perovskites templated by acene alkylamines: crystal structures, optical properties, and piezoelectricity. *Inorg. Chem.* 2017. Vol. 56, no. 15, p. 9291–9302.
67. PASSARELLI, James V., FAIRFIELD, Daniel J., SATHER, Nicholas A., HENDRICKS, Mark P., SAI, Hiroaki, STERN, Charlotte L. and STUPP, Samuel I. Enhanced out-of-plane conductivity and photovoltaic performance in $n = 1$ layered perovskites through organic cation design. *J. Am. Chem. Soc.* 2018. Vol. 140, no. 23, p. 7313–7323.
68. ZHU, Xu-Hui, MERCIER, Nicolas, RIOU, Amédée, BLANCHARDA, Philippe and FRERE, Pierre. $(C_4H_3SCH_2NH_3)_2(CH_3NH_3)Pb_2I_7$: non-centrosymmetrical crystal structure of a bilayer hybrid perovskite. *Chem. Commun.* 2002. no. 18, p. 2160–2161.
69. TAKAHASHI, Yukari, OBARA, Rena, NAKAGAWA, Kohei, NAKANO, Masayuki, TOKITA, Jun-ya and INABE, Tamotsu. Tunable charge transport in soluble organic–inorganic hybrid semiconductors. *Chem. Mater.* 2007. Vol. 19, no. 25, p. 6312–6316.
70. HERCKENS, Roald, VAN GOMPEL, Wouter T. M., SONG, Wenya, GELVEZ-RUEDA, María C., MAUFORT, Arthur, RUTTENS, Bart, D'HAEN, Jan, GROZEMA, Ferdinand C., AERNOUTS, Tom, LUTSEN, Laurence and VANDERZANDE, Dirk. Multi-layered hybrid perovskites templated with carbazole derivatives: optical properties, enhanced moisture stability and solar cell characteristics. *J. Mater. Chem. A.* 2018. Vol. 6, no. 45, p. 22899–22908.
71. DOHNER, Emma R., HOKE, Eric T. and KARUNADASA, Hemamala I. Self-assembly of broadband white-light emitters. *J. Am. Chem. Soc.* 2014. Vol. 136, no. 5, p. 1718–1721.
72. MAO, Lingling, WU, Yilei, STOUMPOS, Constantinos C., WASIELEWSKI, Michael R. and KANATZIDIS, Mercouri G. White-light emission and structural distortion in new corrugated two-dimensional lead bromide perovskites. *J. Am. Chem. Soc.* 2017. Vol. 139, no. 14, p. 5210–5215.
73. DAUB, Michael and HILLEBRECHT, Harald. First representatives of (210)-oriented perovskite variants—synthesis, crystal structures and properties of the new 2D hybrid perovskites $A[HC(NH_2)_2]PbI_4$; $A=[C(NH_2)_3]$, $[HSC(NH_2)_2]$. *Journal.* 2018. Vol. 233, no. 8, p. 555.
74. CORRADI, Anna Bonamartini, FERRARI, Anna Maria, RIGHI, Lara and SGARABOTTO, Paolo. An additional structural and electrical study of polymeric haloplumbates(II) with heterocyclic diprotonated amines. *Inorg. Chem.* 2001. Vol. 40, no. 2, p. 218–223.
75. MITZI, David B., DIMITRAKOPOULOS, Christos D. and KOSBAR, Laura L. Structurally tailored organic–inorganic perovskites: optical properties and solution-processed channel materials for thin-film transistors. *Chem. Mater.* 2001. Vol. 13, no. 10, p. 3728–3740.
76. HAUTZINGER, Matthew P., DAI, Jun, JI, Yujin, FU, Yongping, CHEN, Jie, GUZEI, Iliia A., WRIGHT, John C., LI, Youyong and JIN, Song. Two-dimensional

lead halide perovskites templated by a conjugated asymmetric diammonium. *Inorg. Chem.* 2017. Vol. 56, no. 24, p. 14991-14998.

77. MAO, Lingling, TSAI, Hsinhan, NIE, Wanyi, MA, Lin, IM, Jino, STOUMPOS, Constantinos C., MALLIAKAS, Christos D., HAO, Feng, WASIELEWSKI, Michael R., MOHITE, Aditya D. and KANATZIDIS, Mercouri G. Role of organic counterion in lead- and tin-Based two-dimensional semiconducting iodide perovskites and application in planar solar cells. *Chem. Mater.* 2016. Vol. 28, no. 21, p. 7781–7792.

78. LERMER, Claudia, HARM, Sascha P., BIRKHOLO, Susanne T., JASER, Julian A., KUTZ, Christopher M., MAYER, Peter, SCHMIDT-MENDE, Lukas and LOTSCH, Bettina. Benzimidazolium lead halide perovskites: effects of anion substitution and dimensionality on the bandgap. *Zeitschrift für anorganische und allgemeine Chemie.* 2016. Vol. 642, no. 23, p. 1369-1376.

79. LEMMERERA, Andreas and BILLING, David G. Lead halide inorganic–organic hybrids incorporating diammonium cations. *CrystEngComm.* 2012. Vol. 14, no. 6, p. 1954-1966.

80. ZHU, Xu-Hui, MERCIER, Nicolas, FRERE, Pierre, BLANCHARD, Philippe, RONCALI, Jean, ALLAIN, Magali, PASQUIER, Claude and RIOU, Amédée. Effect of mono- versus di-ammonium cation of 2,2'-bithiophene derivatives on the structure of organic–inorganic hybrid materials based on iodo metallates. *Inorg. Chem.* 2003. Vol. 42, no. 17, p. 5330-5339.

81. JUNG, Eui Hyuk, JEON, Nam Joong, PARK, Eun Young, MOON, Chan Su, SHIN, Tae Joo, YANG, Tae-Youl, NOH, Jun Hong Noh and SEO, Jangwon. Efficient, stable and scalable perovskite solar cells using poly(3-hexylthiophene). *Nature.* 2019. Vol. 567, no. 7749, p. 511.

82. GRANCINI, G., ROLDAN-CARMONA, C., ZIMMERMANN, I., MOSCONI, E., LEE, X., MARTINEAU, D., NARBÉY, S., OSWALD, F., DE ANGELIS, F., GRAETZEL, M. and NAZEERUDDIN, Mohammad Khaja. One-Year stable perovskite solar cells by 2D/3D interface engineering. *Nat. Commun* [online]. 2017. Vol. 8, p. 15684. DOI: 10.1038/ncomms15684. Available from: <https://www.nature.com/articles/ncomms15684>.

83. CHEN, Peng, BAI, Yang, LYU, Miaoqiang, YUN, Jung-Ho, HAO, Mengmeng and WANG, Lianzhou. Progress and perspective in low-dimensional metal halide perovskites for optoelectronic applications. *Solar RRL.* 2018. Vol. 2, no. 3, p. 1700186. DOI: 10.1002/solr.201700186. Available from: <https://onlinelibrary.wiley.com/doi/abs/10.1002/solr.201700186>.

84. BABAYIGIT, Aslihan, ETHIRAJAN, Anitha, MULLER, Marc and CONINGS, Bert. Toxicity of organometal halide perovskite solar cells. *Nat. Mater.* 2016. Vol. 15, no. 3, p. 247-251.

85. PERN, F.J., GLICK, S.H. Photothermal stability of encapsulated Si solar cells and encapsulation materials upon accelerated exposures. *Sol. Energy Mater. Sol. Cells.* 2000. Vol. 61, no. 2, p. 153-188.

86. STOUMPOS, Constantinos C., FRAZER, Laszlo, CLARK, Daniel J., KIM, Yong Soo, RHIM, Sonny H., FREEMAN, Arthur J., KETTERSON, John B., JANG, Joon I. and KANATZIDIS, Mercouri G. Hybrid germanium iodide

- perovskite semiconductors: active lone pairs, structural distortions, direct and indirect energy gaps, and strong nonlinear optical properties. *J. Am. Chem. Soc.* 2015. Vol. 137, no. 21, p. 6804–6819.
87. VOLONAKIS, George, FILIP, Marina R., HAGHIGHIRAD, Amir Abbas, SAKAI, Nobuya, WENGER, Bernard, SNAITH, Henry J. and GIUSTINO, Feliciano. Lead-free halide double perovskites via heterovalent substitution of noble metals. *J. Phys. Chem. Lett.* 2016. Vol. 7, no. 7, p. 1254–1259.
88. SLAVNEY, Adam H., HU, Te, LINDENBERG, Aaron M. and KARUNADASA, Hemamala I. A bismuth-halide double perovskite with long carrier recombination lifetime for photovoltaic applications. *J. Am. Chem. Soc.* 2016. Vol. 138, no. 7, p. 2138–2141.
89. WEI, Fengxia, DENG, Zeyu, SUN, Shijing, XIE, Fei, KIESLICH, Gregor, EVANS, Donald M., CARPENTER, Michael A., BRISTOWE, Paul D. and CHEETHAM, Anthony K. The synthesis, structure and electronic properties of a lead-free hybrid inorganic–organic double perovskite $(MA)_2KBiCl_6$ ($MA =$ methylammonium). *Mater. Horiz.* 2016, Vol. 3, no. 4, p. 328–332.
90. XING, Guichuan, MATHEWS, Nripan, LIM, Swee Sien, YANTARA, Natalia, LIU, Xinfeng, SABBA, Dharani, GRATZEL, Michael, MHAISALKAR, Subodh and SUM, Tze Chien. Low-temperature solution-processed wavelength-tunable perovskites for lasing. *Nat. Mater.* 2014. Vol. 13, no. 5, p. 476–480.
91. ZHANG, Wei, PENG, Lan, LIU, Jie, TANG, Aiwei, HU, HU, Jin-Song, YAO, Jiannian and ZHAO, Yong Sheng. Controlling the cavity structures of two-photon-pumped perovskite microlasers. *Adv. Mater.* 2016. Vol. 28, no. 21, p. 4040–4046.
92. TAN, Zhi-Kuang, MOGHADDAM, Reza Saberi, LAI, May Ling, DOCAMPO, Pablo, HIGLER, Ruben, DESCHLER, Felix, PRICE, Michael, SADHANALA, Aditya, PAZOS, Luis M., CREDGINGTON, Dan, HANUSCH, Fabian, BEIN, Thomas, SNAITH, Henry J. and FRIEND, Richard H. Bright light-emitting diodes based on organometal halide perovskite. *Nat. Nanotechnol.* Vol 9, no. 9, p. 687–692.
93. LING, Yichuan, YUAN, Zhao, TIAN, Yu, WANG, Xi, WANG, Jamie C., XIN, Yan, HANSON, Kenneth, MA, Biwu and GAO, Hanwei. Bright light-emitting diodes based on organometal halide perovskite nanoplatelets. *Adv. Mater.* 2016. Vol. 28, no. 2, p. 305–311.
94. SONG, Tze-Bin, CHEN, Qi, ZHOU, Huanping, JIANG, Chengyang, WANG Hsin-Hua, YANG, Yang (Michael) Yang, LIU, Yongsheng, YOU, Jingbi and YANG, Yang. Perovskite solar cells: film formation and properties. *J. Mater. Chem. A.* 2015, Vol. 3, no 17, p. 9032–9050.
95. GRATZEL, Carole and ZAKEERUDDIN, Shaik. Recent trends in mesoscopic solar cells based on molecular and nanopigment light harvesters. *Mater. Today.* 2013. Vol. 16, no. 1-2, p. 11–18.
96. LEIJTENS, Tomas, EPERON, Giles E., PATHAK, Sandeep, ABATE, Antonio, LEE, Michael M. and SNAITH, Henry J. Overcoming ultraviolet light instability of sensitized TiO_2 with meso-superstructured organometal tri-halide perovskite solar cells. *Nat. Commun* [online]. 2013. Vol. 4, p. 2885. DOI:

- 10.1038/ncomms3885. Available from:
<https://www.nature.com/articles/ncomms3885>.
97. GRATIA, Paul, MAGOMEDOV, Artiom, MALINAUSKAS, Tadas, DASKEVICIENE, Maryte Daskeviciene, ABATE, Antonio, AHMAD, Shahzada, GRATZEL, Michael, GETAUTIS, Vytautas, NAZEERUDDIN, Mohammad Khaja. A methoxydiphenylamine-substituted carbazole twin derivative: an efficient hole-transporting material for perovskite solar cells. *Angew Chem Int Ed*. 2015. Vol. 54, no. 39, p. 11409-11413.
98. YANA, Junfeng and SAUNDERS, Brian R. Third-generation solar cells: a review and comparison of polymer: fullerene, hybrid polymer and perovskite solar cells. *RSC Adv*. 2014. Vol. 4, no. 82, p. 43286-43314.
99. ANSARIA, Mohammed Istafaul Haque, QURASHIB, Ahsanulhaq, NAZEERUDDIN, Mohammad Khaja. Frontiers, opportunities, and challenges in perovskite solar cells: A critical review. *J. Photochem. Photobiol. C*. 2018. Vol. 35, p. 1-24.
100. WANG, Lu, LI, Guo-Ran, ZHAO, Qian, GAO, Xue-Ping. Non-precious transition metals as counter electrode of perovskite solar cells. *Energy Stor. Mater*. 2017. Vol. 7, p. 40-47.
101. ZHOU, Long, CHANG, Jingjing, LIU, Ziyue, SUN, Xu, LIN, Zhenhua, CHEN, Dazheng, ZHANG, Chunfu, ZHANG, Jincheng and HAO, Yue. Enhanced planar perovskite solar cell efficiency and stability using a perovskite/PCBM heterojunction formed in one step. *Nanoscale*. 2018. Vol. 10, no. 6, p. 3053-3059.
102. WANG, Kuo-Chin, JENG, Jun-Yuan, SHEN, Po-Shen, CHANG, Yu-Cheng, DIAU, Eric Wei-Guang, TSAI, Cheng-Hung, CHAO, Tzu-Yang, HSU, Hsu-Cheng, LIN, Pei-Ying, CHEN, Peter, GUO, Tzung-Fang and WEN, Ten-Chin. p-type mesoscopic nickel oxide/organometallic perovskite heterojunction solar cells. *Sci. Rep.* [online]. 2014. Vol. 4, p. 4756. DOI: 10.1038/srep04756. Available from: <https://www.nature.com/articles/srep04756>.
103. HELLMANN, Tim, DAS, Chittaranjan, ABZIEHER, Tobias, SCHWENZER, Jonas A., WUSSLER, Michael, DACHAUER, Ralph, PAETZOLD, Ulrich W., JAEGERMANN, Wolfram, MAYER, Thomas. The electronic structure of MAPI-based perovskite solar cells: detailed band diagram determination by photoemission spectroscopy comparing classical and inverted device stacks. *Adv. Energy Mater*. 2020. Vol. 10, no. 42, p. 2002129.
104. CHEN, Yichuan, ZHANG, Linrui, ZHANG, Yongzhe, GAO, Hongli and YAN, Hui. Large-area perovskite solar cells – a review of recent progress and issues. *RSC Adv*. 2018. Vol. 8, no. 19, p. 10489-10508.
105. SALIBA, Michael, MATSUI, Taisuke, SEO, Ji-Youn, DOMANSKI, Konrad, CORREA-BAENA, Juan-Pablo, NAZEERUDDIN, Mohammad Khaja, ZAKEERUDDIN, Shaik M., TRESS, Wolfgang, ABATE, Antonio, HAGFELDT, Anders and GRATZEL, Michael. Cesium-containing triple cation perovskite solar cells: improved stability, reproducibility and high efficiency. *Energy Environ. Sci*. 2016. Vol. 9, no. 6, p. 1989-1997.

106. IGUAL-MUNOZ, Ana M., CASTILLO, Aroa, DREESSEN, Chris, BOIX, Pablo P. and BOLINK, Henk J. Vacuum-deposited multication tin–lead perovskite solar cells. *ACS Appl. Energy Mater.* 2020. Vol. 3, no. 3, p. 2755-2761.
107. WANG, Xiao, RAKSTYS, Kasparas, JACK, Kevin, JIN, Hui, LAI, Jonathan, LI, Hui, RANASINGHE, Chandana Sampath Kumara, SAGHAEI, Jaber, ZHANG, Guanran, BURN Paul L., GENTLE, Ian R. and SHAW, Paul E. Engineering fluorinated-cation containing inverted perovskite solar cells with an efficiency of >21% and improved stability towards humidity. *Nat. Commun.* 2021. Vol. 12, p. 52. DOI: 10.1038/s41467-020-20272-3. Available from: <https://www.nature.com/articles/s41467-020-20272-3>
108. NREL efficiency chart. Available from: http://www.nrel.gov/ncpv/images/efficiency_chart.jpg, accessed: 26/02/2020.
109. DUNFIELD, Sean P., BLISS, Lyle, ZHANG, Fei, LUTHER, Joseph M., ZHU, Kai, VAN HEST, Maikel F. A. M., REESE, Matthew O. and BERRY, Joseph J. From Defects to degradation: a mechanistic understanding of degradation in perovskite solar cell devices and modules. *Adv. Energy Mater.* 2020. Vol. 10, no. 26, p. 1904054.
110. ASKAR, Abdelrahman M., BERNARD, Guy M., WILTSHIRE, Benjamin, SHANKAR, Karthik and MICHAELIS, Vladimir K. Multinuclear magnetic resonance tracking of hydro, thermal, and hydrothermal decomposition of $\text{CH}_3\text{NH}_3\text{PbI}_3$. *J. Phys. Chem. C* 2017. Vol. 121, no. 2, p. 1013–1024.
111. LEGUY, Aurélien M. A., HU, Yinghong, CAMPOY-QUILES, Mariano, ALONSO, M. Isabel, WEBER, Oliver J., AZARHOOSH, Pooya, VAN SCHILFGAARDE, Mark, WELLER, Mark T., BEIN, Thomas, NELSON, Jenny, DOCAMPO, Pablo and BARNES, Piers R. F. Reversible hydration of $\text{CH}_3\text{NH}_3\text{PbI}_3$ in films, single crystals, and solar cells. *Chem. Mater.* 2015. Vol. 27, no. 9, p. 3397–3407.
112. DUALEH, Amalie, GAO, Peng, SEOK, Sang Il, NAZEERUDDIN, Mohammad Khaja and GRATZEL, Michael. Thermal behavior of methylammonium lead-trihalide perovskite photovoltaic light harvesters. *Chem. Mater.* 2014. Vol. 26, no. 21, p. 6160–6164.
113. NENON, David P., CHRISTIANS, Jeffrey A., WHEELER, Lance M., BLACKBURN, Jeffrey L., SANEHIRA, Erin M., DOU, Benjia, OLSEN, Michele L., ZHU, Kaim BERRY, Joseph J. and LUTHER, Joseph M. Structural and chemical evolution of methylammonium lead halide perovskites during thermal processing from solution. *Energy Environ. Sci.* 2016. Vol. 9, no. 6, p. 2072-2082.
114. WILLIAMS, Alice E. Williams, HOLLIMAN, Peter J., CARNIE, Matthew J., DAVIES, Matthew L., WORSLEY, David A. and WATSON, Trystan M. Perovskite processing for photovoltaics: a spectro-thermal evaluation. *J. Mater. Chem. A* 2014. Vol. 2, no. 45, p. 19338-19346.
115. JUAREZ-PEREZ, Emilio J., HAWASH, Zafer, RAGA, Sonia R., ONO, Luis K. and QI, Yabing. Thermal degradation of $\text{CH}_3\text{NH}_3\text{PbI}_3$ perovskite into NH_3 and CH_3I gases observed by coupled thermogravimetry–mass spectrometry analysis. *Energy Environ. Sci.* 2016. Vol. 9, no. 11, p. 3406-3410.

116. KIM, Nam-Koo, MIN, Young Hwan, NOH, Seokhwan, CHO, Eunkyung, JEONG, Gitaeg, JOO, Minho, AHN, Seh-Won, LEE, Jeong Soo, KIM, Seongtak, IHM, Kyuwook, AHN, Hyungju, KANG, Yoonmook, LEE, Hae-Seok and KIM, Donghwan. Investigation of thermally induced degradation in $\text{CH}_3\text{NH}_3\text{PbI}_3$ perovskite solar cells using *in-situ* synchrotron radiation analysis. *Sci. Rep.* [online]. 2017. Vol. 7, p. 4645. DOI: 10.1038/s41598-017-04690-w. Available from: <https://www.nature.com/articles/s41598-017-04690-w>.
117. LATINI, Alessandro, GIGLIA, Guido and CICCIO, Andrea. A study on the nature of the thermal decomposition of methylammonium lead iodide perovskite, $\text{CH}_3\text{NH}_3\text{PbI}_3$: an attempt to rationalise contradictory experimental results. *Sustainable Energy Fuels*. 2017. Vol. 1, no. 6, p. 1351-1357.
118. ARISTIDOU, Nicholas, SANCHEZ-MOLINA, Irene, CHOTCHUANGCHUTCHAVAL, Thana, BROWN, Michael, MARTINEZ, Luis, RATH, Thomas and HAQUE, Saif A. The role of oxygen in the degradation of methylammonium lead trihalide perovskite photoactive layers. *Angew Chem Int Ed*. 2015. Vol. 54, no. 28, p. 8208-8212.
119. BRYANT, Daniel, ARISTIDOU, Nicholas, PONT, Sebastian, SANCHEZ-MOLINA, Irene, CHOTCHUANGCHUTCHAVAL, Thana, WHEELER, Scot DURRANT, James R. and HAQUE, Saif A. Light and oxygen induced degradation limits the operational stability of methylammonium lead triiodide perovskite solar cells. *Energy Environ. Sci.* 2016. Vol. 9, no. 5, p. 1655-1660.
120. ARISTIDOU, Nicholas, EAMES, Christopher, SANCHEZ-MOLINA, Irene, BU, Xiangnan, KOSCO, Jan, ISLAM, M. Saiful and HAQUE, Saif A. Fast oxygen diffusion and iodide defects mediate oxygen-induced degradation of perovskite solar cells. *Nat. Commun* [online]. 2017. Vol. 8, p. 15218. DOI: 10.1038/ncomms15218. Available from: <https://www.nature.com/articles/ncomms15218>.
121. TAN, Wanliang, BOWRING, Andrea R., MENG, Andrew C. Meng, McGEHEE, Michael D. and McINTYRE, Paul C. Thermal stability of mixed cation metal halide perovskites in air. *ACS Appl. Mater. Interfaces*. 2018. Vol. 10, no. 6, p. 5485-5491.
122. XIA, Rui, FEI, Zhaofu, DRIGO, Nikita, BOBBINK, Felix D., HUANG, Zhangjun, JASIŪNAS, Rokas, FRANCKEVIČIUS, Marius, GULBINAS, Vidmantas, MENSI, Mounir, FANG, Xiaodong, ROLDAN-CARMONA, Cristina, NAZEERUDDIN, Mohammad Khaja and DYSON, Paul J. Retarding thermal degradation in hybrid perovskites by ionic liquid additives. *Adv. Funct. Mater.* 2019. Vol. 29, no. 22, p. 1902021.
123. BAI, Sai, DA, Peimei, LI, Cheng, WANG, Zhiping, YUAN, Zhongcheng, FU, Fan, KAWECKI, Maciej, LIU, Xianjie, SAKAI, Nobuya, WANG, Jacob Tse-Wei, HUETTNER, Sven, BUECHELER, Stephan, FAHLMAN, Mats, GAO, Feng and SNAITH, Henry J. Planar perovskite solar cells with long-term stability using ionic liquid additives. *Nature*. 2019. Vol. 571, no. 7764, p. 245+.
124. RAKSTYS, Kasparas, IGCIJA, Cansu and NAZEERUDDIN, Mohammad Khaja. Efficiency vs. stability: dopant-free hole transporting materials towards stabilized perovskite solar cells. *Chem. Sci.* 2019. Vol. 10, no. 28, p. 6748-6769.

125. YIN, Xinxing, SONG, Zhaoning, LI, Zaifang TANG, Weihua. Toward ideal hole transport materials: a review on recent progress in dopant-free hole transport materials for fabricating efficient and stable perovskite solar cells. *Energy Environ. Sci.* 2020. Vol. 13, no. 11, p. 4057-4086.
126. WALZER, K., MAENNIG, B., PFEIFFER, M. and LEO, K. Highly efficient organic devices based on electrically doped transport layers. *Chem. Rev.* 2007. Vol. 107, no. 4, p. 1233–1271.
127. LUSSEM, B., RIEDE, M., LEO, K. Doping of organic semiconductors. *Phys. Status Solidi Appl. Mater. Sci.* 2013, Vol. 210, no. 1, p. 9–43.
128. SCHLOEMER, Tracy H., CHRISTIANS, Jeffrey A., LUTHER, Joseph M. and SELLINGER, Alan. Doping strategies for small molecule organic hole-transport materials: impacts on perovskite solar cell performance and stability. *Chem. Sci.*, 2019. Vol. 10, no. 7, p. 1904-1935.
129. ABATE, Antonio, LEIJTENS, Tomas, PATHAK, Sandeep, TEUSCHER, Joel, AVOLIO, Roberto, ERRICO, Maria, KIRKPATRIK, James, BALL, James M., DOCAMPO, Pablo, McPHERSONC, Ian and SNAITH, Henry J. Lithium salts as “redox active” p-type dopants for organic semiconductors and their impact in solid-state dye-sensitized solar cells. *Phys. Chem. Chem. Phys.* 2013. Vol. 15, no. 7, p. 2572-2579.
130. HOWIE, W. H., HARRIS, J. E., JENNINGS, J. R., PETER, L.M. Solid-state dye-sensitized solar cells based on spiro-MeOTAD. *Sol. Energy Mater. Sol. Cells.* 2007. Vol. 91, no. 5, p. 424–426.
131. CALIL, Laura, KAZIM, Samrana, GRATZEL, Michael, and AHMAD, Shahzada. Hole-transport materials for perovskite solar cells. *Angew. Chem. Int. Ed.* 2016. Vol. 55, no. 47, p. 14522–14545
132. BI, Dongqin, XU, Bo, GAO, Peng, SUN, Licheng, GRATZEL, Michael, HAGFELDT, Anders. Facile synthesized organic hole transporting material for perovskite solar cell with efficiency of 19.8%. *Nano energy.* 2016. Vol. 23, p. 138-144.
133. XU, Bo, ZHU, Zonglong, ZHANG, Jinbao, LIU, Hongbin, CHUEH, Chu-Chen, LI, Xiaosong, JEN, Alex K.-Y. 4-Tert-butylpyridine free organic hole transporting materials for stable and efficient planar perovskite solar cells. *Adv. Energy Mater.* 2017. Vol. 7, no. 19, p. 1700683.
134. SALIBA, Michael, ORLANDI, Simonetta, MATSUI, Taisuke, AGHAZADA, Sadig, CAVAZZINI, Marco, CORREA-BAENA, Juan-Pablo, GAO, Peng, SCOPELLITI, Rosario, MOSCONI, Edoardo, DAHMEN, Klaus-Hermann, DE ANGELIS, Filippo, ABATE, Antonio, HAGFELDT, Anders, POZZI, Gianluca, GRAETZEL, Michael and NAZEERUDDIN, Mohammad Khaja. A molecularly engineered hole-transporting material for efficient perovskite solar cells. *Nat. Energy* [online]. 2016. Vol. 1, p. 15017. DOI: 10.1038/NENERGY.2015.17. Available from: <https://www.nature.com/articles/nenergy201517>.
135. MAGOMEDOV, Artiom, PAEK, Sanghyu, GRATIA, Paul, KASPARAVICIUS, Ernestas, DASKEVICIENE, Maryte, KAMARAUSKAS, Egidijus, GRUODIS, Alytis, JANKAUSKAS, Vygtintas, KANTMINIENE, Kristina, CHO, Kyung Taek, RAKSTYS, Kasparas, MALINAUSKAS, Tadas,

- GETAUTIS, Vytautas, NAZEERUDDIN, Mohammad Khaja. Diphenylamine-substituted carbazole-based hole transporting materials for perovskite solar cells: influence of isomeric derivatives. *Adv. Funct. Mater.* 2018. Vol. 28, no. 9, p. 1704351.
136. WU, Fei, JI, Yu, ZHONG, Cheng, LIU, Yuan, TAND, Luxi and ZHU, Linna. Fluorine-substituted benzothiadiazole-based hole transport materials for highly efficient planar perovskite solar cells with a FF exceeding 80%. *Chem. Commun.* 2017. Vol. 53, no. 62, p. 8719-8722.
137. WU, Fei, SHAN, Yahan, QIAO, Jianhui, ZHONG, Cheng WANG, Rui, SONG, Qunliang, ZHU, Linna. Replacement of biphenyl by bipyridine enabling powerful hole transport materials for efficient perovskite solar cells. *ChemSusChem.* 2017. Vol. 10, no. 19, p. 3833-3838.
138. LI, Dongmei, SHAO, Jiang-Yang, LI, Yiming, LI, Yusheng DENG, Li-Ye, ZHONG, Yu-Wu and MENG, Qingbo. New hole transporting materials for planar perovskite solar cells. *Chem. Commun.* 2018. Vol. 54, no. 13, p. 1651-1654.
139. DASKEVICIENE, Maryte, PAEK, Sanghyun, WANG, Zhiping, MALINAUSKAS, Tadas, JOKUBAUSKAITE, Gabriele, RAKSTYS, Kasparas, CHO, Kyung Taek, MAGOMEDOV, Artiom, JANKAUSKAS, Vygintas, AHMAD, Shahzada, SNAITH, Henry J., GETAUTIS, Vytautas, NAZEERUDDIN, Mohammad Khaja. Carbazole-based enamine: Low-cost and efficient hole transporting material for perovskite solar cells. *Nano Energy.* 2017. Vol. 32, p. 551-557.
140. DASKEVICIENE, Maryte, PAEK, Sanghyun, MAGOMEDOV, Artiom, CHO, Kyoung Taek, SALIBA, Michael, KIZELEVICIUTE, Ausra, MALINAUSKAS, Tadas, GRUODIS, Alytis, JANKAUSKAS, Vygintas, KAMARAUSKAS, Egidijus, NAZEERUDDIN, Mohammad Khaja and GETAUTIS, Vytautas. Molecular engineering of enamine-based small organic compounds as hole-transporting materials for perovskite solar cells. *Journal of materials Chemistry C.* 2019. Vol 7, no. 9, p. 2717-2724.
141. MAGOMEDOV, Artiom, KASPARAVICIUS, Ernestas, RAKSTYS, Kasparas, PAEK, Sanghyun, GASILOVA, Natalia, GENEVICIUS, Kristijonas, JUSKA, Gytis, MALINAUSKAS, Tadas, NAZEERUDDIN, Mohammad Khaja and GETAUTIS, Vytautas. Pyridination of hole transporting material in perovskite solar cells questions the long-term stability. *J. Mater. Chem. C.* 2018. Vol. 6, no. 33, p. 8874-8878.
142. KAZIM, Samrana, RAMOS, F. Javier, GAO, Peng, NAZEERUDDIN, Mohammad Khaja, GRATZEL, Michael and AHMAD, Shahzada. A dopant free linear acene derivative as a hole transport material for perovskite pigmented solar cells. *Energy Environ. Sci.* 2015. Vol. 8, no. 6, p. 1816-1823.
143. FRANCKEVICIUS, Marius, MISHRA, Amaresh, KREUZER, Franziska, LUO, Jingshan, ZAKEERUDDIN, Shaik Mohammed and GRATZEL, Michael. A dopant-free spirobi[cyclopenta[2,1-b:3,4-b']dithiophene] based hole-transport material for efficient perovskite solar cells. *Mater. Horiz.* 2015. Vol. 2, no. 6, p. 613-618.

144. YIN, Chengrong, LU, Jianfeng, XU, Yachao, YUN, Yikai, WANG, Kai, LI, Jiewei, JIANG, Liangcong, SUN, Jingsong, SCULLY, Andrew D., HUANG, Fuzhi, ZHONG, Jie, WANG, Jianpu, CHENG, Yi-Bing, QIN, Tianshi, HUANG, Wei. Low-cost *N,N'*-bicarbazole-based dopant-free hole-transporting materials for large-area perovskite solar cells. *Adv. Energy Mater.* 2018. Vol. 8, no. 21, p. 1800538.
145. WANG, Linqin, ZHANG, Jinbao, LIU, Peng, XU, Bo, ZHANG, Biaobiao, CHEN, Hong, INGE, A. Ken, LI, Yuanyuan, WANG, Haoxin, CHENG, Yi-Bing, KLOO, Lars and SUN Licheng. Design and synthesis of dopant-free organic hole-transport materials for perovskite solar cells. *Chem. Commun.* 2018. Vol. 54, no. 69, p. 9571-9574.
146. NI, Wang, WAN, Xiangjian, LI, Miaomiao, WANG, Yunchuang and CHEN, Yongsheng. A-D-A small molecules for solution-processed organic photovoltaic cells. *Chem. Commun.* 2015. Vol. 51, p. 4936-4950.
147. LIN, Yuze, WANG, Jiayu, ZHANG, Zhi-Guo. BAI, Huitao, LI, Yongfang, ZHU, Daoben, ZHAN, Xiaowei. An electron acceptor challenging fullerenes for efficient polymer solar cells. *Adv. Energy Mater.* 2015. Vol. 27, no. 7, p. 1170-1174.
148. CHENG, Ming, CHEN, Cheng, AITOLA, Kerttu, ZHANG, Fuguo, HUA, Yong, BOSCHLOO, Gerrit, KLOO, Lars and SUN, Licheng. Highly efficient integrated perovskite solar cells containing a small molecule-PC₇₀BM bulk heterojunction layer with an extended photovoltaic response up to 900 nm. *Chem. Mater.* 2016. Vol. 28, no. 23, p. 8631-8639.
149. CHENG, Ming, AITOLA, Kerttu, CHEN, Cheng, ZHANG, Fuguo, LIU, Peng, SVEINBJORNSSON, Kári, HUA, Yong, KLOO, Lars, BOSCHLOO, Gerrit, SUN, Licheng. Acceptor-Donor-Acceptor type ionic molecule materials for efficient perovskite solar cells and organic solar cells. *Nano Energy.* 2017. Vol. 30, p. 387-397.
150. BIAN, Linyi, ZHU, Enwei, TANG, Jian, TANG, Weihua, ZHANG, Fujun. Recent progress in the design of narrow bandgap conjugated polymers for high-efficiency organic solar cells. *Prog. Polym. Sci.* 2012. Vol. 37, no. 9, p. 1292-1331.
151. LIU, Yongsheng, CHEN, Qi, DUAN, Hsin-Sheng, ZHOU, Huanping, YANG, Yang (Michael), CHEN, Huajun, LUO, Song, SONG, Tze-Bin, DOU, Letian, HONGA, Ziruo and YANG, Yang. A dopant-free organic hole transport material for efficient planar heterojunction perovskite solar cells. *J. Mater. Chem. A.* 2015. Vol. 3, no. 22, p. 11940-11947.
152. PAEK, Sanghyun, QIN, Peng, LEE, Yonghui, CHO, Kyung Taek, GAO, Peng, GRANCINI, Giulia, OVEISI, Emad, GRATIA, Paul, RAKSTYS, Kasparas, AL-MUHTASEB, Shaheen A., LUDWIG, Christian, KO, Jaejung, NAZEERUDDIN Mohammad Khaja. Dopant-free hole-transporting materials for stable and efficient perovskite solar cells. *Adv. Mater.* 2017. Vol. 29, no. 35, p. 1606555.
153. XU, Peng, LIU, Peng, LI, Yuanyuan, XU, Bo, KLOO, Lars, SUN, Licheng and HUA, Yong. D-A-D-typed hole transport materials for efficient perovskite

solar cells: tuning photovoltaic properties via the acceptor group. *ACS Appl. Mater. Interfaces*. 2018. Vol. 10, no. 23, p. 19697-19703.

154. QIU, Jianfeng, LIU, Hongli, LI, Xianggao, WANG, Shirong, ZHANG, Fei. Impact of 9-(4-methoxyphenyl) carbazole and benzodithiophene cores on performance and stability for perovskite solar cells based on dopant-free hole-transporting materials. *Sol. RRL*. 2019. Vol. 3, no. 10, p. 1900202. DOI: 10.1002/solr.201900202. Available from:

<https://onlinelibrary.wiley.com/doi/abs/10.1002/solr.201900202>.

155. PHAM, Hong Duc, DO, Thu Trang, KIM, Jinhyun, CHARBONNEAU, Cecile, MANZHOS, Sergei, FERON, Krishna, TSOI, Wing Chung, DURRANT, James R. JAIN, Sagar M., SONAR, Prashant. Molecular engineering using an anthanthrone dye for low-cost hole transport materials: a strategy for dopant-free, high-efficiency, and stable perovskite solar cells. *Adv. Energy Mater.* 2018. Vol. 8, no. 16, p. 1703007.

156. SUN, Xianglang, WU, Fei, ZHONG, Cheng, ZHU, Linna and LI, Zhong'an. A structure–property study of fluoranthene-cored hole-transporting materials enables 19.3% efficiency in dopant-free perovskite solar cells. *Chem. Sci.* 2019. Vol. 10, no. 28, p. 6899-6907.

157. SHANG, Rui, ZHOU, Zhongmin, NISHIOKA, Hiroki, HALIM, Henry, FURUKAWA, Shunsuke, TAKEI, Izuru, NINOMIYA, Naoya and NAKAMURA, Eiichi. Disodium benzodipyrrole sulfonate as neutral hole-transporting materials for perovskite solar cells. *J. Am. Chem. Soc.* 2018. Vol. 140, no. 15, p. 5018–5022.

158. HUANG, Chuyi, FU, Weifei, LI, Chang-Zhi, ZHANG, Zhongqiang, QIU, Weiming, SHI, Minmin, HEREMANS, Paul, JEN, Alex K.-Y. and CHEN, Hongzheng. Dopant-free hole-transporting material with a C_{3h} symmetrical truxene core for highly efficient perovskite solar cells. *J. Am. Chem. Soc.* 2016. Vol. 138, no. 8, p. 2528–2531.

159. WANG, Yang, CHEN, Wei, WANG, Lei, TU, Bao, CHEN, Tian, LIU, Bin, YANG, Kun, KOH, Chang Woo, ZHANG, Xianhe, SUN, Huiliang, CHEN, Guocong, FENG, Xiyuan, WOO, Han Young, DJURIŠIĆ, Aleksandra B., HE, Zhubing, GUO, Xugang. Dopant-Free Small-Molecule Hole-Transporting Material for Inverted Perovskite Solar Cells with Efficiency Exceeding 21%. *Adv. Mater.* 2019. Vol. 31, no. 35, p. 1902781.

160. CHEN, Huanle, FU, Weifei, HUANG, Chuyi, ZHANG, Zhongqiang, LI, Shuixing, DING, Feizhi, SHI, Minmin, LI, Chang-Zhi, JEN, Alex K.-Y., CHEN, Hongzheng. Molecular engineered hole-extraction materials to enable dopant-free, efficient p-i-n perovskite solar cells. *Adv. Energy Mater.* 2017. Vol. 7, no. 18, p. 1700012.

161. ZHANG, Jing, SUN, Quan, CHEN, Qiaoyun, WANG, Yikai, ZHOU, Yi, SONG, Bo, YUAN, Ningyi, DING, Jianning, LI, Yongfang. High efficiency planar p-i-n perovskite solar cells using low-cost fluorene-based hole transporting material. *Adv. Funct. Mater.* 2019. Vol. 29, no. 22, p. 1900484.

162. JIANG, Kui, WANG, Jing, WU, Fei, XUE, Qifan, YAO, Qin, ZHANG, Jianquan, CHEN, Yihuang, ZHANG, Guangye, ZHU, Zonglong, YAN, He, ZHU, Linna, YIP, Hin-Lap. Dopant-free organic hole-transporting material for efficient

and stable inverted all-inorganic and hybrid perovskite solar cells. *Adv. Mater.* 2020. Vol. 32, no. 16, p. 1908011.

163. MAGOMEDOV, Artiom, AL-ASHOURI, Amran, KASPARAVIČIUS Ernestas, STRAZDAITE, Simona, NIAURA Gediminas, JOŠT, Marko MALINAUSKAS, Tadas, ALBRECHT, Steve, GETAUTIS, Vytautas. Self-Assembled hole transporting monolayer for highly efficient perovskite solar cells. *Adv. Energy Mater.* 2018. Vol. 8, no. 32, p. 1801892.

164. YALCIN, E., CAN, M., RODRIGUEZ-SECO, C., AKTAS, E., PUDI, R., CAMBARAU, W., DEMIC, S. and PALOMARES, E. Semiconductor self-assembled monolayers as selective contacts for efficient PIN perovskite solar cells. *Energy Environ. Sci.* 2019. Vol. 12, no. 1, p. 230-237.

165. KWON, Y. S., LIM, J., YUN, H. J., KIM, Y. H., and PARK. T. Diketopyrrolopyrrole-Containing Hole Transporting Conjugated Polymer for use in Efficient Stable Organic-Inorganic Hybrid Solar Cells based on a Perovskite. *Energy Environ. Sci.* 2014. Vol 7, no. 4, p 1454-1460.

166. LI, Xiaodong, WANG, Ying-Chiao, ZHU, Liping, ZHANG, Wenjun, WANG, Hai-Qiao, and FANG, Junfeng. Improving efficiency and reproducibility of perovskite solar cells through aggregation control in polyelectrolytes hole transport layer. *ACS Appl. Mater. Interfaces*, 2017. Vol. 9, no. 37, p. 31357-31361.

167. XU, Yachao, BU, Tongle, LI, Meijin, QIN, Tianshi, YIN, Chengrong, WANG, Nanna, LI, Renzhi, ZHONG, Jie, LI, Hai, PENG, Yong, WANG, Jianpu, XIE, Linghai and HUANG, Wei. Non-conjugated polymer as an efficient dopant-free hole transporting material for perovskite solar cells. *ChemSusChem*. 2017. Vol. 10, no. 12, p. 2578-2584.

168. WU, Jianchang, LIU, Chang, LI, Bo, GU, Fenglong, ZHANG, Luozheng, HU, Manman, DENG, Xiang, QIAO, Yuan, MAO, Yongyun, TAN, Wenchang, TIAN, Yanqing and XU, Baomin. Side-chain polymers as dopant-free hole-transporting materials for perovskite solar cells-the impact of substituents' positions in carbazole on device performance. *ACS Appl. Mater. Interfaces*. 2019. Vol. 11, no. 30, p. 26928-26937.

169. WU, Jianchang Wu, LIU, Chang, HU, Manman, DENG, Xiang, TAN, Wenchang, TIAN, Yanqing and XU, Baomin. Polystyrene with a methoxytriphenylamine-conjugated-thiophene moiety side-chain as a dopant-free hole-transporting material for perovskite solar cells. *J. Mater. Chem. A*. 2018. Vol. 6, no. 27, p. 13123-13132.

170. CAI, Feilong, CAI, Jinlong, YANG, Liyan, LI, Wei, GURNEY, RobertS., YI, Hunan, IRAQI, Ahmed, LIU, Dan, WANG, Tao. Molecular engineering of conjugated polymers for efficient hole transport and defect passivation in perovskite solar cells. *Nano Energy*. 2018. Vol. 45, p. 28-36.

171. ZHANG, Luozheng, LIU, Chang, ZHANG, Jie, LI, Xiangnan, CHENG, Chun, TIAN, Yanqing, JEN, Alex K.-Y., XU, Baomin. Intensive exposure of functional rings of a polymeric hole-transporting material enables efficient perovskite solar cells. *Adv. Mater.* 2018. Vol. 30, no. 39, p. 1804028.

172. URBANI, Maxence, DE LA TORRE, Gema, NAZEERUDDIN, Mohammad Khaja and TORRES, Tomás. Phthalocyanines and porphyrinoid analogues as hole-

and electron-transporting materials for perovskite solar cells. *Chem. Soc. Rev.* 2019. Vol. 48, no. 10, p. 2738-2766.

173. CHEN, Song, LIU, Peng, HUA, Yong, LI, Yuanyuan, KLOO, Lars, WANG, Xingzhu, ONG, Beng, WONG, Wai-Kwok and ZHU, Xunjin. Study of arylamine-substituted porphyrins as hole-transporting materials in high-performance perovskite solar cells. *ACS Appl. Mater. Interfaces.* 2017. Vol. 9, no. 15, p. 13231–13239.

174. JIANG, Xiaoqing, YU, Ze, LI, Hai-Bei, ZHAO, Yawei, QU, Jishuang, LAI, Jianbo, MA, Wanying, WANG, Dongping, YANG, Xichuan and SUN, Licheng. A solution-processable copper(ii) phthalocyanine derivative as a dopant-free hole-transporting material for efficient and stable carbon counter electrode-based perovskite solar cells. *J. Mater. Chem. A.* 2017. Vol. 5, no. 34, p. 17862-17866.

175. CHENH, Ming, LI, Yuanyuan, SAFDARI, Majid, CHEN, Cheng, LIU, Peng, KLOO, Lars, SUN, Licheng. Efficient perovskite solar cells based on a solution processable nickel(II) phthalocyanine and vanadium oxide integrated hole transport layer. *Adv. Energy Mater.* 2017. Vol. 7, no. 14, p. 1602556.

176. ARORA, Neha, DAR, Ibrahim, HINDERHOFER, Alexander, PELLET, Norman Pellet, ZAKEERUDDIN, Mohammed, GRATZEL, Michael. Perovskite solar cells with CuSCN hole extraction layers yield stabilized efficiencies greater than 20%. *Science.* 2017. Vol. 358, no. 6364, p. 768-771.

177. LIU, Chang, ZHOU, Xianyong, CHEN, Shuming, ZHAO, Xingzhong, DAI, Songyuan, XU, Baomin. Hydrophobic Cu₂O quantum dots enabled by surfactant modification as top hole-transport Materials for efficient perovskite solar cells. *Adv. Sci.* 2019. Vol. 6, no. 7, p. 1801169.

178. ZHANG, Hua, WANG, Huan, ZHU, Hongmei, CHUEH, Chu-Chen, CHEN, Wei, YANG, Shihe, JEN, Alex K.-Y. Low-temperature aolution-processed CuCrO₂ hole-transporting layer for efficient and photostable perovskite solar cells. *Adv. Energy Mater.* 2018. Vol. 8, no. 13, p. 1702762.

179. PORRES, Laurent, MONGIN, Olivier, KATAN, Claudine, CHARLOT, Marina, PONS, Thomas, MERTZ, Jerome, and BLANCHARD-DESCE, Mireille. Enhanced two-photon absorption with novel octupolar propeller-shaped fluorophores derived from triphenylamine. *Org. Lett.* 2004. Vol. 6, no. 1, p. 47-50.

180. SONNTAG, Martin, KREGER, Klaus, HANFT, Doris, STROHRIEGL, Peter, SETAYESH, Sepas and De LEEUW, Dago. Novel star-shaped triphenylamine-based molecular glasses and their use in OFETs. *Chem. Mater.* 2005. Vol. 17, no. 11, p. 3031-3039.

181. SONG, Yabin, DI, Chong'an, YANG, Xiaodi, LI, Shouping, XU, Wei, LIU, Yunqi, YANG, Lianming, SHUAI, Zhigang, ZHANG, Deqing, and ZHU, Daoben. A cyclic triphenylamine dimer for organic field-effect Transistors with high performance. *J. Am. Chem. Soc.* 2006. Vol. 128, no. 50, p. 15940-15941.

182. KUWABARA, Yoshiyuki, OGAWA, Hiromitsu, INADA, Hiroshi, NOMA, Naoki, SHIROTA, Yasuhiko. Thermally stable multilayered organic electroluminescent devices using novel starburst molecules, 4,4',4''-Tri(N-carbazolyl)triphenylamine(TCTA) and 4,4',4''-Tris (3-methylphenylphenylamino)

- triphenylamine (m-MTDATA), as Hole-Transport Materials. *Adv. Mater.* 1994. Vol. 6, no. 9, p. 677-679.
183. TOKITO, Shizuo, TANAKA, Hiromitsu, OKADA, Akane and TAGA, Yasunori. High temperature operation of an electroluminescent device fabricated using a novel triphenylamine derivative. *Appl. Phys. Lett.* 1996. Vol. 69, p. 878.
184. TOKITO, Shizuo, TANAKA, Hiromitsu, NODA, Koji, OKADA, Akane and TAGA, Yasunori. Thermal stability in oligomeric triphenylamine/tris(8-quinolinolato) aluminum electroluminescent devices. *Appl. Phys. Lett.* 1997. Vol. 70, no. 15, p. 1929-1931.
185. EGO, C., GRIMSDALE, A. C., UCKERT, F., YU, G., SRDANOV, G., MULLEN, K. Triphenylamine – substituted polyfluorene – a stable blue – emitter with improved charge injection for light – emitting diodes. *Adv. Mater.* 2002. Vol. 14, no 11, p. 809-811.
186. HSU, Fang-Ming, CHIEN, Chen-Han, SHU, Ching-Fong, LAI, Chin-Hung, HSIEH, Cheng-Chih, WANG, Kang-Wei, CHOU, Pi-Tai. A bipolar host material containing triphenylamine and diphenylphosphoryl-substituted fluorene units for highly efficient blue electrophosphorescence. *Adv. Funct. Mater.* 2009, Vol. 19, no. 17, p. 2834-2843.
187. ZHOU, Guijiang, WONG, Wai-Yeung, YAO, Bing, XIE, Zhiyuan, WANG, Lixiang. Triphenylamine-dendronized pure red iridium phosphors with superior OLED efficiency/color purity trade-offs. *Angew. Chem.* 2007. Vol. 119, p. 1167-1169.
188. MAZZIO, Katherine A. and LUSCOMBE, Christine K. The future of organic photovoltaics. *Chem. Soc. Rev.* 2015. Vol. 44, no. 1, p. 78-90.
189. AGARWALA, Pooja, KABRA, Dinesh. A review on triphenylamine (TPA) based organic hole transport materials (HTM) for dye sensitized solar Cells (DSSCs) and perovskite solar cells (PSCs): Evolution and molecular engineering. *J. Mater. Chem. A.* 2017. Vol. 5, no. 4, p. 1348-1373.
190. WANG, Zijun, ZHANG, Dayong, YANG, Genjie and YU, Junsheng. Exceeding 19% efficiency for inverted perovskite solar cells used conventional organic small molecule TPD as hole transport layer. *Appl. Phys. Lett.* Vol. 118, no. 18, p. 183301.
191. MALINAUSKAS, Tadas, DASKEVICIENE, Maryte, BUBNIENE, Giedre, PETRIKYTE, Ieva, RAISYS, Steponas, KAZLAUSKAS, Karolis, GAIDELIS, Valentas, JANKAUSKAS, Vyngintas, MALDZIUS, Robertas, JURSENAS, Saulius and GETAUTIS, Vytautas. Phenylethenyl-substituted triphenylamines: efficient, easily obtainable, and inexpensive hole-transporting materials. *Chem. Eur. J.* 2013 Vol. 19, no. 44, p. 15044-15056.
192. LE CORRE, Vincent M., STOLTERFOHT, Martin, TORO, Lorena Perdigón, FEUERSTEIN, Markus, WOLFF, Christian, GIL-ESCRIG, Lidón, BOLINK, Henk J., NEHER, Dieter and KOSTER, L. Jan Anton. Charge transport layers limiting the efficiency of perovskite solar cells: how to optimize conductivity, doping, and thickness. *ACS Appl. Energy Mater.* 2019. Vol. 2, no. 9, p. 6280–6287.
193. KAZLAUSKAS, Karolis, KREIZA, Gediminas, ARBAČIAUSKIENĖ, Eglė, BIELIAUSKAS, Aurimas, GETAUTIS, Vytautas, ŠAČKUS, Algirdas and

- JURŠENAS, Saulius. Morphology and emission tuning in fluorescent nanoparticles based on phenylenediacetonitrile *J. Phys. Chem. C*. 2014. Vol. 118, no. 43, p. 25261–25271.
194. KIM, Hobeom, LIM, Kyung-Geun and LEE, Tae-Woo. Planar heterojunction organometal halide perovskite solar cells: roles of interfacial layers. *Energy & Environmental Science*. 2016. Vol. 9, no. 1, p. 12–30.
195. ZHOU, Weiqi, WEN, Zhenhai, and GAO Peng. Less is more: dopant-free hole transporting materials for high-efficiency perovskite solar cells. *Adv. Energy Mater.* 2018. Vol. 8, no. 9, p. 1702512.
196. SHIROTA, Yasuhiko and KAGEYAMA, Hiroshi. Charge carrier transporting molecular materials and their applications in devices. *Chemical reviews*. 2007. Vol. 107, no. 4, p. 953–1010.
197. STROHRIEGL, Peter and GRAZULEVICIUS, Juozas V. Charge-transporting molecular glasses. *Advanced Materials*. 2002. Vol. 14, no. 20, p. 1439–1452.
198. SEK, Danuta, GRABIEC, Eugenia, JANECZEK, Henryk, JARZABEK, Bozena, KACZMARCZYK, Bozena, DOMANSKI, Marian and IWAN, Agnieszka. Structure–properties relationship of linear and star-shaped imines with triphenylamine moieties as hole-transporting materials. *Optical Materials*. 2010. Vol. 32, no. 11, p. 1514–1525.
199. BARONAS, Paulius, KAZLAUSKAS, Karolis, GRUODIS, Alytis, JANKAUSKAS, Vygintas, TOMKEVICIENE, Ausra, SIMOKAITIENE, Jurate, GRAZULEVICIUS, Juozas Vidas and JURSENAS, Saulius. High-triplet-energy carbazole and fluorene tetrads. *Journal of Luminescence*. 2016. Vol. 169, p. 256–265.
200. MALINAUSKAS, Tadas, TOMKUTE-LUKSIENE, Daiva, SENS, Rüdiger, DASKEVICIENE, Maryte, SEND, Robert, WONNEBERGER, Henrike, JANKAUSKAS, Vygintas, BRUDER, Ingmar and GETAUTIS, Vytautas. Enhancing thermal stability and lifetime of solid-state dye-sensitized solar cells via molecular engineering of the hole-transporting material spiro-OMeTAD. *ACS Appl. Mater. Interfaces*. Vol. 7, no. 21, p. 11107–11116.
201. ABATE, Antonio, PAEK, Sanghyun, GIORDANO, Fabrizio, CORREA-BAENA, Juan-Pablo, SALIBA, Michael, GAO, Peng, MATSUI, Taisuke, KO, Jaejung, ZAKEERUDDIN, Shaik M and DAHMEN, Klaus H. Silolothiophene-linked triphenylamines as stable hole transporting materials for high efficiency perovskite solar cells. *Energy & Environmental Science*. 2015. Vol. 8, no. 10, p. 2946–2953.
202. GONZALEZ-PEDRO, Victoria, JUAREZ-PEREZ, Emilio J., ARSYAD, Waode-Sukmawati, BAREA, Eva M., FABREGAT-SANTIAGO, Francisco, MORA-SERO, Ivan, and BISQUERT, Juan. General Working Principles of $\text{CH}_3\text{NH}_3\text{PbX}_3$ perovskite solar cells. *Nano Lett.* 2014. Vol. 14, no. 2, p. 888–893.
203. BI, Dongqin, YANG, Lei, BOSCHLOO, Gerrit, HAGFELDT, Anders and JOHANSSON, Erik M. J. Effect of different hole transport materials on recombination in $\text{CH}_3\text{NH}_3\text{PbI}_3$ perovskite-sensitized mesoscopic solar cells. *Phys. Chem. Lett.* 2013. Vol. 4, no 9, p. 1532–1536.

204. RIQUELME, Antonio, BENNETT, Laurence J., COURTIER, Nicola E., WOLF, Matthew J., CONTRERAS-BERNAL, Lidia, WALKER, Alison B., RICHARDSON, Giles and ANTA, Juan A. Identification of recombination losses and charge collection efficiency in a perovskite solar cell by comparing impedance response to a drift-diffusion model. *Nanoscale*. 2020. Vol. 12, no. 33, p. 17385-17398.
205. CHENG, Yen-Ju, YANG, Sheng-Hsiung and HSU, Chain-Shu. Synthesis of conjugated polymers for organic solar cell applications. *Chem. Rev.* 2009. Vol. 109, no. 11, p. 5868–5923.
206. CAI, Bing, XING, Yedi, YANG, Zhou, ZHANG, Wen-Hua and QIU, Jieshan. High performance hybrid solar cells sensitized by organolead halide perovskites. *Energy Environ. Sci.*, 2013. Vol. 6, no. 5, p. 1480-1485.
207. KIM, Guan-Woo, KANG, Gyeongho, KIM, Jinseck, LEE, Gang-Young, KIM, Hong Il, PYEON, Limok, LEEB, Jaechol and PARK, Taiho. Dopant-free polymeric hole transport materials for highly efficient and stable perovskite solar cells. *Energy Environ. Sci.* 2016. Vol. 9, no. 7, p. 2326-2333.
208. WANG, Shih-Hao, WANG, Teng-Wei, TSAI, Hsieh-Chih, YANG, Po-Chih, HUANG, Chih-Feng and LEE, Rong-Ho. Synthesis of the diketopyrrolopyrrole/terpyridine substituted carbazole derivative based polythiophenes for photovoltaic cells. *RSC Adv.* 2020. Vol. 10, no. 16, p. 9525-9535.
209. YANG, Woon Seok, NOH, Jun Hong, JEON, Nam Joong, KIM, Young Chan, RYU, Seungchan, SEO, Jangwon, SEOK, Sang Il. High-performance photovoltaic perovskite layers fabricated through intramolecular exchange. *Science*. 2015. Vol. 10, no. 6240, p. 1234-1237.
210. VAITUKAITYTĖ, Deimantė, AL-ASHOURI, Amran, DAŠKEVIČIENĖ, Marytė, KAMARAUSKAS, Egidijus, NEKRASOVAS, Jonas, JANKAUSKAS, Vygintas, MAGOMEDOV, Artiom, ALBRECHT, Steve, GETAUTIS, Vytautas. Enamine-based cross-linkable hole-transporting materials for perovskite solar cells. *Sol. RRL*. 2021. Vol. 5, no. 1, p. 2000597.
211. COLON, I and KWIATKOWSKI, G. T. High molecular weight aromatic polymers by nickel coupling of aryl polychlorides. *Polymer chemistry*. 1990. Vol. 28 no. 2, p. 367-383.
212. PERCEC, Virgil, BAE, Jin-Young, ZHAO, Mingyang and HILL, Dale H. Aryl mesylates in metal-catalyzed homocoupling and cross-coupling reactions. 1. Functional symmetrical biaryls. from phenols via nickel-catalyzed homocoupling of their mesylates. *J. Org. Chem.* 1995. Vol. 60, no. 1, p. 176–185.
213. KWIATKOWSKI, G. T., MARTZNER, M. and COLON, I. Aromatic polymers: synthesis via nickel catalyzed coupling of aryl chlorides. *Journal of Macromolecular Science*. Vol. A34, no. 10, p. 1945-1975.
214. NUGRAHA, Adam F., KIM, Songmi, WIJAYA, Farid, BAE, Byungchan and SHIN, Dongwon. Synthetic approaches for poly(phenylene) block copolymers via nickel coupling reaction for fuel cell applications. *Polymers*. 2020. Vol. 12, no. 7, p. 1614.

215. DILIEN, Hanne, CHAMBON, Sylvain, CLEIJ, Thomas J., LUTSEN, L., VANDERZANDE, Dirk, and ADRIAENSENS, Peter. Identification and quantification of defect structures in poly(2,5-thienylene vinylene) derivatives prepared via the dithiocarbamate precursor route by means of NMR spectroscopy on ¹³C-labeled polymers. *Macromolecules*. 2011. Vol. 44, no. 12, p. 4711–4720.
216. ASO, C., KUNITAKE, T., SHINSENI, M. and MIYAZAKI, H. Polymerization of vinyl compounds with heterocyclic groups. IV. Thermal polymerization of 2-vinylthiophene. *Polymer Chemistry*. 1969. Vol. 7, no. 6, p. 1497-1508.
217. MALY, Kenneth E. Acenes vs N-heteroacenes: the effect of N-substitution on the structural features of crystals of polycyclic aromatic hydrocarbons. *Cryst. Growth Des.* 2011. Vol. 11, no. 12, p. 5628–5633.
218. BABAEI, Azin, RAKSTYS, Kasparas, GUELEN, Simon, HAMIDABADI, Vahid Fallah, LA-PLACA, Maria-Grazia, MARTINEZ-SARTI, Laura, SESSOLO, Michele, JOEL, Huckaba Aron, GAUDIN, Olivier P. M., SCHANEN, Vincent, NAZEERUDDIN, Mohammad Khaja and BOLINK, Henk J. Solution processed organic light-emitting diodes using a triazatruxene crosslinkable hole transporting material. *RSC Adv.* 2018. Vol. 8, no. 62, p. 35719-35723.
219. CONNELLY, Neil G and GEIGER, William E. Chemical redox agents for organometallic chemistry. *Chemical Reviews*. 1996. Vol. 96, no. 2, p. 877–910.
220. PAVLISHCHUK, Vitaly V and ADDISON, Anthony W. Conversion constants for redox potentials measured versus different reference electrodes in acetonitrile solutions at 25 C. *Inorganica Chimica Acta*. 2000. Vol. 298, no. 1, p. 97–102.
221. REISS, Howard and HELLER, Adam. The absolute potential of the standard hydrogen electrode: a new estimate. *The Journal of Physical Chemistry*. 1985. Vol. 89, no. 20, p. 4207–4213.
222. HAMBSCHE, Mike, ERDMANN, Tim, CHEW, Annabel R., BERNSTORFF, Sigrid, SALLEO, Alberto, KIRIY, Anton, VOIT, Brigitte and MANNSFELDT, Stefan C. B. Increased charge carrier mobility and molecular packing of a solution sheared diketopyrrolopyrrole-based donor–acceptor copolymer by alkyl side chain modification. *J. Mater. Chem. C*. 2019. Vol. 7, no. 12, p. 3665-3674.
223. FELTER, Kevin M., CASELLI, Valentina M., GUNBAS, D. Deniz, SAVENIJE, Tom J., and GROZEMA, Ferdinand C. Interplay between Charge Carrier Mobility, Exciton Diffusion, Crystal Packing, and Charge Separation in Perylene Diimide-Based Heterojunctions. *ACS Appl. Energy Mater.* 2019. Vol. 2, no. 11, 8010–8021.
224. HUANG, Chuyi, FU, Weifei, LI, Chang-Zhi, ZHANG, Zhongqiang, QIU, Weiming, SHI, Minmin, HEREMANS, Paul, JEN, Alex K.-Y. and CHEN, Hongzheng. Dopant-free hole-transporting material with C_{3h} symmetrical truxene core for highly efficient perovskite solar cells. *J. Am. Chem. Soc.* 2016. Vol. 138, no. 8, p. 2528–2531.
225. GE, Qian-Qing, SHAO, Jiang-Yang, DING, Jie, DENG, Li-Ye, ZHOU, WEN-Ke, CHEN, Yao-Xuan, MA, Jing-Yuan, WAN, Li-Jun, YAO, Jiannian, HU, Jin-Song and ZHONG, Yu-Wu. A two-dimensional hole-transporting material for

- high-performance perovskite solar cells with 20 % Average Efficiency. *Angew. Chem., Int. Ed.* 2018. Vol. 57, no. 34, p. 10959–10965.
226. ROJAS, Diana Elizabeth Meza, CHO, Kyung Taek, ZHANG, Yi, URBANI, Maxence, TABET, Nouar, DE LA TORRE, GEMA, NAZEERUDDIN, Mohammad Khaja and TORRES, TOMAS. Tetrathienoanthracene and tetrathienylbenzene derivatives as hole-transporting materials for perovskite solar cell. *Adv. Energy Mater.* 2018. Vol 8, no. 25, p. 1800681.
227. GARCIA-BENITO, Ines, ZIMMERMANN, Iwan, URIETA-MORA, Javier, ARAGO, Juan, MOLINA-ONTORIA, Agustin, ORTI, Enrique, MARTIN, Nazario and NAZEERUDDIN, Mohammad Khaja. Isomerism effect on the photovoltaic properties of benzotrithiophene-based hole-transporting materials. *J. Mater. Chem. A.* 2017. Vol. 5, no. 18, p. 8317–8324
228. TANG, Qin, ZHANG, Dieqing, WANG, Shenglong, KE, Ning, XU, Jianbin, YU, Jimmy C. and MIAO, Qian. A meaningful analogue of pentacene: charge transport, polymorphs, and electronic structures of dihydrodiazapentacene. *Chem. Mater.* 2009. Vol. 21, no. 7, p. 1400–1405.
229. KLUES, Michael and WITTE, Gregor. Crystalline packing in pentacene-like organic semiconductors. *CrystEngComm.* 2018. Vol. 20, no. 1, p. 63-74.
230. CURTIS, M. David, CAO, Jie, and KAMPF, Jeff W. Solid-state packing of conjugated oligomers: from π -stacks to the herringbone structure. *J. Am. Chem. Soc.* 2004. Vol. 126, no. 13, p. 4318–4328.
231. MA, Zhiying, GENG, Hua, WANG, Dong and SHUAI, Zhigang. Influence of alkyl side-chain length on the carrier mobility in organic semiconductors: herringbone vs. π - π stacking. *J. Mater. Chem. C.* 2016. Vol. 4, no. 20, p. 4546-4555.
232. GU, Xiao, SHAN, Bowen, HE, Zikai and MIAO, Qian. N-phenylated N-heteroacenes: synthesis, structures and properties. *Chempluschem.* 2017. Vol. 82, no. 7, p. 1034-1038.
233. LI, Minghan, WANG, Yanyan, XU, Haoyuan, ZHANG, Houcheng, ZHANG, Jing, ZHU, Yuejin and HU, Ziyang. Performance improvement of perovskite solar cells via spiro-OMeTAD pre-crystallization. *Journal of Materials Science.* 2020. Vol. 55, no. 26, p. 12264-12273.
234. COWIE, J. M. G., REID, V. M. C., MCEWEN, I. J. Effect of side chain length on the glass transition of copolymers from styrene with n-alkyl itaconimides and with n-alkyl itaconimides. *British Polymer Journal.* 1990. Vol. 23, no. 4, p. 353-357.
235. DANEKAMP, Benedikt, DROSEROS, Nikolaos, TSOKKOU, Demetra, BREHM Verena, BOIX, Pablo P., SESSOLO, Michele, BANERJI, Natalie, and BOLINK, Henk J. Influence of hole transport material ionization energy on the performance of perovskite solar cells. *J. Mater. Chem. C.* 2019. Vol. 7, no. 3, p. 523-527.
236. BUBNIENE, Giedre, MALINAUSKAS, Tadas, DASKEVICIENE, Maryte, JANKAUSKAS, Vygtintas and GETAUTIS, Vytautas. Easily functionalizable carbazole based building blocks with extended conjugated systems for optoelectronic applications. *Tetrahedron.* 2010. Vol. 66, no. 17, p. 3199–3206.

237. MALINAUSKAS, Tadas, TOMKUTE-LUKSIENE, Daiva, DASKEVICIENE, Maryte, JANKAUSKAS, Vygintas, JUSKA, Giedrius, GAIDELIS, Valentas, ARLAUSKAS, Kestutis and GETAUTIS, Vytautas. One small step in synthesis, a big leap in charge mobility: diphenylethenyl substituted triphenylamines. *Chemical communications (Cambridge, England)* [online]. 2011. Vol. 47, no. 27, p. 7770–2. DOI 10.1039/c1cc12700d. Available from: <http://www.ncbi.nlm.nih.gov/pubmed/21643601>.
238. LIN, Yuze, FAN, Haijun, LI, Yongfang and ZHAN, Xiaowei. Thiazole-based organic semiconductors for organic electronics. *Adv. Mater.* 2012. Vol. 24, no. 23, p. 3087–3106.
239. LI, Wei, WANG, Zheming, DESCHLER, Felix, GAO, Song, FRIEND, Richard and CHEETHAM, Anthony K. Chemically diverse and multifunctional hybrid organic–inorganic perovskites. *Nat Rev Mater.* 2017. Vol. 2, no. 3, p. 16099. DOI: 10.1038/natrevmats.2016.99. Available from: <https://www.nature.com/articles/natrevmats201699>.
240. TRIFILETTI, Vanira, DEGOUSEE, Thibault, MANFREDI, Norberto, FENWICK, Oliver, COLELLA, Silvia and RIZZO, Aurora. Molecular Doping for Hole Transporting Materials in Hybrid Perovskite Solar Cells. *Metals* [online]. 2020. Vol. 10, no. 1, p. 14. DOI: 10.3390/met10010014. Available from: <https://www.mdpi.com/2075-4701/10/1/14>.
241. ZHANG, Mingyu and ZHAN, Xiaowei. Nonfullerene n-type organic semiconductors for perovskite solar cells. *Adv. Energy Mater.* 2019. Vol. 9, no. 25, p. 1900860.
242. MALI, Sawanta S. and HONG, Chang Kook. p-i-n/n-i-p type planar hybrid structure of highly efficient perovskite solar cells towards improved air stability: synthetic strategies and the role of p-type hole transport layer (HTL) and n-type electron transport layer (ETL) metal oxides. *Nanoscale.* 2016. Vol. 8, no. 20, p. 10528-10540.
243. KASPARAVICIUS, Ernestas, MAGOMEDOV, Artiom, MALINAUSKAS, Tadas, GETAUTIS, Vytautas. Long-term stability of the oxidized hole-transporting materials used in perovskite solar cells. *Chem. - A Eur. J.* 2018. Vol. 24, no. 39, p. 9910–9918.
244. BABAEI, Azin, ZANONI, Kassio P. S., GIL-ESCRIG, Lidón, PEREZ-DEL-REY, Daniel, BOIX, Pablo P., SESSOLO, Michele, BOLINK, Henk J. Efficient vacuum deposited p-i-n perovskite solar cells by front contact optimization. *Frontiers in chemistry.* 2020. Vol. 7, p. 936. DOI: 10.3389/fchem.2019.00936. Available from: <https://www.frontiersin.org/articles/10.3389/fchem.2019.00936/full>.
245. BABAEI, Azin, DREESSEN, Chris, SESSOLO, Michele and BOLINK, Henk J. High voltage vacuum-processed perovskite solar cells with organic semiconducting interlayers. *RSC Adv.* 2020. Vol. 10, no. 11, p. 6640-6646.
246. PEREZ-DEL-REY, Daniel, GIL-ESCRIG, Lidón, ZANONI, Kassio P. S., DREESSEN, Chris, SESSOLO, Michele, BOIX, Pablo P. and BOLINK, Henk J. Molecular passivation of MoO₃: band alignment and protection of charge transport

- layers in vacuum-deposited perovskite solar cells. *Chem. Mater.* 2019. Vol. 31, no. 17, p. 6945–6949.
247. YUAN, Dandan, TIAN, Lei, LI, Zhida, JIANG, Hong, YAN, Chao, DONG, Jing, WU, Hongjun and WANG, Baohui. Solar thermo-coupled electrochemical oxidation of aniline in wastewater for the complete mineralization beyond an anodic passivation film. *Sci. Rep.* 2018. Vol. 8, p. 3103. DOI: 10.1038/s41598-018-21473-z. Available from: <https://www.nature.com/articles/s41598-018-21473-z>.
248. BUTOI, Bogdan, GROZA, Andreea, DINCA, Paul, BALAN, Adriana and BARNA, Valentin. Morphological and structural analysis of polyaniline and poly(o-anisidine) layers generated in a DC glow discharge plasma by using an oblique angle electrode deposition configuration. *Polymers* [online]. 2017. Vol. 9, p. 732. DOI: 10.3390/polym9120732. Available from: <https://www.mdpi.com/2073-4360/9/12/732>.
249. PUODZIUKYNAITE, E., BURBULIS, E., GRAZULEVICIUS, J.V., JANKAUSKAS, V., UNZENAS, A., LINONIS, V. Aniline-based bis(enamines) as new amorphous molecular charge transport materials. *Synthetic Metals.* 2007. Vol. 157, no. 18, p. 696-701.
250. GARCIA, M.C. Alonso and BALENZATEGUI, J.L. Estimation of photovoltaic module yearly temperature and performance based on Nominal Operation Cell Temperature calculations. *Renewable Energy.* 2004. Vol. 29, no. 12, p. 1997-2010.
251. MIYAMOTO, Eiichi, YAMAGUCHI, Y and YOKOYAMA, M. Ionization potential of organic pigment film by atmospheric photoelectron emission analysis. *Electrochemistry.* 1989. Vol. 28, p. 364–370.
252. CARDONA, Manuel and LEY, Lothar. Photoemission in solids I. Photoemission in Solids I: General Principles. 1978.
253. VAEZI-NEJAD, S M. Xerographic time of flight experiment for the determination of drift mobility in high resistivity semiconductors. *International Journal of Electronics Theoretical and Experimental.* 1987. Vol. 62, no. 3, p. 361–384.
254. CHAN, ARCHIE Y C and JUHASZ, C. Xerographic-mode transient charge technique for probing drift mobility in high-resistivity materials. *International Journal of Electronics Theoretical and Experimental.* 1987. Vol. 62, no. 4, p. 625–632.
255. WANG, Ming, LI, Cuihong, LV, Aifeng, WANG, Zhaohui, BO, Zhishan, ZHANG, Fengling. Synthesis and photovoltaic behaviors of benzothiadiazole- and triphenylaminebased alternating copolymers. *Polymer.* 2012. Vol. 53, no. 2, p. 324-332.
256. HUANG, Sheng-Tung, LIAW, Der-Jang, HSIEH, Li-Ga, CHANG, Chin-Chuan, LEUNG, Man-Kit, WANG, Kun-Li, CHEN, Wen-Tung, LEE, Kueir-Rarn, LAI, Juin-Yih, CHAN, Li-Hsin, CHEN, Chin-Ti. Synthesis and electroluminescent properties of polyfluorene-based conjugated polymers containing bipolar groups. *Journal of Polymer Science: Part A: Polymer Chemistry.* 2009. Vol. 47, no. 22, p. 6231–6245.

257. YUAN, Mao-Sen, ZHAO, Li and ZHANG, Ran-rong. 9-Ethyl-9H-carbazole-3-carbaldehyde. *Acta Crystallographica Section E* [online]. 2010. Vol. 66, no. 8, p. O1885-U1717. DOI: 10.1107/S1600536810025183. Available from: <http://scripts.iucr.org/cgi-bin/paper?S1600536810025183>.
258. KOUNO, Hironori, KAWASHIMA, Yusuke, TATEISHI, Kenichiro, UESAKA, Tomohiro, KIMIZUKA, Nobuo and YANAI, Nobuhiro. Nonpentacene Polarizing Agents with Improved Air Stability for Triplet Dynamic Nuclear Polarization at Room Temperature. *J. Phys. Chem. Lett.* 2019. Vol. 10, no. 9, p. 2208-2213.
259. BIAN, Lei, MA, Jie, FENG, Xiaotong, WANG, Yuanhang, ZHAO, Lizhi, ZHAO, Lei, WANG, Xiayan, GUO, Guangsheng and PU Qiaosheng. Wavelength selective photoactivated autocatalytic oxidation of 5,12-dihydrobenzo[b]phenazine and its application in metal-free synthesis. *RSC Advances*. 2020. Vol. 10, no. 17, p. 9949-9954.
260. CHEN, Jing, DENG, Xianping, YANG, Daobin, HUO, Erfu, CHEN, Yunqing, HUANG, Yan and LU, Zhiyun. Synthesis and Photovoltaic Properties of Conjugated Copolymers Bearing bis(9,9-di(2-ethylhexyl)-9H-fluoren-2-yl)quinoxaline Subunit with Deep HOMO Level. *Asian Journal of Chemistry*. 2014. Vol. 26, no. 18, p. 5959-5966.
261. DEGUTYTE, Rimgaile, DASKEVICIENE, Maryte, STUMBRAITE, Jolanta and GETAUTIS, Vytautas. Synthesis of a bifunctional 1,2,3,4-tetrahydroquinoline derivative: 1,8-bis(9-ethyl-9H-carbazol-3-yl)-1,2,3,4,5,6,7,8-octahydroquino[5,6-f]quinoline-3,6-diol. *ARKIVOC* [online]. 2009. Vol. 2009, p. 115-122. DOI:10.3998/ark.5550190.0010.b11. Available from: <https://quod.lib.umich.edu/a/ark/5550190.0010.b11/1/--synthesis-of-a-bifunctional-1234-tetrahydroquinoline?page=root;size=150;view=text>
262. MOULIN, Emilie, NIESS, Frederic, MAALOU, Mounir, BUHLER, Eric, NYRKOVA, Irina and GIUSEPPONE, Nicolas. The Hierarchical Self-Assembly of Charge Nanocarriers: A Highly Cooperative Process Promoted by Visible Light. *Angew. Chem. Int. Ed.* 2010. Vol. 49, no. 39, p. 6974-6978.

8. CURRICULUM VITAE

Personal information

Name, Surname Matas Steponaitis
Date of birth January 08, 1992
Place of birth Lithuania
Nationality Lithuanian
e-mail m.steponaitis@gmail.com, matas.steponaitis@ktu.lt

Education

since 2017 Kaunas University of Technology – Chemistry PhD studies
2015–2017 Kaunas University of Technology – Master of chemistry
2011–2015 Kaunas University of Technology – Bachelor of chemistry
2003–2011 Kaunas Varpo Secondary School

Work experience

Since May 2020 Project junior researcher
May 2018 – May 2020 Project junior researcher
Jan 2018 – Apr 2018 Project engineer
Oct 2014 – Jan 2017 Project researcher

Languages

Lithuanian - mother tongue. English (C1), German (B1)

Scientific work

Sept 2013 – present Scientific work at prof. dr. Vytautas Getautis scientific group

Aim of the work: synthesis and characterization of stable organic photo semiconductors for novel applications in perovskite solar cells

Feb–Mar 2016 Internship at prof. Henry Snaith (Oxford Department of Physics) group. Aim of the internship: fabrication of perovskite solar cells

Awards

Feb 20, 2018 Research Council of Lithuania annual award for student scientific work *Organiniai pyridinio ir ketvirtinio amonio dariniai: sintezė ir puslaidininkinių savybių tyrimas*

9. LIST OF AUTHOR'S PUBLICATIONS AND CONFERENCES

Publications in peer-reviewed journals

1. Steponaitis, M., Komskis, R., Kamarauskas, E., Malinauskas, T., Jursenas, S., Getautis, V. Investigation of photophysical properties of triphenylamine phenylethenyl derivatives containing tertiary amine groups. *Dyes and Pigments*. 2019. Vol. 166, p. 122-129. (IF=4.018; Q1)
2. Steponaitis, M., La-Placa, M. G., Kaya, I. C., Bubniene, G., Jankauskas, V., Daskeviciene, M., Sessolo, M., Malinauskas, T., Bolink, H. J. and Getautis, V. Enamine-based hole transporting materials for vacuum-deposited perovskite solar cells. *Sustainable Energy & Fuels*. 2020. Vol. 4, p. 5017-5023. (IF=5.503; Q1)

Presentations in conferences

- 2020.05.26 Conference „HOPV20”, online. Poster presentation „Easily Obtainable Hole Transporting Materials for Vacuum-deposited Perovskite Solar Cells“
- 2019.11.03 Conference „nanoGe Fall Meeting19”, Berlin, Germany. Poster presentation „Polymeric triphenylamine derivatives for perovskite solar cells“
- 2019.10.03 Conference „43-ioji Lietuvos nacionalinė fizikos konferencija”, Kaunas, Lithuania. Poster presentation „Charge transport properties of novel enamines with different central group“
- 2019.08.19 21 international conference-school „Advanced materials and technologies 2019“, Palanga, Lithuania. Poster presentation „Investigation of properties of triphenylamine derivatives containing quaternary ammonium groups“
- 2019.07.07 Conference „OP 2019”, Vilnius, Lithuania. Poster presentation „Triphenylamine polymers as hole transporting materials for application in perovskite solar cells“
- 2019.05.16 Conference „Chemistry & Chemical Technology 2019”, Vilnius, Lithuania. Poster presentation „Investigation of properties of triphenylamine phenylethenyl derivatives containing tertiary amine groups“
- 2018.09.17 Conference „E-MRS fall meeting”, Warsaw, Poland. Poster presentation „Additive-free triphenylamine derivative polymeric hole transport materials for stable perovskite solar cells“
- 2017.10.11 Conference „Youngchem 2017”, Lublin, Poland. Poster presentation „Novel additive-free triphenylamine based polymers for applications in perovskite solar cells“

10. ACKNOWLEDGEMENTS

The credit for this thesis cannot go solely to me since I received great help from Assoc. prof. Dr. T. Malinauskas who has been guiding me through murky scientific waters for the last eight years, Prof. Dr. V. Getautis who gave me the opportunity to work in his science group and travel through Europe presenting our research, coauthors and colleagues who did the measurements that I was ill-equipped for or whenever I lacked the scientific knowledge or expertise to accomplish them.

UDK 547.233+621.383.51](043.3)

SL 344. 2021-*-* , * leidyb. apsk. I. Tiražas 16 egz. Užsakymas *
Išleido Kauno technologijos universitetas, K. Donelaičio g. 73, 44249 Kaunas
Spausdino leidyklos „Technologija“ spaustuvė, Studentų g. 54, 51424 Kaunas